Chaos and high-frequency self-pulsations in a laser diode with phase-conjugate feedback.

Andreas Karsaklian Dal Bosco Karsaklian Dal Bosco

Supélec

N^o d'ordre: 2013-16-TH

SUPELEC

École Doctorale EMMA

"Énergie, Mécanique et Matériaux"

THÈSE DE DOCTORAT

DOMAINE : SPI

Spécialité: Photonique

Soutenue le 24 septembre 2013

par :

Andreas KARSAKLIAN DAL BOSCO

Chaos and high-frequency self-pulsations in a laser diode with phase-conjugate feedback

Directeur de thèse:	Marc SCIAMANNA	Professeur, Supélec, Metz
Directeur de thèse:	Delphine WOLFERSBERGER	Professeur, Supélec, Metz

Composition du jury:

Président du jury:	Thomas ERNEUX	Directeur de recherches FNRS, Université Libre de Bruxelles
Rapporteurs :	Frédéric GRILLOT	Maître de conférences, Télécom ParisTech, Paris
	Cristina MASOLLER	Professeur, Universitat Politècnica de Catalunya, Barcelone
Examinateur:	Jamal DAAFOUZ	Professeur, Université de Lorraine, Nancy
	K. Alan SHORE	Professeur, Bangor University, Pays de Galles

Remerciements

Je souhaite remercier tout d'abord mes directeurs de thèse Delphine Wolfersberger et Marc Sciamanna qui m'ont accompagné pendant ces trois années de thèse. Leur attention, leurs conseils et leur soutien m'ont permis de mener à terme l'étude présentée dans ce manuscrit. Un grand merci aussi à mes collègues de bureau Vianney, Martin et Mathieu ainsi que Bilal, Lucie et Édouard pour la bonne ambiance quotidienne sans oublier tous les doctorants du LMOPS avec qui nous avons passé de très bons moments entre thésards. Je tiens aussi remercier les membres du service technique du campus de Metz de Supélec pour leur disponibilité et leur aide apportée.

J'adresse un grand merci aux personnes qui ont aussi contribué rendre mon quotidien Supélec agréable, en parallèle des activités liées à la thèse:
- les professeurs de langues vivantes Beate, Daniela, Giuliana, Ludmila, Maroun, Marta, Nuria et Yumi pour l'occasion qu'ils m'ont donnée de m'ouvrir un peu à d'autres langues et de me changer les idées de temps en temps.
- La communauté du D20 qui m'a suivi et encouragé de près ou de loin tout le long de ma thèse, et surtout Loïs-Brian, Jean-François, Laurian, Jonathan, Claire-Astrid, Damien, Irène et William.
- Les différentes promos d'élèves de Supélec présents sur le campus de Metz avec qui je garde d'excellents souvenirs, en particulier Guillaume, Romain, Achile, tous les Shakes'beer ainsi que les Toqu'art.
- Et bien évidemment, Bilal et Rémi pour tout le temps pass fidèlement ensemble parsemé de discussions métaphysiques fructueuses autour des repas.

Un grand merci final à tous ceux qui ont montré de l'intérêt pour mon travail de thèse.

Je souhaite enfin bon courage à Martin, Mathieu, Noémi et Émeric qui poursuivent ou démarrent leur aventure de thèse dans le labo.

Contents

Chapter 1

Introduction

LASER stands for "Light Amplification by Stimulated Emission of Radiation". The first laser device was designed in 1960 by Theodore Maiman who used a solid state ruby crystal to generate a red laser light [1]. In 1962 the first semiconductor laser was born and since then advances in the technology have put laser devices at the center of our quotidian lives. Nowadays, semiconductor lasers –or laser diodes– are the most commonly used laser devices in the world.

Laser diodes find applications in many fields of technology, engineering and research: telecommunications, measurement, controls, medical therapeutics, data storage etc. Their reduced cost, the possibility to produce them at large scales on semiconductor wafers and to cover large wavelength spans have resulted in their fast and effective integration in many domains of activity. The semiconductor laser thriving development is drawing more and more theoretical and experimental research topics such as range-finding, photonic sampling for analog-to-digital conversion, optical code-division-multiple-access systems for secure communication, infra-red countermeasures, spectroscopic sensing, atomic clock state preparation, quantum key cryptography, water purification and photodynamic therapy. Laser devices have the particularity to generate single-frequency coherent beams showing narrow linewidth, which makes them suitable for interferometric and spectroscopic applications.

In this manuscript, we focus on the study of the laser dynamics when subject to optical feedback. We speak of optical feedback when part of the emitted beam is partially sent back towards the laser, typically after reflection. Feedback is not only due to reflections on mirrors inserted on the beam's path on purpose. It often comes from an undesired reflection on an interface such as an optical fibre connector. Optical feedback is a well-known phenomenon which causes instabilities in the laser power. That is why laser systems usually try to reduce it as much as possible, by inserting for instance optical isolators on the beam's path in order to prevent back reflections.

Our purpose here is indeed to study how optical feedback destabilizes the laser dynamics. More specifically, we will focus on a particular nature of feedback termed phase-conjugate feedback. This nonlinear optical phenomenon will be properly defined in the next chapter. Optical feedback is typically an undesired situation mostly because of the induced instabilities in the power and the resulting impossibility to control the device. Yet we show here that feedback can make the laser exhibit a huge wealth of dynamics, among which high-frequency pulsations and chaos. Indeed, the presence of feedback enables the laser to follow a cascade of bifurcations leading to nonlinear dynamics, by contrast to the ordinary laser applications which operate mostly in steady state.

Nonlinear systems are inherent to nature and most physical systems are nonlinear, among which the most famous are atmospheric behaviors and fluid dynamics. The equation describing such systems are difficult to solve and are at the origin of particular phenomena such as chaos. Chaos theory was initiated by Henri Poincaré at the end of the 19^{th} century with the study of the three-body problem. Chaotic systems are deterministic systems showing sensitivity to initial conditions. A famous illustration of this sensitivity is the "Butterfly Effect" presented in a conference talk by Edward Lorenz in 1972 before the American Association for the Advancement of Science: *Does the Flap of a Butterfly's Wings in Brazil Set Off a Tornado in Texas?* Indeed, a slight change in the initial conditions of a chaotic system may lead to totally different behaviors in the long term [2].

Therefore we combine here both nonlinear system dynamics and nonlinear optics in order to characterize a laser diode with phase-conjugate feedback. A semiconductor laser with feedback can be seen as a nonlinear oscillator governed by internal and external parameters, each one being characterized by its own time scale. As we are about to discuss, in its free running operation a laser diode is a damped nonlinear oscillator showing relaxation oscillations. Then with the addition of a time-delayed optical feedback, the laser undergoes a cascade of bifurcations that depends on the feedback strength and on the interplay between the time scales of both the relaxation oscillations and the feedback delay. The configuration using phase-conjugate feedback adds another nonlinear optics time scale which is the feedback build-up time. Its impact on the laser dynamics remains to be clarified. Consequently, the laser dynamics is strongly dependent on the relative strengths of these factors which are always present and show their own signatures in the laser power and spectrum.

We present here theoretical and experimental results on the dynamics of a laser diode with phase-conjugate optical feedback. We also discuss the fundamental differences that are expected compared to the case of conventional feedback. Besides the interest in terms of applications of a laser diode showing nonlinear dynamics, the fundamental understanding of a nonlinear system with time-delayed feedback is our purpose here. Indeed, the feedback not only causes the laser to show unpredictable fast fluctuations typical of chaotic states but self-pulsing states at high frequencies can also be achieved, opening thus a way to other kinds of applications.

Although phase-conjugate feedback has been studied for more than 30 years, several issues remain to be addressed. Moreover, as demonstrated in this manuscript, new physical phenomena are still likely to be discovered with this configuration.

Outline of the manuscript

In chapter 2, we briefly remind the reader of the laser physics and the state of the art of laser diodes with optical feedback. We also define the terms and parameters that will be studied in the following chapters.

Chapter 3 presents the experimental setup that we designed in order to study the nonlinear dynamics of the laser diode. Phase-conjugate feedback generation techniques and suitable media are presented. Then the properties of the phase-conjugate mirror in terms of reflectivity and response time are discussed. The effects of a very low feedback ratio on the laser threshold current and spectral width are illustrated as well.

In chapter 4, we present the theoretical model on the basis of which we will be carrying out simulations of the laser dynamics. The validity of the model coding, the first bifurcation diagrams depicting a route to chaos and comparisons with another simulated model of the system are discussed.

Chapter 5 extends the study of the nonlinear dynamics initiated in chapter 4 to larger feedback ratio values. We show evidence of a chaos crisis and chaos suppression undergone by the laser as the feedback ratio increases. The consequent birth of bistability between pulsing solutions is highlighted as well. Then, the influence of the simulation parameters is discussed to show both that the presented results cover large spans of parameters and how the system's dynamics evolves as the operational parameters are varied.

The first in-depth experimental analysis is presented in chapter 6. We show evidence of self-pulsing solutions and the way they get stabilized and destabilized according to the variation of the feedback ratio. We also bring theoretical confirmation to those experimental observations with qualitatively good accordance. We further demonstrate experimentally and theoretically that pulsing solutions at multiples of the external cavity frequency are possible. This major contrast to the case of conventional optical feedback is discussed as well.

Chapter 7 establishes a comparison between four well-known configurations in which a laser with optical feedback shows pulsing dynamics. The spectral characteristics of each of these configurations are discussed and compared. We focus on the main spectral differences between the self-pulsing states seen in the case of phase-conjugate feedback and other well-known pulsing states studied in the literature.

Chapter 8 reports on results that have been observed in the experiment in the continuity of the configuration of chapter 6. More precisely, as we will discuss all along this manuscript, changing the feedback delay induces a dramatic change in the laser dynamics. The experimental configuration in chapter 8 is the same as in chapter 6 but for the feedback delay, which is increased. We show evidence of extreme events appearing in the laser power and the interesting evolution in their number and their statistical time distribution as the feedback strength increases. A brief theoretical confirmation of the presence of extreme events is illustrated too.

In chapter 9, the feedback delay is further increased compared to chapter 8, which unlocks another dynamical state in the laser power. We tackle the birth and evolution of low-frequency fluctuations. We find that the time interval separating power dropouts can show optimal regularity for a given value of the feedback ratio. As we will discuss, this situation corresponds to a deterministic case of coherence resonance. We also confirm with numerical simulations the transition to the low-frequency fluctuations dynamics with time traces and spectra showing qualitatively different features according to the feedback ratio.

Finally, we bring a summary of the results with the main novelties compared to the existing studies in the domain. We also suggest perspectives and research directions in nonlinear laser dynamics with phase-conjugate feedback for a further experimental and theoretical continuation of this work.

Chapter 2
Background and motivations

Nothing has such power to broaden the mind as the ability to investigate systematically and truly all that comes under thy observation in life. Marcus Aurelius

Before entering in the systematic study of the nonlinear dynamics of laser diodes, we begin with a short presentation of the physical principles of laser beam generation. We also define in this section parameters on which we will focus later.

2.1 Laser diodes: physics and dynamics

2.1.1 Laser beam generation

All laser devices have common properties about beam generation. The photons emitted by the laser are originated by stimulated emission in a gain medium bounded by a resonator. Within a laser cavity, three optical phenomena are in competition: spontaneous emission –in which photons are randomly generated without correlation–, stimulated emission –where the generation of coherent photons is induced by an initial photon– and photon absorption. They are illustrated in Fig.2.1.

Naturally, absorption is an undesired effect since it causes photon loss in the laser cavity. Besides, spontaneous emission acts against the process of laser beam emission since the emitted photons are incoherent. In contrast to spontaneous emission, stimulated emission of photons is a cascade phenomenon in which an initial photon causes a coherent generation of a multitude of identical photons.

The laser operating point is decided by the interplay between those three competing phenomena. According to the injection current, one in favored compared to the two others. The laser light-current characteristic plots the optical power emitted by the laser P versus the injection current I. When the current reaches a particular value termed laser threshold current I_{th}, the laser operates in the stimulated emission state. Fig.2.2 illustrates the laser operating states versus the current.

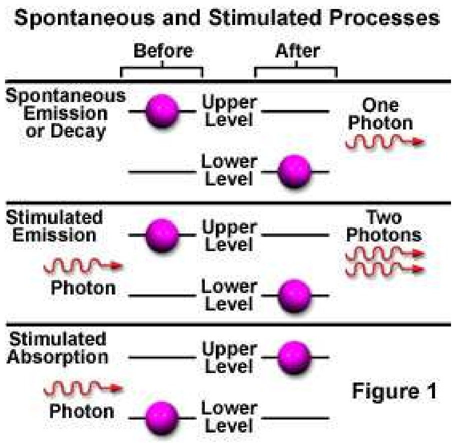

Figure 2.1: Principles of spontaneous emission, stimulated emission and absorption.

At threshold, the optical gain achieved thanks to stimulated emission compensates the cavity losses and subsequently, any addition of carriers through the electrical driving current is proportionally converted into stimulated photons. This corresponds to the linear part of the L-I laser characteristic in Fig.2.2 tagged "laser light emission".

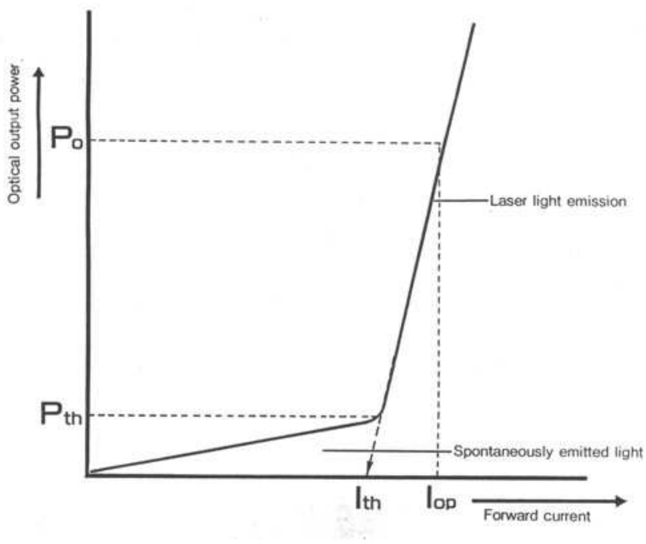

Figure 2.2: Typical light-current laser characteristic. For values of the current beneath the threshold ($I < I_{th}$), the laser operates in a spontaneous emission state. When the current is above I_{th}, stimulated emission is favored and the laser is operational.

The three main ingredients constituting a laser are:
1/ A gain medium, in which stimulated emission and beam amplification occur.
2/ A resonator bounding the gain medium and performing wavelength selection.
3/ A source of energy, termed pumping, to perform carrier inversion.

2.1.2 Semiconductor lasers

Gain medium

In a semiconductor laser –or laser diode–, the gain medium is a semiconductor. The choice of the medium depends on the wavelength for which the laser is designed. Indeed, the energy of the emitted photons E –which is related to their wavelength λ by: $E = h\frac{c}{\lambda}$, where h is the Planck constant– depends on the gap energy of the semiconductor constituting the gain medium. Fig.2.3 displays the ranges of wavelength that can be reached with common semiconductor media. As a consequence, a given medium is able to generate photons in a given span of wavelengths, for which the gain g is sufficient.

It is interesting to notice that the family of ternary and quaternary materials AlGaAs, InGaAsP and InGaAsSb allows to grow epitaxial layers with varying bandgaps while keeping the value of the lattice constant almost constant.

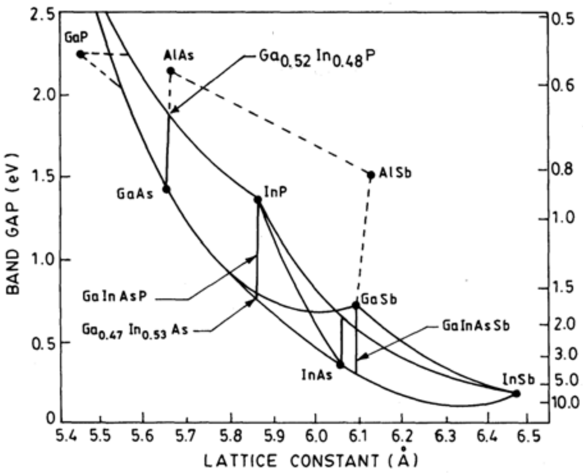

Figure 2.3: Diagram showing the relationship between the emitted wavelengths, the material bandgaps and lattice constants for semiconductor active media.

Resonator

The resonator is shaped by cleaving the semiconductor medium. The facets have the role of both natural mirror and output facets. The standard reflectivity of the cleaved facets in edge-emitting semiconductor lasers is 30%. This value is due to the contrast of refractive index n at the interface between the semiconductor ($n_{semiconductor} \simeq 3.5$) and the air ($n_{air} \simeq 1$). Another important role of the cavity is the wavelength selection. Indeed, the cavity only allows the propagation of waves, termed longitudinal cavity modes, which wavelengths fulfill the condition $2L = p\lambda$ where L is the cavity length – which is the distance between the two facets– and p an integer. This condition is termed phase condition.

As we mentioned, the semiconductor is both a gain medium (suitable for stimulated emission) and a loss medium (absorption and spontaneous emission). Therefore, a given medium is convenient to generate a laser beam when the gain compensates all the losses. The mathematical formulation of the gain condition is $\Gamma g = \alpha_i + \alpha_m$, where Γ is the optical confinement factor, α_i represents the intracavity losses and α_m represents the losses due to the mirrors. According to the injection current, the values of g, α_i and α_m change. The gain condition is fulfilled when the current reaches I_{th}.

Electrical pumping

The beam of a laser diode is a flow of photons generated by recombination of charge carriers (electrons and holes) injected into a semiconductor material. The operating point of the laser is driven by the injection current I. Its role is to favor stimulated emission with respect to spontaneous emission and absorption. Indeed it can be shown that in a semiconductor medium the energy separation of quasi-Fermi levels for the electrons and the holes increases with the increase of the pumping current. As a result, increasing the current leads excited carriers to occupy the conduction band. As demonstrated by Einstein in 1917, this situation –termed population inversion– is a condition for which the stimulated emission rate is higher than both the spontaneous emission and the absorption rates.

As a consequence, the laser is capable to emit beams which wavelengths comply both with the gain and the phase conditions. It is thus operational when the injection current value is large enough to trigger population inversion and to induce an optical gain larger than the cavity losses, *i.e.* when $I \geq I_{th}$. When the current reaches the threshold current value, the gain saturates at the value corresponding to the threshold gain g_{th} and all the charge carriers further injected in the laser for larger current values undergo recombination process to generate photons by stimulated emission.

The standard semiconductor laser structure is the double heterostructure and was first designed by Kroemer in 1963 [3]. It is a semiconductor structure made of layers of dissimilar materials, as presented in Fig.2.4. Heterostructures have the particular property to achieve electrical confinement of the injected carriers in the active layer through potentiel barriers. Besides, optical confinement is achieved through an inhomogeneous refractive index, compelling the generated photons to remain in the active layer as well. This major advance in the laser technology allowed to reach threshold currents of a few tens of mA, as a consequence of a great diminution of the cavity losses.

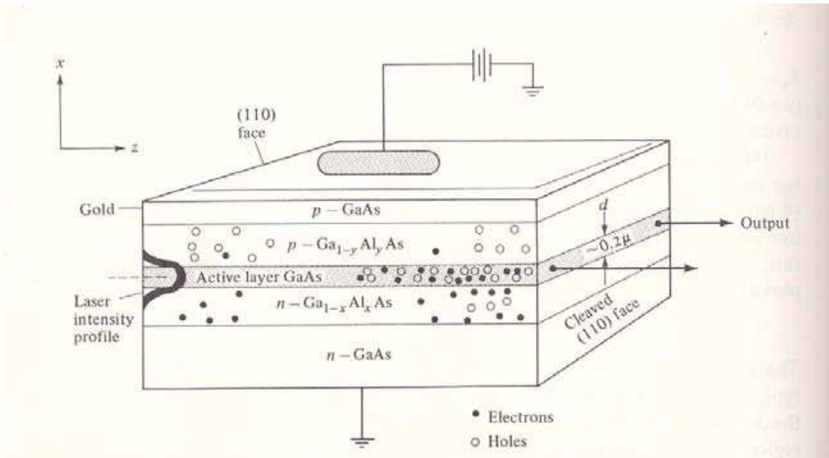

Figure 2.4: Double heterostructure in a GaAs-GaAlAs laser. Image from [4].

Nowadays, research in laser technology shows a non-stop movement towards new ways to have a better control of the emitted beam with a lower threshold current. Breakthroughs in quantum dot and vertical-cavity surface-emitting lasers (VCSELs) are the challenges for the next years in the laser technologies. VCSELs are microcavity lasers with smaller threshold current and larger modulation bandwidth [5]. Quantum dot devices show three-dimensional quantum confinement properties which allow to achieve much higher gain per injected carrier, hence reducing the threshold current below mA [6, 7].

2.1.3 Laser properties

Beam properties

Due to the nature of the stimulated emission process, laser beams are constituted of identical photons. More precisely, a laser beam is a directional, coherent and potentially very powerful beam. The directivity and the coherence of the beam stem from the fact that in the stimulated emission, a generated photon has the same direction and phase as the stimulating photon. The properties of the emitted laser beam are determined by several parameters such as the cavity geometry and the injection current. The simplest beam shape is the Gaussian distribution in which the power radially decreases from the center to the edges of the beam. Yet transverse mode confinement causes higher order transverse modes to appear. Higher order modes have relatively larger widths compared to the Gaussian mode, and thus the fundamental Gaussian mode of a laser may be selected by placing an appropriately sized aperture in the laser cavity [8]. Indeed, the aperture of the cavity controls both the emitted beam power and the beam's shape. Small aperture lasers show Gaussian distributions but have limited power, as in our experiment ($P \leq 50\ mW$). In contrast, large aperture lasers can show powers of some hundreds of mW, yet this high beam power may cause beam instabilities in the cavity such as filamentation [9, 10]. Furthermore, the power distribution of the beam is no longer Gaussian in that case

As the gain in the laser cavity is high and the beam section is usually made very small by the means of a lens apposed to the emitting edge, laser beams show very high optical intensity. As a consequence, they are capable to trigger nonlinear effects in the media through which they propagate.

Relaxation oscillations

The interplay between the oscillation field in the resonator and the electronic state inversion is at the origin of the phenomenon of relaxation oscillations. An increase in the intracavity power results in an increased rate of stimulated emission and consequently in a reduction in the carrier inversion. This in turn causes a reduction in the power and so on. This phenomenon is illustrated in Fig.2.5. Relaxation oscillations are not specific to semiconductor lasers and occur at different time scales according to the nature of the laser. They have been experimentally studied in dye lasers by Gurian *et al.* in 2010 where their frequency has been reported to be close to 25 MHz [11]. In semiconductor lasers the inversion changes in a nanosecond time scale while the photon lifetime ranges some picoseconds [12]. As a consequence, the relaxation oscillation phenomenon occurs at frequencies typically ranging from

1 to 10 GHz.

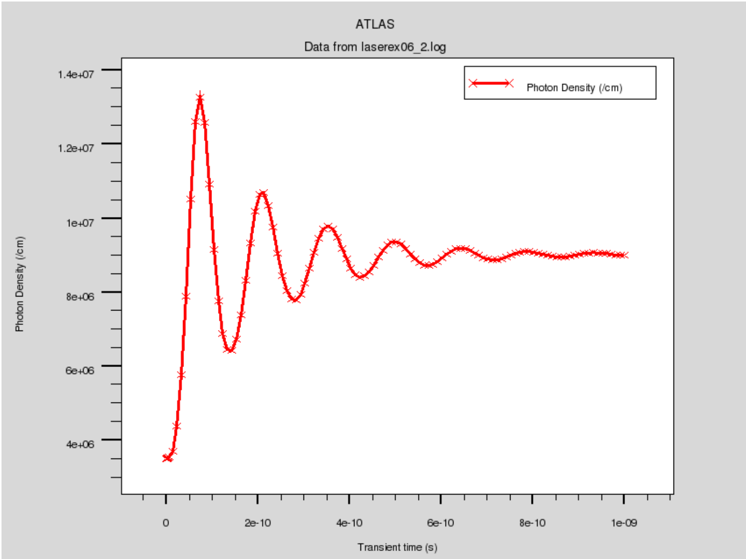

Figure 2.5: Result of a small injection current perturbation, obtained by numerical simulation of a laser diode component using Silvaco. The simulated laser diode is a InP/InGaAsP edge-emitting laser diode. An increase in the carrier density in the laser (caused by the small current impulse) will cause an increase in the gain which results in a rise in the photon density inside the laser. This increase in photon density causes an increase in the stimulated recombination rate which decreases the carrier density. As a result, the photon density falls, which causes the carrier density to rise, and so on. A damped oscillatory process is therefore established at a characteristic frequency termed relaxation oscillation frequency (here close to 7.5 GHz).

The dependance of this frequency on the injection current follows a square root law: $f_{RO} = \frac{1}{2}\sqrt{\frac{1}{\tau_c \tau_p}(\frac{I}{I_{th}} - 1)}$ [12]. τ_c is the carrier lifetime and τ_p is the photon lifetime. The relaxation oscillation frequency is close to the direct modulation frequency limit of a laser diode, *i.e.* the modulation achieved by modulation of its driving current.

Relaxation oscillations can be observed when making a step input in the injection current. Yet, with no external action, they gradually decay if the perturbation is small enough. However, as we will see, under the action of a moderate optical feedback, their decay can be suppressed, allowing thus the laser to show sustained oscillations at the relaxation oscillation frequency.

Linewidth enhancement factor

The laser linewidth enhancement factor, or parameter α, is defined as the ratio of the variation of the real part of the refractive index with carrier density to the variation of the imaginary part of the refractive index with carrier density [12]. The corresponding mathematical formulation is $\alpha = \frac{dn_r}{dN}/\frac{dn_i}{dN}$, where the refractive index of the active layer is written $n = n_r + i.n_i$. n_i is related to the optical gain of the active layer. N is the carrier density. Usually, the values of the α parameter range from 1 to 7 in semiconductor lasers [12]. The parameter α was first introduced by Lax in 1967 [13] and then adapted by Henry in 1982 for the case of semiconductor materials [14] to account for the increased linewidth of laser diodes with respect to what is expected from phase noise. In nonlinear dynamics, it is known that α plays a role in the undamping of the relaxation oscillations and therefore on the nonlinear laser dynamics, self-pulsing and chaos [15]. The value of α gives birth to complex laser dynamics and is responsible for the broad linewidth of laser oscillations. As we will see in chapter 5, a high value of α results in more developed instabilities in the laser power.

Laser rate equations

The dynamics of the solitary laser is described by the laser rate equations. These equations show the interplay between the electric field amplitude S, the phase ϕ and the carrier density n. In the case of a single-mode laser, the rate equations are as given in equation (2.1) [16].

$$\begin{cases} \dfrac{dS}{dt}(t) = \dfrac{1}{2}G_n[n(t) - n_{th}]S(t) \\ \dfrac{d\phi}{dt}(t) = \dfrac{1}{2}\alpha G_n[n(t) - n_{th}] \\ \dfrac{dn}{dt}(t) = \dfrac{J}{ed} - \dfrac{n(t)}{\tau_s} - G_n[n(t) - n_0]S^2(t) \end{cases} \tag{2.1}$$

In those equations, G_n is the linear gain and n_{th} the carrier inversion at threshold. α is the laser linewidth enhancement factor, J the injection current density, e the electric charge and d the thickness of the active layer. τ_s is the carrier lifetime in the laser cavity and n_0 the carrier density at transparency. Those three equations represent the physical phenomena in the active layer. The first equation is the balance of photon gain and losses. The second one describes the coupling between the phase and the carriers, which is ruled by the parameter α. The third equation represents the carrier dynamics, showing their injection J and the competition between the stimulated emission of photons, the spontaneous emission of photons and the non-radiative carrier recombination (characterized by τ_s). This system of equation is the basis of the models on which we will focus to carry on simulations of the laser dynamics.

2.1.4 Unlocking nonlinear dynamics

Lasers are classified in three classes –from A to C– according to their dynamics. This classification was established by Arecchi *et al.* in 1984 [17] and is related to the interplay of three time constants: the relaxation time of the field, the relaxation time of the polarization of the medium and the relaxation time of the carrier inversion. In some cases, one or two among those time constants may be adiabatically eliminated from the rate equations. In this case one or two rate equations are enough to model the laser dynamics.

In class C lasers, the three time scales have the same order of magnitude. Therefore, the three whole rate equations are needed to describe the laser dynamics. Examples of class C lasers are NH_3 and Ne-Xe lasers [16]. Since their dynamics is ruled by differential equations showing three degrees of freedom, they spontaneously show instability and chaos if pumped above a certain threshold.

In class B lasers, the time constant of the medium polarization is small enough –compared to the two other time scales– to be removed from the equations. The dynamics of the laser can be described with only two rate equations. Most semiconductor lasers belong to class B [16] and are the main object of our research. As we mentioned earlier, a laser diode exhibits a rather simple dynamical behavior which are the damped relaxation oscillations. Nonlinear dynamics can be achieved when the laser is further subject to an optical external input beam. This beam can stem from another laser, in which case we speak of optical injection. Chaos and instabilities in semiconductor lasers induced by optical injection have been largely studied [17–19]. Another technique is to send part of the emitted laser beam back into the active layer after reflection on a mirror. This corresponds to the case of optical feedback, which we study in this manuscript.

Class A lasers are easily described by a single equation since the population inversion and medium polarization time constant are very small compared to the relaxation time of the field. Their dynamics are simpler than class B and class C lasers. Yet, they can exhibit chaos when subject to optical feedback as will be discussed in chapter 9. Visible He-Ne and dye lasers are examples of class A lasers [16].

As we are about to discuss, the presence of a feedback beam, even in very small ratios, has dramatic dynamical consequences on the laser. The feedback ratio is a crucial parameter as it decides for the laser dynamical state. Indeed, the feedback ratio can trigger undamped relaxation oscillations, initiating thus a route to chaos through a succession of various states of qualitatively different dynamics. We will illustrate this route to chaos induced by the feedback in the next chapters with theoretical and experimental observation of pulsing and chaotic dynamics. Besides, the feedback time delay is also a very important parameter which determines the resulting dynamical states and impacts on the pulsating temporal waveforms and spectral signatures.

In the following chapters, we study the nonlinear dynamics of a laser diode (class B laser) subject to phase-conjugate feedback. In particular, we will focus on the influence of the feedback rate and the related time delay.

2.2 Laser diodes with conventional optical feedback

2.2.1 Optical feedback generation

Conventional Optical Feedback (COF) is introduced into a laser diode by sending part of its emitted beam back into the laser cavity. Basically optical feedback is performed by aligning a mirror on the beam's path. The distance of the laser to the mirror L is typically of the order of several centimeters and is experimentally precisely tuned by micrometric positioning mechanics. Fig.2.6 shows the common setup to introduce COF in a laser diode.

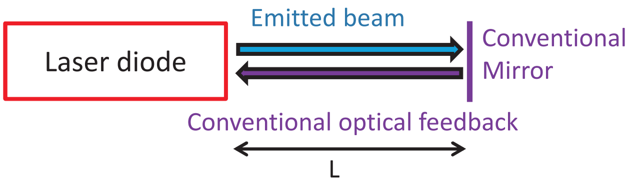

Figure 2.6: Laser diode subject to COF: the mirror reflects part of the beam emitted from the laser back to its cavity.

The introduction of optical feedback results in many dynamical effects on the characteristics of the solitary laser diode, depending on the feedback ratio –or mirror reflectivity– and the distance to the mirror. The feedback ratio is defined as the ratio of the power of the beam entering the laser cavity after reflection on the mirror to the power of the emitted beam: $R = \frac{P_{feedback}}{P_{emitted}}$. Optical feedback dramatically changes the laser features and can be either disadvantageous, as it may be source of instabilities in the laser output power, or advantageous as it can enhance some laser properties such as contributing to side mode suppression, linewidth narrowing, tunability and frequency stability [19–27]. Depending on the feedback ratio, the laser can switch from a given operating state to another, each one being characterized by specific dynamical features.

2.2.2 Route to chaos

In 1986 Tkach and Chraplyvy identified five operating states –or regimes– and classified them on the basis of their spectral properties. As presented in Fig.2.7, the transitions from a regime to another depend on both the feedback ratio and the distance to the mirror.

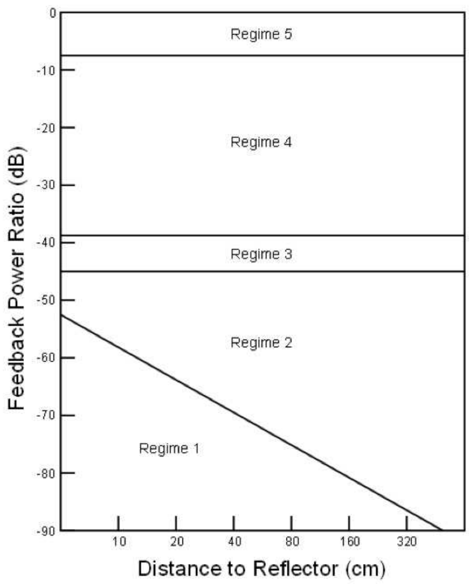

Figure 2.7: Five regimes of operation of a laser diode subject to COF. The amount of feedback and the distance to the mirror determine the operating regime. Figure from [28].

Regime 1 corresponds to the lowest level of feedback ($R < 0.01\%$). The laser shows linewidth narrowing or broadening according to the phase of the feedback beam, that is according to the distance to the mirror.

Regime 2 is reached for feedback ratios up to 0.1%. Mode hopping between external cavity modes induced by the feedback phase occurs. External cavity modes are the modes of the corresponding cavity bounded by the laser output facet and the external mirror. External cavity modes are associated with frequencies multiples of $\frac{c}{2L}$, where c is the celerity of light in the air (assimilated to its velocity in vacuum). Mode hopping phenomena in external cavity lasers have been characterized by Mørk *et al.* in 1990 [29].

Regime 3 exists for a small range of feedback ratio values (close to 1%) and causes linewidth narrowing. In this regime, the distance to the mirror has no consequence.

In regime 4, the feedback ratio is moderate ($R \simeq 1\%$). The laser spectrum shows growing side modes separated from the main mode by the relaxation oscillation frequency. Those side modes are originated from the undamped relaxation oscillations induced by the feedback ratio. The laser spectrum broadens significantly. Besides, the laser may exhibit oscillations, enter coherence collapse state and exhibit chaos. As a consequence, the noise level greatly increases. Again the laser dynamics is insensitive to the feedback phase.

Lastly, for very high values of feedback ratios ($R > 10\%$), the laser enters regime 5. The external cavity behaves as an extension of the laser internal cavity. The system is then equivalent to a short active medium within a very long cavity bounded by the laser back facet and the conventional mirror. Yet, this regime requires an anti-reflection coating on the laser output facet. The laser usually operates on a single narrow-linewidth longitudinal mode defined by the distance to the mirror. The feedback phase has no influence.

The very large number of scientific publications in this field demonstrates the interest in mastering the dynamical properties of laser diodes in order to develop new laser applications taking advantage of their feedback-induced improved features. Researches in the effects of COF on the characteristics of semiconductor lasers have unveiled many interesting dynamical states that are nowadays well-known key results:

1/ Observation of hysteresis and multistability in the laser power have been reported [30].

2/ Laser noise [31–34] and linewidth [35–39] improvement have been performed.

3/ Routes to chaos through undamping of the relaxation oscillations have been identified [40–42] along with pulsing dynamics [43–45] and coherence collapse state [46]. The impact of coherence collapse state on optical transmissions has been experimentally studied [47] as well.

4/ A particular form of chaos named Low-Frequency Fluctuations (LFF) has also been subject to dedicated studies [48–51].

5/ In short cavity configurations, laser diodes show pulsations at the time-delay period modulated by a slower enveloppe. This dynamics was termed Regular Pulse Packages [52] and its bifurcation has been analyzed in detail [53, 54].

6/ Chaotic dynamics can have the dynamical signature of excitability [55] and show coherence resonance when subject to an optimal amount of noise [56].

Several hundreds of papers have been published reporting both theoretical and experimental results in the last decades. However, in spite of extensive research there are still many dynamical aspects of laser diodes with feedback that are not fully understood or explained.

2.2.3 External cavity modes

In order to simulate the dynamics of a laser diode with COF, a commonly-used mathematical model is the system of equations known as the Lang-Kobayashi rate equations [57–59]. This model stems from semiconductor laser rate equations describing the temporal evolution of the photon number, the carrier density and the phase inside the laser active layer when subject to conventional optical feedback. It takes into account the feedback ratio, the external cavity length and other intrinsic parameters of the laser. The Lang-Kobayashi equations write as follows for the complex electric field E and the carrier inversion N [12]:

$$\begin{cases} \dfrac{dE}{dt}(t) = (1+i\alpha)N(t)E(t) + \kappa e^{-iC_p}E(t-\tau) \\ T\dfrac{dN}{dt}(t) = P - N(t) - (1+2N(t))|E(t)|^2 \end{cases} \tag{2.2}$$

P is the normalized pump current above threshold $P = \frac{I-I_{th}}{I_{th}}$, where I_{th} is the laser threshold current. T is the ratio of carrier to photon lifetime and α is the linewidth enhancement factor. The feedback rate κ is proportional to the square root of the mirror reflectivity. τ is the external cavity delay and C_p is the phase of the feedback beam. This system of equations is a valid model for single-mode operating lasers with a moderate feedback ratio and takes into account only one round-trip in the external cavity.

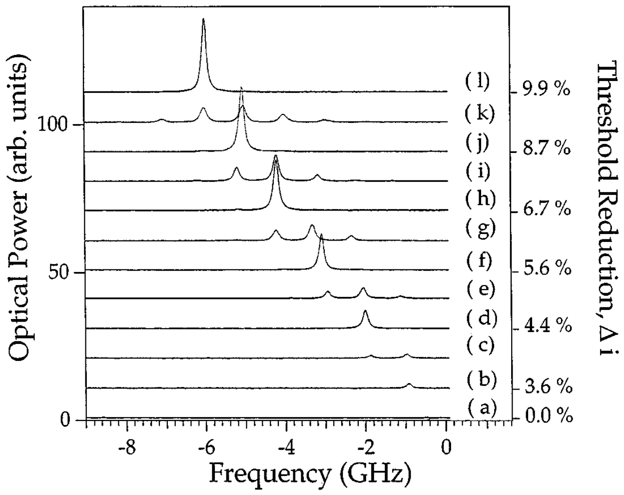

Figure 2.8: Experimental identification of a route to chaos in the optical spectrum of a laser with COF. In this curve, the feedback ratio is calculated from the laser threshold current reduction Δi. Image from [60].

This model has been extensively studied and has shown good compliance with many an experiment as reported in [12]. More precisely, the bifurcation cascade from steady state to chaos through undamped relaxation oscillations and stabilization and destabilization of external cavity modes has been experimentally identified by Hohl and Gavrielides in 1999 [60]. External Cavity Modes (ECMs) are solutions of equations (2.2) of the form $E(t) = Ce^{i\sigma t}$ where C and σ are both constants. The spectral illustration of this bifurcation cascade is given in Fig.2.8 where the evolution of the optical spectra of the laser with the feedback ratio is presented.

In the spectra displayed in Fig.2.8, traces (b), (d), (f), (h), (j), and (l) represent steady states corresponding to stable ECMs. The constant frequency shifting is clearly seen as the feedback ratio increases. The transition between two stable ECMs is depicted in traces (c), (e), (g), (i) and (k) in which sidebands located at the relaxation oscillation frequency rise in the spectra. This illustrates the ECM destabilization process in which the steady states undergo bifurcations leading to oscillating states and further to chaos.

As reported by Petermann in 1995 [20], when a laser diode is subject to COF, a typical route to chaos begins with the appearence of fluctuations at the relaxation oscillation frequency. Then if the feedback ratio increases, successive period doublings occur until a chaotic attractor is created, making

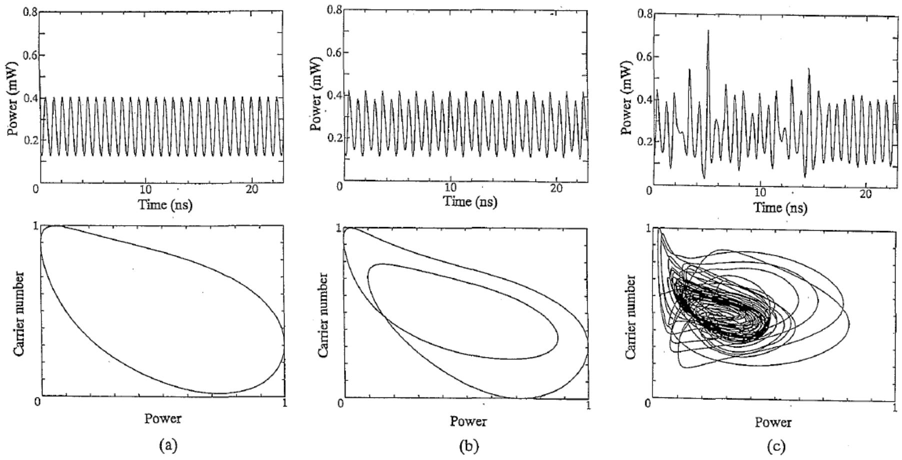

Figure 2.9: Numerical examples of the laser output power and their corresponding attractors for a laser with COF. Trace (a) is a period-one oscillation close to the relaxation oscillation frequency of the solitary laser. The corresponding reflectivity is $R = 1.6\%$. Trace (b) is its corresponding period-two ($R = 1.8\%$), generated by period doubling of trace (a). Trace (c) shows a chaotic state, as expected when the feedback ratio increases ($R = 2\%$). Image from [61].

the laser exhibit chaos. Fig.2.9 illustrates the theoretical route to chaos with simulations carried out by Ohtsubo in 1999 [61].

As illustrated in those experiments and simulations, nonlinear dynamics emerge from bifurcations of ECMs. Each ECM is associated with a lasing frequency defined by the distance from the laser to the external mirror [62]. Indeed, as illustrated in Fig.2.10, the ECM frequencies are distributed on the basis of the external cavity frequency $f_{cav} = \frac{c}{2L}$. Fig.2.10 plots the normalized intensity ($A = |E|^2$) and frequency ($\Delta = \omega_s \tau$) of the ECMs as the feedback rate η varies. The simulated model is the same as in equations (2.2) except that κ is written η. All ECMs but the first one appear in pairs as η increases. The bifurcation through which these ECMs are created is a saddle-node bifurcation. In other words, one of the ECMs is a saddle –also called antimode– and corresponds to the branch of smaller intensity and the other one is a node –also called mode– and corresponds to the branch of higher intensity in Fig.2.10.(a). The ECMs are therefore said to appear in pairs of mode/antimode. An antimode is always an unstable solution while a mode can be stable depending on the value of the feedback ratio.

Fig.2.10.(b) shows that the frequency difference between ECM2 (bottom

curve) and ECM1 (straight line) is close to $\Delta_2 - \Delta_1 = (\omega_{s_2} - \omega_{s_1})\tau = 2\pi(f_{s_2} - f_{s_1})\tau \simeq 2\pi$. Between two consecutive modes, Δ is close to 2π, therefore $f_{mode_2} - f_{mode_1} \simeq \frac{1}{\tau}$. But between a mode and the following antimode, Δ is close to π and $f_{antimode_2} - f_{mode_1} \simeq \frac{1}{2\tau}$. f_1 and f_2 are the frequencies of ECM1 and ECM2 and the detuning between them depends on the feedback ratio. In first approximation, the frequency shift between two consecutive modes equals the external cavity delay: $f_2 - f_1 = \frac{1}{\tau}$.

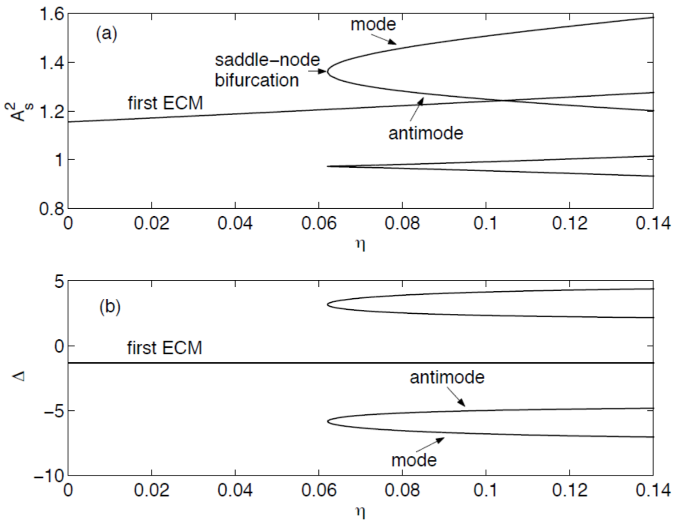

Figure 2.10: Illustration of the frequency shift equal to the external cavity frequency between two consecutive ECMs. This frequency shift depends on the feedback ratio η. For values of η high enough, we can consider that $f_{mode_2} - f_{mode_1} \simeq \frac{1}{\tau}$ and $f_{antimode_2} - f_{mode_1} \simeq \frac{1}{2\tau}$. Image from [63].

Besides, lasers with COF have been reported to exhibit mode hopping between two stable ECMs. Indeed, Sivaprakasam *et al.* showed evidence of external cavity mode hopping [64], as illustrated in Fig.2.11 where the influence of the feedback level on the hopping frequency is studied.

This mode hopping dynamics is an illustration of regime 2 introduced in Fig.2.7, in which the frequency of the mode hopping is depicted for two values of the feedback ratio. The model adopted to obtain the traces displayed in Fig.2.11 is a potential model from which the study of a laser with low feedback level has been extended. The switchings from the non lasing level to the lasing level of one of the ECMs are displayed. Frequency locking has also been reported in the route to chaos [65].

Generally speaking, the exploitation of this model predicts that, when the feedback ratio increases, chaos tends to spread and regions of ECMs tend to

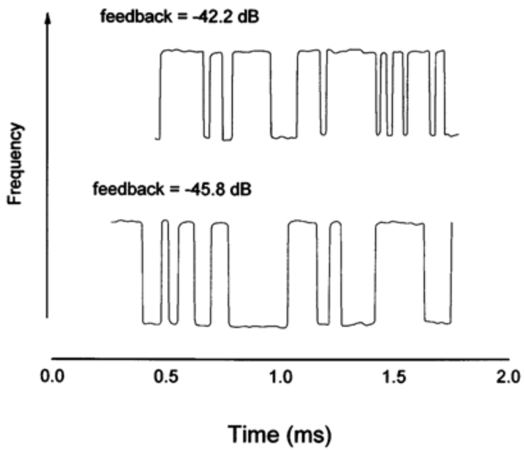

Figure 2.11: Mode hopping as can be seen in regime 2. The mode hopping frequency varies with the feedback ratio. Image from [64].

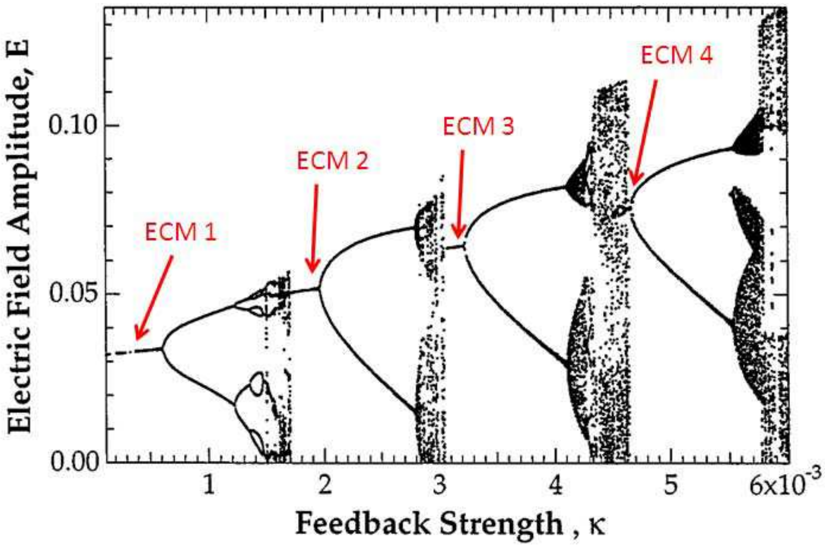

Figure 2.12: Typical bifurcation diagram of a laser with COF. As the feedback strength κ increases the regions of chaos broaden in spite of the regions of stable ECMs. Image from [60].

shrink consequently. This phenomenon is displayed in Fig.2.12 in which the stability domains of the ECMs shrink as the feedback ratio increases. By contrast, the regions of chaos widen consequently.

2.3 Phase-conjugate feedback

We focus here on another type of optical feedback which is Phase-Conjugate Feedback (PCF). PCF is performed with a Phase-Conjugate Mirror (PCM), as presented in Fig.2.13. The experiment is yet more complicated than in the case of a simple COF. Indeed, the PCM is not a single optical component like a conventional mirror. It has to be built and is actually a nonlinear medium in which beam interactions generate the PCF. Yet, from the point of view of the laser, the whole setup to perform PCF is equivalent to a single optical component. Further details about PCF generation will be given in chapter 3.

When optical feedback is performed by phase conjugation, the effects on the operating characteristics of the laser are globally similar in many aspects to those induced by conventional optical feedback. Indeed, in the case of PCF, the laser also exhibits instabilities, linewidth reduction, self-pulsing dynamics and chaos. However, when looking in detail at how the transitions between dynamical states occur, many fundamental differences are found. As a result, in the PCF case, when the feedback ratio increases, the laser undergoes a cascade of bifurcations of a totally different nature from the COF case [66]. The study of laser diodes subject to PCF has attracted considerable attention both theoretically and experimentally. Theoretical analysis is motivated by the fact that the mere addition in the rate equations of a complex conjugate feedback electrical field instead of a conventional one leads to significantly modified nonlinear dynamics compared to the case of COF.

From an experimental point of view, a crucial novelty in the case of PCF compared to the case of COF is the self-alignment of the feedback beam with respect to the emitted beam. This brings the advantage of enhancing the beam coupling parameter since no additional manual alignment of the mirror is required. Moreover, this self-aligning PCF makes the dynamics induced by the feedback less sensitive to the variations of the feedback phase.

Fig.2.13 illustrates PCF generation from a PCM. An incident electromagnetic plane wave of amplitude E, angular frequency ω and propagating in the forward z direction may be written $E(x, y, z, t) = E_0 cos(\omega t - kz - \phi(x, y, z))$. After reflection on the PCM, the corresponding phase-conjugate wave is written $E_{conj}(x, y, z, t) = rE_0 cos(\omega t + kz + \phi(x, y, z))$.
r is the amplitude reflectivity factor of the PCM. Actually those two equations represent the same wave but the longitudinal component of the wave vector k and the transverse phase component ϕ have opposite signs. Further details about phase-conjugate beam generation and wavefront properties will

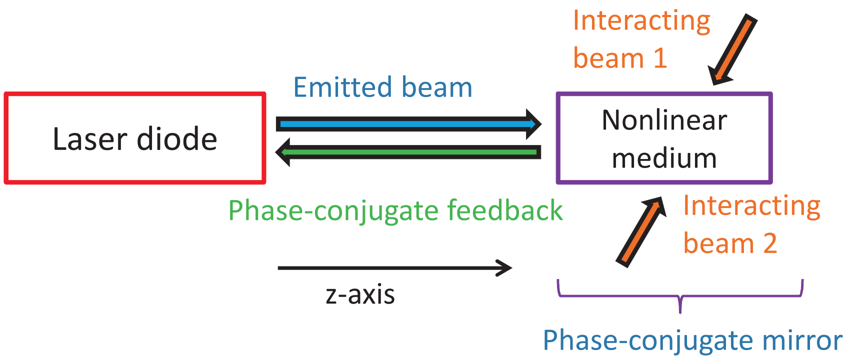

Figure 2.13: Laser subject to phase-conjugate feedback. PCF generation is based on interactions between the laser emitted beam and two other interacting beams in a nonlinear medium. The generation process used in this case is termed Four-Wave Mixing (FWM) [67].

be given in chapter 3.

2.3.1 Theoretical predictions and comparison to the COF case

Naturally, theoretical analysis of laser dynamics with PCF has been carried out along with experimental studies. The most commonly used model of equations for the case of a self-pumped phase conjugator are directly derived from the previous Lang-Kobayashi rate equations (2.2) in which the feedback term has been adapted to take into account the complex conjugate electrical field:

$$\begin{cases} \dfrac{dE}{dt}(t) = (1+i\alpha)N(t)E(t) + \gamma E^*(t-\theta) \\ T\dfrac{dN}{dt}(t) = P - N(t) - (1+2N(t))|E(t)|^2 \end{cases} \tag{2.3}$$

A deeper analysis of this system of equations and its parameters will be given in chapter 4. Briefly, E is the slowly varying optical field, N the carrier inversion, P the normalized pump current with respect to the laser threshold, γ the normalized feedback ratio and θ is the normalized external time delay. The time t is also normalized and is therefore dimensionless. The normalization parameter is the photon lifetime τ_p. The relationship between γ and the feedback rate κ introduced in equations (2.2) is $\gamma = \kappa\tau_p$. γ is dimensionless and in all that follows, it will be referred to as the feedback ratio. We rename here the time delay –previously written τ– into θ which is a dimensionless parameter too. In the following chapters, we use τ to refer to the physical time delay (which has a temporal dimension) and θ to refer to the dimensionless time delay in the equations ($\theta = \frac{\tau}{\tau_p}$). α is the linewidth enhancement factor and T is the ratio of carrier to photon lifetime.

However, this quite simple model has a few limitations since it does not take into account several experimental features. Indeed, it does not consider the physical finite response time of the phase-conjugate mirror. As presented in Fig.2.13, the phase-conjugate beam is created by nonlinear interaction. This process takes a certain amount of time, ranging typically from femtoseconds in vapor cells [68] to several seconds in barium titanate crystals [69]. Consequently the generation of the PCF is not instantaneous. As a result, the PCM is physically characterized by a finite response time. In the model, this response time is not taken into account and the PCM is hence assumed to show instantaneous response to the incident wave. Besides, this system of equations is standardly used whichever the phase conjugation medium and setup.

Nonetheless, this model predicts routes to chaos and a very rich set of dynamical solutions depending on the feedback ratio γ have been reported [70–72] in good qualitative accordance with experiments. More sophisticated models of rate equations taking into account the finite penetration depth and the response time of the phase-conjugate mirror have also been proposed more recently [73,74]. The main difficulty in the models with finite response time stems from the gap between the order of magnitude of the laser relaxation oscillation time period and the time of propagation in the cavity (ranging from hundreds of picoseconds to some nanoseconds) on the one hand and the mirror response time (usually ranging several seconds) on the other hand. Thus in order to take into account those three time scales simultaneously, the computation time required would be extremely long since the integration steps are limited by the most quickly varying parameters. Additionally, the resulting integro-differential equations make the bifurcation analysis more difficult.

For all these reasons, in all that follows, we restrict the study to a simple model of the type of equations (2.3) and discuss its limitations in the conclusions and perspectives.

In both cases, (differential or integro-differential models) theoretical comparisons of the laser dynamics between PCF and COF cases have been carried out. When looking closely at bifurcation diagrams in the case of PCF, a first fundamental difference compared to the COF case [75] is noted. Indeed, when the feedback ratio increases, starting from 0%, once the first transition from steady state to chaos is overcome, the system never stabilizes back to a steady state. By contrast to the COF case, in which steady states –named in that case external cavity modes– are recovered after chaotic regions, in the PCF model these so-called external cavity modes are actually pulsing states which frequencies are imposed by the external cavity time delay. This phenomenon is illustrated in Fig.2.14 where a comparison of bifurcation diagrams in the case of COF and PCF is presented. Erneux *et al.* showed that the complex electrical field of the laser beam in ECM state can be written, under legitimate approximations reported in [75], $E_0(t) = A_1 exp(i\omega t) + A_2 exp(-i\omega t)$ where A_1 and A_2 are scalar constants. ω is the pulsing angular frequency and is related to the external cavity length by $\omega = 2\pi \frac{c}{2L_{cav}}$.

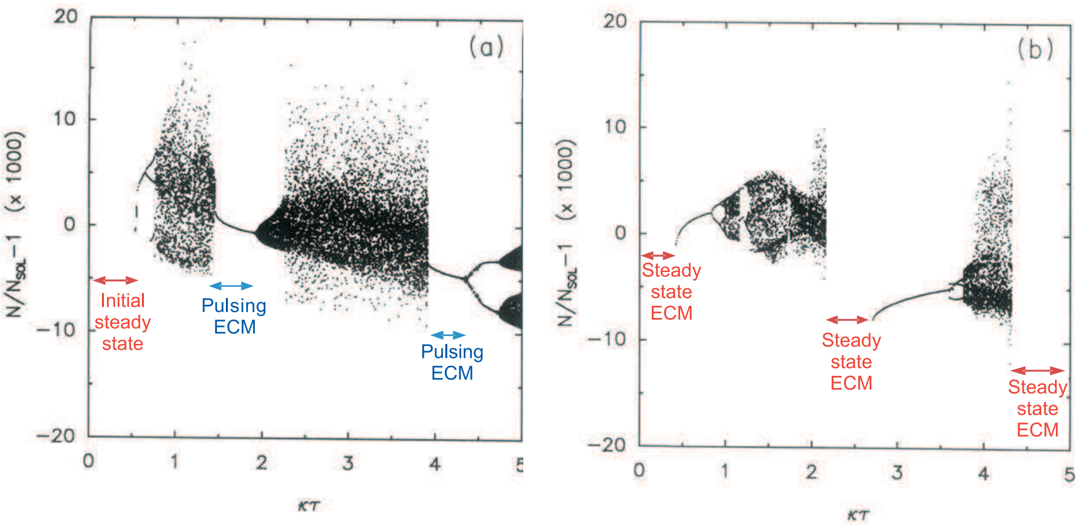

Figure 2.14: Bifurcation diagrams in the PCF case (a) and COF case (b) for the same values of all parameters. N is the electron population and N_{sol} is its steady-state value in the absence of feedback. κ is the feedback rate and τ the round-trip time in the external cavity. Figure from [66].

This major difference between COF and PCF –which stems from the different nature of the solutions of the laser rate equations in both cases– induces significant changes in the bifurcation diagrams and in the cascade of dynamical states, as illustrated in Fig.2.14. In these two bifurcation diagrams, a dot is reported when the fluctuating laser power reaches a certain threshold value. Hence, for a given value of $\kappa\tau$, a steady state region shows no dots at all. A harmonic time series shows one dot which is the maximum value of the oscillations. A quasi-periodic state shows several dots, one for each local maximum in the time trace. Lastly, a chaotic dynamics is represented by a lot of dots, illustrating the complexity of the fluctuations.

We can see in Fig.2.14 that the routes from the initial steady state to chaos are similar in both cases (a) and (b). However, in trace (a), there is only one steady state region in the whole diagram. Actually this solution showing constant output power is already a first ECM. The regions of chaos are interspaced by continuous lines representing the self-pulsating external cavity modes of the PCF case. In contrast, in trace (b), there are two regions of steady states following two regions of chaos. This main difference leads to the conclusion that after going through a chaotic region, the laser recovers steady state in the COF case, while in the PCF case the laser bifurcates to a self-pulsing state. In the latter case, once the initial steady state is overcome through the first bifurcations to undamped oscillation relaxations, the laser never exhibits steady state any more. This major difference illustrates the dynamical nature of the external cavity modes in the COF case – in which they are steady states– and in the PCF case – in which they are self-pulsing states.

2.3.2 Still few experimental studies

Despite many fruitful theoretical predictions and simulations, there have been few experiments to study the dynamics of laser diodes with phase-conjugate feedback. Many experiments have addressed the question of the creation of phase-conjugate beam and of the optimization of its generation process parameters such as the nonlinear beam interaction gain in order to reach maximum mirror reflectivity [76, 77]. Experiments on materials that show different response time have also been reported [68,69,78]. Yet most of them do not make use of the generated phase-conjugate beam as feedback, blocking it by inserting an optical isolator on its self-aligned way back to the laser cavity.

The aim of those experiments is not to study the dynamical effects induced by the feedback on the laser but rather the optimization of the phase-conjugate beam itself along with the phase conjugation media in terms of stability, power and nonlinear beam interaction time scale. Therefore, in those experiments, in spite of the ability to generate a potentially intense phase-conjugate beam, the laser always operates in steady state since no feedback is directed to it. Those experiments brought advanced results from the point of view of the suitable media and techniques to perform phase conjugation but not from the proper point of view of the laser dynamics. Although they remain scarce, we can mention here some experimental results that present interesting dynamical features of a laser with PCF.

Undamping of the relaxation oscillations

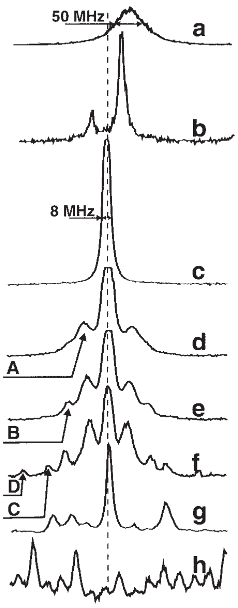

Figure 2.15: Optical spectra illustrating the route to chaos of a laser diode subject to PCF. PCF is achieved by four-wave mixing in rubidium vapor with a detuned pump beam with respect to the laser (signal) beam. Trace (a) is the free-running laser, (b) shows a small and a big peak symmetrically placed around the frequency of the pump beam. Trace (c) shows the locking to this same pump beam frequency. Trace (d) shows two symmetrical side bands around the locked frequency corresponding to the relaxation oscillation frequency (peak A at 3.9 GHz). Then, successive period doublings are undergone: peak B at 7.8 GHz in (e), peaks C and D at 12 and 16 GHz in (f) rise in the spectrum. Trace (g) is a broad spectrum and (h) corresponds to the coherence collapse state. Figure from [79].

A pioneering experiment showing self-excitation of the relaxation oscillations and period doublings in a laser with PCF was made by Andersen *et al.* in 1999. They brought experimental evidence to the theoretical predictions of a route to chaos with undamped relaxation oscillations and period doublings [79]. In particular, the appearance of the relaxation oscillation frequency followed by several period doublings until reaching the coherence collapse state is clearly illustrated in 2.15.

PCF-induced operating regimes and spectral properties

Other major experimental results in this field were brought by Lawrence and Kane in 2001. A comparison between spectral properties and operating laser regimes of a laser with COF and a laser with PCF has been carried out in [80]. Fig.2.16 shows the comparison between transitions from regime III to regime V as a function of the external cavity length in a laser with COF and in a laser with PCF. The same study of regime transitions has also been carried out as a function of the injection current [80].

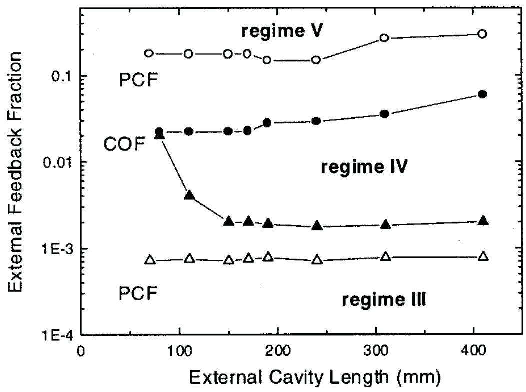

Figure 2.16: Transitions between stable and unstable output states as a function of the external cavity length. The feedback fractions at which transitions between stable and unstable output states occur for PCF (open data points) and COF (solid data points) as a function of external cavity length are presented. The points mark transitions from stable single-mode regime III into coherence collapse regime IV (triangles), and from coherence collapse regime IV into stable single-mode regime V (circles). Figure from [80].

In the distribution of regimes displayed in Fig.2.16, the very small phase sensitivity of the laser subject to PCF compared to its COF counterpart is clearly visible, especially in the transition from regime III to regime IV.

The evolution of the optical spectra of a laser with COF and with PCF displayed in Fig.2.17 illustrates the difference in the routes to chaos of both cases. Fig.2.17.(i) shows a stable single-mode state (a) followed by a transition to a state of excited external cavity modes (b) and (c). With an increased feedback, the output power evolves into a broadband multimode spectrum indicative of chaos in (d) and (e), before switching back to stable single-mode

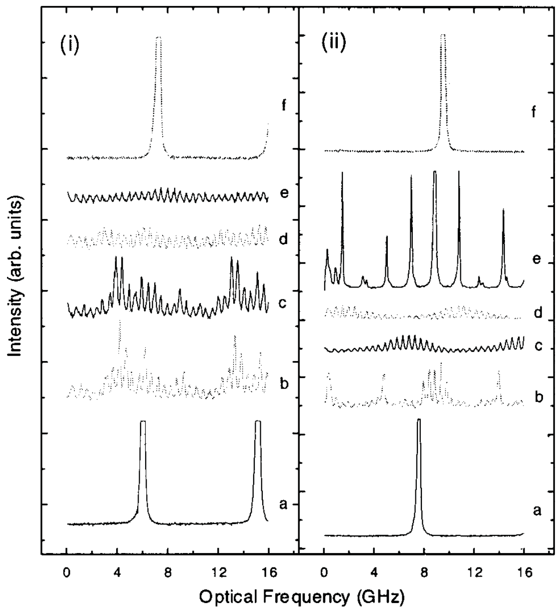

Figure 2.17: Optical spectra for increasing feedback ratio for a laser with COF (i) and PCF (ii). The feedback ratios are, from a to f, for the COF case: 0.15%, 0.20%, 0.70%, 1.5%, 2.5% and 5.0%. For the PCF case : 0.04%, 0.06%, 0.5%, 5.0%, 22% and 25%. Figure from [80].

behavior (f). The similar evolution for PCF is shown in Fig.2.17.(ii), even though the broadband chaotic spectra (c) and (d) develop more rapidly and appear to have fewer features spaced by the external cavity frequency spacing than for comparable COF ratios.

Low-frequency fluctuations

The observation of Low-Frequency Fluctuations (LFF) has also been reported in [80] in a laser subject to PCF near the transition from coherence collapse state (regime IV) to single-mode high feedback regime state (regime V).

Fig.2.18 illustrates the LFF instability. This dynamics is characterized by intermittent breakdown events, called power dropouts, followed by a slower recovery to equilibrium. The distribution of the time separating consecutive dropout events is determined by the injection current and the feedback ratio.

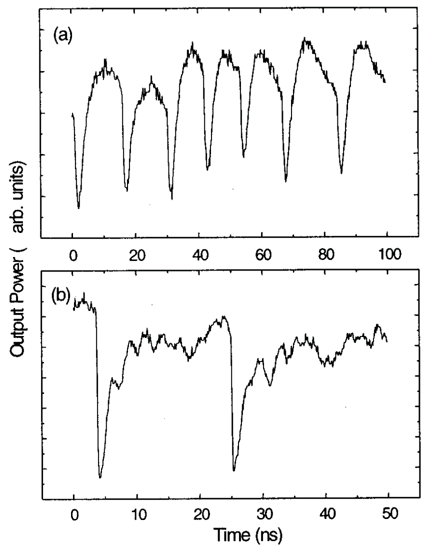

Figure 2.18: Low-frequency fluctuations induced by phase-conjugate feedback, near the transition from coherence collapse to stable single-mode high feedback regime V. The feedback fraction is 20% in (a) and 10% in (b). Solitary laser diode injection current is 35 mA ($= 1.1 \times I_{th}$). Figure from [80].

2.4 Why further study laser diodes with PCF?

It is worth carrying both theoretical and experimental researches in the field of laser dynamics with PCF. Indeed, as we already mentioned, simulations of laser diode with PCF have provided many theoretical predictions that have never been experimentally confirmed. Due to either technology limitations or difficulties in terms of experimental stabilization and suitable conditions, few reports of the huge dynamical diversity that a laser diode with PCF can exhibit have been published in the literature.

Extension of the study of the external cavity modes

As we will see in chapter 4, the theory forecasts that, in a certain range of feedback parameters, the laser output power is expected to show purely time-periodic harmonic self-pulsing states with a frequency precisely defined by the time delay. We refer here to the previously-mentioned external cavity modes for PCF [75]. To our knowledge there has been no experimental report of such a pulsing state. Yet despite this lack of evidence, the existence of pulsing external cavity modes is commonly accepted and assumed to count among the most characteristic features of a laser with PCF. We bring in chapter 6 experimental illustration to this particular dynamical state and detail the configuration that allows to see self-pulsing external cavity modes.

Dynamical transitions induced by varying the time delay

Due to the complexity of the system, the modification of one among the quite numerous parameters that enter in its model can give birth to a great deal of unexpected dynamics. Yet, in a system ruled by a delayed feedback, the features of the feedback are crucial parameters that significantly influence the way the system's dynamics evolves. Consequently, changing the time delay –through the modulation of the external cavity length– induces dramatic changes in the bifurcation diagram. The expected dynamics are not similar when switching from a short external cavity to a long one. We will see all along this manuscript how crucial the external cavity delay is on the dynamics exhibited by the laser. The experimental results presented in chapters 6 (self-pulsing ECMs), 8 (extreme events) and 9 (LFF) are obtained by successively increasing the time delay, through an increase of the external cavity length. Simulated bifurcation diagrams, time series and spectra confirm the dynamical transitions observed as the cavity length increases.

Chaos crisis induced by increasing the feedback ratio

Although most of the theory of a laser with PCF is known, there are still many points that have not been explored. For instance, in the literature there are many reports of theoretical studies of the laser dynamics for weak values of PCF rate. Yet questions about expected scenarios for higher feedback values have scarcely been addressed. In chapter 5 we bring theoretical predictions of totally different scenarios that are undergone by the laser when operating under higher feedback ratios. Indeed we show that the laser is likely to exhibit suppression of chaos and bistability between external cavity modes when the feedback ratio reaches high values.

Application perspectives: chaos suppression and source of optical self-pulsations

From an application point of view, a great motivation to study the dynamics of a laser with PCF is to be able to unveil a whole dynamical scenario, identifying the bifurcations that make the laser exhibit successive operating states of different dynamics. The simulations presented in chapter 5 predict stabilization of chaos. Indeed the model shows that in the case of PCF, suppression of chaos is seen for feedback values under which, in the COF case, the laser only shows a developed coherence collapse state.

Moreover, the experimental self-pulsing dynamics that will be presented in chapter 6 confirm the theoretical predictions about the possibility to generate optical harmonic signals, known as the previously-mentioned ECMs in PCF. In chapter 7, we will discuss the main novelty about the self-pulsing states in the PCF case compared to the COF case. Actually, it stems from the different nature of the ECMs in both cases.

By mastering the laser dynamics as a function of the feedback parameters (feedback delay and feedback ratio), we therefore address crucial concerns such as stabilization and chaos suppression along with all-optical generation of high-frequency signals at several tens of GHz.

Impact of the PCM response time on the dynamics

Further research in the simulated model could lead to a more realistic, yet also more complex, set of rate equations. A change in the theoretical scenario could be expected if the equations took into account the phase-conjugate mirror response time [81]. And naturally the discrepancy between the PCF generation time scale –or PCM response time scale– and the laser own internal time scale would have a great impact on the dynamical predictions. Still speaking of materials' response time, the great variety of media that are suitable to perform phase conjugation (photorefractive crystals, Kerr media, broadband laser diodes) represent as many time scales that experimentally affect the running laser, each one having a stronger or a weaker influence. An interesting question is the effect of the PCM response time on the laser dynamics. We expect that the smaller the difference between the PCM response time and the external cavity time delay the stronger its impact on the laser state. This also stimulates the research of new media with build-up times ranging different orders of magnitude. As we will discuss in chapter 3, several types of media are suitable to generate phase conjugation and their related grating build-up times range from femtoseconds (vapor cells [68]) to several seconds (in photorefractive barium titanate crystals [69]).

Time-scale interplay in a nonlinear system

This study of nonlinear dynamics of laser diode with PCF can also be seen as a test bed for the study of new phenomena in time-delayed systems. Although we focus here on the specific case of nonlinear dynamics in laser diode with phase-conjugate feedback, the models, the methods and some conclusions that we are about to present can be compared to analogous time-delayed systems. Indeed, studying a laser subject to PCF is equivalent, from a wider point of view, to study any nonlinear system ruled by the interplay of three different time scales. Like in the various nonlinear systems subject to feedback that are found in other fields of physics –such as hydrodynamics, electricity, and mechanics–, we use analogous methods to analyse bifurcations, identify operating states like chaos, simulate models and understand the general behavior of the system. For example, the studies of extreme events and coherence resonance presented in chapters 8 and 9 are analogous to other reports of observations of the same behaviors in other domains of physics. After all, if removed from its optical context and seen from a purely dynamical point of view, a laser diode with PCF is a mere nonlinear system subject to its own feedback, similar to those that can be found in many other physical frames.

Chapter 3
Experimental setup

No amount of experimentation can ever prove me right; a single experiment can prove me wrong. Albert Einstein

In this chapter is presented the experimental setup that we designed to perform phase conjugation in order to unveil the nonlinear laser dynamics when subject to phase-conjugate feedback. We first present the laser diode device, the dynamics of which is the main purpose of our research. Then we discuss the phase conjugation process along with the suitable techniques, materials and gain configurations to perform phase-conjugate feedback. Finally, we present the whole experiment and the corresponding measuring devices and give first illustrations of the laser behavior when subject to PCF.

3.1 Presentation of the laser diode

Our laser diode is an edge-emitting single transverse mode semiconductor laser (JDS Uniphase DL-SDL-5400). The active layer is made of quantum wells in $AlGaAs$. The operating wavelength is $\lambda = 852 \pm 4$ nm. We work therefore in the near infrared domain and use a photosensitive card to localize the beam path and to perform beam alignments. This kind of laser diode is largely used in common applications such as printing, point-to-point communications and image recording. Without optical feedback, the laser diode is driven by means of a direct current and operates according to the linear light- current characteristic shown in Fig.3.1. Most of the time, we will be operating with a current of $I = 60\ mA$, which gives an available maximal optical output power of 45 mW. Without feedback the laser operates in steady state, which means that for a given value of the control current I the optical output power is constant as illustrated in Fig.3.2. The very small variations that can be seen are due either to optical noise coming from the laser itself or electrical noise stemming from the photodiode and the oscilloscope.

Now what we aim to illustrate here is the great dynamical diversity that can be seen in a laser diode when subject to its own optical feedback – that is when part of the emitted light is sent back into the laser cavity

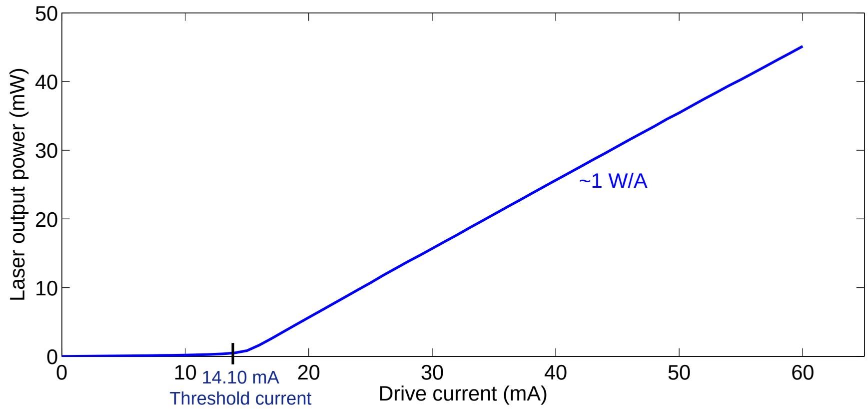

Figure 3.1: Laser diode characteristic when operating solitary. We measured the threshold current at 14.10 mA.

after reflection on a mirror. Therefore we mean to go beyond the otherwise steady state of the laser and reach for dynamical states that emerge with the presence of feedback. As we mentioned in chapter 2, we discriminate two kinds of optical feedbacks: Conventional Optical Feedback (COF) –where the emitted beam returns to the laser after reflection on a common mirror– and Phase-Conjugate Feedback (PCF)–where reflection is made on a phase-conjugate mirror. Our whole research tackles the effect of phase-conjugate feedback on the laser dynamics and the bifurcation scenarios leading to chaos [72, 74, 80–82]. This brings us to the point of the PCF generation process and its injection back into the laser.

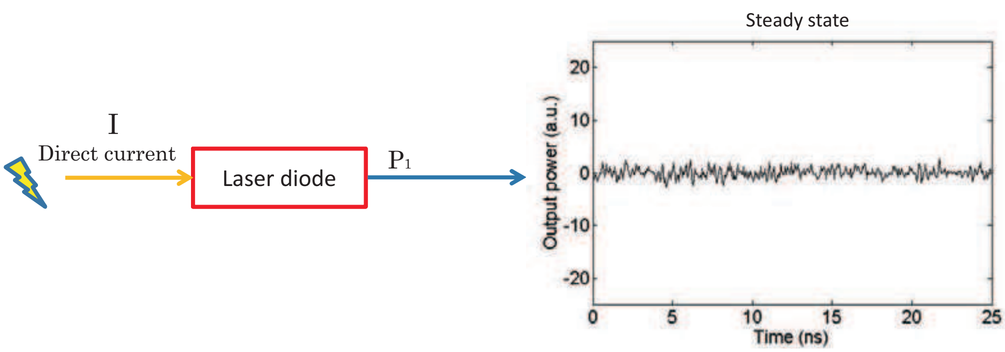

Figure 3.2: Steady state of the laser diode when operating solitary. The emitted optical power versus P_1 is constant. Here it equals zero here since DC has been cut off by the photodiode.

3.2 Phase-conjugate feedback

3.2.1 Definition and background

The first experimental study of a laser diode with feedback from a phase-conjugate mirror was reported by Cronin-Golomb *et al.* in 1985 [83]. Besides the possibility to enable a laser to exhibit nonlinear dynamics, phase-conjugate feedback has many utilities. It is a commonly-used technique to perform wavefront distortion correction [69], to stabilize a laser diode by means of phase and mode locking [84–86], to enhance frequency stability [87–89] and to achieve spectral linewidth and intensity noise improvement [90–94].

Unlike COF, PCF has the particularity to be a self-correcting and self-aligned feedback [95]. Indeed, the geometry of the PCF generation layout compels the PCF beam to be self-aligned with the incident laser beam on the phase-conjugate mirror. Naturally, the PCF beam is counter-propagating with respect to its incident counterpart. Moreover, as demonstrated in [95], any phase shift and spreading that the laser beam could undergo in the way from the laser to the mirror due to propagation in the air or through distorting media is compensated in the backward trip.

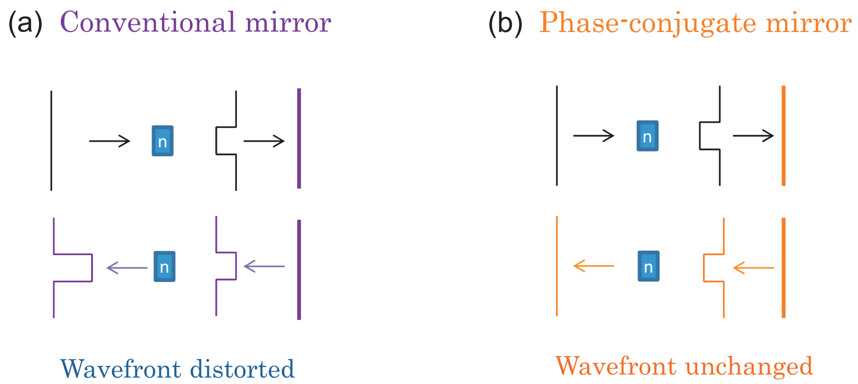

Figure 3.3: Phase-conjugate mirror versus conventional mirror. The wavefront of the COF beam is distorted after one round-trip through the distorting medium of refractive index n (a) while the PCF beam is unchanged (b).

This property is illustrated in Fig.3.3 where one can see that the PCF beam keeps at each point of the backward trip to the laser the same wavefront as in the forward trip to the mirror. In other words, when entering back into the laser cavity, the photons have exactly the same phase as at the moment they were emitted out of it. This is why phase conjugation is also called time reversal [96]. One might see it as if, once the beam has reached the phase-conjugate mirror, it would travel back in time until the instant when it was emitted. An illustration of phase conjugation is displayed in Fig.3.4 where the wavefront distortion correction operated by the phase-conjugate mirror is compared to the conventional mirror case. As we mentioned in chapter 2, this feedback with unchanged phase makes the laser behave quite differently compared to the case of conventional feedback.

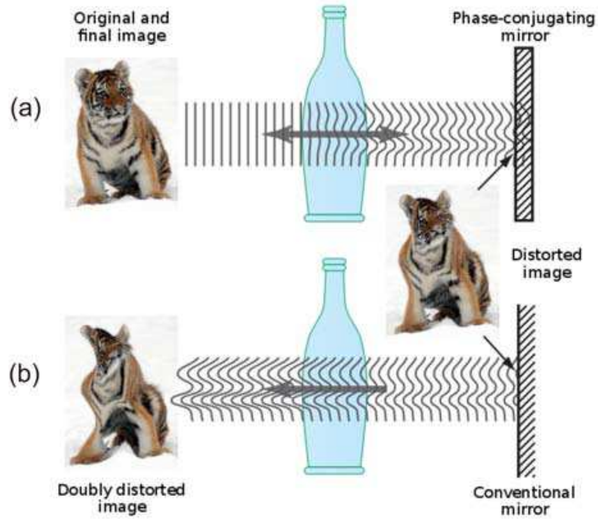

Figure 3.4: Wavefront distortion correction of an image operated by a phase-conjugate mirror (a), compared to the double distortion operated in the case of a conventional mirror (b). Picture from Wikipedia.

3.2.2 Suitable media to perform phase conjugation

Many ways to perform phase conjugation using different media have been studied so far. The most commonly used media are vapor cells –which are Kerr media– and photorefractive crystals. Kerr media have the property to perform phase conjugation at very short time scales. Phase-conjugate feedback has been generated in vapor cells with response times down to some femtoseconds [68]. In photorefractive crystals the response time is much larger, usually several hundreds of milliseconds in strontium barium niobate (SBN) [78] crystals and several seconds in barium titanate ($BaTiO_3$) crystals [69]. Broad-area laser diodes are also suitable media for phase conjugation. In AlGaAs, nanosecond response times have been reached at wavelengths close to 800 nm [87, 97–100]. Media based on InP have also been used to perform phase conjugation with response times of some milliseconds at wavelengths close to 970 nm [101] and 1.3 μm [101, 102].

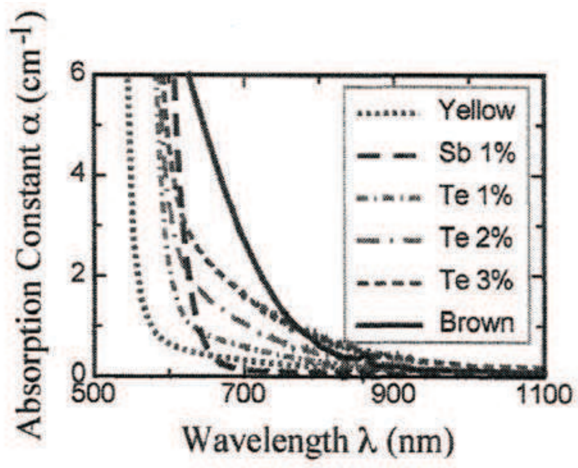

Figure 3.5: Absorption spectra of SPS crystal with different dopings at room temperature. In our experiment we use the $Sn_2P_2S_6 : Te$ (1%) one. Image from [76].

In our experiment we use a tellurium-doped tin hypothiodiphosphate $Sn_2P_2S_6 : Te$ (1%) semi-conductor crystal, commonly referred to as SPS crystal. This choice is motivated by two features. The first is the fact that it has been demonstrated to show low absorption and high gain properties in the near infrared domain [76] as shown in Fig.3.5. We expect thus to achieve reasonable gain with a laser operating at 850 nm without the need for external electrical field to improve its photorefractive properties. The second is its expected short response time which ranges only several milliseconds [77]. SPS crystals can show response times about a thousand times smaller than SBN and $BaTiO_3$ crystals [103]. Moreover, to our knowledge there has been no experimental study of laser dynamics using phase-conjugate feedback performed in SPS crystals.

Thus we report here on a still unexplored configuration. Semiconductor broad-area laser diodes would also be attractive media due to their short response time ranging nanoseconds. Yet our aim is to insert in the laser dynamics a new time scale, different from the nanosecond which is close to the period of the relaxation oscillations. With the SPS crystal the system is subject to a dynamics which time scale (microseconds) is intermediate between other photorefractive crystals (seconds) and the laser relaxation oscillations (nanoseconds). This difference between these three orders of magnitudes allows to discriminate the influence of each time scale on the laser dynamics.

Photorefractive crystals may be used in several configurations to generate phase conjugation as presented in Fig.3.6. The principle of phase conjugation with a photorefractive crystal is based on four-wave mixing. The interferences between two pump beams result in the generation of a refractive index grating within the crystal. Then a signal beam is sent on this grating and its own scattering on the grating results in a fourth beam which properties are to be counter-propagating and phase-conjugate with respect to the signal beam.

3.2.3 Phase conjugation techniques

A mathematical theory of phase conjugation generation by four-wave mixing in photorefractive media has been developed by Cronin-Golomb *et al.* [104] and has been extended in experimental phase-conjugate mirror characterizations [105]. There are two possibilities to perform four-wave mixing : either using an external pumping configuration –in which a secondary laser provides the pump beams– or a self-pumped configuration –in which the signal beam and the two pump beams are emitted by the same laser. Among all those possibilities, the most commonly used to study nonlinear laser dynamics in the literature are configurations (a), (c) and (d) in Fig.3.6.

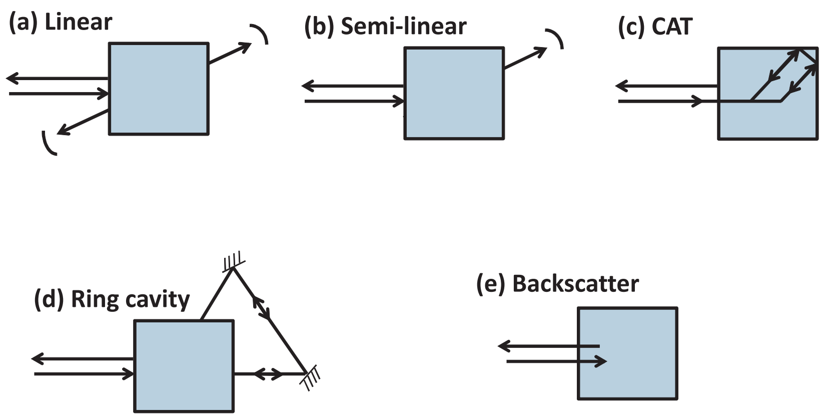

Figure 3.6: Configurations to perform phase conjugation in photorefractive crystals. Image adapted from [106].

Using external pumping may prove useful when the signal to conjugate comes from lasers for which the emitted power is too small to perform phase conjugation in the crystal with a reasonable gain. One may also want to take advantage of the detuning between the pump beams and the signal beam to yield a better spatial and spectral beam resolution [98]. Configuration (c) uses a crystal polished on four faces which allows internal beam reflections on the crystal faces that play thus the role of mirrors. This configuration is interesting for its a priori experimental simplicity since it requires neither external pumping nor the use of mirror and lenses. It has provided many advanced results in terms of laser dynamics so far [80]. For our study we have decided to work with a self-pumped ring mirror setup like configuration (d) where the incident beam propagates through the crystal a first time and re-enters it after reflection on two common mirrors bounding the ring cavity.

3.3 Phase conjugation in SPS crystal

The photorefractive effect is a phenomenon in which the local refractive index of a medium is changed by the illumination of a beam light with spatial variation of the intensity [67]. This effect was observed in SPS for the first time in 1991 [107]. Then deeper analysis of its photorefractive properties have been carried out since Odoulov *et al.* showed evidence of the interesting features of SPS in the infrared domain [108,109]. Our SPS crystal is presented in Fig.3.7. Its dimensions are $6 \times 6 \times 11\ mm^3$. The two faces intersecting the z-axis are polished and are used as entrance and exit faces for the laser beam through the crystal[1].

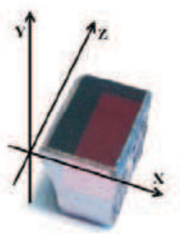

Figure 3.7: Our SPS crystal sample. The laser beam propagates following the z-axis and is horizontally polarized in the direction of the x-axis.

3.3.1 Beam fanning

In order to use this crystal as a PCF generation medium we need first to determine two particular angles. The first one is the angle formed by the

[1]We thank Dr. Alexander Grabar for providing us with the SPS crystal sample and for the fruitful discussions about photorefractive systems.

incident beam and the first polished face which is responsible for Fresnel losses. The second one is the angle of the ring cavity. As we mentioned before, phase conjugation is performed by four-wave mixing within the crystal. In this process the values of the angles between the beams are important parameters since the gain of the wave mixing process depends on them.

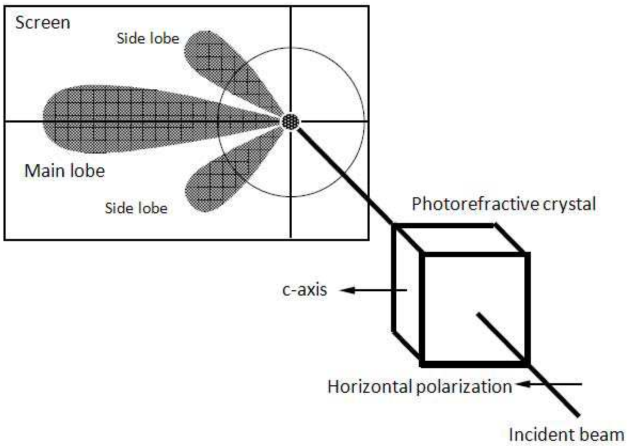

Figure 3.8: Beam fanning seen on a screen after propagating through a photorefractive crystal. If the laser polarization and the c-axis are collinear, the beam fanning occurs in the direction of the c-axis. A main lobe and side lobes can be seen, resulting from the deviation of part of the laser beam when propagating through the crystal due to its photorefractive properties. Image adapted from [106].

In order to maximize the phase conjugation gain, one should choose the angles that provide the highest gain in the four-wave mixing process which also correspond to the highest gain measured in two-wave mixing [77]. In the two-wave mixing process a pump beam and a signal beam interfere in the crystal and an energy transfer is operated from one beam to the other. The way energy is transferred depends on the beams' propagation direction in the crystal. Indeed the c-axis of the crystal is responsible for the orientation of the beam fanning and thus imposes the direction according which a beam can be amplified. When a beam propagates through the photorefractive crystal following the z-axis, part of it is deviated in the direction of the c-axis shaping thus a light lobe in this direction and side lobes as shown in Fig.3.8. Feinberg accounted for this phenomenon called beam fanning as the appearance of an asymmetric high refractive index area in the crystal towards the c-axis due to its photorefractive properties [110].

In our crystal the beam fanning is developed in the direction opposite to the x-axis. This phenomenon is illustrated in Fig.3.9 where we defined and oriented the c-axis according to the beam fanning direction, that is in the direction opposite to the x-axis. In the picture of the beam intercepted with a photosensitive card the main beam fanning lobe is clearly visible in the direction of the c-axis. However we could not properly see the also expected side lobes probably because of a lack of contrast. They might actually be present but with too small intensity, making them difficult to be seen.

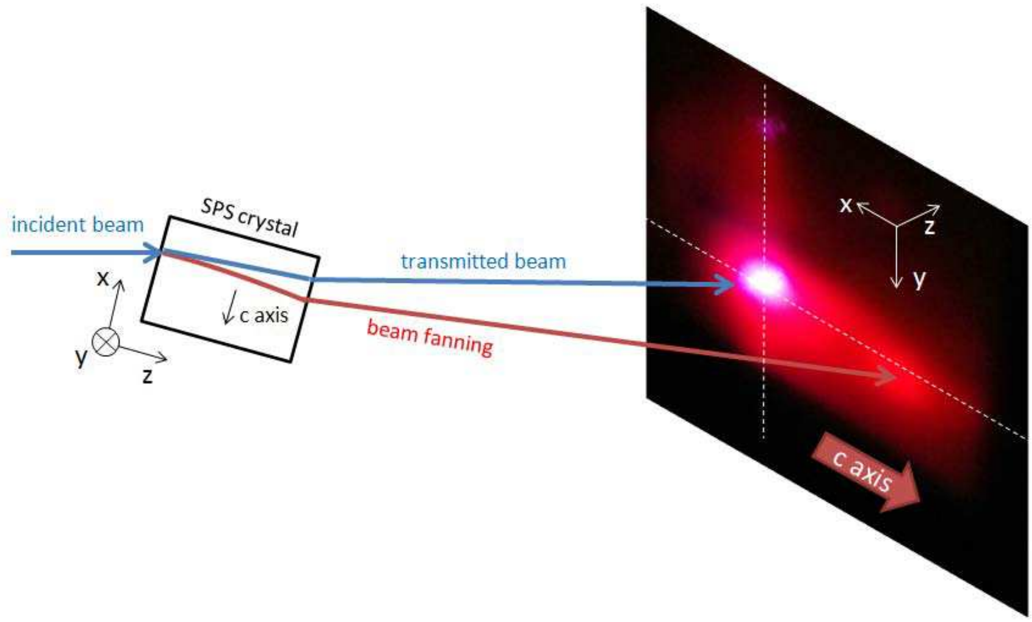

Figure 3.9: Picture of the beam fanning seen with our SPS crystal and detected with a near-infrared photosensitive card. The main lobe is clearly visible and shows the direction of the beam deviation to the right in the direction of the c-axis.

3.3.2 Two-wave mixing gain

Once the direction of the beam fanning –and thus the c-axis– are clearly identified, we can look for the angle that will bring the highest two-wave mixing gain. The two-wave mixing setup is presented in Fig.3.10.

The pump beam enters the crystal with the optical power P1, the signal beam with the optical power P2 where $P1 > P2$. Then those two beams

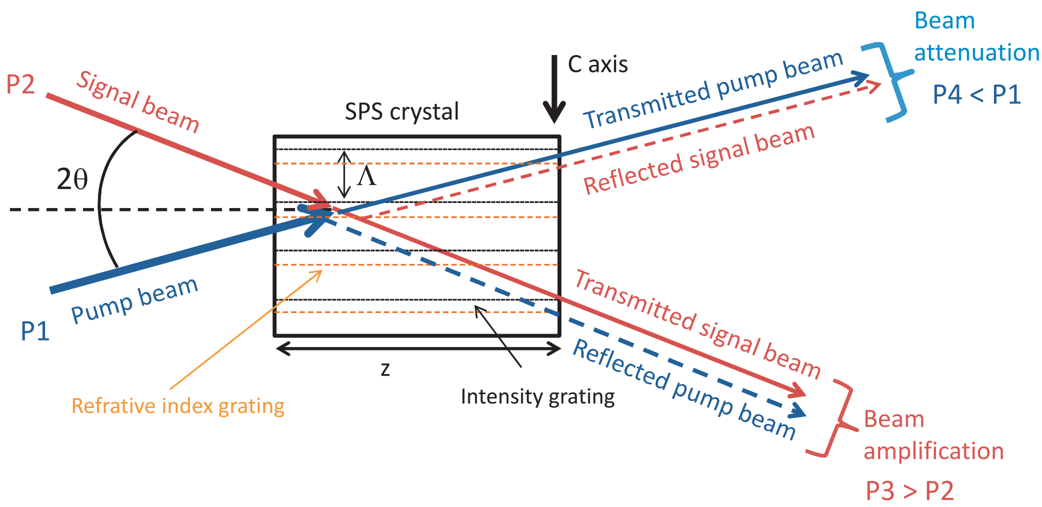

Figure 3.10: Two-wave mixing principle in photorefractive crystal. The pump beam transfers part of its power to the signal beam when scattering on the grating.

interfere inducing an intensity grating, which induces the generation of a spatially phase-shifted refractive index grating within the crystal via the photorefractive effect. The scattering of the beams on this generated grating results in an energy transfer from one beam to the other.

The position of the beams with respect to the c-axis determines the direction in which amplification is performed. The two-wave mixing theory predicts that the constructive interferences between the transmitted and reflected beams, and hence the beam amplification, occur in the direction of the c-axis [67]. By contrast, destructive interferences and hence beam attenuation occur in the direction opposite to the c-axis. Therefore, in the configuration presented in Fig.3.10, the signal beam is amplified and the pump beam is attenuated. As a consequence, the amplified signal beam exits the crystal with the power $P3 > P2$ while the attenuated pump beam exits the crystal with the power $P4 < P1$. Experimentally we observe that if beams 1 and 2 are switched, the amplification still occurs in the direction given by the c-axis, therefore the energy transfer occurs from the signal beam to the pump beam.

The grating spacing Λ is given by $\Lambda = \frac{\lambda}{2\sin(\theta)}$. To be precise, the energy transfer gain depends more directly on the grating spacing rather than on the angle 2θ [77] since the beam amplification depends on the way the beams scatter on the grating. Usually, the gain of the two-wave mixing process is

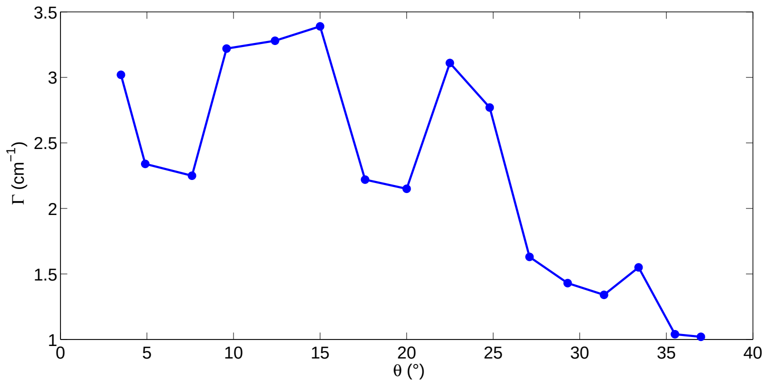

Figure 3.11: Two-wave mixing gain in SPS crystal versus θ.

defined as follows: $\Gamma = \frac{1}{z}\ln(\frac{P_{on}}{P_{off}})$ [77]. P_{on} is the power of the amplified signal beam exiting the crystal when the pump is on, P_{off} is the power of the signal beam exiting the crystal when the pump is off, and z is the crystal length (in our case, $z = 11\ mm$).

Naturally, since Γ depends on the angle 2θ between the interfering beams, it is crucial to know the values of 2θ that correspond to the higher values of Γ. The two-wave mixing gain versus θ measured in our experiment is presented in Fig.3.11 where one can distinguish that maximum gain ($\Gamma = 3.4\ cm^{-1}$) is achieved when $\theta \simeq 15^o$. We keep therefore this value of θ as a parameter value for the orientation of the mirrors in the phase-conjugate mirror cavity.

3.3.3 Reflection and transmission gratings

The whole phase-conjugate mirror is described in Fig.3.12. The pump beams interfere producing a grating on which a third beam scatters giving birth to a fourth beam which constitutes the phase-conjugate feedback. However, within the crystal, two kinds of gratings can be generated according to which beams are considered to be the pumps. When the pumps are counter-propagating the induced grating is a reflection grating (in blue in Fig.3.12). For instance in Fig.3.12, beams 1 and 2 can be pumps and generate the grating, then beam 4 would be the result of the scattering of signal beam 3 on this grating. But beams 1 and its self-diffracting beam 3 could also be pumps and generate the grating, then beam 2 would play the role of the signal beam and its scattering on the grating would result in the generation of beam 4. In the case where the pumps are co-propagating like in the latter example, the grating induced by their interferences is a transmission grating (in red in Fig.3.12).

As a consequence, both kinds of gratings may coexist in the crystal [77]. The ability of the crystal to create gratings depends on the electro-optic coefficients that are preferentially excited by the propagating beams and the angle 2θ between the pump beams as demonstrated by D'yakov *et al.* in 1991 [111]. Therefore it depends on the crystal orientation with respect to the beams at stake in the four-wave mixing process. Nonetheless if the mirror loop is long enough beams 1 and 2 can become incoherent and the creation of the reflection grating induced by their interferences is prevented. In our experiment we usually generate PCF with a transmission grating. However we will discuss in chapter 6 the possibility to excite a reflection grating and the consequences on the feedback-induced laser dynamics.

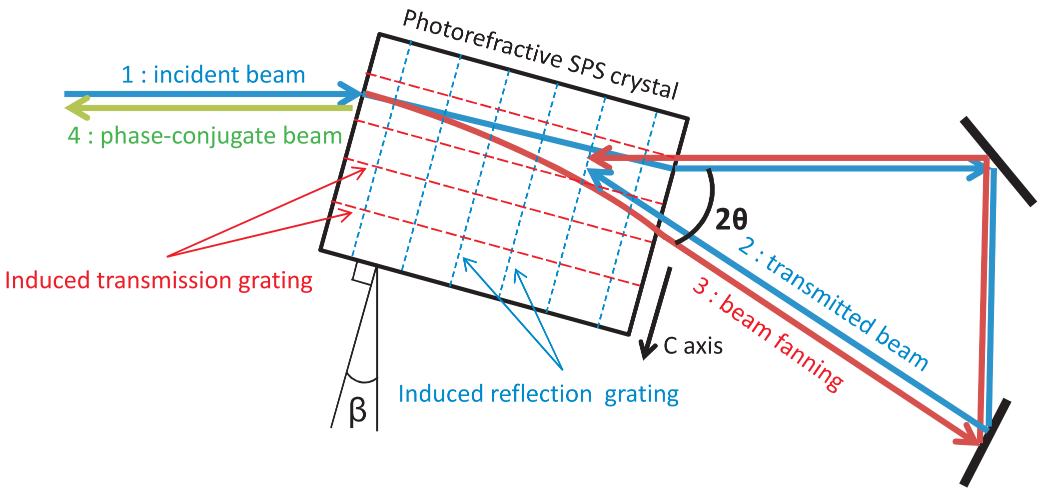

Figure 3.12: Phase-conjugate mirror principle: four-wave mixing within SPS crystal showing reflection (blue) and transmission (red) gratings.

We set the configuration in order to work with a transmission grating-induced phase-conjugate mirror. Therefore beams 1 and 3 are the pumps and generate the transmission grating on which beam 2 scatters creating thus beam 4. The angle 2θ is set according to the two-wave mixing maximum gain: $2\theta = 30^o$. The angle β between the incident laser beam and the crystal face has been set manually at the value of 26^o for which we saw experimentally that the Fresnel losses of the beam entering the crystal were minimum. This angle β also prevents any feedback in the laser that would come from reflection on the crystal's front face. Due to the geometry of the setup we are sure that no conventional feedback is sent back in the laser. Besides, according to the theory of PCF generation, since the phase-conjugate beam and the incident beam are self-aligned, the only beam directed towards the laser is its own phase-conjugate feedback beam.

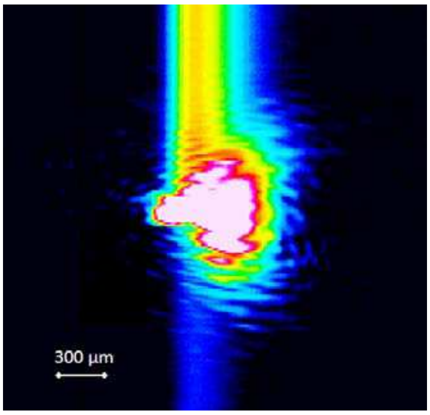

Figure 3.13: Transversal picture of the laser beam at the point it enters the SPS crystal. The beam has the shape of an ellipse in which the dimensions of the major axis and minor axis are approximately 1100 μm and 900 μm. The vertical yellow trace is a defect of the camera.

In a self-pumped configuration, the laser must be powerful enough to enable the nonlinear effects in the crystal and provide an optical feedback reasonably strong. Actually the important parameter about the beams' interaction in the crystal is the intensity $J = \frac{P}{S}$ where P is the optical power and S the beam section. According to [77], in SPS crystals, the incident beam intensity threshold above which the ring loop behaves like a phase-conjugate mirror is $J_{th} \simeq 1\ W.cm^{-2}$. A transversal picture of the laser beam as it enters the crystal taken with an infrared-sensitive camera is displayed in Fig.3.13. We measured approximatively the major and minor axis of the elliptic beam : 1100 μm and 900 μm. In the experiment the order of magnitude of the intensity of the beams is about $J = 3.5\ W.cm^{-2}$ which fulfills the requirement to enable photorefractive effects and phase conjugation in the SPS crystal.

3.3.4 SPS crystal response time

As we mentioned previously one of the main interests of working with a SPS crystal is its short response time or, in other words, its short grating build-up time which is expected to be some milliseconds.

In Fig.3.14 the measured response time of our SPS sample is displayed. The laser optical power is represented in blue and the phase-conjugate feedback power in red. The curves are plotted in the same temporal scale but

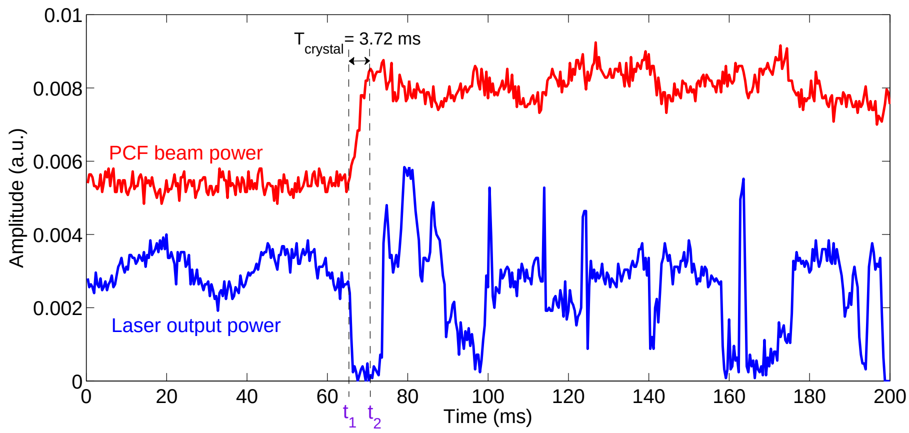

Figure 3.14: Measured SPS crystal response time. The blue curve shows how the laser dynamics is affected when enabling phase conjugation once the grating build-up time $T_{crystal}$ is elapsed.

have been vertically shifted and amplified for clarity. While $t < t_1$, a shutter is placed between the laser and the crystal. Therefore the PCF power is zero and the laser operates in steady state, emitting theoretically constant optical power but experimentally we can guess small noise-induced fluctuations around the constant mean value. When $t = t_1$ the shutter is removed, allowing the laser beam to enter the crystal and phase conjugation is enabled. We measure in Fig.3.14 the PCF rising time which corresponds to the crystal grating build-up time simply called crystal response time: $T_{crystal} = t_2 - t_1 = 3.72\ ms$. $T_{crystal}$ is defined as the time in which the PCF value rises from 10% to 90% of its average saturation value. In the laser output power time trace, the dynamical change in the emitted laser power with the appearance of high peaks of short duration that are inexistant for $t < t_1$ is highlighted. This results from the effect of the PCF on the laser dynamics, causing it to exhibit fluctuations under the action of the feedback.

3.4 Whole operational experimental setup

Once the phase-conjugate mirror is set, the whole experimental setup naturally comes as displayed in Fig.3.15. Some important parameters still remain to be focused on, though.

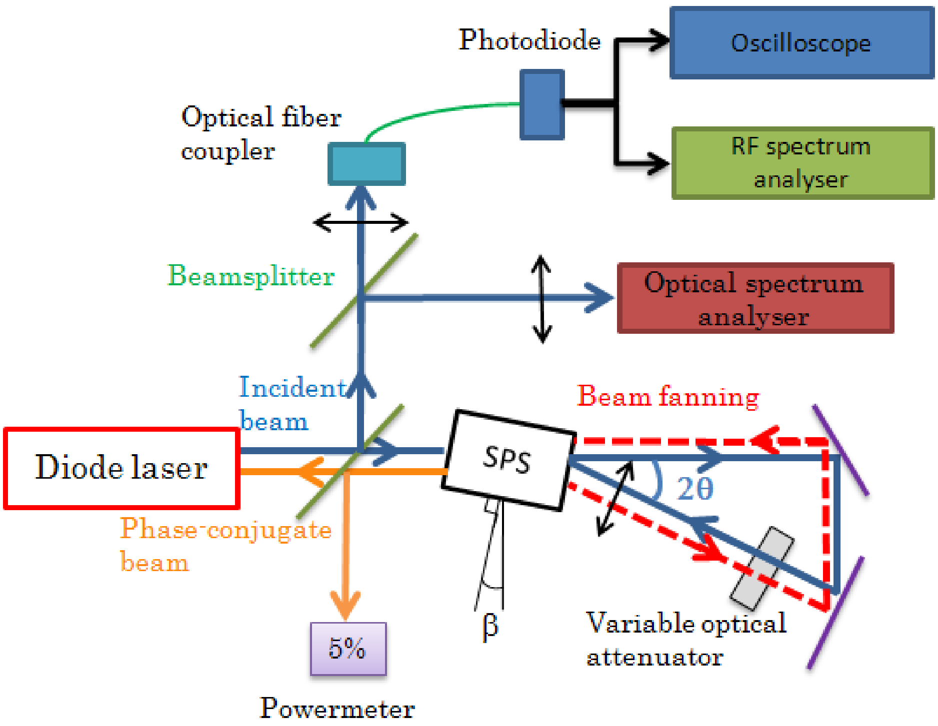

Figure 3.15: Whole experimental setup. Optical measuring instruments and a powermeter –giving the PCF power value, from which the PCM reflectivity is calculated– are introduced to be able to see and to quantify the laser dynamics when subject to PCF.

3.4.1 Mirror reflectivity

The crystal is placed in front of the laser with the parameters detailed previously. The four-wave mixing gain in the crystal defines the maximal reflectivity of the phase-conjugate mirror. The PCM reflectivity R is a parameter in which we show great interest since we will study the laser dynamics when the feedback strength changes.

Therefore our means to quantify the amount of light that enters back into the laser is the value of the PCM reflectivity. We define R as the ratio of the power of the phase-conjugate beam that exits the crystal on the power of the incident beam in the crystal. With the notations of Fig.3.12, we can write $R = \frac{Power\ of\ beam\ 4}{Power\ of\ beam\ 1}$. We consider that the system made of the crystal and the ring cavity behaves like only one component: a phase-conjugate mirror which reflectivity R is tunable. We achieve maximum reflectivity of 9%. We can thus explore the laser dynamics in a range of reflectivities between 0 and

9%. A variable optical attenuator is inserted in the ring cavity in order to change the power of the four-wave mixing beams and consequently to change the mirror reflectivity.

3.4.2 External cavity length

As we discussed in chapter 2, besides the mirror reflectivity, a very important parameter in the dynamics of a laser subject to feedback is the external cavity length L_{cav}. This length is defined as the path followed by the beam from the instant it has been emitted to the instant it comes back into the laser. L_{cav} is thus related to the corresponding propagating time called external cavity time delay –to which we will refer as time delay or delay– defined as $\tau = \frac{L_{cav}}{c}$.

We saw that two kinds of gratings could be generated within the crystal: the reflection grating and the transmission grating. In the case of a reflection grating, the crystal behaves like a common mirror, reflecting thus the incident beam when it enters the crystal. Therefore L_{cav} is equal to the length of one round-trip between the laser and the crystal. In the case of a transmission grating the phase-conjugate beam originates from a beam that goes through the whole ring cavity before coming back to the laser. Therefore L_{cav} also takes into account the ring cavity length and $L_{cav_{transmission\ grating}} = L_{cav_{reflection\ grating}} + L_{ring\ cavity}$. The effective external cavity length –and therefore the related time delay– is larger when operating with a transmission grating than with its reflection counterpart. Fig.3.16 illustrates the difference between the two effective cavity lengths.

As we will see in chapter 6, it is possible to take advantage of the coexistence of both gratings in order to tune somehow the phase-conjugate mirror to change the value of the time delay. This property allows to operate with a shorter or a longer effective L_{cav} without changing the setup.

3.4.3 Optical measurement devices

As described in Fig.3.15, an unbalanced beamsplitter is inserted between the laser and the crystal in order to deviate part of the beams for optical measurements. This beamsplitter has a forward transmission ratio of 78% and a leftward deviation ratio of 18%. Therefore the PCF beam coming from the PCM is partially sent to the powermeter which allows to calculate the reflectivity R. Symmetrically, part of the light emitted from the laser is deviated towards optical temporal and spectral measurement devices.

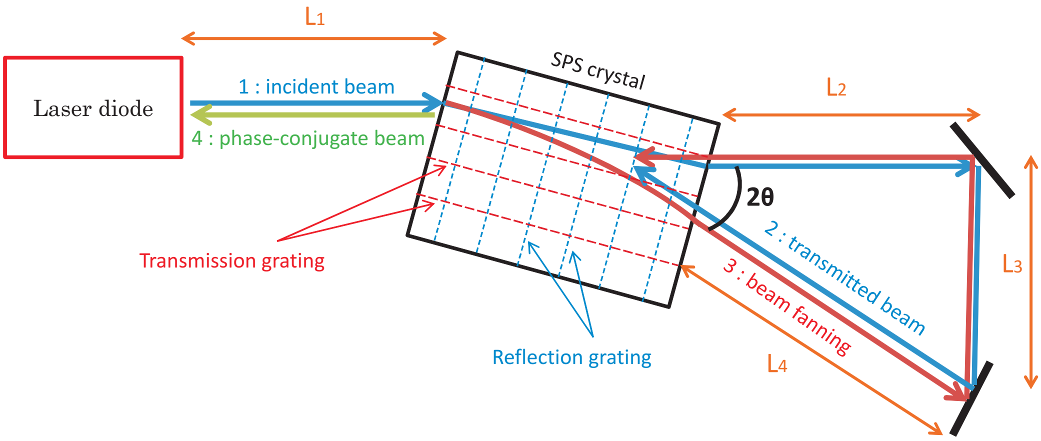

Figure 3.16: Cavity length dependence on the grating. $L_{cav_{reflection\ grating}} = 2L_1$ while $L_{cav_{transmission\ grating}} = 2L_1 + L_2 + L_3 + L_4$. The propagation through the crystal is not taken into account here.

We have simultaneously access to three complementary sources of information to study the laser dynamics. Temporal and spectral data are provided by the following devices. The oscilloscope is a 4-GHz-bandwidth Tektronix CSA 7404, 20 GS/s, the RF spectrum analyser is a 9 kHz-30 GHz-bandwidth Rohde & Schwarz FSP30, with a resolution bandwidth of 6 MHz. They take as input signal the electric conversion of the laser power operated by the photodiode (12-GHz-bandwidth Laser 2000 New Focus 1554-B). The optical spectrum analyser is a 10-GHz-free spectral range confocal interferometer Thorlabs SA210-8B which finesse is 150. Most of the time we keep the laser driving current fixed at 60 mA and change the mirror reflectivity using the optical variable attenuator.

The reflectivity value is calculated from the powermeter's measurement while the temporal and spectral effects of the phase-conjugate feedback on the laser dynamics are observed on the measuring devices. A picture of the whole experimental setup is presented in Fig.3.17.

3.5 Laser subject to weak phase-conjugate feedback

We will focus in deeper details on several particular dynamical features in the following chapters. We present here some effects of a rather weak phase-conjugate feedback on the laser temporal and spectral properties.

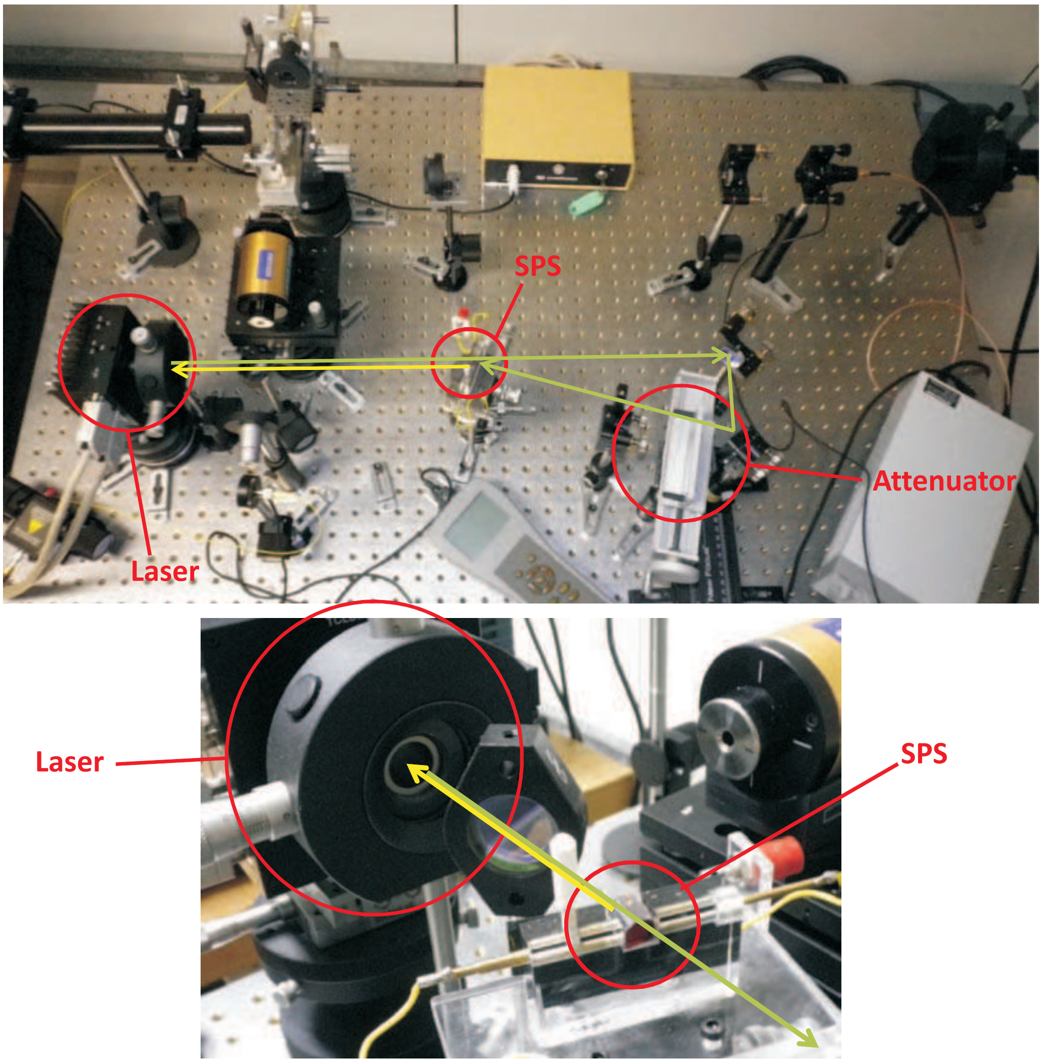

Figure 3.17: Experimental setup. The laser emits the green beam which propagates through the SPS crystal and the ring cavity. The generated PCF beam is represented in yellow.

3.5.1 Laser threshold reduction

The first characterization to note is the change in the threshold current I_{th} when the laser operates with PCF. In the literature it has been demonstrated experimentally that in the case of conventional feedback I_{th} tends to curb [22]. In the case of PCF, it has been shown that increasing the feedback ratio leads to a decrease of laser threshold current and of the output power. Consequently, a decrease of the slope efficiency is also observed [112, 113].

Theoretical predictions have demonstrated that the threshold gain decreases proportionally to the increase of the feedback ratio [95].

In order to demonstrate the relationship between the threshold current and the feedback strength, we resolve the laser rate equations with feedback in the stationary state. The equations write as follows [16]:

$$\begin{cases} \dfrac{dA}{dt}(t) = \dfrac{1}{2}G_n[n(t) - n_{th}]A(t) + \dfrac{\kappa}{\tau_{in}}A(t-\tau)cos\theta(t) \\ \dfrac{d\phi}{dt}(t) = \dfrac{1}{2}\alpha G_n[n(t) - n_{th}] - \dfrac{\kappa}{\tau_{in}}\dfrac{A(t-\tau)}{A(t)}sin\theta(t) \\ \dfrac{dn}{dt}(t) = \dfrac{J}{ed} - \dfrac{n(t)}{\tau_s} - G_n[n(t) - n_0]A^2(t) \end{cases} \tag{3.1}$$

A is the field amplitude, G_n is the linear gain, n the carrier density, n_{th} the carrier density at threshold and n_0 the carrier density at transparency. κ is the dimensionless feedback ratio, τ_{in} the round-trip time in the laser intra cavity and τ the feedback delay. J is the current density, e the elementary charge and d the active layer's thickness. The difference between the COF and the PCF cases stems in the expression of θ. In the case of COF, $\theta = \omega_0\tau + \phi(t) - \phi(t-\tau)$ while in the case of PCF, $\theta = 2\delta(t-\frac{\tau}{2}) + \phi(t) + \phi(t-\tau) + \phi_{PCM}$. In these expressions, ω_0 is the angular oscillation frequency of the laser, $\phi(t)$ the phase of the emitted beam and $\phi(t-\tau)$ the phase of the feedback beam. δ is the detuning and can be considered as zero in our case since we work in a self-pumped configuration.

Considering the stationary solutions, the field and the carrier density are given by: $A_s^2 = \frac{J/ed - n_s/\tau_s}{G_n(n_s - n_0)}$ and $n_s = n_{th} - \frac{2\kappa cos(\theta_s)}{\tau_{in}G_n}$. As a consequence, considering that at the threshold, the laser power is zero –or, equivalently, $|A_s|^2 = 0$–, the threshold current can be written $J_{th} = \frac{ed}{\tau_s}(n_{th} - \frac{2\kappa cos(\theta_s)}{\tau_{in}G_n})$. Therefore, the effect of the feedback is to change the threshold current value, depending on the feedback ratio κ and the phase θ_s. In the case of COF, in the stationary state, $\theta_{COF} = \omega_0\tau$ while in the case of PCF, $\theta_{PCF} = 2\phi_s + \phi_{PCM} \simeq 2\phi_s$ since ϕ_{PCM} can be considered equal to zero [114]. This difference between the expression of θ_s in the COF and the PCF cases results in totally different dynamical behavior. Indeed, in the case of COF, the laser is very sensitive to small variations of the external cavity delay –such as small tilts for instance–, through the dependance of θ_{COF} on τ. In contrast, the phase of a laser with PCF does not change if a small variation of the mirror position is operated. This is due to the absence of $\omega_0\tau$ phase shift in the expression of θ_{PCF}.

A closer look to the equation demonstrated above $J_{th} = \frac{ed}{\tau_s}(n_{th} - \frac{2\kappa cos(\theta_s)}{\tau_{in}G_n})$ may lead one to wonder whether the presence of a feedback could cause an increase in the threshold current. Indeed, values of θ_s satisfying the condition $\frac{\pi}{2} \leq \theta_s \leq \frac{3\pi}{2}$ induce an increase of J_{th}. Yet, to our knowledge there is no report of an increase of J_{th} induced by optical feedback. We believe that the laser spontaneously chooses the solution corresponding to a minimal threshold gain, or equivalently to a minimal threshold current.

Consequently, a good mirror alignment would rather make θ_s close to zero and therefore a reduction of the threshold current would be induced by the presence of the feedback. To our opinion, it is the same kind of dependence that causes linewitdh narrowing or broadening induced by the feedback in regime 1 discussed in chapter 2. It is likely that, according to the quality of the mirror alignment, the spectral narrowing is enhanced the same way as the sensitivity of the threshold current to the feedback ratio. The ideal case would be $\theta_s = 0$, which corresponds to the highest possible threshold diminution for a given feedback ratio.

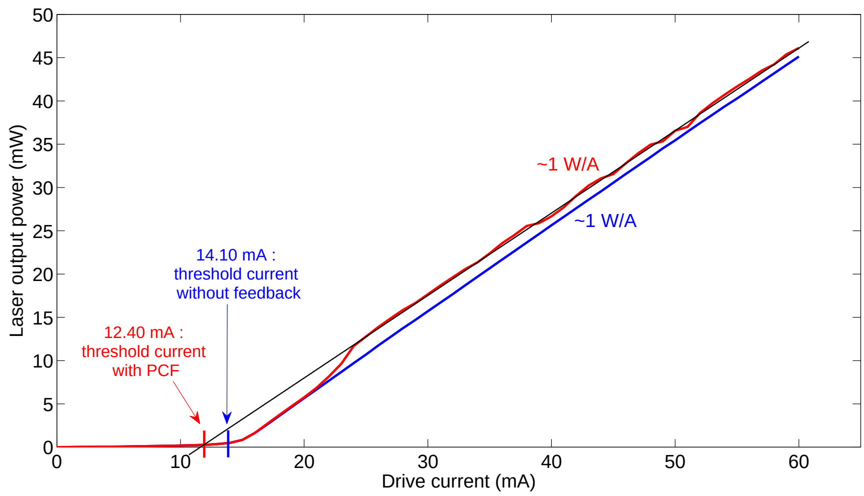

Figure 3.18: Effect of the phase-conjugate feedback on the laser current threshold. I_{th} is reduced by 12% when PCF is enabled.

We show in Fig.3.18 that when the laser is subject to PCF the value of I_{th} is reduced: it shifts from 14.10 mA to 12.40 mA, which represents a decrease of 12%. This threshold current value has been estimated by extrapolating the laser characteristic when subject to PCF for higher current values. Indeed since the phase conjugation process requires a minimum optical power to be enabled, the effect of the feedback on the laser output power cannot be visible experimentally under a certain current value (24 mA). The external cavity length is $L_{cav} = 132\ cm$.

We can also note from Fig.3.18 that the slope of the laser characteristic is unchanged when subject to feedback compared to the no-feedback case. Indeed, in both cases the laser shows a progression close to 1 W/A. In contrast to the COF case, the PCM reflectivity depends on the laser power. Fig.3.19 displays the values of R corresponding to the same current span as in Fig.3.18. We note that, once the PCF generation is enabled ($I > 24\ mA$), the measured reflectivity fluctuates around an average value of 6.6%. These fluctuations –ranging from 5.3% to 8.1%– are due to the instabilities in the laser power triggered by the PCF. The reflected power is almost constant although the injection current is increased. This means that there is a non-linear relationship between the feedback efficiency and the pumping power. This contrast to the COF case was highlighted by Lawrence and Kane in 2000 [112], where it has been reported that the reflected power is constant over a wide range of incident powers in a similar experiment using a barium titanate crystal in a CAT configuration.

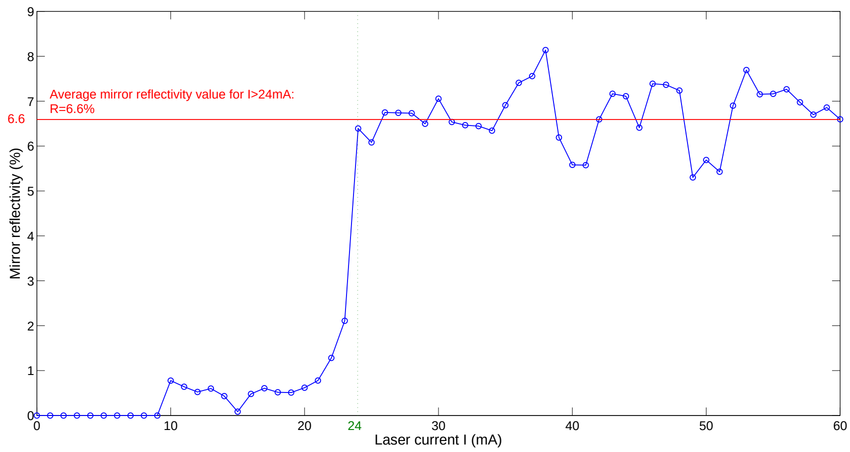

Figure 3.19: Evolution of the mirror reflectivity versus the current. For $I > 24\ mA$, the reflectivity values are averaged values of the fluctuating laser power.

A change in the slope of the light-current characteristic is expected from previous works showing that the slope efficiency decreases when the feedback ratio increases [113]. A close inspection of the calculated relationship between A_s^2 and J reveals that an increase of the slope efficiency of the laser light-current characteristic is expected when the mirror reflectivity increases.

However experiments in both COF and PCF cases show the opposite trend. This points out the fact that even though R is constant with the current, the laser slope efficiency decreases. We believe that although the mirror reflectivity is constant, the coupling factor η might vary when the current increases. This is all the more true in the PCF case as a variation of the current induces changes in the beam properties, modifying its section. As a result, the PCF generation gain can be altered consequently.

Besides, it is worth mentioning that in the presence of feedback, the laser no longer operates in steady state, therefore the stationary solutions of the laser rate equations cannot predict the laser behavior with accuracy. In all cases, no changes in the slope efficiency of the light-current characteristic is seen in our experiment in the reflectivity span. Yet we believe that, provided a wider achievable reflectivity span, this behavior would be an interesting feature to analyze. Fig.3.20 shows how the laser output power is affected when the mirror reflectivity varies both in the COF and the PCF cases.

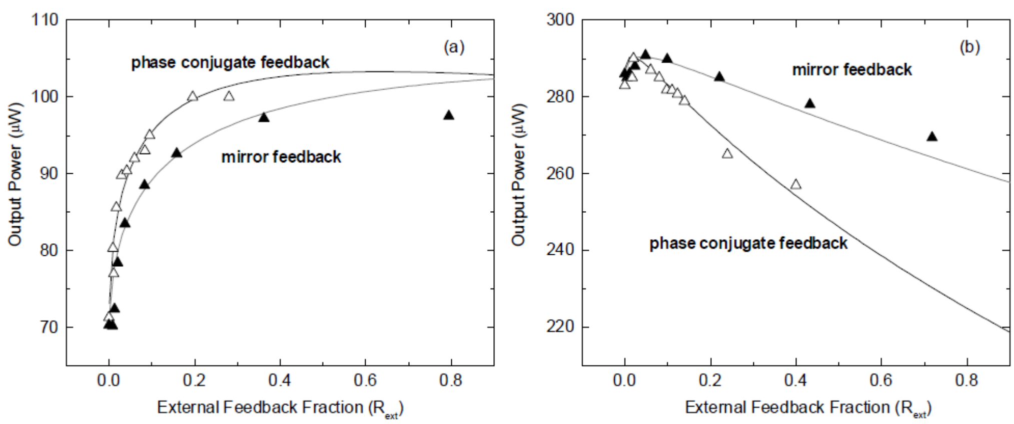

Figure 3.20: Output power versus external feedback fraction for conventional optical feedback and phase-conjugate feedback. The injection current is 40 mA in (a) and 70 mA in (b). Solid lines are theoretical fittings to the experimental data points. Image from [113].

In our experiment this trend could not be observed. Yet the 12%-reduction of the laser threshold current confirms the fact that an increase of the feedback ratio leads to a decrease of the threshold current. A thorough study of the influence of the PCF on the laser threshold current would require both good stability of the feedback ratio and the possibility to achieve much higher PCM reflectivity values, as done in [113] where the maximum reflectance is 50 % and PCF is performed using a CAT configuration in a $BaTiO_3$ crystal.

3.5.2 Examples of dynamical diversity

When the laser diode operates under optical phase-conjugate feedback, it tends to forsake its otherwise solitary steady state and to exhibit more complicated dynamics. Even a very small amount of feedback –equivalent to a very small mirror reflectivity– is enough to destabilize the laser into periodic self-pulsing or chaotic dynamics. In Fig.3.21 and by contrast to Fig.3.2, we show some examples of how the laser behaves with small reflectivities due to the presence of PCF.

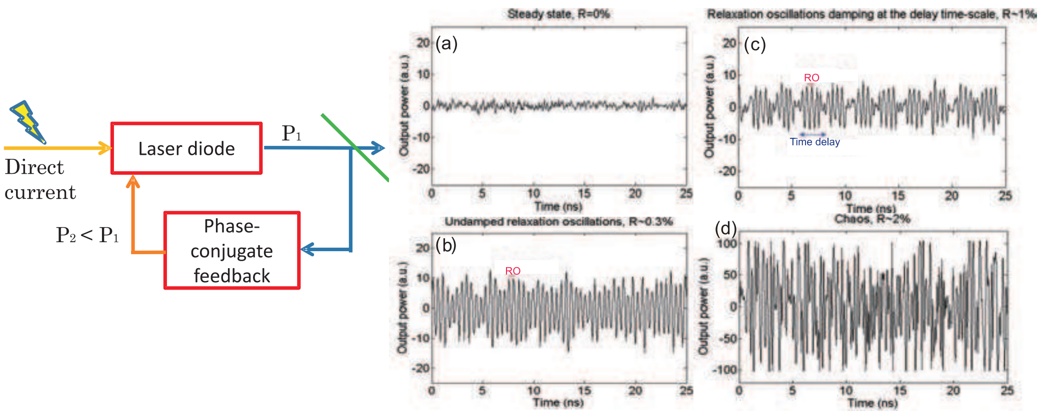

Figure 3.21: Dynamical diversity when the laser diode is subject to low phase-conjugate feedback ($R < 2\%$). A first transition from steady state (a) to chaos (d) is illustrated through the observation of relaxation oscillations (b), which can be damped at the external cavity delay (c).

The general trend is as follows: when $R = 0\%$ the laser is in steady state (a). Then when R increases up to about 1% we can see periodic traces showing free relaxation oscillations (tagged RO in Fig.3.21.(b)). A slight further increase of R gives way to the modulation of the relaxation oscillation pulses at the period of the time delay (c). For higher values of R the laser exhibits chaos (d).

3.5.3 Spectral properties

The presence of feedback in the laser diode, even in a small ratio, is immediately seen in the laser spectrum. Both the RF spectrum and the optical spectrum show evidence of the feedback-induced dynamics. In Fig.3.22 is displayed the influence of a very low feedback level ($R = 0.06\%$) on the laser optical spectrum.

As expected from the laser classification in regimes from 1 to 5 when the feedback strength varies [80], for a low feedback ratio the main peak in the laser optical spectrum becomes much thinner and higher than in the no-feedback condition. Indeed the side peaks that exist when the laser operates solitarily are removed and the main peak gains a 70% line width sharpening. Fig.3.22 illustrates improvement of the laser coherence under the action of the feedback.

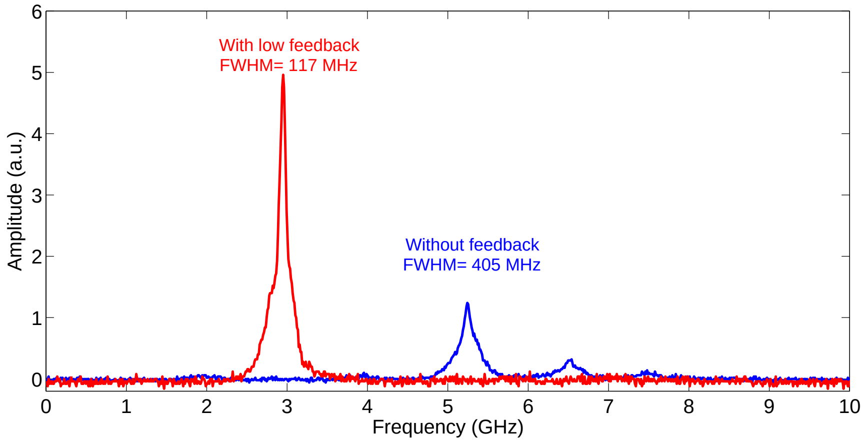

Figure 3.22: Laser optical spectrum without feedback (in blue) and when $R = 0.06\%$ (in red). FWHM changes from 405 MHz to 117 MHz, inducing thus a linewidth sharpening ratio of 70%.

Besides the properties visible on the optical spectrum, the RF spectrum also shows the effect of the feedback on the frequencies at stake in the power fluctuations. Indeed, as we mentioned before, the cavity length L_{cav} is associated with the time delay $\tau = \frac{L_{cav}}{c}$ which is the round-trip time of the photons in the external cavity. We can also define the external cavity frequency $f_{cav} = \frac{1}{\tau} = \frac{c}{L_{cav}}$. f_{cav} is a particular value since the RF spectrum shows peaks at each of its multiples. The external cavity length, through the PCF time delay, shows its signature in the laser spectrum by means of these peaks repeating themselves at the pace of f_{cav}. Fig.3.23 shows how L_{cav} affects the frequencies in the laser power time series and how it can be estimated from a RF spectrum, here measured when $R = 0.09\%$. Indeed the RF spectrum operates a Fourier transform of the laser time series, which allows to see the frequency content in the power fluctuations. In this figure, $f_{cav} = 224\ MHz$ corresponds to the experimental external cavity length of $L_{cav} = 130\ cm$. Naturally the shorter the external cavity length the larger the frequency separation between RF peaks which form actually new frequencies in the laser power time series.

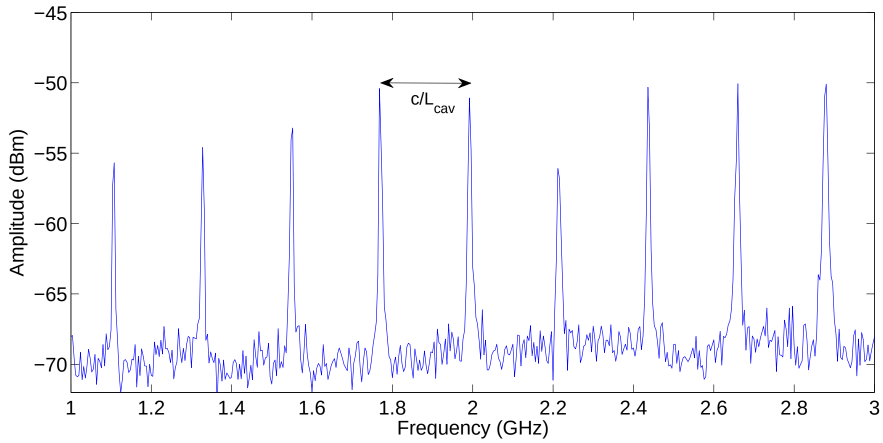

Figure 3.23: Laser RF spectrum when $R = 0.09\%$. The frequency peaks induced by the external cavity appear at $f_{cav} = \frac{c}{L_{cav}}$ and its multiples.

The temporal and spectral properties shown in Fig.3.21, Fig.3.22 and Fig.3.23 are seen when R is very low. When the mirror reflectivity is increased the laser undergoes a cascade of bifurcations leading to a lot of dynamics more complicated [66,95,115]. As we discussed in chapter 2, countless different dynamics can be reached with the experimental setup presented here by merely changing the value of the PCM reflectivity, even in a short range. Some behaviors have been predicted in theoretical models but have hardly or never seen in the experiments, mostly because of the experimental toughness of the setup and its great sensitivity to mechanical and temporal instabilities as well as beam misalignment.

On the contrary, some experimental observations have never been focused on in the theory because they are unexpected in the usual model and cannot be theoretically accounted for. As for the exploitation of our experiment, in the present work we aim to report a detailed study on three particular features that we had the opportunity to see experimentally:
- birth and destabilization of self-pulsing external cavity modes.
- birth and evolution of extreme events in chaos.
- coherence resonance of low-frequency fluctuations.

Before presenting the experimental observations and conclusions, in the next chapter we focus on the theoretical model predicting the nonlinear laser dynamics when subject to PCF. The next chapter introduces the equations on the basis of which we simulate the system behavior along with the state-of-knowledge of the laser dynamics subject to PCF.

CHAPTER 4

Theoretical model and route to chaos

He who loves practice without theory is like the sailor who boards ship without a rudder and compass and never knows where he may cast. Leonardo da Vinci

In all domains of physics, in order to fully understand various observed phenomena, theoretical models are developed and bring mathematical formulation to experimental behaviors and physical units. In complex systems such as nonlinear laser dynamics, simulations based on theoretical models are commonly carried out to predict the laser dynamics. In this chapter we present the model that we exploit in order to both extend the theoretical background and demonstrate qualitative accordance with experimental observations.

4.1 Lang-Kobayashi system of equations for PCF

As presented in chapter 2, the theoretical model to study the laser dynamics is the commonly-used Lang-Kobayashi rate equations adapted for the case of PCF. This model is rather simple and is thus easy to tamper with. That is why it has been largely used to study and predict laser nonlinear dynamics [66, 72, 75, 114]. This system of equations writes as follows.

$$\begin{cases} \dfrac{dE}{dt}(t) = (1+i\alpha)N(t)E(t) + \gamma E^*(t-\theta) \\ T\dfrac{dN}{dt}(t) = P - N(t) - (1+2N(t))|E(t)|^2 \end{cases} \tag{4.1}$$

θ is the normalized external cavity time delay. The normalization factor is the photon lifetime τ_p, which, according to Ref. [75], we take equal to $\tau_p = 1.4\, ps$. Then $\theta = \frac{\tau}{\tau_p}$. The physical link with the cavity length is $\tau = \frac{L_{cav}}{c}$. α is the linewidth enhancement factor and T the ratio of electron to photon lifetime. E is the slowly varying complex envelop of the electrical field, N

is the carrier inversion and P the normalized pump current above threshold: $P = \frac{I-I_{th}}{I_{th}}$ where I_{th} is the laser threshold current. γ is the normalized feedback ratio: $\gamma = \tau_p \kappa$ where $\kappa = \frac{1-R_m}{\tau_L}\sqrt{\eta_c \frac{R}{R_m}}$. R_m is the reflection power of the laser output facets, η_c is the coupling efficiency coefficient, R is the PCM reflectivity. τ_L is the laser intracavity round-trip time: $\tau_L = \frac{2nL_{laser\ cavity}}{c}$ where n is the refractive index of the semiconductor material on which the laser cavity is built.

If the drive current is fixed, we can consider that γ is proportional to the square root of the PCM reflectivity. Therefore, the conversion between the physical PCM reflectivity R and the feedback ratio γ is not easily guessed. Since we do not aim at doing quantitative comparisons, it is sufficient to keep in mind that $R = 100\%$ is equivalent to $\gamma = 0.256$ to have an idea of the orders of magnitudes of the feedback ratio ranges that will be presented in the simulations. The parameters that we choose to calculate γ for a given R are: $\eta_c = 1$, $\tau_L = 7\ ps$, $R_m = 0.3$ and $\tau_p = 1.4\ ps$.

However, as we discussed in chapter 2, this model does not take into account several points that are physically intrinsic to the experiment. The first one is the way phase conjugation is performed, thus the PCM build-up time does not appear and is supposed to be zero. Phase conjugation is then considered to be instantaneous. Secondly, the feedback ratio γ and the pumping current P are two independent parameters in the model. This point differs from reality since in our self-pumped configuration the gain of the phase conjugation process depends on the powers of both the pump and the signal beams in the four-wave mixing interaction. As a consequence, the mirror reflectivity depends on the laser drive current. However, as we saw in Fig.3.19, the dependence of the mirror reflectivity on the injection current is significant only for small current values. Indeed, in our experimental case, the PCM reflectivity is almost constant (close to 6.6%) in the span of current ranging from 30 mA to 60 mA. Therefore, we can consider that the dependence of R on I is very little for the experimental current values. As a consequence, the fact that the model considers that γ and P are independent is not contradictory to the experiment. As we mentioned in the previous chapter, this reflectivity saturation was reported in [112]. Furthermore, as usual when studying lasers subject to PCF, the phase shift at the phase-conjugate mirror can be considered to be zero: $\phi_{PCM} = 0$ [114].

The aim of those adapted Lang-Kobayashi equations for PCF is to provide, using a simple model, with a general trend of the evolution of the laser dynamics. In the literature, more complex sets of equations have been suggested in order to enhance the compliance of the model with the physical nature of the system. This has been done by extending the equations by either taking into account the phase-conjugate feedback build-up time [73,74,81] or modeling the laser cavity by a saturable gain medium [72]. However, our aim is to provide a general prediction of the laser dynamics with a quite simple model which is able to show qualitative compliance with particular experimental results. Indeed, we do not intend to use this model to carry out quantitative predictions to be further confirmed experimentally. We rather use it to provide theoretical guidance and background to observations. We will see that, if the range of parameters is properly chosen, the Lang-Kobayashi equations for PCF show good accordance with experimental results. Moreover, since equations (4.1) stem from the standard Lang-Kobayashi equations for the COF case (equations 2.2), theoretical comparisons with the well-known and largely-studied COF case are facilitated.

4.2 Bifurcation diagram

A pioneering theoretical analysis of the laser dynamics and bifurcations with PCF has been carried out by Krauskopf *et al.* in 1998 [72] who produced an in-depth account of the evolution of the bifurcation diagram and the route to chaos along with the transitions through the three first chaotic regions –called "chaos bubbles"– undergone by the laser. The bifurcation diagram in Fig.4.1 predicts the laser dynamics with the same parameters as in [72] and computed with equations (4.1).

4.2.1 Bubbles of chaotic dynamics

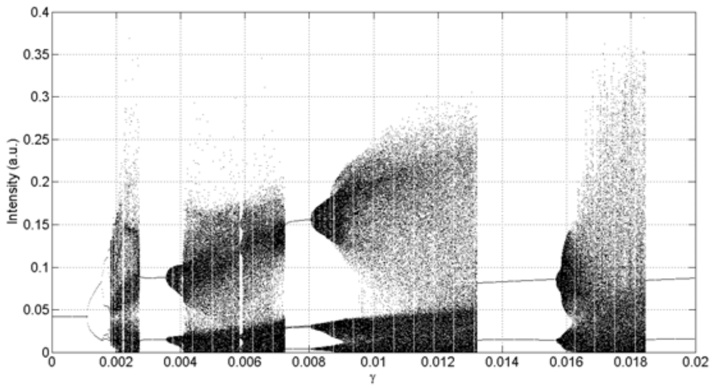

Figure 4.1: Bifurcation diagram for θ=476, P=0.0417, T=1428 and $\alpha = 3$.

Fig.4.1 is a typical bifurcation diagram for a laser diode with PCF. The x-axis is the feedback ratio γ and the y-axis is the laser output power. The bifurcation diagram counts, for each value of γ, all the possible minimum and maximum values in the laser output power. In the diagram, each laser operating state is represented by as many dots as extremum values in the corresponding time trace. The way we plot the bifurcation diagram is further illustrated in Fig.4.2. A steady state shows only one dot (a) while a harmonic signal counts two dots (b). A signal showing double periodicity is represented by four dots (c) and if a second double periodicity is undergone, the diagram counts eight dots (d). Complex chaotic fluctuations are represented by a multitude of dots which almost show a continuum of values.

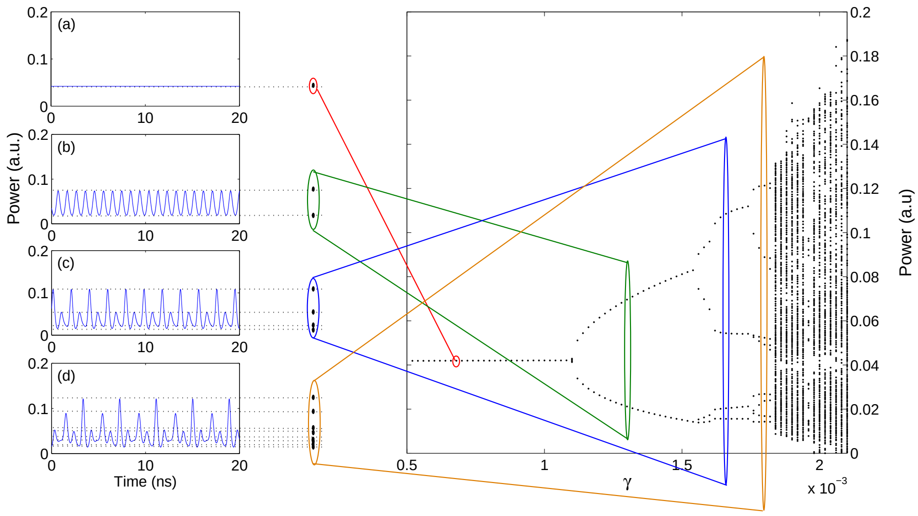

Figure 4.2: Sketching a bifurcation diagram from the detection of the extrema in the laser time trace.

In Fig.4.1, the values of the parameters correspond to usual orders of magnitude found in experiments: $\theta = 476$ is equivalent to a 20-cm-long round-trip in the external cavity, P=0.0417 corresponds to a drive current slightly above the laser threshold, T=1428 and α=3 are common values for standard laser diodes such as those used in optical communications.

4.2.2 Bifurcations

The bifurcation diagram displays the successive dynamical states that the laser exhibits when the feedback ratio varies. The dynamical transitions undergone in the route to chaos are ruled by bifurcations which occur for given values of γ and have the effect to change the dynamics of the laser power.

Bifurcations are classified according to the corresponding qualitative changes in the dynamics. For example, Hopf bifurcations change a fixed point into a limit cycle branching from the fixed point. Period-doubling bifurcations double the phase plane trajectory of a limit cycle. Fig.4.3 presents the cascade of bifurcations undergone by the laser as a route to chaos is initiated.

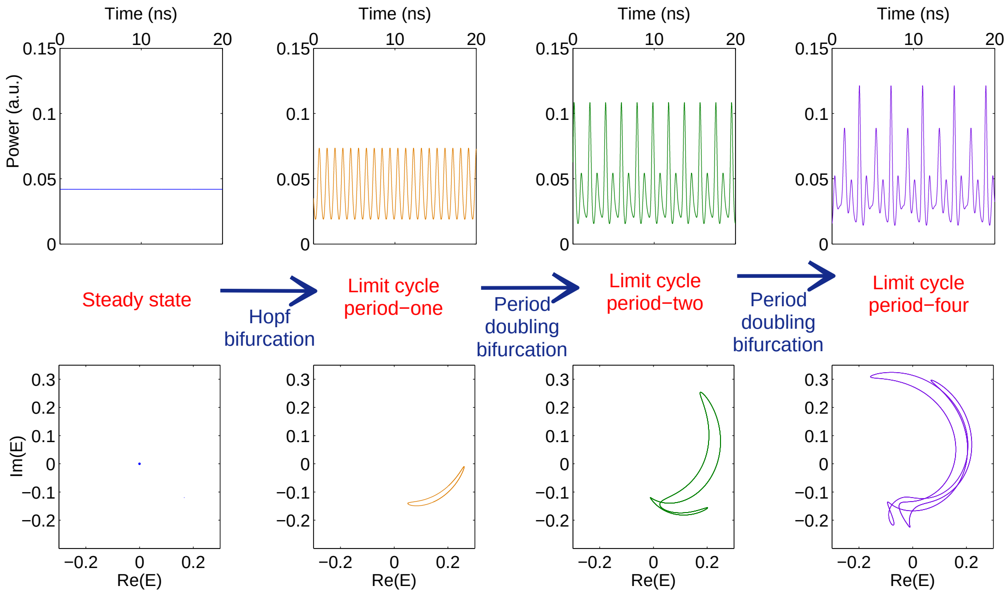

Figure 4.3: Successive bifurcations from an initial steady state to a period-four limit cycle. The dynamical transitions from a state to another are seen in the time traces at the top and in the phase planes at the bottom.

Other bifurcations such as torus – that change a limit cycle into a torus showing quasi-periodicity– or saddle-node bifurcations are also at stake in the bifurcation diagram. As we will see in chapter 5, they are responsible for the stabilization and destabilization of pulsing ECMs and the resulting chaos suppression.

4.3 Laser dynamical evolution

4.3.1 Route to chaos: small feedback ratio values

Fig.4.4 is a zoom of the bifurcation diagram presented in Fig.4.1 on the lower values of the feedback, where the route to chaos occurs. Different dynamical regions are tagged from (A) to (H) and their temporal and spectral features are presented in Fig.4.5. The well-known bifurcation scenario of the laser subject to PCF is as follows. When the feedback ratio γ is increased starting from zero, the laser first begins by operating in steady state (region tagged A in Fig.4.4) in which the emitted power is constant in time until the first Hopf bifurcation occurs.

This bifurcation modifies the laser operating state, making it oscillate (B) at the relaxation oscillations' frequency (here 1.036 GHz). The amplitude of those oscillations increases along with the increase of γ. Then a sequence of bifurcations is undergone through two successive period doublings (C) and (D), making new frequencies appear in the laser spectrum. Indeed, in Fig.4.5, the first period doubling brings the laser to oscillate at 0.517 GHz (b.3) –which is half the frequency of the relaxation oscillations'. Then a second period doubling halves this new frequency, reducing it to 0.259 GHz (b.4). The effect of period doubling can be clearly seen in time trace (a.3) where one on every two peaks is amplified and the other one is attenuated compared to the fundamental pulsing state of trace (a.2).

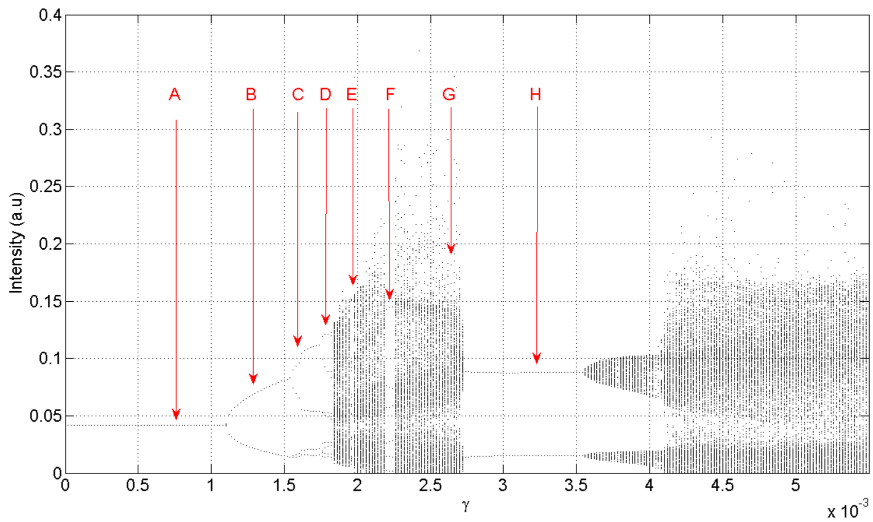

Figure 4.4: Same bifurcation diagram as in Fig.4.1 but limited to small feedback ratios.

As the feedback ratio increases further, the laser enters the first chaotic region (E). When operating in chaotic state, the laser output power exhibits irregular fluctuations with no apparent correlation as shown in (a.5). The corresponding spectrum (b.5) shows that there are no more preferential frequencies and the average level of all frequency components increases. Both traces (E) and (G) show typical chaotic dynamics. It may happen that tiny regions of time-periodic dynamics appear between regions of chaos, as pointed in (F). In the short range of feedback values in which the time trace (a.6) and the spectrum (b.6) are seen, the laser exhibits locking to a time-periodic dynamics. Then a slight increase of γ makes the laser resume chaos (G) until the next bifurcation occurs, inducing a dramatic change of the laser dynamics. Indeed, chaos vanishes in the time trace (a.8) and in the spectrum (b.8), leaving the laser in a self-pulsing dynamics with perfectly regular sinusoidal fluctuations (H). This state has been identified by Erneux *et al.* in [75] as external cavity modes for a laser with PCF, where the time series shows periodic pulses at frequencies proportional to the external cavity frequency : $f = \frac{c}{L_{cav}}$. We will bring a deeper analysis of those self-pulsing states in chapters 5 and 6. Then, when further increasing γ, the laser undergoes a new sequence of bifurcations and re-enters a region of chaos.

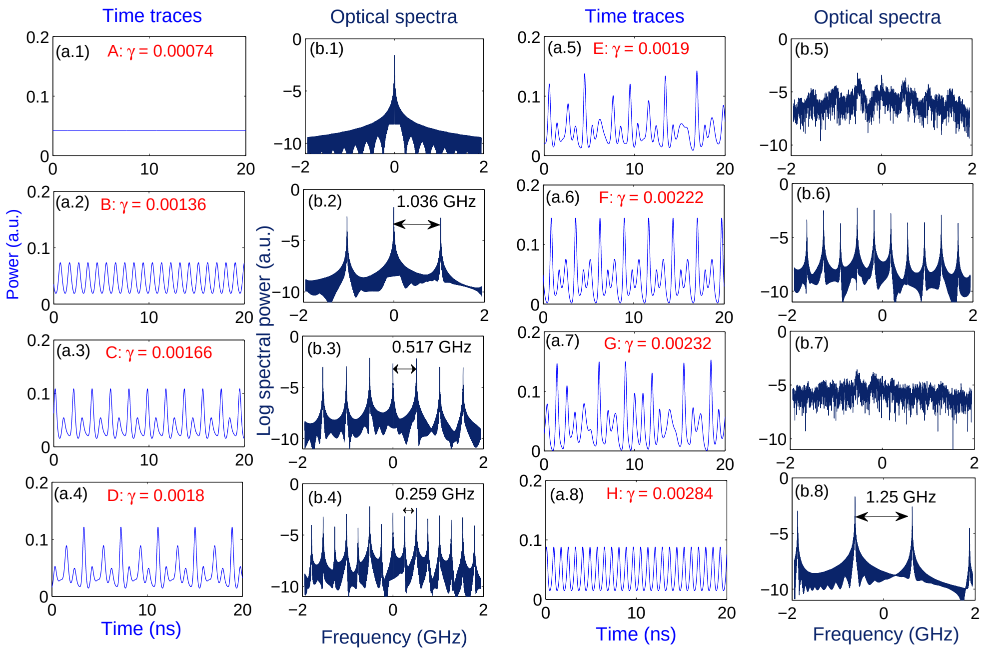

Figure 4.5: Evolution of the time traces and optical spectra when the laser undergoes route to chaos. The tags (A) to (H) refer to the different regions in the bifurcation diagram in Fig.4.4.

4.3.2 Intermediate feedback ratios and validation of the model

We extend now the study of the laser dynamics predicted by the model to states that emerge when γ is higher than 0.005. To validate this model, we carry out the same simulations as the ones led by Krauskopf *et al.* in [72] about the transition through the first three bubbles of chaos. We look for confirmation of the predicted succession of dynamical states reported in [72] and represented in Fig.4.6.

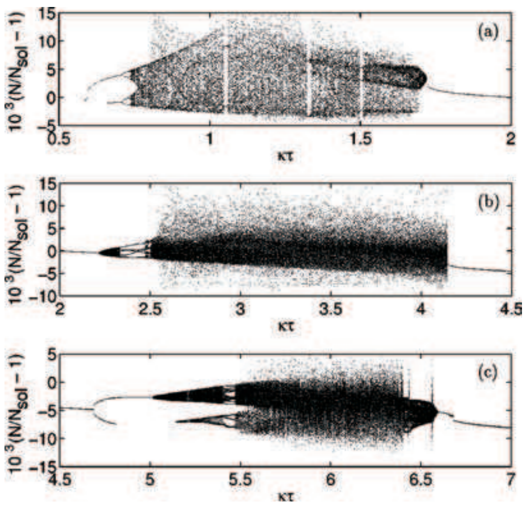

Figure 4.6: Three first chaos bubbles identified by Krauskopf *et al.* Picture from [72].

Those same three bubbles of chaos computed with the model of equations (4.1) are represented in the bifurcation diagram in Fig.4.7. Yet, the diagrams are not identical since in our model we do not use gain saturation.

In this range of feedback ratio values, the system is expected to exhibit a succession of chaotic states and self-pulsing ECMs, as presented in Fig.4.8. In order to do the comparison, the computed evolution of the laser dynamics is presented in Figs.4.9, 4.10 and 4.11 for each chaos bubble. We identify the same evolution of the successive laser states when the feedback ratio varies. In this range of γ values, the system undergoes a succession of stabilizing and destabilizing bifurcations leading to self-pulsing external cavity modes interspaced by regions of chaos.

The succession of dynamical states depicted in Fig.4.9 begins with the limit cycle (A) corresponding to the undamped relaxation oscillations pulsing at 1.036 GHz. Then as, γ increases, the laser undergoes period doubling

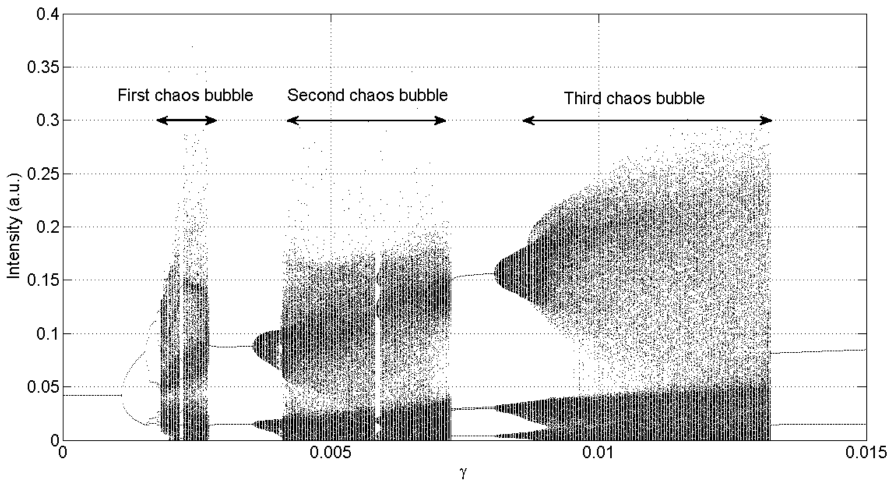

Figure 4.7: Simulation of the same three chaos bubbles as presented in Fig.4.6 computed with equations 4.1.

(B) until a chaotic attractor is created (C). As the laser exhibits developed chaos (D and F), a window of periodic dynamics is observed (E) as was noticed in the first bubble of chaos in Fig.4.8.(f). Chaos terminates as the attractor gradually shrinks toward a quasi-periodic state (G). A further increase of the feedback ratio makes the laser exit the first bubble of chaos and exhibit self-pulsing dynamics, corresponding the first external cavity mode (H) which frequency is 1.3 GHz.

The transition through the second bubble is depicted in Fig.4.10 and is to be compared to the middle column in Fig.4.8. As the laser just exited the first bubble, it operates in a self-pulsing state at the external cavity frequency (A). A bifurcation occurs causing quasi-periodicity and reshaping the limit cycle into a torus (B). Then this torus changes shape and switches to a chaotic attractor (C). Temporarily, the chaotic dynamics gives way to a region of locking, the periodicity of which is seen in (D). Yet this region of locking is not seen in the traces in Fig.4.8. Then chaos is quickly resumed as a chaotic attractor is regenerated (E). Eventually chaos ceases brutally as the attractor is reshaped in a limit cycle (F) which is definitely reached as the system shows regular self-pulsations (G). Yet it is not a purely sinusoidal pulsing state, as can be guessed from the bifurcation diagram in Fig.4.7 and asymmetric trajectory in the phase plane in Fig.4.10. Indeed, although the spectrum (G) shows pulsations at the second ECM frequency (2.7 GHz), by contrast to the case presented in the middle column in Fig.4.8.(h), the limit

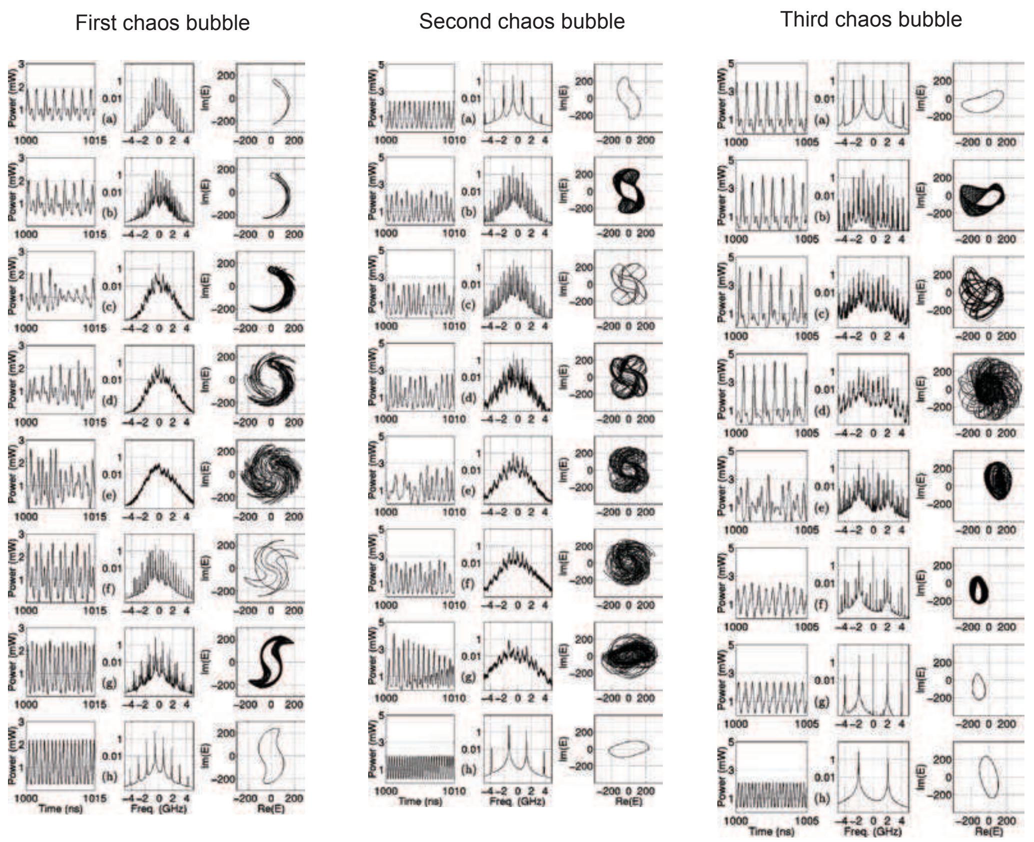

Figure 4.8: Time traces, spectra and trajectories in the E-plane corresponding to the evolution of the laser through the chaos bubbles presented in Fig.4.6. Pictures from [72].

cycle of the generated ECM when exiting the second bubble of chaos is not symmetric and the laser does not operate in an ECM state. It is likely that the second ECM is already unstable when the laser exits the second chaos bubble.

The transition through the third bubble of chaos is presented in Fig.4.11. The same trend as depicted in the right column in Fig.4.8 is observed. The asymmetric limit cycle (A) becomes unstable and the laser bifurcates to chaos anew as can be seen in traces (B) to (D). In the study carried out in [72], and as can be seen in Fig.4.8, the system has been reported to show a nonsymmetric limit cycle (right column in Fig.4.8.(e-g)) before bifurcating to the symmetric limit cycle representing the self-pulsations of the third external cavity mode (right column in Fig.4.8.(h)). In our case, the symmetry breaking is also present as off the end of second chaos bubble (Fig.4.10.G), and

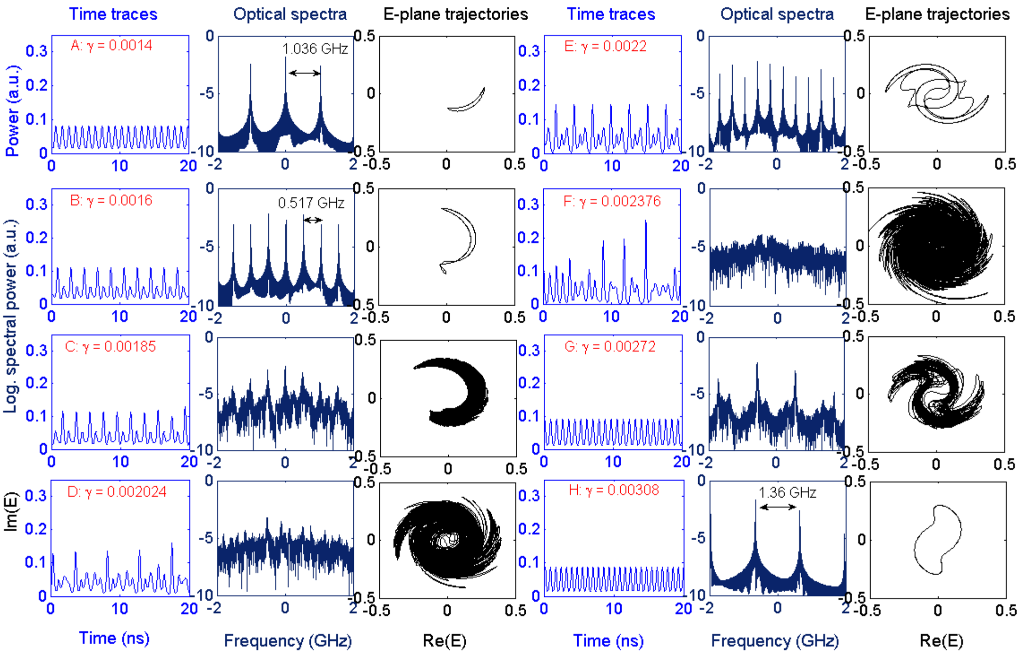

Figure 4.9: Time traces, spectra and trajectories in the E-plane corresponding to the evolution of the laser through the first chaos bubble presented in Fig.4.7. Those traces are to be compared to the ones presented in Fig.4.8 in the left column.

the symmetry restauration occurs when the chaotic attractor in Fig.4.11.(E) is changed into an asymmetric off-centered limit cycle. This limit cycle drifts then to the center of the Poincaré map where symmetry is restored (F). This limit cycle pulses at 4.1 GHz and is characteristic of the third self-pulsing external cavity mode, announcing the end of the third chaos bubble.

4.3.3 Conclusions

The simulations presented in this chapter show good accordance with the same theoretical study carried out by Krauskopf *et al.* [72] in which the model is slightly different since it uses a saturable gain medium. This comparison is useful in that it reminds the reader of the ECMs and their bifurcations to chaos as expected for small values of the feedback strength. This also validates our simulation tools which will be further used in the next chapters to analyze new bifurcations and dynamical features, hence extending the previous works carried out by Krauskopf, Green and Erneux [72, 75, 114].

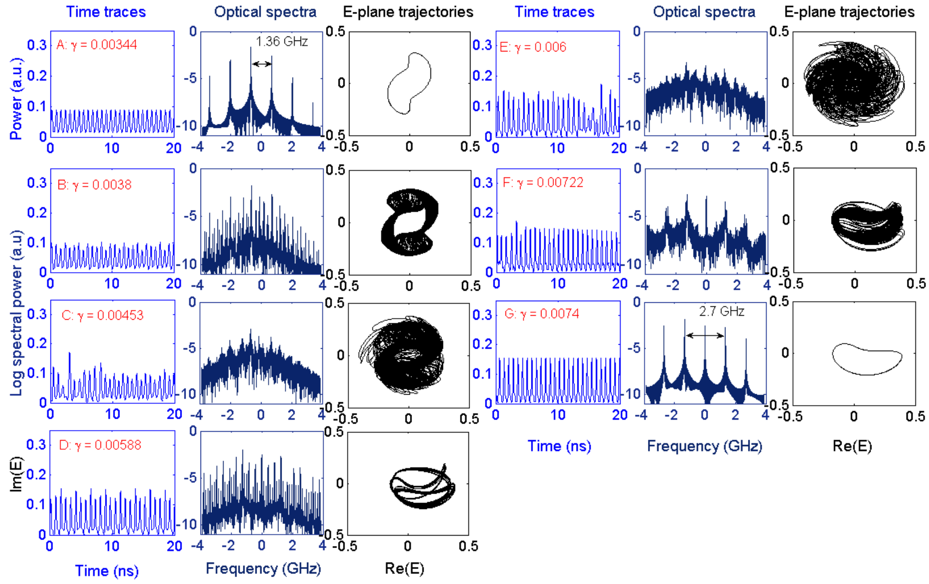

Figure 4.10: Time traces, spectra and trajectories in the E-plane corresponding to the evolution of the laser through the second chaos bubble presented in Fig.4.7. Those traces are to be compared to the ones presented in Fig.4.8 in the middle column.

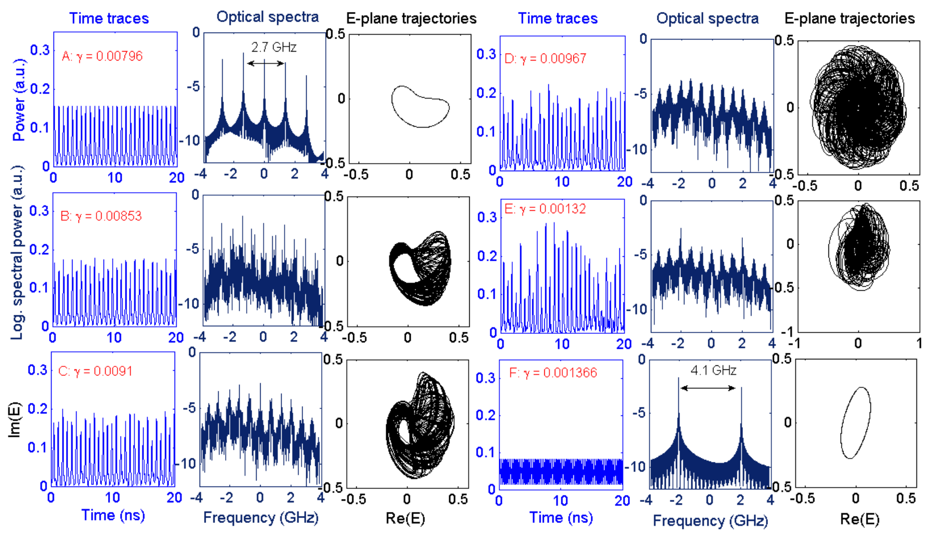

Figure 4.11: Time traces, spectra and trajectories in the E-plane corresponding to the evolution of the laser through the third chaos bubble presented in Fig.4.7. Those traces are to be compared to the ones presented in Fig.4.8 in the right column.

CHAPTER 5

Chaos crisis and ECM bistability

In all chaos there is a cosmos, in all disorder a secret order. Carl Jung

The simulations results presented in this chapter have been carried out thanks to the fruitful work of Martin Virte as he was doing a five-month internship in the laboratory.

We have seen that theoretical simulations predict the following scenario when the feedback strength increases. The laser diode is first destabilized from steady state and undergoes a route to chaos through a sequence of bifurcations. As we saw in Fig.4.1 in chapter 4, the chaotic regions are interspaced by regions of self-pulsing dynamics called external cavity modes (ECMs). The mechanism of appearance and evolution of these ECMs has been extensively studied in the case of weak feedback configurations [114, 116]. As for larger values of feedback, although experiments seem to indicate that ECM restabilization occurs [80], no theoretical study has been reported accounting for this evolution. In all cases it is a major contrast to the COF case in which an increase of the feedback strength leads to more and more developed chaos [46]. In this chapter we extend the theoretical study of the laser bifurcation cascade for larger values of the feedback ratio computed with the same set of rate equations as in the previous chapter (see equation 4.1): the Lang-Kobayashi rate equations adapted for PCF.

5.1 Chaos crisis and chaos suppression

5.1.1 Transition from chaos to self-pulsing external cavity mode

Fig.5.1 is the extension of the bifurcation diagram presented in Fig.4.1 for higher feedback ratio values. One can notice that the regions of chaos tend to shrink when the feedback ratio increases. Indeed the seven successive regions of chaos grow thinner while, on the contrary, the self-pulsing external cavity

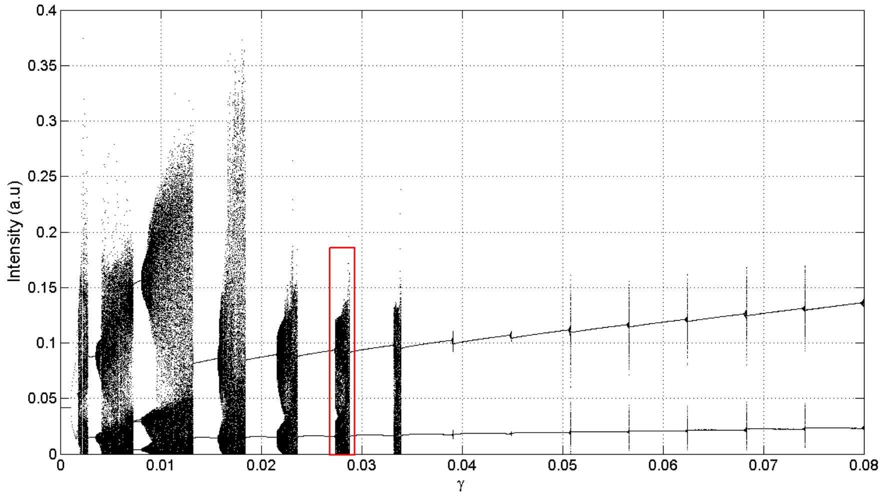

Figure 5.1: Bifurcation diagram for θ=476, P=0.0417, T=1428 and α=3. Same as Fig.4.1 but for wider ranges of feedback ratio. Seven chaos regions that gradually shrink and end up by vanishing are counted.

modes' stability domains cover larger feedback spans. Eventually, when γ is higher than 0.035 chaos is suppressed and only successive self-pulsing states at frequencies multiples of the external cavity frequency are observed. This process in which regions of chaos vanish gradually is indicative of a chaos crisis. As the feedback ratio is increased, the system goes through chaos bubbles until chaos is totally suppressed. Then the laser remains in a purely self-pulsing dynamics and no longer shows bifurcation to stable chaotic attractors. If γ is further increased, the laser undergoes bistable switching between ECMs pulsing states of increasing frequencies instead of bifurcations to chaos.

In order to understand this crisis and the abrupt transitions from chaos regions to self-pulsing states, we present if Fig.5.2 what happens close to the end of the sixth region of chaos (in the red box in Fig.5.1) fades. A zoom on this sixth region of chaos is represented in Fig.5.2.(a) where the transition from chaos to pulsing ECM is presented. Fig.5.2.(b.1) is the time trace just before chaos disappears (γ=0.028796), the trace in (b.2) is a zoom on the red dashed box in the time series in (b.1). Figures (c.1) and (c.2) are the corresponding trajectories in the phase space. The red ellipse is the limit cycle characteristic of the self-pulsing ECM to which the laser bifurcates once this chaotic region is overcome –that is when γ reaches 0.02896. This ECM state is presented in Fig.5.2.(b.3) along with the corresponding trajectory in the phase plane (c.3). The phenomenon causing the regions of chaos to terminate and the consequently observed chaos crisis emerges from the fact that the chaotic attractor born from the previous ECM grows in size until taking the shape of the limit cycle trajectory of the next ECM. Indeed, in Fig.5.2.(b.1) and (c.1), although the laser operates in chaotic state, fragments of the next ECM self-pulsing dynamics are seen both in the time traces – like the periodic curve in (b.2)– and the shaping of the limit cycle in (c.2), announcing the shortly-expected transition to the new ECM state displayed in (b.3) and (c.3).

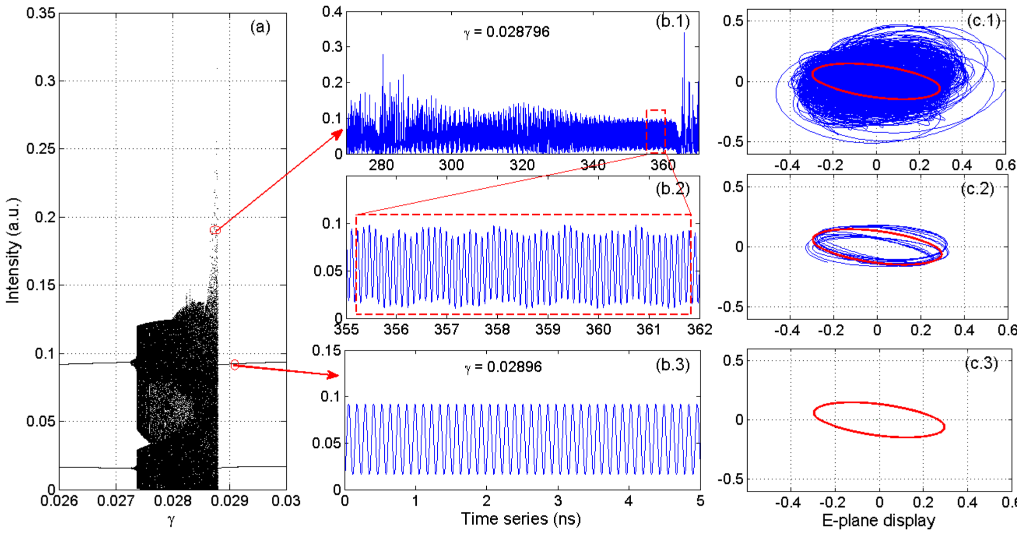

Figure 5.2: Time traces and phase trajectories at the transition from the sixth region of chaos to self-pulsing ECM. Figure (a) is the bifurcation diagram focused on the sixth chaos bubble in Fig.5.1. Trace (b.1) is the chaotic time trace for $\gamma = 0.028796$. Figure (b.2) is the zoom on the dashed red box in figure (b.1) and shows in advance the periodic dynamics of the self-pulsing ECM represented in (b.3). The corresponding trajectories in the phase plane are displayed in figures (c.1), (c.2) and (c.3), where the red ellipse is the limit cycle the ECM emerging from the chaos disappearance.

This scenario repeats itself whenever a region of chaos gives way to a self-pulsing ECM state as has been suggested in [72].

5.1.2 Bifurcation mechanism of chaos crisis

To bring an explanation to this chaos crisis phenomenon, we have complemented the numerical study with mathematical continuation techniques using the DDE-BIFTOOL package [117]. Indeed, usual numerical techniques to solve the laser equations only take into account the stable solutions, ignoring thus the unstable branches in the bifurcation diagram. Continuation methods allow to follow both stable and unstable solutions along with their related branches of steady states and periodic solutions. An in-depth analysis of the stability domains of the system can be thoroughly carried out with this continuation method.

All bifurcation points showing ECM stabilization and destabilization and the corresponding ECM branches are represented in Fig.5.3 along with the bifurcation diagram of Fig.5.1. For each ECM branch, the stable parts are displayed with a thick line and the unstable parts with a thin line. The continuation method shows that every ECM rises from a saddle-node bifurcation (square) and vanishes with a torus bifurcation (circle) making it unstable. A very interesting parameter is the "length" –in terms of feedback span– in which ECMs are stable. A closer look at Fig.5.3 shows that the stable ECM branches grow longer when the feedback ratio increases. As a consequence, the intervals between the torus bifurcation of an ECM and the saddle-node bifurcation of the next ECM –or in other words, the intervals of feedback values in which chaos is observed– decrease. That is why regions of chaos get gradually shorter when γ increases. As the feedback ratio increases, regions corresponding to stable external cavity modes tend to grow and invade the otherwise chaotic regions, causing the diminution of the latter.

But the real disappearance of chaos occurs for values of γ higher than 0.035. At that range of feedback ratios, the saddle-node bifurcations that create the next stable ECMs occur for feedback ratios smaller than the torus bifurcation that destabilize the previous ECMs. In other words, the stabilization process of ECM_{n+1} is complete before ECM_n is destabilized. Therefore, when reaching the end of ECM_n, the system has the possibility to directly jump to ECM_{n+1} without bifurcating to chaos. As a result, the mechanism inducing the chaos crisis is present as soon as ECM_n gets destabilized. Consequently chaos is not observed any more if the system spontaneously jumps to the next stable ECM.

In this model of laser dynamics, the combination of a chaos crisis mechanism and a bifurcation mechanism making the position of the torus and saddle-node bifurcation on limit cycle dependent on the feedback ratio is a remarkable feature. This phenomenon opens fruitful ideas of research to-

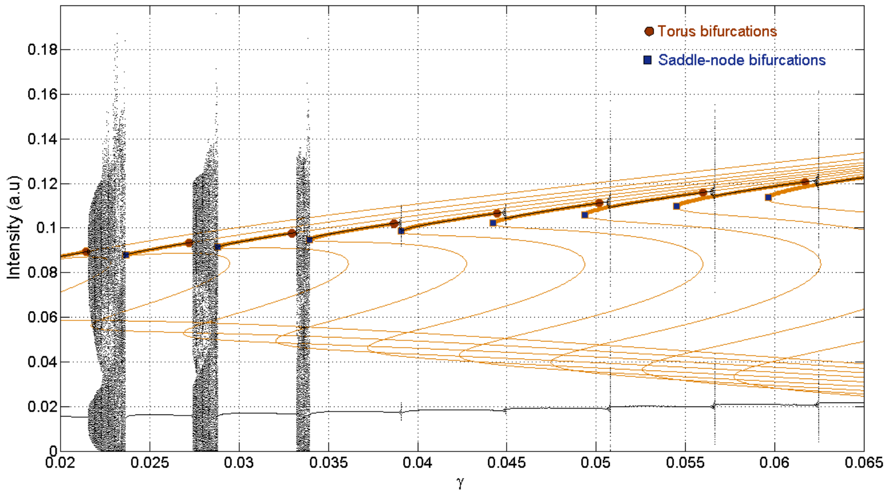

Figure 5.3: Continuation method applied to the bifurcation diagram. The stable ECMs are represented by thick yellow lines and the unstable ones by thin lines. As γ increases, the regions of stable ECMs grow in spite of the regions of developed chaos.

wards control and full suppression of chaos in laser diodes. Again, this feature is particular to the case of PCF since, as we mentioned before, in the COF case regions of chaos widen when the feedback ratio increases [60].

These conclusions on suppression of chaos are not generalizable to every range of feedback level, though. Fig.5.4 shows that when the feedback ratio is higher than 0.065, in the case of a bifurcation diagram computed with decreasing values of feedback, the system goes through a quasi-periodic state before hopping to the next ECM. Indeed, when an ECM is terminated, it is possible that the torus bifurcation occurs before the next saddle-node bifurcation. In that case the system initiates a route to chaos through quasi-periodicity before recovering a pulsing state. That is why the black curve in Fig.5.4 counts small regions of chaos between consecutive ECMs when γ is higher than 0.065. Nevertheless, this fact does not change the general mechanism reported before about chaos suppression induced by saddle-node bifurcation on limit cycle.

5.2 Bistability of pulsing external cavity modes

The fact that the torus and saddle-node bifurcation points –and thus the ECM stability domains– depend on the feedback ratio brings us to the ob-

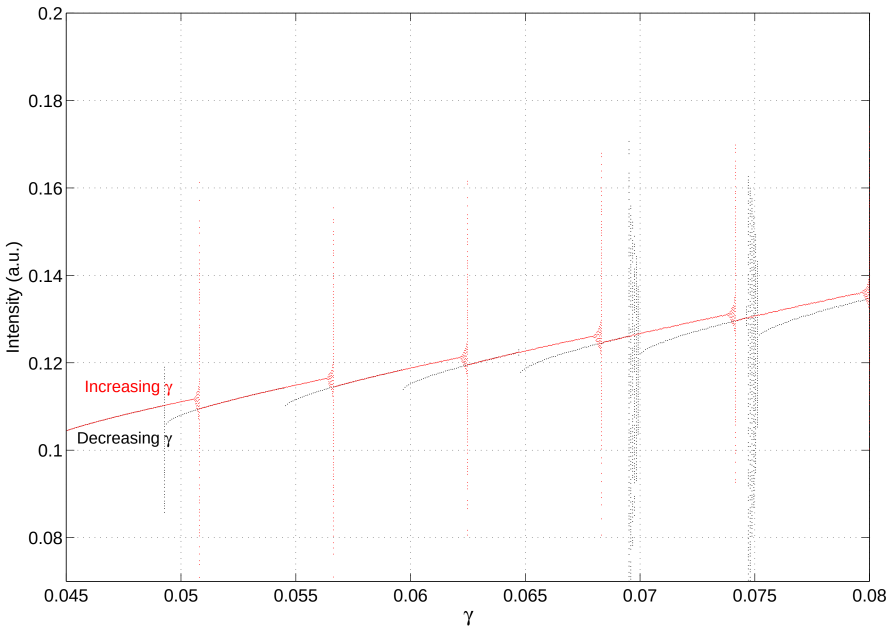

Figure 5.4: Bifurcation diagrams computed for increasing (in red) and decreasing (in black) values of γ.

servation of ECM bistability. Evidence of bistability has been reported by Green *et al.* in 2002 [116] but only in a small range of the parameters with solutions having a small basin of attraction with respect to other stable attractors. In our case the scenario of bifurcations leading to bistability is of a different kind. Moreover, bistability is seen in large spans of feedback ratio values, those spans growing wider as the feedback level is increased.

In Fig.5.5.(a) are presented the bifurcation diagrams built for increasing (in red) and decreasing (in black) values of γ. The laser undergoes successive transitions to self-pulsing ECMs as the feedback ratio varies. As γ increases, the value of the feedback ratio that destabilizes ECM_n through quasi-periodicity gets smaller than the value the feedback ratio value that stabilizes the next ECM (ECM_{n+1}) through a saddle-node bifurcation. As a result, there are regions of γ where two stable ECMs coexist and the system shows bistability. Those regions of bistability are represented by pairs of vertical dashed lines, for which two stable pulsing states are allowed for each value of the feedback: one for each stable ECM of the bistability region. Moreover, bistability regions get wider when the feedback ratio increases, as the overlap intervals of successive ECMs also grow wider.

Fig.5.5.(b) displays the frequencies of the pulsing ECM solutions as they

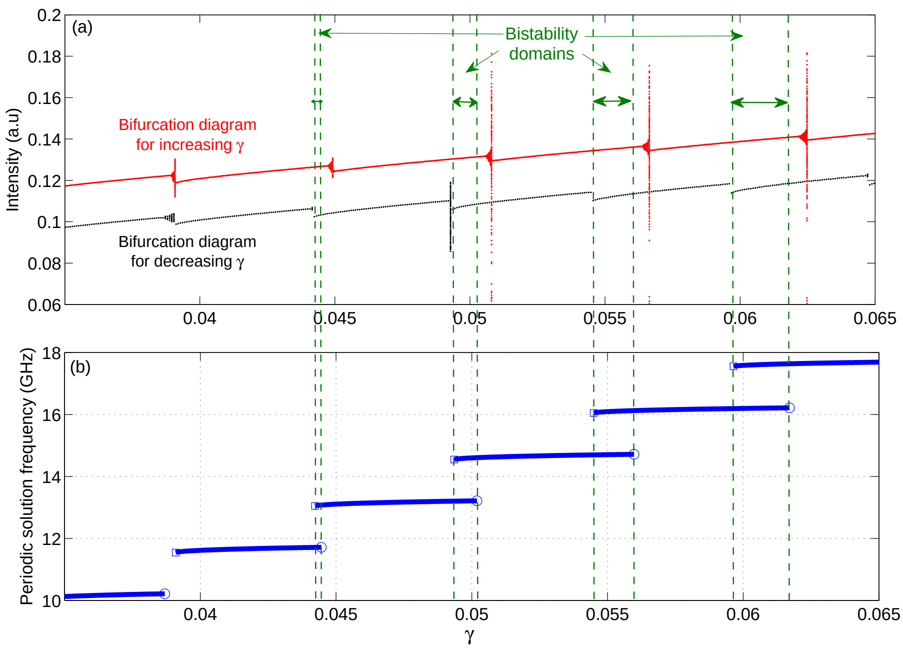

Figure 5.5: Bistability regions. Figure (a) shows in red the bifurcation diagram computed for increasing values of γ and in black the one computed for decreasing values. They have been vertically shifted for legibility. Figure (b) shows the self-pulsing solution and their frequencies. The bistability domains (within the green dashed vertical lines) correspond to intervals of γ where two pulsing solutions are permitted.

bifurcate when increasing the feedback ratio. The frequency separation between two consecutive ECMs is close to the external cavity frequency. In our case the normalized external frequency is $f_{ext} = \frac{1}{\theta}$, which corresponds to a pulsing frequency of 1.5 GHz. To illustrate the coexistence of two pulsing external cavity mode solutions with different and possibly high frequencies, we show in Fig.5.6 the time series of the two regular self-pulsing dynamics with different frequencies observed for a normalized feedback ratio of $\gamma = 0.0611$. Traces (a) and (c) are observed for the same feedback ratio value but their frequencies are different, due to bistability. Their corresponding optical spectra are traces (b) and (d). The zero frequency in Fig.5.6.(b) and (d) corresponds to the free running laser frequency. The optical spectrum (b) shows two peaks at about 8 GHz and -8 GHz. Similarly, the optical spectrum (d) shows peaks at 8.75 GHz and -8.75 GHz. Since the complex field trajectory is symmetric in the phase plane and is centered on the (0; 0) point, the optical spectrum shows no component at the zero frequency and shows symmetric peaks on negative and positive frequencies. One complete cycle for the complex field E being equivalent to two cycles for $|E|^2$, the time series of the optical power in (a) shows modulations at about 16 GHz and the one in (c) at 17.5 GHz.

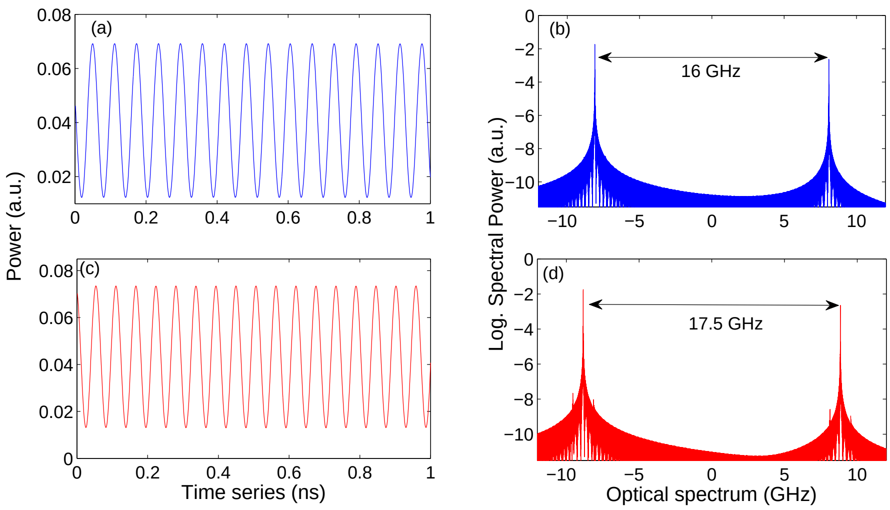

Figure 5.6: Time series and optical spectra of the two ECMs at stake in the bistability region corresponding to $\gamma = 0.0611$.

Those two possible pulsing solutions at 16 GHz and 17.5 GHz for a same value of $\gamma = 0.0611$ illustrates bistability in the laser solutions. The system would initially select one of the two coexisting self-pulsations at high frequencies. However a sustained perturbation or noise may induce random hoppings between these two ECMs with, as a result, a time-averaged RF spectral signature being made of two peaks, slightly shifted by a frequency related to the external cavity length.

As we will discuss in detail in chapter 6, the frequency detuning between two consecutive self-pulsing external cavity modes is fixed by the external cavity length: $f = \frac{c}{L_{cav}}$ where L_{cav} is the effective length of the path followed by the beam. In the simulations, with the parameters chosen to build the bifurcation diagram in Fig.4.1, the external cavity frequency is about 1.5 GHz. Indeed, an analysis of the frequencies of the self-pulsing ECM shows that the frequencies are distributed on a regular basis, each ECM having a frequency equal to the previous ECM frequency plus the external cavity frequency. The frequency distribution of the ECMs in Fig.5.5.(b) illustrates this frequency shift of 1.5 GHz –equivalent to the external cavity frequency– between consecutive ECMs. The bifurcation diagram of Fig.4.1 is recalled in Fig.5.7 and summarizes this property as the feedback ratio increases.

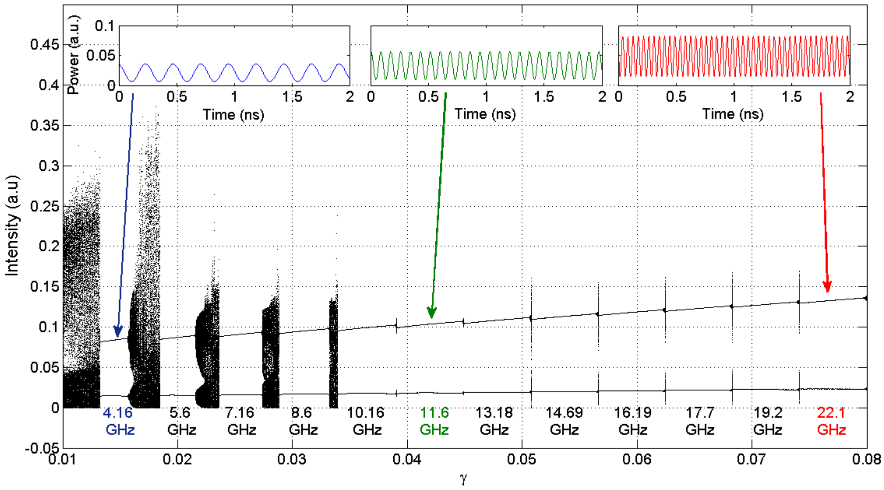

Figure 5.7: Bifurcation diagram with the values of the self-pulsing external cavity modes. Consecutive ECMs states oscillate at frequencies separated by the external cavity frequency: $f_{ECM_{n+1}} = f_{ECM_n} + 1.5\ GHz$.

As γ increases, the frequencies of the self-pulsing solutions increase at the pace of the external cavity frequency and can reach very high values. From an application point of view, by simply varying the feedback ratio value, the laser could ideally be changed into a tunable optical oscillating source at several tens of GHz without the need for current modulation. Additionally the chaos crisis mechanism makes these self-pulsing solutions very stable and robust to modifications of γ.

5.3 Influence of the simulation parameters

We study now how the values of the parameters T, P, α and θ influence the laser dynamical properties through a possible modification of the bifurcation diagram. In order to test the robustness of the conclusions on the evolution of the laser dynamics with γ, we carry out simulations for different values of parameters T, P, α and θ.

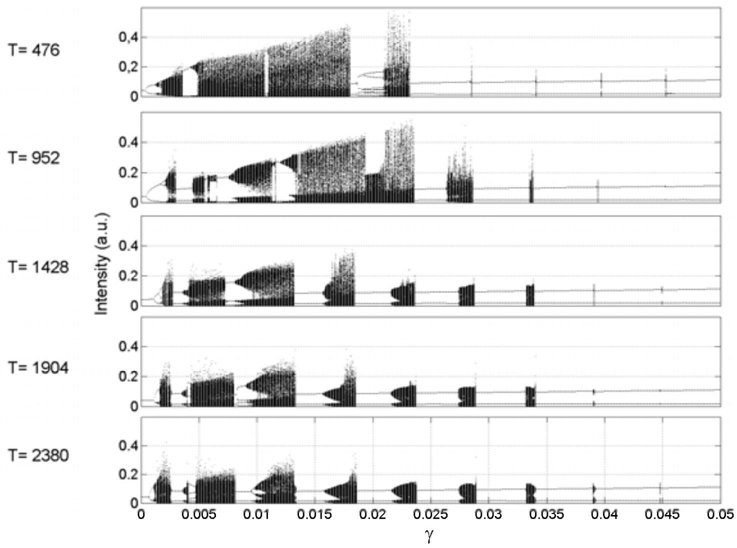

Figure 5.8: Effect of the variation of parameter T on the bifurcation diagram. All other parameters are identical to Fig.4.1.

5.3.1 Changing T, P and α

The influence of the variation of parameter T in the bifurcation diagram in Fig.5.8 is only visible when T is weak and mostly for small values of the feedback ratio. For increasing values of T higher than 1428 the bifurcation diagram remains almost unchanged: a cascade of bifurcations to either regions of self-pulsing dynamics or chaos is still observed. Yet a smaller value of T leads to a larger region of chaotic dynamics for smaller values of γ.

Increasing the pump current P leads to modifications in the bifurcation diagram. First the amplitude of the fluctuations increases, as can be noticed from the re-scaling of the y-axis in Fig.5.9. Then the sequence of bifurcations is strongly changed for the weak feedback ratios. The general trend is that regions of self-pulsing oscillations disappear as chaotic regions get more developed. As a result, there are fewer self-pulsing ECM states when P increases. Yet, a closer look at the diagram reveals that the γ values at which bifurcation between ECM occur are quite insensitive to the variations of P.

The same observation is made when the linewidth enhancement factor α changes, as displayed in Fig.5.10. The bifurcation positions slightly drift towards the smaller values of γ when α increases. In addition to this, when the value of α increases the system generally loses stability since the chaotic

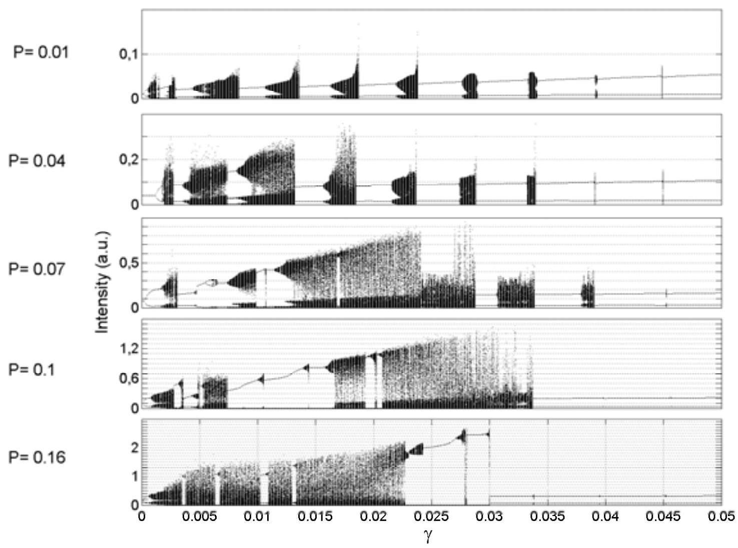

Figure 5.9: Effect of the variation of parameter P on the bifurcation diagram. All other parameters are identical to Fig.4.1.

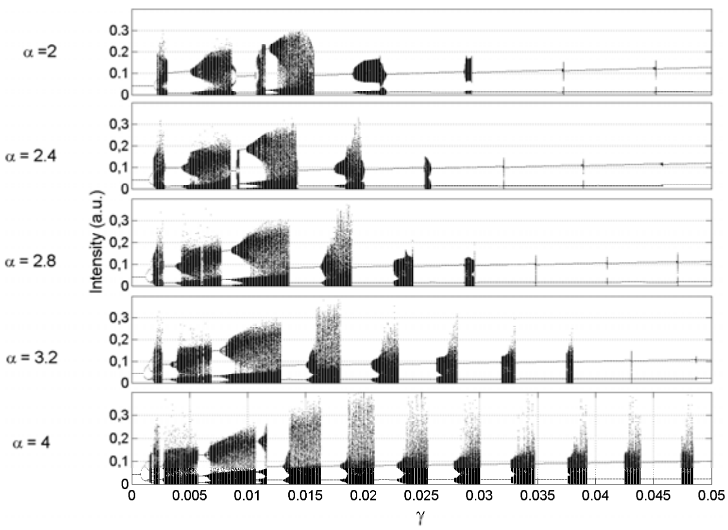

Figure 5.10: Effect of the variation of parameter α on the bifurcation diagram. All others are identical to Fig.4.1.

regions get wider and more intense. A high value of α tends to force the laser to show more chaos, making chaotic regions wider and more numerous. Besides, chaos suppression occurs for values of γ much larger than in the case of a smaller α. This result in coherent with the constatation made in the COF case in [118] where it has been reported that a smaller linewidth enhancement factor tends to stabilize the laser [15].

5.3.2 Changing the time delay θ

Whereas changing the values of parameters P, T and α causes little difference in the dynamics of the system as we saw in the bifurcation diagrams in Figs.5.8, 5.9 and 5.10, changing the time delay induces dramatic effects. Indeed, Fig.5.11 illustrates the particular fact that when θ increases, all the bifurcation points drift towards smaller values of γ and end up by merging. This results in larger regions of chaos. Another way to see this phenomenon is to say that a given bifurcation occurs for a higher value of γ when working with a short cavity than when working with a long one.

We will see in chapters 8 and 9 that this simulated prediction is confirmed in the experiment and that changing the cavity length allows, for a given value of the feedback ratio, to see totally different dynamics. A similar observation was already made in the literature. Indeed, Gray *et al.* reported that a decrease of the external cavity length causes the bifurcation points to drift to higher γ values [66].

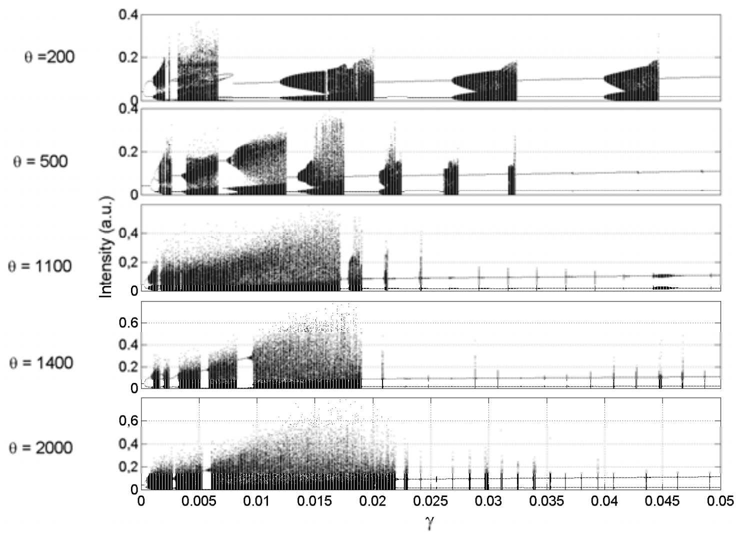

Figure 5.11: Effect of the variation of parameter θ on the bifurcation diagram. All other parameters are identical to Fig.4.1.

Another consequence from Fig.5.11 is related to the observation of the pulsing fundamental external cavity mode solutions. When θ increases, regions of chaos broaden and ECM are almost fully destabilized. As a consequence, the possibility to see the first pulsing ECMs diminishes greatly when the external cavity length increases.

5.3.3 Discussion and transition to the experiment

Although they present theoretical interest, we do not focus on the dynamical effects induced by the variations of T, P and α. As we already mentioned, our objective in the simulations is to bring qualitative accordance with the experiment. We keep working at a fixed injection current of 60 mA in order to maximize the PCM reflectivity. Therefore, P, T and α are fixed parameters.

In contrast, in the following chapters, the experiment will illustrate the trend seen by the simulations which predicts that for a given value of γ the dynamical states exhibited by the laser change if θ varies. As displayed in Fig.5.11, this phenomenon is due to the drifting of the bifurcation points induced by the modification of θ. Therefore, the experimental results reported in the following chapters will be presented in the order they are observed as the external cavity length increases.

CHAPTER 6

Self-pulsing external cavity modes

In this chapter, we bring experimental evidence of the appearance and destabilization of self-pulsing external cavity modes in a laser diode subject to PCF. As expected from the theoretical predictions formulated in chapter 4, the laser exhibits sinusoidal pulsing modes at frequencies multiples of the external cavity frequency. With the theoretical background, it is possible to reconstitute the scenario of bifurcations of the observed self-pulsing external cavity modes from their birth to the transition to successive ECMs. Besides, good qualitative theoretical accordance about the cascade of stabilizing and destabilizing bifurcations leading to those ECM pulsing states is achieved. As we mentioned in chapter 2, there is to our knowledge no experimental evidence of pulsing external cavity modes reported in the literature. As a consequence, no experimental confrontation with the theoretical predictions has been carried out so far either.

6.1 Experimental identification

In the PCF configuration, external cavity modes are self-pulsing solutions, by contrast to the case of COF where ECMs are steady states [72, 75]. The theory expects the frequencies of the external cavity modes to be multiples of the fundamental external cavity frequency f_{cav} related to the physical cavity length L_{cav} by $f_{cav} = \frac{c}{L_{cav}}$ [75]. Therefore the frequency of the ECM numbered n is expected to be $f_n = \frac{n.c}{L_{cav}} = nf_{cav}$. We remind the reader that what we call cavity length and write L_{cav} is the effective length of the path followed by the photons between the instant they are emitted from the laser facet and the instant they re-enter the laser after undergoing phase-conjugation. In the case of a conventional mirror, L_{cav} would be merely twice the distance of the laser to the mirror. But as we explained in chapter 3, the expression of L_{cav} changes according to the experimental set-up used to generate PCF.

6.1.1 Experimental setup

The experimental configuration with which we saw self-pulsing external cavity modes is as described in chapter 3: the laser diving current is set at 60 mA and the SPS crystal is oriented with the angles $\beta = 26^o$ and $2\theta = 30^o$ in order to optimize the PCF generation gain. The distance between the laser and the crystal is $L_1 = 22\ cm$ and the ring cavity length is $L_2+L_3+L_4 = 88\ cm$. Consequently, the total external cavity length $L_{cav} = L_{tot} = 2L_1+L_2+L_3+L_4 = 132\ cm$ is the whole ring cavity length plus one round-trip between the laser and the crystal. The related time delay is $\tau = 4.5\ ns$. Fig.6.1 summarizes the experimental conditions.

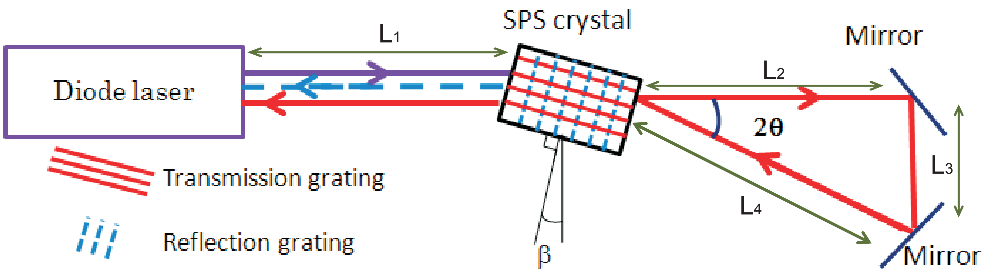

Figure 6.1: Experimental conditions.

Fig.6.2 shows a quasi-sinusoidal time trace, pulsing at $f = 1360\ MHz$ that has been observed with this setup. Yet, 1360 MHz in not an expected ECM oscillating frequency from what we said above. Indeed, a time delay of 4.5 ns is equivalent to a frequency of 222 MHz. In the theory, f is expected to be a multiple of the round-trip frequency in the external cavity, that is $f = \frac{n.c}{L_{cav}} = n \times 222\ MHz$ where n is an integer. However in the case shown in Fig.6.2, f does not correspond to one of the above-mentioned frequencies. Actually, the trace displayed in Fig.6.2 is indeed a self-pulsing ECM, which frequency is $f = \frac{2c}{2L_1}$. In other words, the cavity length which is to be taken into account is not the whole round-trip in the ring cavity but only the round-trip in the space between the laser and the SPS crystal which is $2L_1 = 2 \times 22\ cm$. Consequently, the parameter L_{cav}, which represents the effective path of the beam is now written $L_{cav} = 2L_1 = 44\ cm$.

This means that the PCF has only the signature of the round-trip propagation between the laser and the crystal. The explanation relies on the fact that what creates the PCF in this case is a photorefractive reflection grating within the crystal. As explained in chapter 3, both reflection and transmission grating may be generated within the crystal. The difference is that in

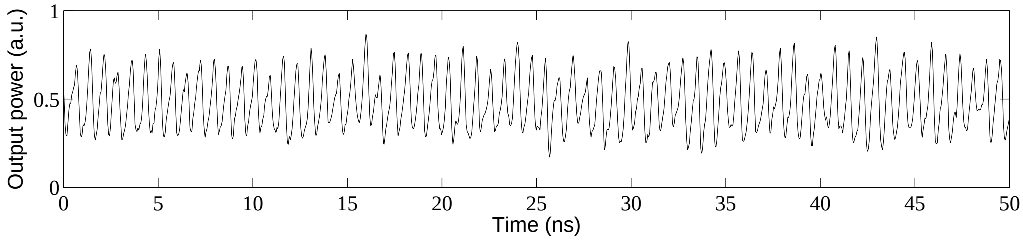

Figure 6.2: Typical example of a pulsing external cavity mode in the PCF case. Here the oscillating frequency is $f = 1360\ MHz$.

the case of a reflection grating, the effective external cavity length is shorter than in the case of a transmission grating since the mirror loop is not taken into account. Indeed, in this case, the photons undergo phase conjugation as they first enter the crystal, without propagating in the ring cavity. This is a major contrast to the case of PCF generation with a transmission grating. We managed to switch the nature of the grating by changing the beam's section at the point it re-enters the crystal after going through the ring loop. Therefore we come to the conclusion that the fundamental external cavity frequency is then $f_{cav} = \frac{c}{2L_1} = 680\ MHz$. As a consequence, the pulsing ECM shown in Fig.6.2 is the second ECM of this experimental configuration since its frequency is $f_2 = 1360\ MHz = 2f_{cav}$.

This possibility to generate PCF from the crystal's reflection grating is a useful tool because it allows to work with a shortened external cavity and thus with a shorter-delayed feedback. Indeed the round-trip time with the transmission grating is $\tau_{tra} = \frac{L_{tot}}{c} = 4.5\ ns$ while the round-trip time with the reflection grating is $\tau_{ref} = \frac{2L_1}{c} = 1.47\ ns$. According to the predictions in chapter 4, a shorter time delay causes secondary bifurcations to chaos to occur for reflectivity values larger than in the case of a long time delay. This property gives a wider span of feedback ratio values to see the ECMs between two chaotic regions, making them more likely to be detected and resolved experimentally. This phenomenon has been presented in Fig.5.11 where the intervals of feedback strength γ where self-pulsing ECMS are stable are wider in the case of shorter cavities than in the case of longer cavities.

Fig.6.3 illustrates this property with the two experimental values of the time delay. Indeed, the bifurcation diagram in (a), calculated for $\theta = 1050 \Leftrightarrow \tau_{ref} = 1.47\ ns$, is more likely to show self-pulsing states than the one in (b), where $\theta = 3200 \Leftrightarrow \tau_{ref} = 4.5\ ns$ and for which only developed chaos is visible. Moreover, further experimental results that will be presented in chapters 8 and 9 confirm the crucial influence of the operating effective cavity length

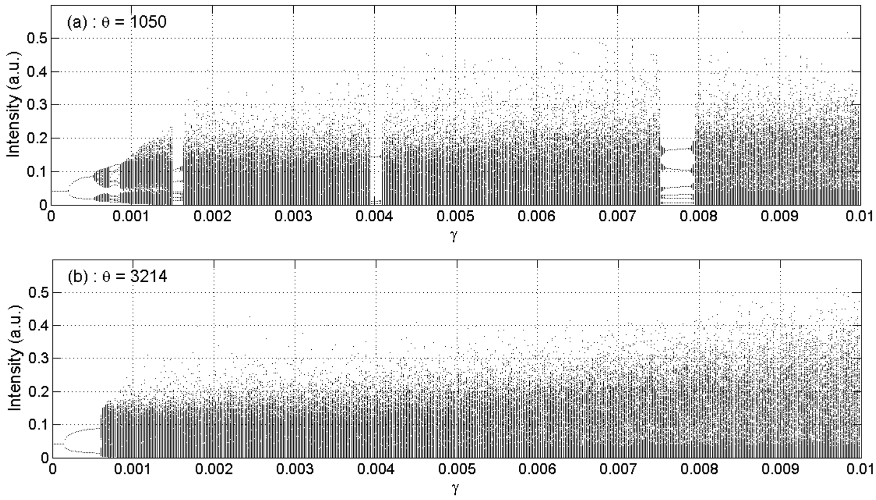

Figure 6.3: Bifurcation diagrams computed with time delay values corresponding to the experimental conditions: $\tau_{ref} = 1.47\ ns \Leftrightarrow \theta = 1050$ (a) and $\tau_{tra} = 4.5\ ns \Leftrightarrow \theta = 3214$ (b). P, T and α are the same as in Fig.4.1. Pulsing solutions are visible only in the case of $\theta = 1050$ and yet in very small intervals of feedback ratio values.

on the nature of the dynamical states that the laser is able to exhibit within our reflectivity range.

Although self-pulsing external cavity modes can be seen provided suitable experimental conditions are fulfilled, they show to be very sensitive states. This means that the laser often switches from ECM state to quasi-periodic or other pulsing solutions under the sole effect of the experimental noise. This sensitivity makes stable observation of those self-pulsing states quite difficult. Furthermore, the likeliness to see a full scenario showing successively several ECMs and their transitions is very poor. Yet, we could identify two external cavity modes pulsing at multiples of the fundamental frequency. Experimental evidence of the process that destabilizes them is given as well.

6.1.2 Birth and evolution of self-pulsing ECMs

Fig.6.4 shows some experimental time traces of the laser output power and the corresponding RF and optical spectra when the laser undergoes a route to chaos as the feedback ratio increases. Trace (a) is the laser steady state as it can be seen for the smallest feedback strength values. The time traces show very small fluctuations in the laser power due to the experimental noise. The RF spectrum is totally flat and the optical spectrum only shows the solitary running laser frequency.

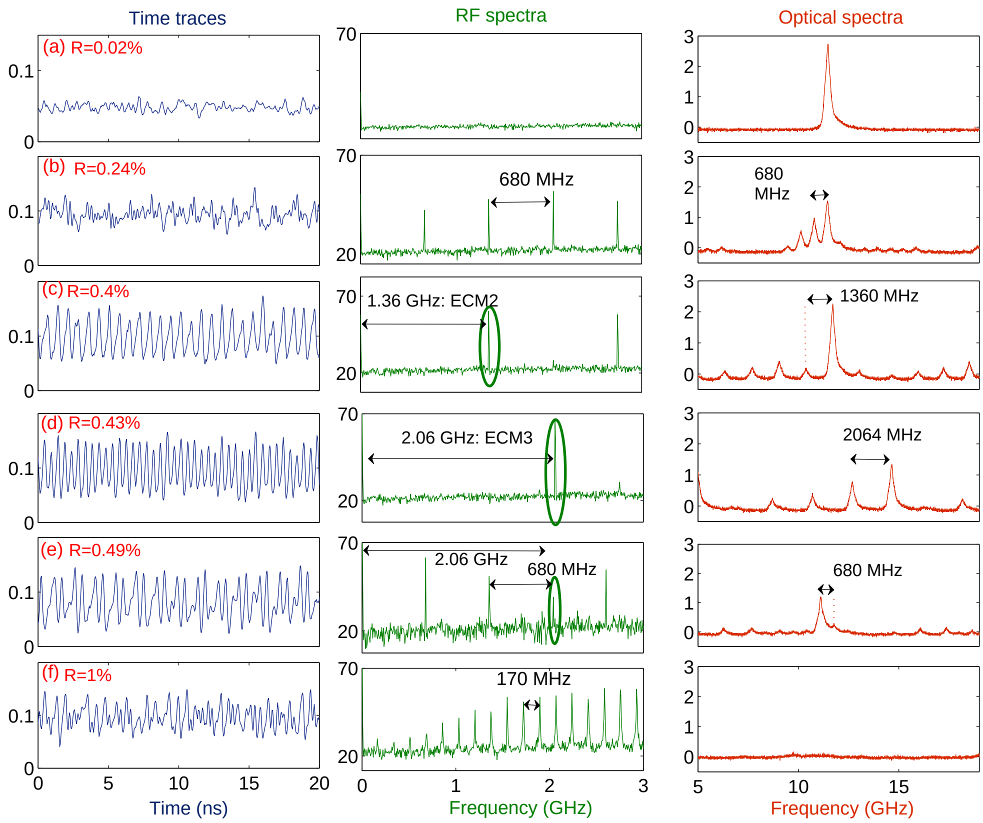

Figure 6.4: Evolution of the time traces and corresponding RF and optical spectra when R is increased. Y-axis are in arbitrary units (linear scale for the time traces and Log scale for the spectra).

As the mirror reflectivity increases, several fast-fluctuating dynamics are seen until trace (b) is generated –when R=0.24%– with the signature of the delay time-scale $f_{cav} = 680\ MHz$. Trace (b) pulses with a complex frequency content but with a very strong signature of the external cavity delay as can be seen from the regular peaks interspaced by 680 MHz in the corresponding RF spectrum. The related optical spectrum also accounts for this fact with peaks separated by the external cavity frequency. This trace (b) marks the end of a chaotic attractor about to switch to the limit cycle related to the second self-pulsing external cavity mode (c). As a comparison, trace (b) is similar to the theoretical trace (b.1) in Fig.5.2.

Then we distinguish two pulsing ECMs: trace (c) which pulses at 1.36 GHz and trace (d) at 2.06 GHz. We reckon they are respectively the second and the third ECMs since they pulse at $2f_{cav}$ and $3f_{cav}$ as encircled in the RF spectra of traces (c) and (d). The corresponding optical spectra confirm the oscillation frequencies by showing peaks separated by intervals of 1.36 GHz and 2.06 GHz. ECM2 originates from trace (b) and gives way to ECM3 with a very short transition: experimentally the solution switches from ECM2 to ECM3 so quickly that it is hardly possible to see how the destabilization of ECM2 and the associated reshaping from its limit cycle into ECM3's occurs. Yet, both traces (c) and (d) are experimental quasi-sinusoid pulsing at frequencies multiples of the external cavity fundamental frequency. They illustrate the self-pulsing dynamics of the so-called external cavity modes in PCF that have been for a long time predicted by the theoretical model. To our knowledge, this experimental evidence is the first confirmation of the ECMs in the PCF case.

Then when R is further increased, a route to chaos by period multiplying is initiated: ECM3 undergoes period tripling giving birth to trace (e) in which it can be clearly seen that one on every three peaks is skipped compared to trace (d). In the RF spectrum the main frequency at 2.06 GHz stemming from trace (d) is encircled and we can see that peaks interspaced by 680 MHz appear, changing thus the quasi-sinusoid of trace (d) into a quasi-periodic signal (e) by period tripling. The related optical spectrum begins to lose accuracy as new small frequencies under the optical spectrum analyzer's finesse rise and modulate the laser power.

When further increasing the feedback strength, the route to chaos continues with trace (f) originated from trace (e) which shows the contribution of many frequencies. The RF spectrum corresponding to trace (f) shows a multitude of peaks, separated from each other by 170 MHz –which is a fourth of 680 MHz–, along with a higher overall level for all frequencies. The related optical spectrum is flat since too many frequencies very close to each other are present in this case. This evolution suggests that at that point the laser enters chaos. Indeed, for values of R higher than 1% the experiment shows only chaos and no self-pulsation at higher frequencies such as ECM4 or other are seen. Therefore, the sequence of bifurcations corresponding to ECM generation and transitions occur for very weak values of the feedback ratio: they initiate the route to fully developed continuous chaos.

Although we were not able to see other self-pulsing ECMs, an interesting trace has been spotted, confirming what we just discussed. Indeed, Fig.6.5.(a) shows an experimental time trace that has the same dynamical properties as trace (e) in Fig.6.4. We identify it as the quasi-periodic state that is present in the process of destabilization of the fifth external cavity mode. The plain self-pulsing ECM5 at 3.3 GHz could not be seen, though. Yet the corresponding post process calculated RF spectrum in Fig.6.5.(b) reveals a main frequency peak at 3.3 GHz along with several side peaks. An immediate comparison to the RF spectrum corresponding to trace (e) in Fig.6.4 allows to follow a reasoning analogous to the destabilization process of ECM3 that we reported previously. The peaks at 680 MHz in Fig.6.5.(b) are responsible for the slow modulation of the otherwise self-pulsing dynamics at 3.3 GHz –that is ECM5– and which would be expected to be seen for a reflectivity value slightly smaller. Since the RF spectrum in (b) has been computed from the data of time trace (a), its accuracy is not as high as the one in the RF spectra gathered by the RF spectrum analyzer and displayed in Fig.6.4. Yet, this figure illustrates the existence of a self-pulsing fifth external cavity mode. This brings further confirmation to the theoretical predictions related to the evolution of the ECMs and the evolution of their frequency as the PCM reflectivity increases.

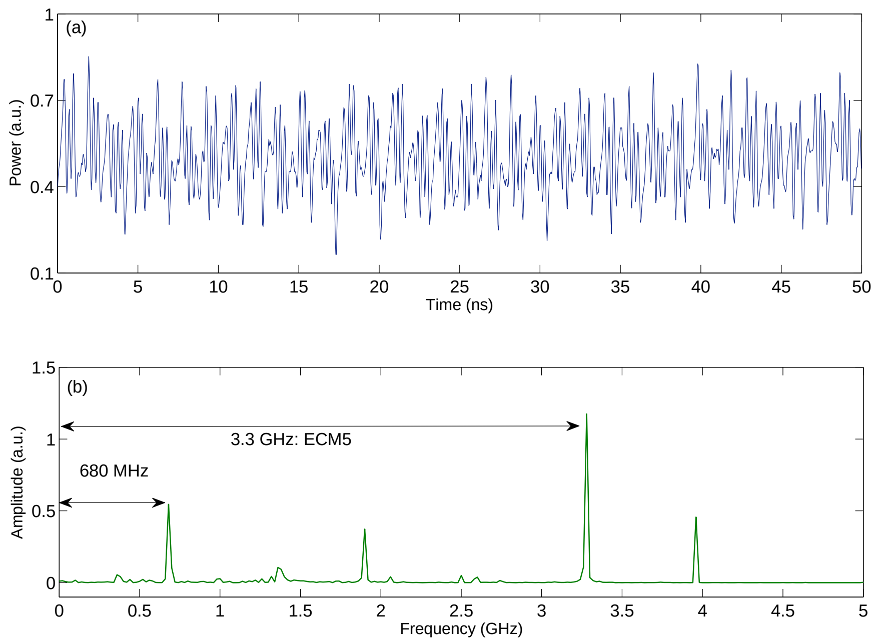

Figure 6.5: Experimental observation of a destabilizing self-pulsing external cavity mode at the frequency $f_5 = 3.3\,GHz$ (a). Trace (b) is the post process calculated square modulus of the Fourier transform of trace (a).

It is experimentally very difficult to see a whole continuous scenario of bifurcations leading the laser from an ECM state to quasi-periodic or chaotic states with all the related successive time series and spectra. That is why even though we could only see the destabilization through quasi-periodicity related to ECM3, we believe that this phenomenon also occurs with ECM2 and that period multiplying is at stake in the transition from ECM2 to ECM3 as well. Generally speaking, we expect every ECM to follow the same process as we saw for the destabilization of ECM3. We provide in the following section a theoretical scenario accounting for the destabilization process of the external cavity modes.

6.2 Theoretical confirmation

Although there has been no report in the literature showing experimental pulsing ECMs, several theoretical studies have been done to simulate the laser behavior when subject to delayed PCF. We present here a simulated model in order to show qualitative accordance with the experimental traces shown above in Fig.6.4. We model the laser system using the same system of equations as presented in chapter 2 and already used to do the theoretical predictions in chapters 4 and 5: the Lang-Kobayashi equations for PCF (equations 4.1).

Due to the great number of parameters and possible ranges of study, a given set of parameters may show compliance with experimental results, yet under another set of parameters a totally different scenario can be predicted by the simulation. As we mentioned before, the model we use is quite simple on the one hand but on the other hand it can show very complex results that are difficult to fit to the experimental observations since the parameters often range values very different from the experimental ones. Therefore, any quantitative comparison is hardly possible.

6.2.1 Simulated self-pulsing ECMs

Since we aim at bringing theoretical confirmation to the observations of self-pulsing external cavity modes reported above, we carry out simulations in order to show qualitative simulated compliance with the experimental results. A computed simulation of the model with the following parameters: $\theta = 1050$, $P = 0.04$, $T = 1000$, and $\alpha = 2.2$ reveals the bifurcation diagram displayed in Fig.6.6.

Among those parameters only θ has the same value as in the experiment. Since it is normalized with respect to the photon lifetime $\tau_p = 1.4\ ps$, $\theta \times \tau_p = 1050 \times 1.4\ ps = 1.47\ ns = \tau_{ref}$. Therefore, in the simulations the periodic

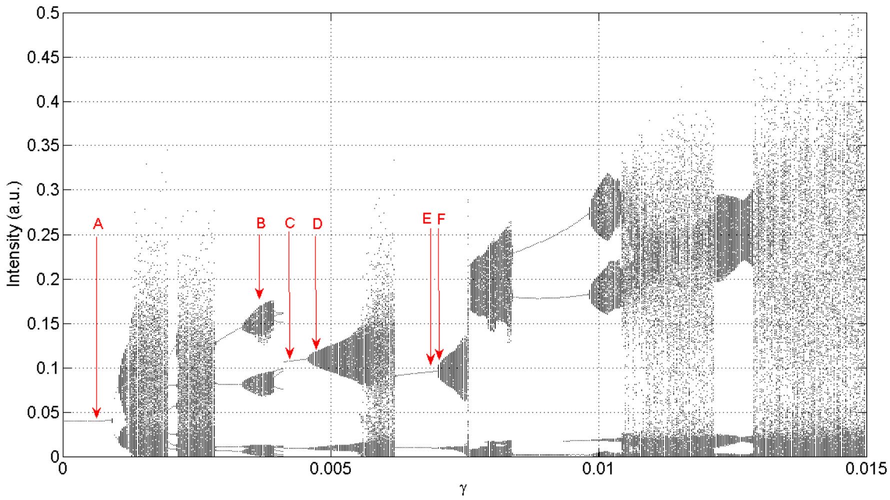

Figure 6.6: Bifurcation diagram for $\theta = 1050$ which corresponds to the physical time delay in our experiment (1.47 ns). $P = 0.04$, $T = 1000$, and $\alpha = 2.2$.

solutions pulse at frequencies very close to the experimental ones which have been reported in Fig.6.4. The value of P is smaller than in the experiment. However, it is important to remind that physical the dependance of the feedback ratio γ on the injection current P is not taken into account in the model while it is inherent to the PCF generation process. A careful look at the pulsing and quasi-periodic states in Fig.6.6 brings us to the dynamical evolution presented in Fig.6.7.

Fig.6.7 displays simulated predictions of the laser time traces and the corresponding RF and optical spectra, which are tagged from A to F in Fig.6.6. The scenario begins with the steady state displayed in trace (A) in which no fluctuations are seen and the optical spectrum shows no frequency besides the solitary laser one. It is the simulated counterpart of trace (a) in Fig.6.4.

Then, as γ increases, we come to trace (B) which shows irregular fluctuations with the signature of the external cavity time delay in the spectra. In the simulations, the value of θ of 1050 gives a frequency signature in the spectra of about 650 MHz. This trace (B) is the initial state from which the external cavity modes will be generated and is the simulated equivalent of trace (b) in Fig.6.4.

Trace (C) originates from trace (B) and reveals a sinusoidal self-pulsing solution at 1.34 GHz. Trace (C) is a clear illustration of the experimental ECM2 seen in Fig.6.4.(c). This ECM2 is then made unstable when γ increases and

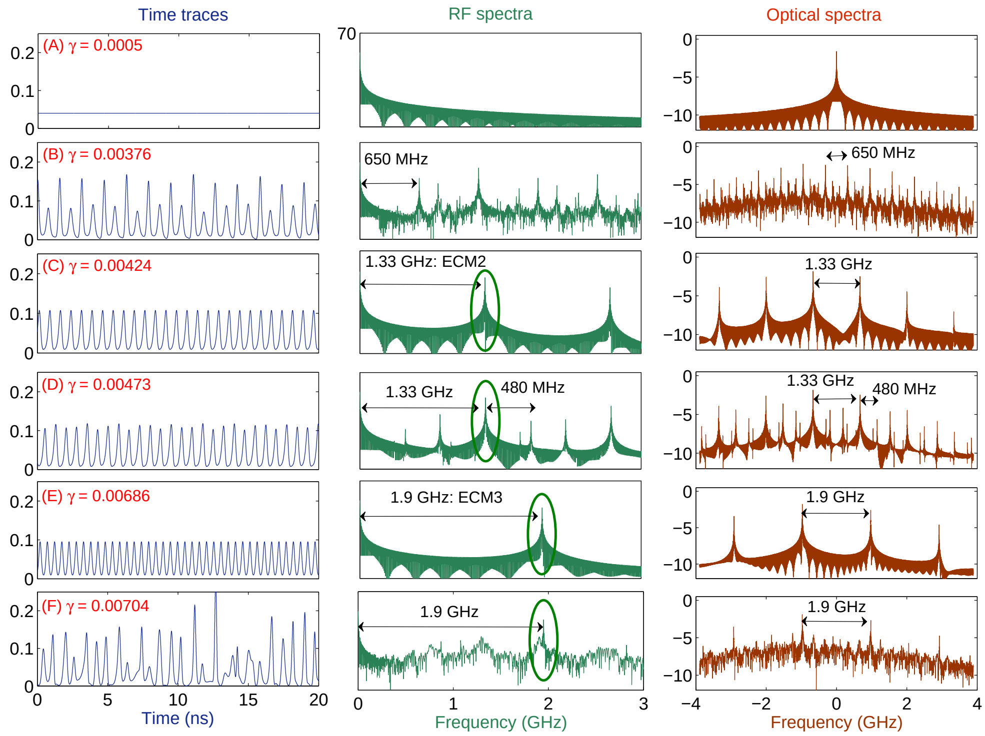

Figure 6.7: Simulated time series and spectra corresponding to traces A to F in the bifurcation diagram (Fig.6.6). Y-axis are in arbitrary units (linear scale for the time traces and Log scale for the spectra).

gives way to trace (D), the experimental counterpart of which was not resolved but which contains the same features as trace (e) in Fig.6.4. Indeed, trace (D) in Fig.6.7 shows the destabilization of ECM2 by quasi-periodicity making new peaks rise in the spectrum at the frequency of 480 MHz. The value of this frequency of 480 MHz which appears when ECM2 bifurcates to quasi-periodicity is unclear to us. It would require a careful an complex analysis of the secondary bifurcations on ECMs to account for this value. Still, it is quite close to the 650 MHz of the external cavity frequency. As a comparison, it is exactly homologous to the frequencies at the delay time scale that are visible in Fig.6.4.(e). As we saw, those peaks rising at the cavity frequency initiate the destabilization of the ECMs.

Trace (D) is followed by a region of chaos which ends up by giving way to the next external cavity mode pulsing at 1.9 GHz (trace (E)). Again good accordance is seen with trace (d) in Fig.6.4 both in the pulsing frequency and the signal shape. In Fig.6.6, in the transition from the limit cycle of ECM2 (C) to the limit cycle of ECM3 (E), the system goes through a region of chaos that was not observed in the experiment. Indeed as we mentioned before, the experimental transition from ECM2 to ECM3 occurred very quickly and we could not observe the full scenario.

Then if γ is further increased, the laser follows another route to chaos from ECM3 giving birth to trace Fig.6.7.(F) in which the main frequency at 1.9 GHz is still visible. Yet, it is this time surrounded by many frequencies covering the whole spectrum and inducing fast irregular fluctuations. For values of γ above 0.01, the bifurcation diagram in Fig.6.6 shows no more self-pulsing solutions. The systems enters and remains essentially in chaotic state in a wide span of feedback ratio values, as was the case in the experiment for values of R larger than 1%. The phenomena of chaos crisis and chaos suppression is seen for high values of γ, though.

6.2.2 Confrontation to the experiment

The confrontation between the simulated results of Fig.6.7 and the experimental traces of Fig.6.4 brings us to a few discussion points. First in none of them the fundamental pulsation of ECM1 at the fundamental external cavity frequency of 680 MHz could be seen. As we mentioned before, ECM1 is expected to be the first periodic solution related to the external cavity to appear but it is also expected to be very quickly destabilized as the first bifurcations to chaos occur. Hence we are not surprised not to be able to see it. We find that ECM1 could be visible in the simulation with a smaller value of θ or with another set of laser and feedback parameters but we chose in this theoretical confrontation to work with the same delay as in the experiment. The aim is indeed to provide a theoretical result close to the experimental conclusions.

Secondly no quantitative accordance can be expected from this experiment-simulation comparison. Indeed the iteration pace of the simulation is $\tau_p = 1.4$ *ps* while our oscilloscope resolution is limited by its 4-GHz-bandwidth. Hence the simulations –which were by the way undertaken without addition of noise in the model– provide results which accuracy is far beyond our experimental reach. Besides, the value of P is much lower in the simulation ($P = 0.04$) than in the experiment, where the laser was operating with an equivalent normalized pump ratio of about 4. Again a high value of P causes regions of self-pulsing states to shrink dramatically in bifurcation diagram. That is why we chose a smaller value of P in the simulation. The same reason justifies the value chosen for α.

Nonetheless the theoretical predicted scenario displayed in Fig.6.7 shows good qualitative accordance with the experimental observations reported in Fig.6.4. This compliance leads to the conclusion that the transition from a self-pulsing external cavity mode to the following one shows a destabilization by period multiplying and quasi-periodicity including the external cavity frequency and its multiples.

6.3 Other scenario of self-pulsations

Among the diversified dynamics that can be exhibited by the laser diode, we focus here on a particular destabilization process of a self-pulsing harmonic state that was spotted in the experiment. Fig.6.8 displays a self-pulsing ECM undergoing a destabilization process totally different from the one reported previously. The initial state is similar since it is a quasi-sinusoid, as in Fig.6.4.(c) and (d). Yet, as the feedback ratios increases, successive period multiplyings of a different nature occur. Indeed, in contrast to the scenario presented in Fig.6.4, the pulsing state undergoes a period doubling followed by a period tripling which results in a state exhibiting very short pulse packages made of two or three pulses oscillating at a high frequency.

Although the spectra in Fig.6.8.(b.1-b.3) seem to follow each other in a scenario pretty much alike the one shown in Fig.6.4.(d-f), the evolution of the corresponding time traces is totally different. Indeed, in the case of Fig.6.4.(f), the period multiplying gives way to chaos with very fast fluctuations with a constant amplitude in average. Now, in the case shown in Fig.6.8, the amplitude of the power fluctuations is dramatically reduced while only very high peaks are visible and distributed at regular intervals of 310 MHz. This frequency corresponds to the sixth of the self-pulsing frequency of Fig.6.8.(a.1) and (a.2). This behavior has been observed in the experiment very few times. Actually, it is rather a transition from a harmonic dynamics to a train-of-pulses-like emission state. Yet, it is an interesting illustration of the dynamical diversity of a laser with phase-conjugate feedback, different from the previously reported one.

Another interesting feature of the harmonic trace displayed in Fig.6.8.(a.1) is its fundamental frequency. The experimental conditions under which this trace is seen are as follows. The crystal is located at a distance of 12 cm from the laser and the ring loop ranges 30 cm. The total cavity length is thus 54 cm and the related external cavity frequency is $f_{ext} = 550\ MHz$. Yet the pulsing frequency in Fig.6.8.(b) is 1.87 GHz, which is not a multiple of f_{ext}. The laser pulses consequently at a frequency different from the one expected from the external cavity length. Even taking into account only the

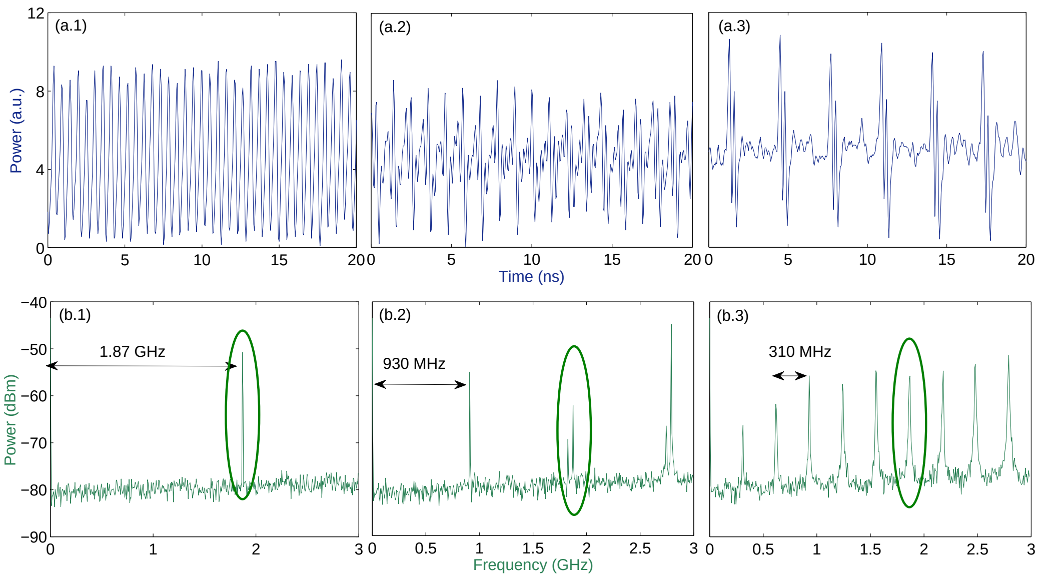

Figure 6.8: Self-pulsing state with successive destabilizations by period multiplying. A first period doubling brings the lower frequency from 1.87 GHz (a) to 930 MHz (b). Then the system undergoes period tripling, resulting in very short power pulses at the frequency of 310 MHz (c).

distance of the crystal to the laser, as we did in the case of a PCF generated by means of a reflection grating, the expected equivalent frequency (1.25 GHz) would not fit to the observation either. We found no theoretical conditions of parameters which could account for this phenomenon so far.

Yet this result brings an experimental evidence to the fact that a self-pulsing ECM in the case of PCF can undergo two different destabilization processes of totally different dynamics. The first is the destabilization by period multiplying leading to chaos and to ECMs of higher frequencies as presented in Fig.6.4 and for which we brought theoretical account. The second is the the destabilization by period multiplying leading to trains of pulses such as the traces presented in Fig.6.8 to which no theoretical model has been suggested to our knowledge.

6.4 Conclusions

We brought in this chapter the first experimental report of self-pulsing external cavity modes in a laser diode with PCF. The experiment confirms the theoretical predictions about the pulsing frequencies and the scenario of bifurcations on the successive ECMs. In particular, ECMs pulsing at twice and three times the external cavity frequency are well resolved experimentally and their bifurcations are supported by numerical simulations.

In the next chapter, we present a deeper analysis of self-pulsing ECMs. Their corresponding oscillating mechanism and spectral features are to be compared to other pulsing states reported in both PCF and COF cases.

Chapter 7

Self-pulsation in a laser with feedback

Time-periodic self-pulsing dynamics in laser diodes subject to optical feedback have been reported in the literature with both theoretical and experimental illustrations. As we saw in the bifurcation diagrams through the previous chapters, several kinds of pulsing dynamics can be exhibited in the laser power both in COF and PCF cases.

In this chapter, we carry out a comparison between pulsing states of different natures. We will especially focus on their spectral characteristics. We consider and compare four fundamental self-pulsing dynamics: undamped relaxation oscillations, mode locking, bridges between steady state ECMs in the COF case and self-pulsing ECMs in the PCF case.

7.1 Undamped relaxation oscillations

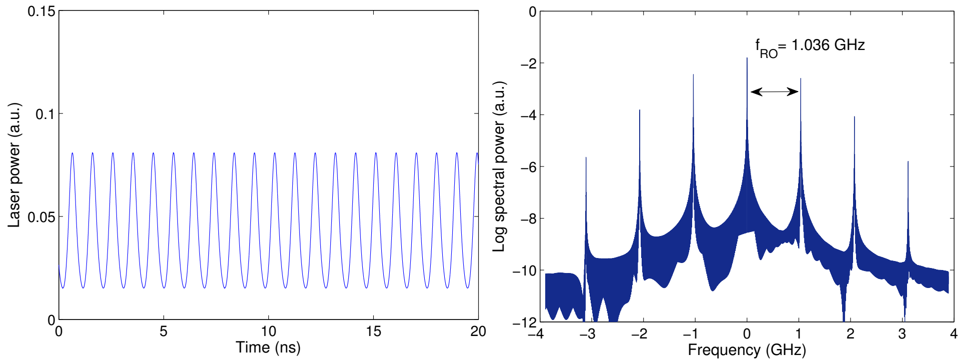

Figure 7.1: Simulated relaxation oscillations seen in the power and the optical spectrum. Same traces as in Fig.4.9.(A).

As we saw in chapter 4, the normally damped laser relaxation oscillations can become undamped for small values of feedback ratio. The laser power exhibits then harmonic time-periodic oscillations at a frequency close to the relaxation oscillation frequency. This frequency is totally determined by the laser injection current according to the relation $f_{RO} = \frac{1}{2}\sqrt{\frac{1}{\tau_c \tau_p}(\frac{I}{I_{th}} - 1)}$ given in chapter 2. Therefore f_{RO} is proportional to the square root of the injection current.

Fig.7.1 displays simulated time trace and optical spectrum of undamped relaxation oscillations pulsing at 1.036 GHz. The spectrum shows the solitary laser frequency at the center and symmetrical repeating side-bands separated from it by the value of f_{RO}.

From a dynamical point of view, relaxation oscillations show little interest to us since their frequency cannot be changed either by a modulation of the feedback ratio or the time delay. Usually, f_{RO} ranges from 1 GHz to 10 GHz [16].

7.2 Mode locking

The presence of an external cavity can make the laser show mode locking on external cavity modes. Indeed, oscillations which wavelengths are sub-multiples of the length of the cavity bounded by the laser back facet and the mirror are supported. Yet, the individual phase of the light waves in each mode is usually random.

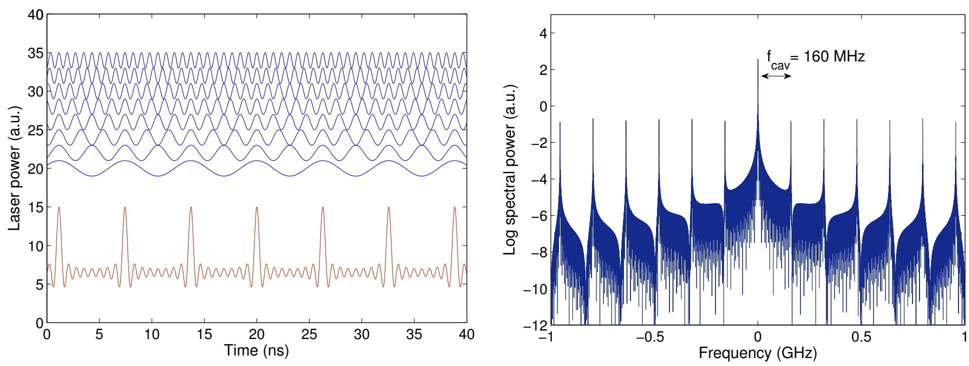

Figure 7.2: Simulated mode locking. In the time trace at the left, all ECMs in blue are in phase and result in the generation of a train of pulses in red at the external cavity frequency. At the right, the optical spectrum corresponding to the red time trace is displayed. The frequency peaks are interspaced by the external cavity frequency f_{cav}.

If instead of oscillating independently, the phases of each mode are synchronized with –or locked on– the others', the modes of the laser interfere constructively. As a result, intense pulses of light are generated, with the periodicity of the fundamental external cavity frequency. With the presence of optical feedback, it is possible to sustain mode locking and take advantage of this phenomenon to generate time-periodic short pulses [86, 119].

There are several techniques to perform mode locking. Active mode locking is controlled by an externally applied signal such as an acousto-optic modulator. In passive mode locking, the mechanism occurs through nonlinear optical phenomena in the laser cavity, by means of a saturable absorber for instance. Mode locking can be applied to a wide variety of lasers to generate pulses which widths range from 10 fs to 1 ns [120].

Mode locking is schematically shown in Fig.7.2. We consider the constructive interference of many external cavity modes. The resulting field is of the form $E(t) = \sum_q E_q e^{i\phi_q} e^{-i\omega_q t}$ where E_q is the amplitude of the q^{th} mode, ϕ_q its phase and ω_q its angular frequency. If we consider the real parts only, with all E_q equal to E_0 and $\phi_q = 0$ –corresponding to the configuration where all modes are in phase–, the constructive interferences of many external cavity modes result in the generation of a train of pulses as displayed in red in Fig.7.2. Since all the external cavity modes have frequencies multiples of the fundamental external cavity frequency f_{cav}, the resulting beam also pulses at f_{cav}. The corresponding optical spectrum shows characteristic frequency peaks interspaced by f_{cav}. Besides, the temporal extension of the resulting pulse is inversely proportional to the number of excited modes [85, 121].

7.3 Bridges between ECMs in the case of COF

Pulsing states have been reported in a laser with COF since 1994 by Tager and Petermann [119]. This kind of self-pulsations in a laser with COF correspond to a bridge connecting two Hopf bifurcations associated with two frequency-detuned ECMs.

This oscillating dynamics can be seen as a beating between two stable competing ECM solutions, as reported in [122, 123]. Fig.7.3 illustrates this beating of two ECM solutions with bifurcation diagrams from the Lang-Kobayashi equations without feedback (2.2) for different values of α. Configuration (d) displays a stable closed branch on two ECM solutions and corresponds to a regime of beating between ECMs. As a result, the laser shows oscillations which frequency equals the frequency difference of the two ECM solutions. Fig.7.4 illustrates this pulsing state in the case of COF. The spectrum displays frequencies of the two ECMs that beat and connect through the bridge of Hopf bifurcations.

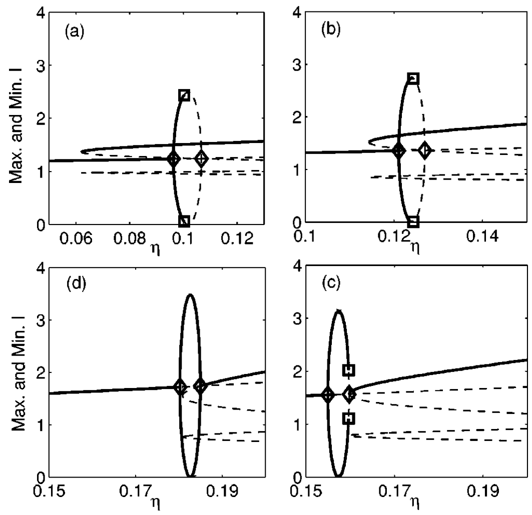

Figure 7.3: Bifurcation diagrams showing a pulsing state due to a bridge between stable ECMs in the COF case calculated for $\alpha = 4$ (a), $\alpha = 2$ (b), $\alpha = 1.25$ (c) and $\alpha = 1$ (d). η is the feedback ratio. The diamonds are Hopf bifurcations and the squares are torus bifurcations. Configuration (d) corresponds to the case where the torus bifurcation occurs for a feedback rate higher than the second Hopf bifurcation. As a consequence, a bridge between those two stable ECM solutions is built and the system shows beating between them. Picture from [62].

The bifurcation mechanism leading to those pulsations is a Hopf bifurcation on an external cavity mode (steady state). The self-pulsing dynamics mathematically corresponds to a bridge of time-periodic solution connecting two Hopf bifurcations belonging to two ECMs which frequencies are separated by the external cavity frequency. Sciamanna *et al.* demonstrated that the pulsing frequencies are limited to the external cavity frequency f_{cav}. Fig.7.4 shows the spectral signature of the ECM beating presented in Fig.7.3.(c). The main spectral feature of this pulsing state is the presence of two peaks. Each one can be individually identified to a single ECM and the frequency difference between them defines the oscillation frequency of the laser power which is $f_{ECM2} - f_{ECM1}$. The beating frequency between the ECMs depends on both the stability of the solutions emerging from the saddle-node bifurcation and the feedback ratio. As we mentioned in chapter 2, the beating can occur either between two consecutive modes or between a mode and the following anti-mode. In all cases, the beating frequency ranges between $\frac{f_{cav}}{2}$ and f_{cav} [62]. Further illustration of this phenomenon is displayed in Fig.7.5, where the self pulsing dynamics corresponding to a

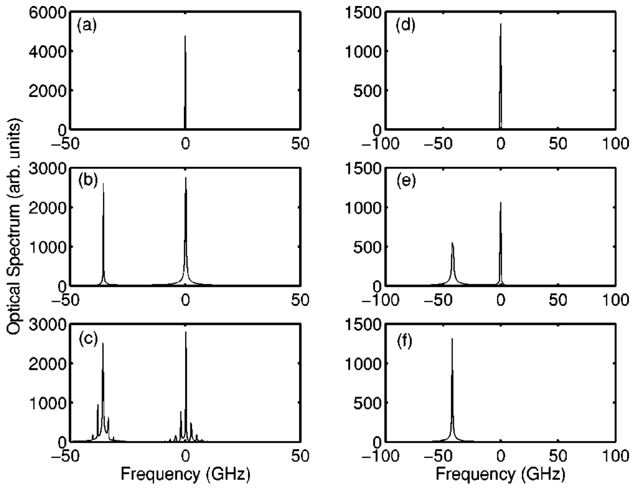

Figure 7.4: Optical spectra showing ECM beating and the consequent oscillating solution at the frequency equal to the frequency difference between the two ECMs. The left column illustrates the typical spectra of a mode-antimode bridge. Trace (a) displays a single ECM. In trace (b), the peak corresponding to an antimode is also represented. The beating between the two ECMs leads to a pulsing state that eventually gets destabilized as seen in trace (c). The right column corresponds to a stable mode-mode bridge, yet calculated for different parameters compared to the left column. Again, trace (d) is a stable ECM. A second stable ECM rises in trace (e), representing the beating where each peak stands for each ECM. When further increasing the feedback ratio, the first ECM gets destabilized and only the second one remains stable as presented in trace (f). Picture from [62].

beating between two adjacent ECMs is plotted.

Moreover, as one of the connecting ECMs is typically an unstable solution, the self-pulsing dynamics gets easily destabilized, leading thus to quasi-periodicity and chaos as the feedback ratio is slightly changed. This makes the observation of such ECM beating and Hopf bridge quite difficult. In addition, self-pulsing dynamics at the external cavity frequency resulting from this ECM beating are typically limited to so-called short external cavity in the COF case [119].

7.4 Self-pulsing ECMs in the case of PCF

In the PCF case, the laser has only one stable steady state solution which is the initial steady state. Under the action of the feedback, it gets destabilized

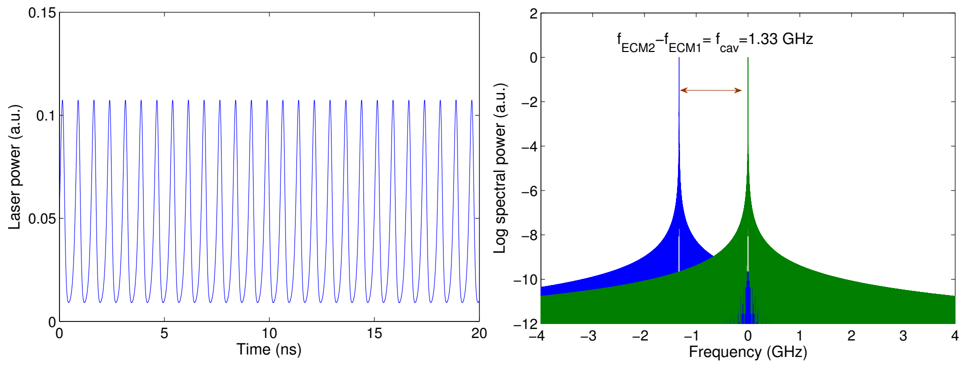

Figure 7.5: Simulated pulsing state corresponding to the beating between two consecutive ECMs in the case of COF. The spectrum at the right displays one steady-state peak for each ECM. The corresponding frequency detuning is f_{cav}.

through a Hopf bifurcation to a stable self-pulsing solution. As mentioned before, since the frequency of that solution is close to the external cavity frequency, that solution has been called ECM. Yet by contrast to the COF case, an ECM in the PCF case is a rotating solution with time-periodic intensity instead of an intensity constant in time. The laser creates new ECM solutions as the feedback increases, but all originate from the same and single initial steady state branch.

Furthermore, as we discussed in chapter 5, the stability of the external cavity self-pulsing dynamics in PCF is determined by the interplay between a saddle-node bifurcation and a torus bifurcation, hence it is still possible to observe a robust and fully stable self-pulsing dynamics when increasing the feedback ratio or the external cavity length. Fig.7.6 recalls the self-pulsing ECM analyzed in chapter 6 in Fig.6.7.(C). Compared to the case of Fig.7.5, the major difference in the spectrum is the repetition of the frequency peaks.

Fig.7.6 shows peaks symmetrically located in both sides of the zero frequency corresponding to the free running laser frequency. Yet, by contrast to the COF case, those peaks do not individually represent single ECMs that could be characterized by their position in the spectrum. Indeed, only the frequency span between two consecutive peaks has a physical meaning and represents the self-pulsing frequency, which is a multiple of the external cavity fundamental frequency.

In other words, the individual peaks in the optical spectrum in Fig.7.6 do not represent single ECM solutions as in the case of Fig.7.5 for the COF case. Indeed, we identify them as side-bands of the self pulsation at any multiple

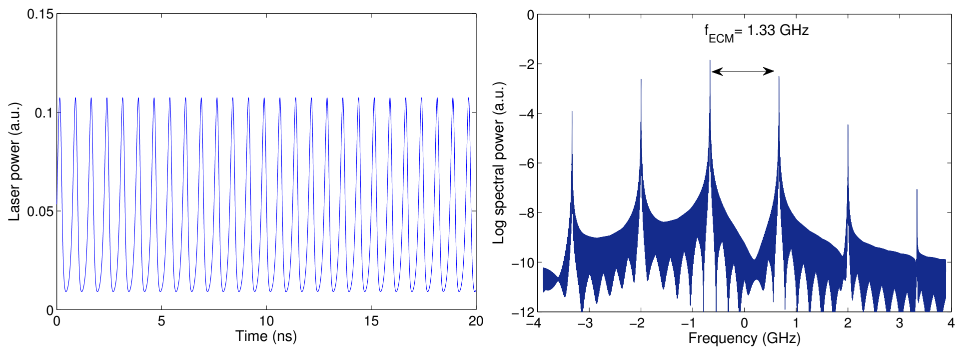

Figure 7.6: Example of a self-pulsing ECM in the PCF case. Same traces as in Fig.6.7.(C).

of the external cavity frequency. In addition, while in the COF case only self pulsations between $\frac{f_{cav}}{2}$ and f_{cav} can be stable, in the PCF case self-pulsing dynamics at higher multiples of the external cavity frequency can become stable when increasing the feedback strength. Experimental evidence of some of those self-pulsations at twice and thrice the external cavity frequency has been demonstrated in chapter 6.

7.5 Discussion

The purpose of this chapter is to compare the different mechanisms leading to self pulsations in a laser diode with optical feedback. We emphasize how the self-pulsing dynamics seen in the case of PCF has temporal and spectral signatures very different from the other cases of pulsations.

Fig.7.7 summarizes the spectral differences between pulsations due to undamped oscillation relaxation (a), mode locking (b), ECM beating in the case of COF (c) and self-pulsing ECM in the case of PCF (d). In the case of the relaxation oscillations (a), the spectrum is easily identified by the side-bands separated from the central laser solitary frequency by the relaxation frequency, which does not depend of the feedback rate or delay. Case (c) is immediately identified as corresponding to the beating between ECMs since the spectrum shows only two peaks, each one being associated with one of the ECMs at stake. In the case of mode locking (b), the spectrum shows many frequencies repeating at the external cavity frequency only and qualitatively shows the same features as the case of a self-pulsing ECM in PCF at the fundamental frequency f_{cav}. However, this ambiguity is suppressed as soon as the self-pulsing ECM starts pulsing at a frequency multiple of f_{cav} –for

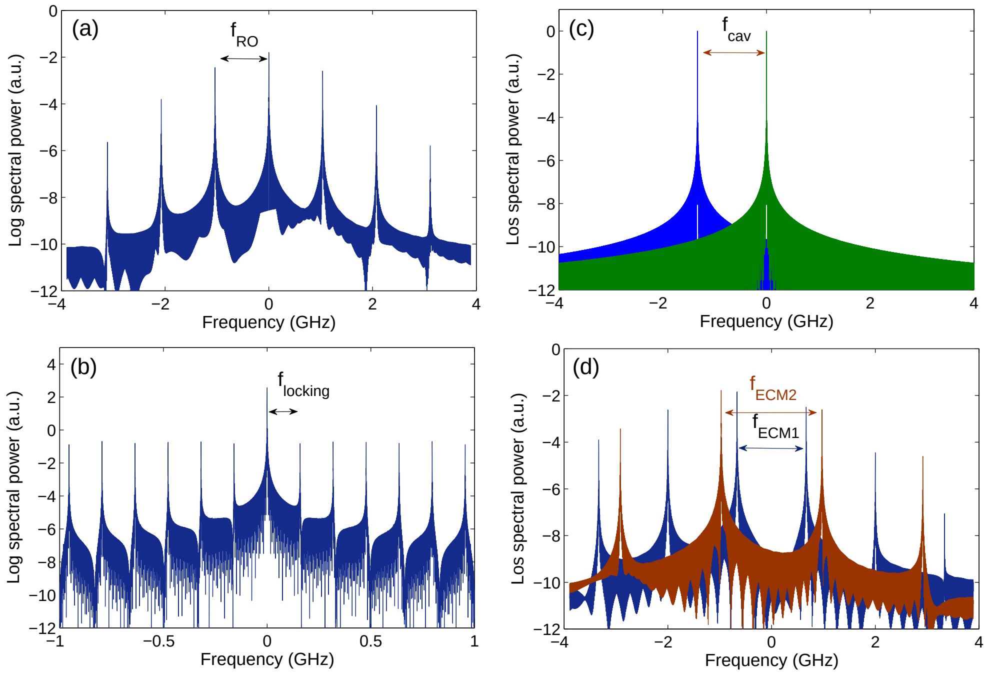

Figure 7.7: Confrontation of the four possible pulsing states in a laser diode with feedback. The optical spectra and frequency properties are compared for the identified cases: oscillation relaxation (a), mode locking (b), ECM beating in the case of COF (c) and self-pulsing ECM1 (in blue) and ECM2 (in red) in the case of PCF (d).

example under the effect of an increasing feedback ratio–, since the related spectrum would then show peaks interspaced by nf_{cav} and not f_{cav} any more.

Among the four pulsing states, the only one that shows a possibility to be easily tuned in a large frequency span is the one corresponding to self-pulsing ECM in the PCF case. Indeed, the relaxation oscillations are fixed by the laser injection current. Besides, the pulsation frequency of mode locking and ECM bridges between ECMs in the COF case are limited to f_{cav}. By contrast, a self-pulsing ECM in the PCF case is expected to pulse at any multiple of f_{cav}.

In table 7.1, the four physically different fundamental mechanisms that may lead a laser diode to exhibit oscillations are identified by the four corresponding optical spectra. Indeed, each one has specific signatures from which the nature of the oscillations and the parameters that drive them can be determined. For a given value of the external cavity length, the pulsing frequency can be tuned in the case of the PCF only, through the feedback ratio.

Frequency properties of pulsing states for given values of P, T and α			
Nature of the pulsing state	**Is the frequency tunable?**	**Frequency expression**	**Spectral features**
Undamped relaxation oscillations	No	$f_{RO} \propto \sqrt{\frac{I}{I_{th}} - 1}$	Side bands separated from the solitary laser frequency by f_{RO}
Mode-locking train of pulses	Yes, with a modulation of Ł$_{cav}$ (or θ)	$f_{locking} = \frac{c}{L_{cav}}$	Frequency peaks separated by $f_{locking}$ and covering the whole spectrum
Bridges between ECMs in the case of COF	Yes, with a modulation of Ł$_{cav}$ (or θ)	$\frac{c}{2L_{cav}} \leq f_{bridges} \leq \frac{c}{L_{cav}}$	Only two peaks are displayed, each one representing an identified ECM
Self-pulsing ECMs in the case of PCF	Yes, with a modulation of Ł$_{cav}$ (or θ) or with a modulation of R (or γ)	$f_{ECM} = n\frac{c}{L_{cav}}$, where $n \in \mathbb{N}$ and depends on R (or γ)	Frequency peaks separated by f_{ECM} and covering the whole spectrum

Table 7.1: Comparing spectral features of the four pulsing states in laser diodes.

As we mentioned in chapter 2, the possibility to tune the pulsing frequency of a laser diode shows great advantages in the field of optical communications. Mastering the self-pulsing ECM pulsations will certainly extend the horizon of laser applications.

In the next chapter, another particular dynamics exhibited by the laser is presented. The experimental modification causing the transition from this chapter to the next one is the increase of the effective external cavity length.

Chapter 8
Extreme events in the laser power

Figure 8.1: *The Great Wave off Kanagawa*, Katsushika Hokusai.

Recently, a new matter of interest and discussion has emerged throughout all domains of physics. It is often designated as rogue waves, extreme events or disruptive events among other names. When they occur in a nonlinear system, they are seen as events of very high amplitude rising far above the mean level of their peers but remaining in few supply compared to them.

8.1 Definition and intuitive illustration

Extreme events can be visible in many contexts. Nature is a prolific source of extreme events. In order to figure out qualitatively what an example of extreme event can be, let us imagine a forest in which the heights of the trees are distributed with a gaussian law, by which nature often abides. In this forest, most trees are about as high one as another, let us say from about 6 to about 10 meters high and close to the average forest height –about 8 meters. However, like in every gaussian-distributed population, some samples belonging to the tails of the distribution have extreme values either in highness or in smallness. Therefore some trees of the forest –the highest ones–

can reach heights far above the forest mean level, although they are very few.

Now let us suppose that there could be a means to control the rate of very high trees in the forest. For example if increasing the annual precipitation rate in the forest could stimulate the growth of very high trees, it would be possible to make them grow even higher and be more numerous in the forest. We could imagine that for a certain value of the precipitation rate, 5% of the trees grow much higher than others, reaching about 12-14 meters high. Then not only would they belong to the set containing the highest trees of the forest, but they would also affect the statistical distribution of the height which would show a larger standard deviation and a non-gaussian tail would appear for high values. Indeed only the population of very high trees would swell following a non-gaussian law. Those highest trees are then called extreme event. An illustration of an extreme event in a forest is given in Fig.8.2.

Figure 8.2: Extreme events in nature: one of the trees rises much higher than the average level of the forest. Picture from *National Geographic, Reedwoods: The Super Trees, October 2009.*

To quantify this phenomenon, one must define a condition to discriminate among a whole set of events which are extreme and which are not. In our research, we use the mathematical tool known as abnormality index, written AI. This term is actually borrowed from studies of oceanic rogue waves [124]. In a population of N events we write Hf_n the value associated with the n^{th} event E_n. In our example each tree is an event and Hf_n is the difference between height of the n^{th} tree and the average height of the forest. We write

Hs the significant value of the whole population. Hs is actually defined in [124] as the average value among one third of the highest values of Hf the whole population. In other words, Hs is the average difference between the height of each tree and the average height value of the forest, calculated in the third of the forest composed only of the highest trees. Now for each event E_n we can calculate the associated abnormality index: $AI_n = \frac{Hf_n}{Hs}$. The threshold to which compare an event to know if it is an extreme event, according to the definition of [124], is $AI = 2$. Therefore event E_n is an extreme event if $AI_n \geq 2$.

Fig.8.3 shows an illustration of the extreme events' distribution in the example of the forest mentioned above. The distribution of a population of 10,000 trees with heights randomly distributed around the mean value of 6 m with a standard deviation of 1 is presented in Fig.8.3.(a). The red vertical line is the extreme event threshold $AI = 2$ which corresponds to 10.1 meters high. Some trees have an abnormality index above 2, yet they are in few supply (155 trees) and do not reach very high AI values since the maximum value is 11.9 meters high which corresponds to $AI = 2.3$.

According to what we just said, all the trees which abnormality index is larger than 2 could be considered as extreme events. However those trees do not induce a distortion of the gaussian distribution since they stem from a normal law. Therefore we take into account a second criterion. In order to be counted as an extreme event, an event must comply with two conditions: showing $AI \geq 2$ and belonging to a set of events that induces a distortion of the gaussian tail, typically showing new concavity. Otherwise any gaussian distribution would be likely to exhibit extreme events. That is why, in addition to the abnormality index criterion, the statistics's reshaping into a long-tailed shape is also commonly used to identify extreme events [125].

Actually, what is really interesting in the study of extreme events is to see how their number, their regularity and their amplitude –through their AI value– evolve and tend to increase when changing the value of a control parameter. Considering again the forest, since the precipitation rate stimulates the appearance of extreme events (5% of trees reaching 12-14 m) it is also responsible for the distribution reshaping shown in Fig.8.3.(b). The presence of the high trees shifts the position of the $AI = 2$ threshold since the value of each event counts in the calculation of the threshold. This time, the condition $AI = 2$ corresponds to an 11-meter-high tree. In our example, 452 trees have heights larger than 11 meters. In other words there are 452 extreme events in the forest. Since its population is 10,000, the ratio of extreme events is 4.52%.

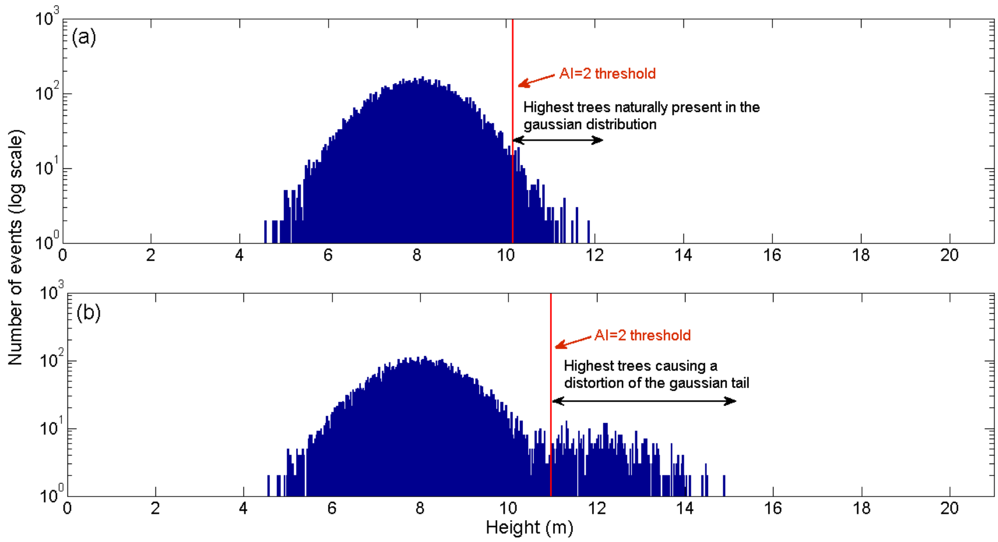

Figure 8.3: Statistical distributions of the tree heights in a population of 10,000 trees. In (a) all the tree heights are distributed with a gaussian statistics and 155 trees reach naturally the $AI = 2$ threshold with a maximum AI value of 2.3 but there is no distortion of the gaussian distribution. Therefore they are not extreme events. In (b) 5% of the trees are artificially made very high, inducing thus a distortion of the gaussian distribution. 452 trees fulfill the $AI \geq 2$ condition and induce a distribution reshaping, making thus as many extreme events. Maximum AI here is 2.7.

8.2 Extreme events in physics

The concept of extreme events can be easily adapted to almost any kind of population: all that matters is to define, in each context, the quantity to compare to the threshold value or, in other words, to define the abnormality index. This formality being set, extreme events can be studied in a number of diversified systems beyond reckoning: amplitude of an electric voltage, speed of the wind, height of the swell, price of a market share, population in a hive, cardiac beating rhythm and so on. Fig.8.4 illustrates extreme events in oceanography (a), plasma physics (b) and electromagnetism (c). Researches are being carried out in various fields of science to report on their appearance and to try to find a law by which extreme events could possibly abide. Besides, results predicted or measured in one area may be expected to be generalizable to many.

Historically the first extreme events have been spotted in the ocean by

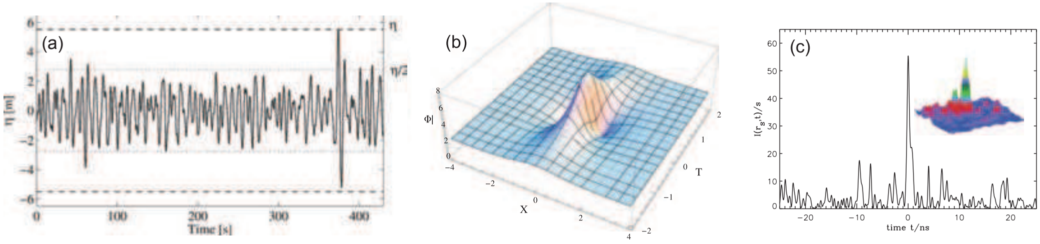

Figure 8.4: Examples of extreme events in different domains of physics. Fig.(a) shows an example of an unexpected wave from a simulation of the sea surface [126]. Fig.(b) depicts the profile of a rogue pulse of negative ions density and mass in unmagnetized electronegative plasma in Titan's atmosphere [127]. Fig.(c) displays a rogue wave (or hot spot) in the intensity of a microwave transport experiment in a resonator conical scatterer [128].

sailors and were then described as huge lone waves arising very high above the calm average water level without warning and causing pretty much damage to sailors' ships. Many studies have been done to account for their origin and their probability to occur in various systems. Nowadays, they are deeply studied in many fields such as hydrodynamics [124], plasma physics [129] and optics [130–132]. Whichever the domain, extreme events always show the characteristic property to be waves of very high amplitude that can appear on a rare and irregular basis in a signal, breaking thus its otherwise smooth or regular evolution. Researchers agree to say that extreme events are scarce, very intense and unpredictable phenomena making them both amazing and potentially dangerous events. In optics, besides their first report in microstructured optical fibers showing supercontinuum emission [130], extreme events have been reported in mode-locked lasers [133, 134] and laser diodes with optical injection [135, 136].

8.3 Extreme events in a laser diode with PCF

We study here the features of extreme events in our time-delayed optical system with phase-conjugate feedback. Although the occurrences of extreme events cannot be predicted, their number and their intensity can be driven by some parameters, just like the precipitation rate in the forest was a command parameter for extremely high trees. In our case, the command parameter is the feedback ratio which we vary changing the phase-conjugate mirror reflectivity. We will see that the evolution of R causes significant impact on the ratio, the regularity and the shape of the extreme events that the laser exhibits when operating in chaotic regime. The experimental setup is as described in chapter 3. This time the effective external cavity length has been extended –compared to chapter 6– to $L_{cav} = 66\ cm$: 12 cm between the laser and the crystal (L_1 in Fig.3.16) and 42 cm in the ring loop length ($L_2+L_3+L_4$). Consequently, the associated time delay is $\tau = 2.2\ ns$. Fig.8.5 displays a typical example of extreme event rising up above the average laser output power level. The peak in red is an extreme event since its abnormality index is larger than 2. Yet, in the particular case of this example, we do not study the deviation from the assumed gaussian distribution of the power peaks.

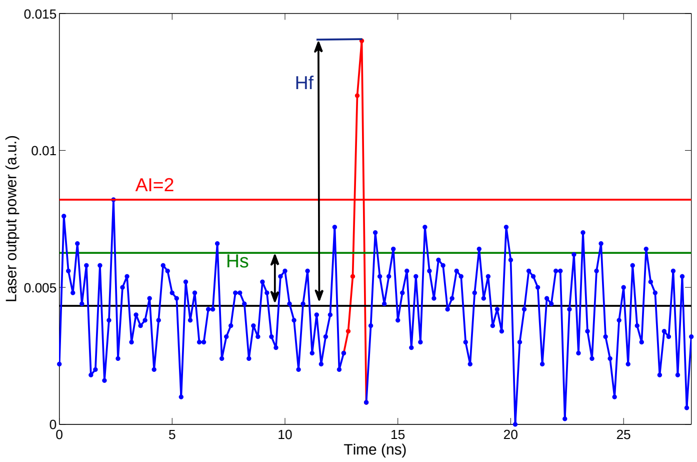

Figure 8.5: Typical example of an extreme event in the chaotic temporal trace of the laser. The black horizontal line is the signal average value and the green one its significant height Hs. The peak in red reaches $AI = \frac{Hf}{Hs} = 5 > 2$ and is an extreme event.

8.3.1 General evolution with the feedback ratio

In order to study the occurrences of extreme events in the laser output power, we will be operating in chaotic regime, which is reached in our setup when R is larger than 1.3%. As a laser in chaotic regime emits a very quickly fluctuating power over time, some of those fluctuations have very high magnitudes with respect to the average laser power level. As a consequence, they are good candidates to be extreme events. In the system we study, an event is a whole power peak. Therefore we first perform maxima detection in the laser time series to detect events and then we calculate for each peak the corresponding ratio $\frac{Hf}{Hs}$. Although in the discrete example of the forest each tree height counted as an event, in the analogous fluctuation of the laser power we consider that an event has a wave shape like in the first accounts of extreme events in the sea where they were huge waves. That is why we count as many events –or waves– as maxima detected in the laser power series instead of counting each sampling point as one itself. For example, in Fig.8.5, the peak in red counts as a single extreme event even though it is obtained by interpolating 5 sampling points. Seeing extreme events in a chaotic signal is something quite expected since chaos is typically made of a succession of peaks of many different intensities. What we analyze in deeper details is the evolution of the extreme events when R increases and the reshaping of their statistical distribution.

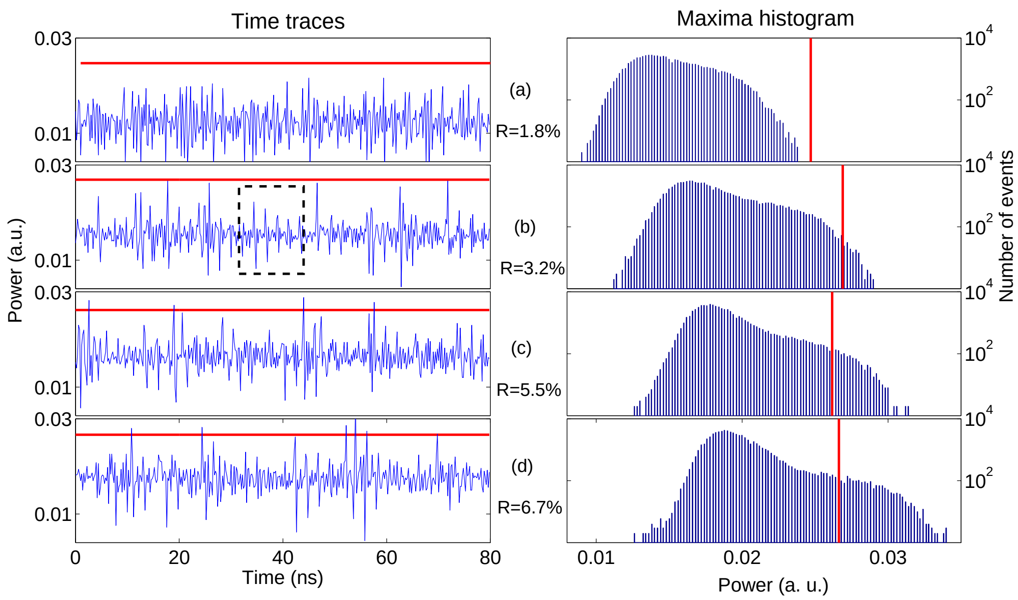

Figure 8.6: Time traces and histograms of the maxima in the laser power for increasing values of R. The red horizontal and vertical lines are the $AI = 2$ thresholds. The dashed box is shown in details in Fig.8.10.

Fig.8.6 shows the evolution of the laser output power versus time and the histograms of the maxima detected in the power time series when R increases. The red line is the extreme event threshold associated with each time trace ($AI = 2$ level). The general trend in the laser power distribution when R increases is a drift towards higher values, meaning that the average power globally increases. Besides, the number of events that show abnormality indices larger than 2 also increases, starting from zero. Indeed when R=1.8% there is no pulse above the threshold therefore the signal shows no extreme events. When R increases some high pulses start to appear and to rise far above the signal's significant height. This induces both a continuously increasing number of events above the threshold in the statistics' tail and a resulting stretching of the statistics' shape showing new concavity. In the experiment, the higher the feedback strength the more numerous the extreme events and the bigger the distribution's distortion compared to its initial shape.

The time series on which this analysis is based have been collected in a succession of single shots for values of R continuously increasing. Therefore the curves displayed in the figures are not an average of several shots. However, we observed experimentally that re-iterating the same operation leads to the same conclusions about the extreme events' properties. The time traces have been collected within a time span of 40 μs with a sampling time of 200 ps. We work thus with 200,000 samples per time series and no a posteriori filtering is operated on the signals.

8.3.2 Events getting more and more numerous

Fig.8.7 summarizes the evolution of the number of extreme events as R increases (a) and the ratio of extreme events with respect to the number of all events in the signal (b).

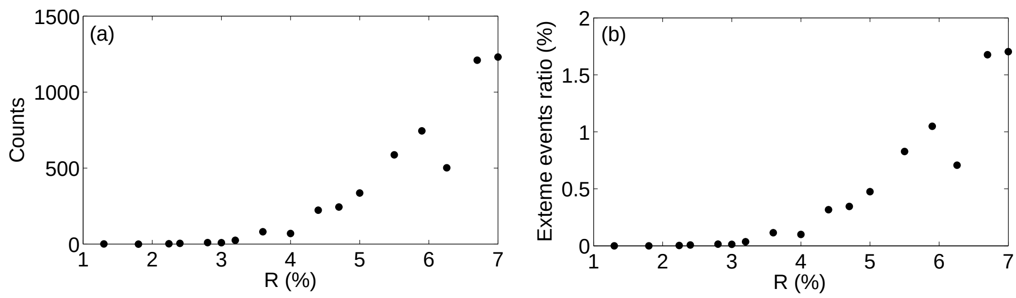

Figure 8.7: (a): number and (b): ratio of extreme events detected in the laser power for increasing values of R in signals counting in average 71,000 events.

We can discriminate two trends in the curves presented in Fig.8.7. First, for the smallest values of the mirror reflectivity, very few extreme events are visible and their growth with R is very limited. Then there is like a threshold value around $R = 3\%$ above which the number of extreme events starts to increase at a significant pace. The ratios in curve (b) are calculated for each value of R since the number of events varies with R. Each one equals the ratio of the number of extreme events to the total number of events in the laser power, for a given value of R.

The total number of events –or total number of maxima in the laser power– increases very slowly with R: it ranges from 70,899 events when $R = 1.3\%$ to 72,252 when $R = 7\%$. Therefore the variation of the ratio follows the same trend as the variation of the number of extreme events –which is much more significant– making curves (a) and (b) in Fig.8.7 pretty much alike. The value when $R = 6.2\%$ in Fig.8.7.(a) and (b) is unexpectedly low. Indeed we would intuitively expect a value between the previous and the following ones according to the general trend of the curve. We believe it is an experimental incoherence due to a mistake or a transient instability at the moment when the time trace was recorded rather than a local minimum with physical interpretation. Indeed a new iteration of the measurements did not show this low value point but a continuously growing number and ratio of events when R increases.

Since in our experiment we cannot reach PCM reflectivities much larger that 7% we have no experimental results to carry out an analysis for higher values of R. However, the number of extreme events when $R = 7\%$ is only little higher than when $R = 6.7\%$. We believe that this might be the beginning of a region where a saturation of the number of extreme events is seen in the laser output power. Naturally we have not enough data to confirm this trend but we cannot expect the number of extreme events to grow on limitless either. Indeed if too many events had very high amplitudes, the whole signal's significant level H_s and the $AI = 2$ threshold would both become higher and the number of events likely to reach this level would curb consequently.

Besides the number of extreme events, the laser power level is also affected by the feedback. Indeed the maxima histograms in Fig.8.6 also show a drift of the average level towards higher power values. This means that the feedback ratio induces an increase of the general signal level along with the increase of the number of extreme events.

8.3.3 Reshaping the distribution

As mentioned previously, the statistics' shape undergoes a stretching when R increases. The transition from a gaussian-like shaped statistics of the pulses' power when R is small to a long-tailed statistics with increasing probability for high amplitude peaks when R is larger is illustrated in Fig.8.8.

In Fig.8.8, the maxima histogram envelope shows new concavity for in-

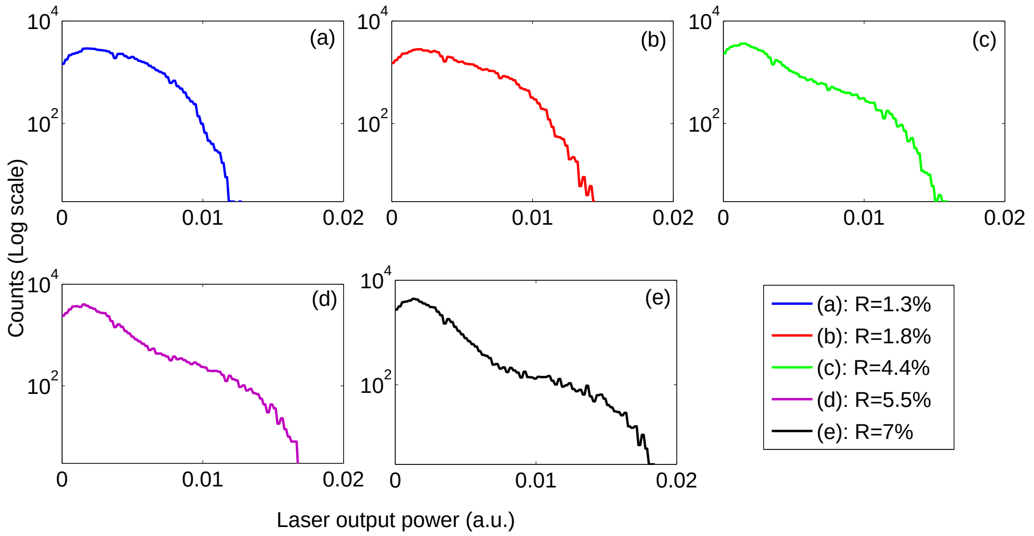

Figure 8.8: Evolution of the shape of the tail of the events' distribution in the laser power for increasing values of R. The continuously growing new concavity shows a long-tailed distributed power peaks.

creasing R values due to a higher number of power peaks of high amplitude. By comparison to the histograms shown in Fig.8.6, in Fig.8.8 the average level of the signal has been subtracted in order to compare relative distortions, inducing a shifting of the x-axis to lower values, starting at zero. The stretching of the distribution is the result of the presence of peaks of higher amplitude in the laser power. These peaks contribute to increase the standard deviation of the maxima histogram and the abnormality index span. The evolution of maximum AI for each trace versus R is presented in Fig.8.9. Again the curve shows the same trend as seen in Fig.8.7. Maximum abnormality index value is achieved ($AI_{max} = 3.3$) when $R = 6.7\%$.

The variation of maximum AI for each trace versus R is a means to quantitatively estimate the distortion of the statistics since we can see how far from the average value the highest peaks range. Considering the case when $R = 1.3\%$ as a starting point and the associated distribution shape as a reference, the stretching of the distribution reaches at its maximum 150% of its initial value when $R = 6.7\%$. Therefore the reflectivity value, through the associated number of extreme events, dramatically induces a modulation of the width of the laser power distribution. Consequently, a long-tailed reshaping of the distribution is induced as well, directly caused by the increasing number of high-amplitude peaks in the laser power.

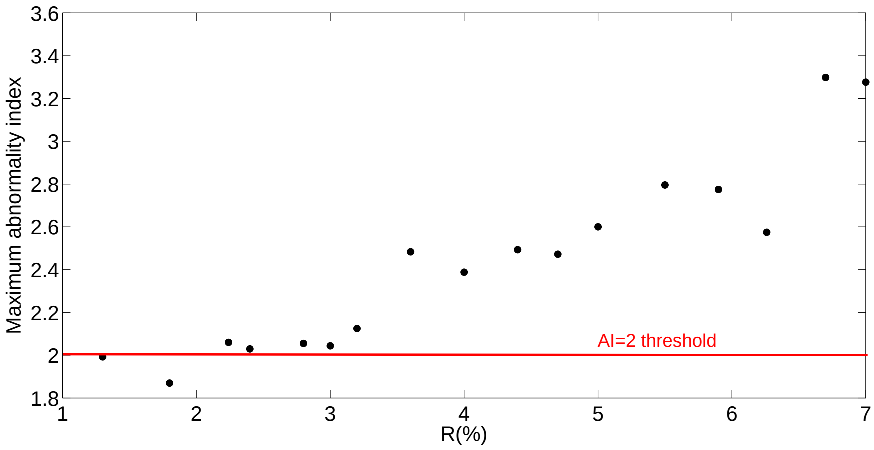

Figure 8.9: Evolution of the maximum value of abnormality index reached in each trace versus R.

Extreme events are a very good example and illustration of how the mere variation of a single parameter can induce an alteration in the major properties of the overall dynamics of a system. The delayed feedback strength is therefore a command control for the occurrences of extreme events in a laser diode. Extreme events become more and more numerous and show increasing abnormality indices when R is increased.

8.4 Lone pulses versus multiple pulses

A careful analysis of the time traces in Fig.8.6 allows us to go deeper in the analysis of the features of the detected extreme events and to classify them in two groups. Generally, in chaotic dynamics most pulses are not regularly spaced in time. Yet, in our feedback laser system there are some which are clearly separated by regular time intervals like those shown in Fig.8.10, which is a zoom on the dashed box in Fig.8.6.(b). Those regularly spaced peaks also get amplified when R increases and count as extreme events if their amplitudes reach $AI = 2$.

We sort the extreme events in two groups according to their type. In group I we gather the isolated extreme events, which are those like the one shown in Fig.8.5. An extreme event belonging to group I is basically a single high pulse with no correlation with its precedent and its following counterparts. In other words, group I is made of lone extreme event which temporal distribution is randomly set. Group II contains what we call "bunches of

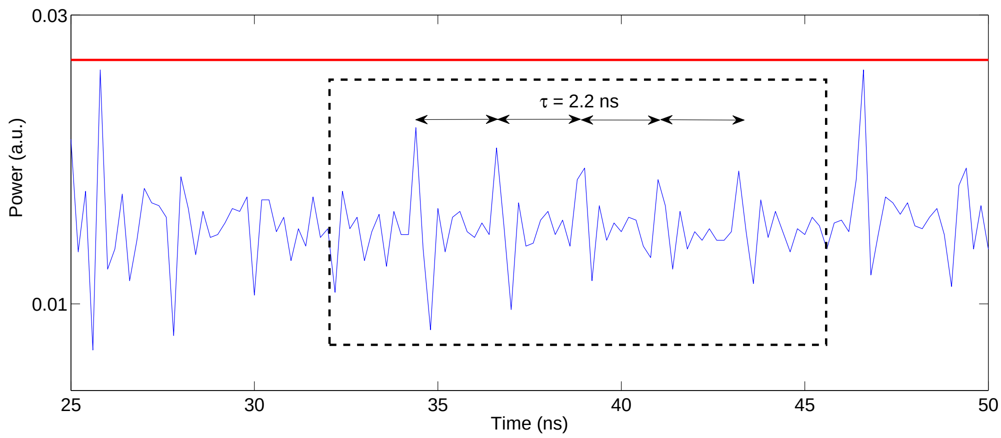

Figure 8.10: Zoom on the time trace (b) in Fig.8.6 showing examples of peaks distributed at the pace of the time delay $\tau = 2.2\ ns$.

extreme events". Those bunches are made of pulses that not only comply with the $AI \geq 2$ condition but have also the characteristic property to be distributed in regular time intervals. To be more precise, we saw experimentally that bunches of peaks could appear showing perfectly regular time intervals between consecutive peaks. By measuring this interval, we noticed that the time span between two peaks of a same bunch is constant and equals the external cavity delay τ. As can be seen in Fig.8.10, a bunch of events is made of about four or five peaks, separated from each other by the time delay $\tau = 2.2\ ns$. The histograms in Fig.8.6 take into account both types of extreme events since they only count how many peaks reach $AI = 2$. To discriminate those two kinds of extreme events, we consider that consecutive events separated by times below thrice the delay belong to the same bunch.

First, for smaller R values like in Fig.8.6.(b)-(c), extreme events appear as high lone peaks. Then as shown in Fig.8.6.(d) bunches of small pulses that are separated by the time-delay period grow and end up by reaching the threshold as well, each pulse might thus count as an extreme event as illustrated in Fig.8.12. These two situations of extreme events, either isolated pulses from group I or bunches of pulses with the time-delay periodicity from group II, coexist in a single time series. However, we find more extreme events of type I (isolated pulses) than of type II (bunches of pulses). Their ratio varies when increasing the mirror reflectivity, though.

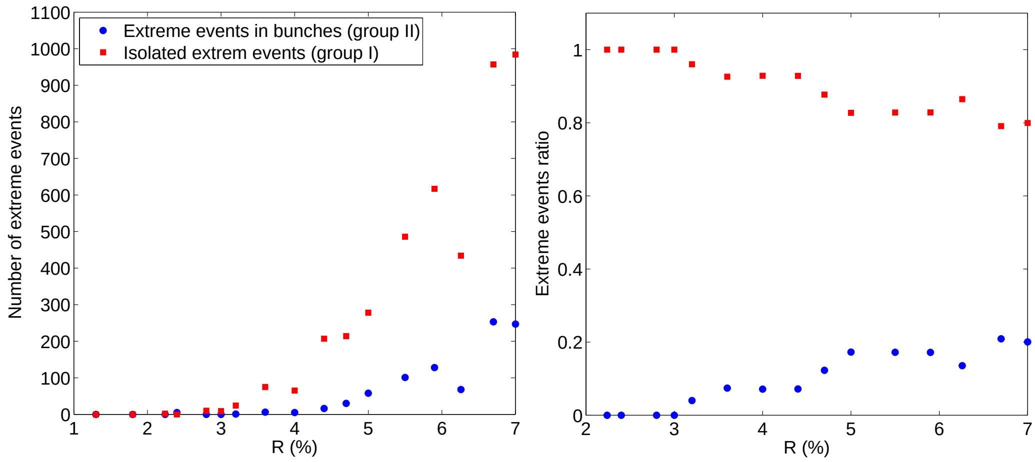

Figure 8.11: Distribution of the number (left) and the ratio (right, calculated on the basis of all extreme events) of the two kinds of extreme events in the laser power.

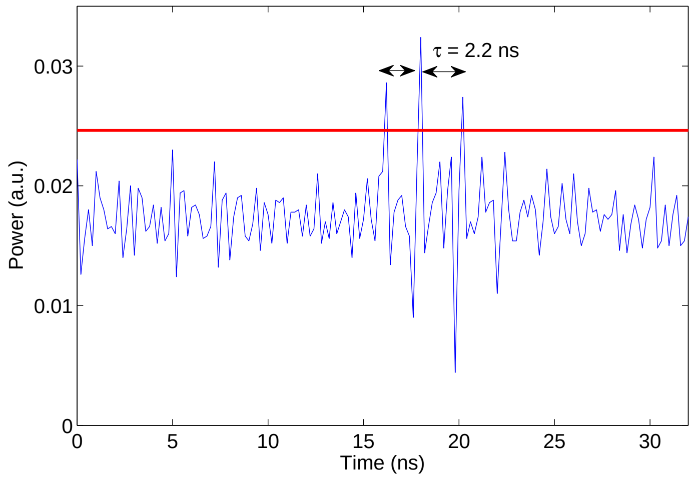

Figure 8.12: Extreme event of group II, made of a bunch of three peaks separated by the delay τ.

8.4.1 Relative evolution of the extreme events

Fig.8.11 illustrates the distribution of the two kinds of extreme events for each value of the mirror reflectivity. We notice that single pulses are always in higher supply than the pulses appearing in bunches. Indeed for the smallest values of R, only extreme events of group I are seen. Then when R is increased the number of both kinds of events increase, the events of group

II always remaining fewer than those of group I in our reflectivity span. As for the ratios of the two kinds of extreme events, we notice an interesting feature. When R increases, although the number of both kinds of extreme events increase, the evolution of the ratios of each kind shows that the proportion of events of group II increases gradually in spite of the proportion of events of group I. In other words, extreme events distributed in bunches are more likely to appear when the feedback ratio is larger.

We account for this observation with the argument that the delayed feedback somehow tends to impose its own time scale on the chaotic laser dynamics, which is exhorted by moments to oscillate at the delay time scale. Therefore when the feedback strength is larger, more extreme events separated by the delay τ are seen than when the feedback is low. Consequently, the ratio of extreme events in bunches increases while the ratio of the randomly time-distributed isolated extreme events curbs. It is worth emphasizing that both types of extreme events are pulses (or pulse packages) that occur at randomly distributed time intervals much larger than the system's time scale, hence they can be considered as scarce events. Note that when counting the extreme events, each peak showing $AI \geq 2$ counts as one, whether belonging to group I or group II. Thus a single bunch made of five peaks counts as five extreme events, provided the $AI \geq 2$ condition is fulfilled for each peak.

8.4.2 Delay-induced coherence in extreme events

We just saw that the feedback delay has a characteristic impact on the temporal distribution of the extreme events in the laser output optical power. We have identified the extreme events that appear regularly in bunches (group II) and discriminated them from the isolated ones (group I) which are randomly distributed in time. Actually, even when extreme events appear as isolated pulses, they differ from the usual model of lone pulses totally uncorrelated with any other pulse that has been reported so far and those isolated pulses keep the signature of the time-delayed feedback. This phenomenon is illustrated in Fig.8.13.

A single extreme event is basically made of a very short pulse surrounded by fast fluctuations of lower amplitude. As shown in Fig.8.13.(a) and previously seen in Fig.8.6, a single extreme event pulse is anticipated and followed by other pulses that repeat periodically at the delay time scale. Fig.8.13.(b) shows the superposition of 70 time series exhibiting extreme events of group I when R=4.4%, each one being centered on the main pulse and plotted in a 20-ns time span. We are sure there is no extreme event of group II among those traces since only one peak per trace reaches the red $AI = 2$ threshold line in a time span of 20 ns. The criterion that we choose to sort the extreme events into group II is as follows: two consecutive extreme events must be separated by a time interval smaller than three times the delay – that is $3 \times 2.2 = 6.6$ ns – to belong to the same bunch. This criterion is never fulfilled in the traces in Fig.8.13.

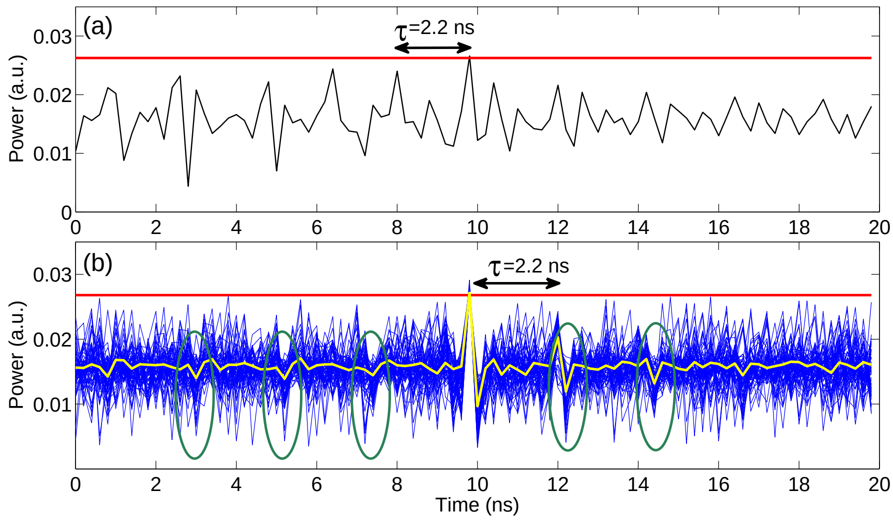

Figure 8.13: (a): single time series centered on one single extreme event of group I. (b): superposition of 70 extreme events of group I with the corresponding average curve in yellow. Power dropouts (green ellipses) occur about three time at intervals of τ at each side of the central pulse. As a result, a sketching in packages made of fuzzy pulses repeating themselves at the delay time scale is observed.

In all cases, a single extreme event has a well-defined pulse shape which is surrounded by pulses repeating at multiples of the time delay. From one time series to another, although the central peaks are superimposed, the smaller pulses at the time delay periodicity remain uncorrelated and overlap with each other with no apparent regularity. However a general patterning is sketched when many traces are simultaneously plotted. Indeed, they show power dropouts at each side of the main peak at multiples of the time delay and within a time interval of about two or three times the delay. It is interesting to see that even the extreme events that appear as single pulses show temporal properties related to the time delay. Naturally, they are different from the extreme events of group II which are very precisely spaced by τ.

Nonetheless the patterning of overlapping fast oscillations in fuzzy packages separated by the delay time scale in Fig.8.13 leads to the conclusion that, in our system, extreme events are not merely single high-intensity pulses with immediate recovery to an average as reported in [135]. Indeed, extreme events are rather pulses of high amplitude coming along with very fast oscillations of smaller amplitude damped with the delay time scale.

However, as we mentioned before, although the influence of the feedback delay is clear when looking at an extreme event of group II, its influence is much weaker on those of group I. That is why we need to superimpose many traces of extreme events of group I before being able to see this special patterning at the delay time scale. When looking at time spans lager than two or three times the delay τ, this patterning induced by the delay ends up by fading. Repeating this analysis for other R values leads to the same observation, confirming thus the coherence induced by the delay in the temporal distribution of the extreme events.

8.5 Reflectivity-dependent temporal distribution

As we demonstrated with the experimental results, the external cavity time delay induces regularity in the temporal distribution of some extreme events: those that appear in bunches (group II). We analyse now the statistics of the time between extreme events in order to see if the occurrences of extreme events abide by a special law. As has been measured in a spatially extended nonlinear optical system [125], the distribution of the waiting time between extreme events is expected to follow a Poisson distribution. The representation of the histogram of the occurrences of the elapsed times between two extreme events using an x-axis in log scale is convenient to us. Indeed as explained in details in [137], a Poisson distribution of times $(t_k)_{k\in\mathbb{N}}$ in linear scale is equivalent to a straight line when the abscissa values are $(w_k = \ln(t_k/t_{k-1}))_{k\in\mathbb{N}^*}$. Therefore a deviation from the Poisson distribution would induce a deviation from the straight line and would be easily pointed out. The same temporal study of the extreme events occurrences as the one done in [125] applied to our PCF laser results in the curves presented in Fig.8.14.

The curve in Fig.8.14.(a) is a straight line as expected from [125], we can then conclude that the time between extreme events is distributed ac-

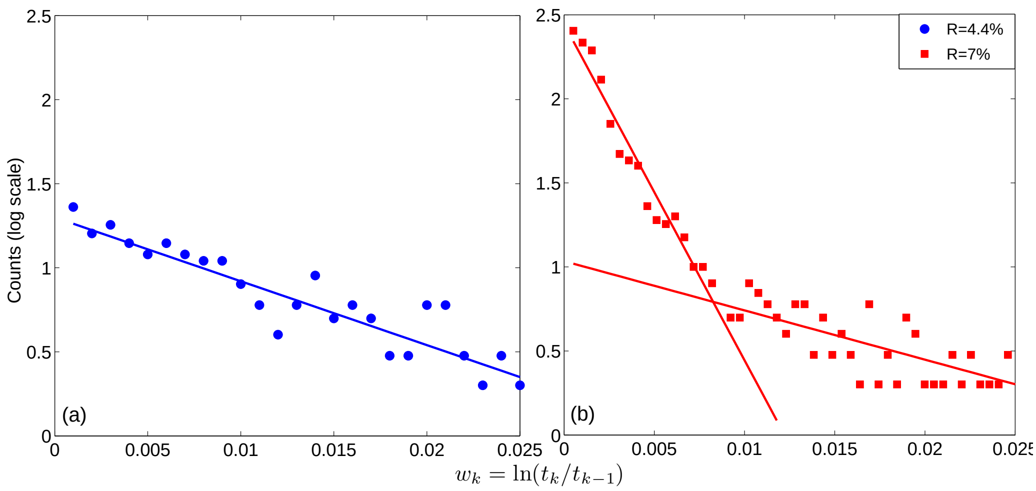

Figure 8.14: Statistical distribution of the times between extreme events for $R = 4.4\%$ (a) and $R = 7\%$ (b).

cording to a Poisson law. However, in Fig.8.14.(b), the distribution shows a deviation from the monotonous straight line. Indeed when R is small, the distribution follows a Poisson law since the points form a straight line. But increasing the feedback strength leads to a deviation from the log-Poisson statistics. And this deviation occurs mostly for small values of w_k, where the events are still distributed linearly in log scale but with a different slope. In Fig.8.14.(b), the distribution of the time elapsed between extreme events shows two trends represented by two straight lines with different slopes. In other words, the time intervals corresponding to small values of w_k follow their own log-Poisson law and the time intervals corresponding to larger values of w_k follow another log-Poisson law with a different slope. The above mentioned small w_k values correspond to values of $t_k - t_{k-1}$ that are comparable to the time delay, hence the deviation originates from the delayed feedback.

Again, the parameter that causes the deviation from a single Poisson distribution to two Poisson distributions with different slopes is the feedback strength through the mirror reflectivity value R. As expected, we noticed experimentally that the larger the value of R the larger the difference between the slopes of the two log-Poisson distributions.

Actually, this trend is also expected from Fig.8.13 where pulsating dynamics showing the periodicity of the time delay occur along with isolated extreme events. These secondary pulses become themselves extreme events when R increases, increasing thus the number of extreme events belonging to group II to the statistics. Therefore the signature of the delay τ in the time between extreme events is stronger when R is higher.

8.6 Extreme events seen in simulation

Extreme events are also predicted in the theory. Fig.8.15.(a) displays the same bifurcation diagram as Fig.4.1 with two time traces (b) and (c) showing very high peaks. We identified those peaks as extreme events since they show abnormality indices larger than 2. As indicated in the bifurcation diagram (a), time traces exhibiting extreme events such as those in Fig.8.15.(b) and (c) are found in the two last chaos bubbles, that is for values of γ above 0.025. For lower γ values, no such behavior is seen and for higher γ values chaos suppression occurs. We do not bring here quantitative compliance with the experimental results since we simply aim at providing with a theoretical confirmation of the dynamics seen in the experiment about the extreme events. Indeed, a thorough study of extreme events would require to carry out simulations with much larger time and feedback ratio spans, along with a detailed study of the distortion of the distribution.

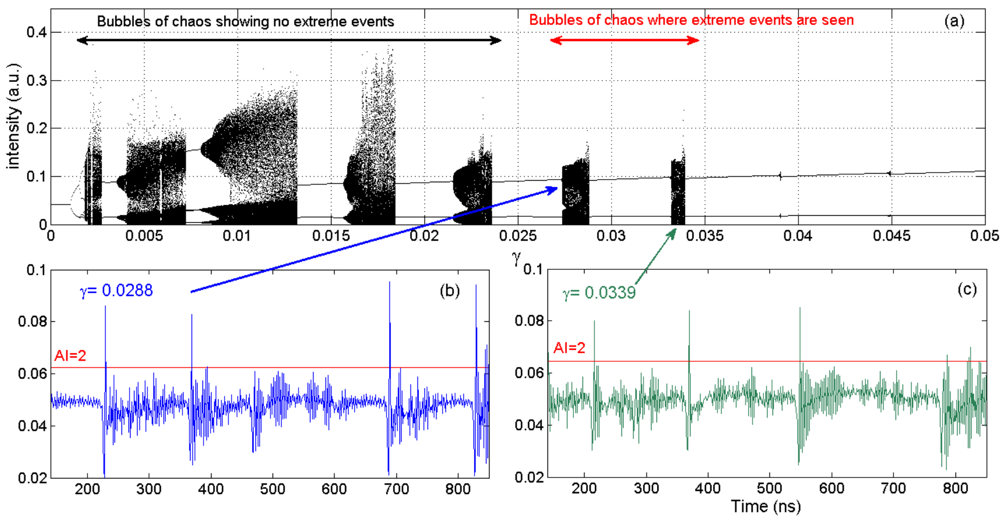

Figure 8.15: Bifurcation diagram (a) with time traces showing theoretical evidence of extreme events in the laser power (b) and (c). The parameters of the simulation are the same as in Fig.4.1. The red horizontal lines in the time traces are the $AI = 2$ extreme event threshold.

Yet il could be of great interest to carry out simulations in order to do an extensive study of the evolution of the extreme events and a statistical analysis of their occurrences similar to the one we reported about the experimental observations. We expect that a further statistical study of the time between extreme events in simulated long time traces –maybe with other simulation parameters to be closer to the experiment– could result in the same conclusions as we presented in this chapter. For example, an increasing ratio of extreme events of group II for large values of γ could be expected.

We also believe that the extreme events stem from destabilized external cavity modes that give their temporal signature to the time interval between their occurrences. This could account for the fact that several ECM destabilizations need to occur before extreme events can be seen. Indeed, in the simulation, they are visible only for feedback ratios higher than a certain value, which, in Fig.8.15.(a) is located in the sixth chaos bubble.

8.7 Discussion and interpretation

In conclusion, extreme events occurring in a laser diode with phase-conjugate feedback operating in chaotic regime have a double nature. They show both general features commonly seen in extreme events throughout many field of physics and particular features associated with the time-delayed nature of the laser system. As we discussed in this chapter, extreme events in the laser power are high peaks or pulses that fulfill the condition $AI \geq 2$ and which number and amplitude increase along with the value of the command parameter R. Moreover they induce a stretching of the initial Gaussian distribution of the power peaks into a long-tailed shape as often reported in the researches tackling extreme events in physical systems. Now the fact that our system is driven by a time-delayed feedback adds characteristic properties to the extreme events detected. Indeed they show a double nature and can be sorted in two groups according to whether they are single isolated pulses (group I) or distributed in bunches of regularly-spaced pulses with the time delay time scale (group II). Since the strength of the signature of the delay is directly dependent on the value of R, the mirror reflectivity is again a control parameter of the proportion of extreme events of both nature, as well as their temporal distribution law.

By contrast to reported extreme events seen in optics the fact that we work with a time-delayed feedback configuration somehow adds a constrain to the extreme events that are prevented to behave freely with a totally random time distribution. The delayed feedback, even in a range of values that may seem small ($R \leq 7\%$), clearly imposes its own time scale on the system's dynamics through privileged values of the times between extreme events that are more likely to occur than others. And this last point is not only related to extreme events since we also see bunches of peaks in the laser power that do not reach the extreme event threshold as well as we can see many single peaks that do not show $AI \geq 2$ in any common chaotic dynamics.

This brings us to the conclusion that the extreme events that we report here show an interesting ambivalency. Their occurrences are clearly unforeseeable since they originate from chaotic fluctuations in the laser power. However, depending on the feedback ratio their likeliness to occur at a precise time scale –naturally the one ruled by the external cavity delay– can be foreseen. This property makes our PCF laser system show extreme events of a kind different from those that can be seen in a system without feedback.

The simulation results presented along with the experimental study bring confirmation to the fact that extreme events are also expected from the theory. Yet, no quantitative accordance with the experiment about the evolution of their number and the time between their occurrences is targeted in the simulations presented here. Nonetheless, as we already mentioned, an in-depth study of this phenomenon could unveil interesting new trends.

Now, increasing further the external cavity length leads to a transition to another laser dynamics, causing the suppression of this extreme events behavior. The next chapter focuses on this particular chaotic dynamics.

Chapter 9
Low-frequency fluctuations

Figure 9.1: *Sisyphus*, Franz von Stuck.

Low-Frequency Fluctuations (LFF) are randomly distributed dropouts of the laser power followed by slower recoveries. LFF in laser diodes have been largely studied in the case of conventional optical feedback [60, 138]. Due to this particular succession of abrupt dropouts and slow recoveries, LFF regime is also known under the name of Sisyphus effect, as a reference to the myth of Sisyphus in the Greek mythology. Their first experimental observation was made by Risch and Voumard in 1977 in the output intensity of a laser diode coupled to an external optical cavity [139]. They have been since then theoretically accounted for with the model of the Lang-Kobayashi rate equations where they originate from a sequence of bifurcations on a large number of external cavity modes. They are generally expected to occur when the laser operates close to threshold. However they also occur for higher current values when the laser operates in a fully developed chaotic regime, close to the so-called coherence collapse state [46].

In the case of conventional feedback, the features of the LFF have been experimentally studied as a function of the laser current or the feedback ratio.

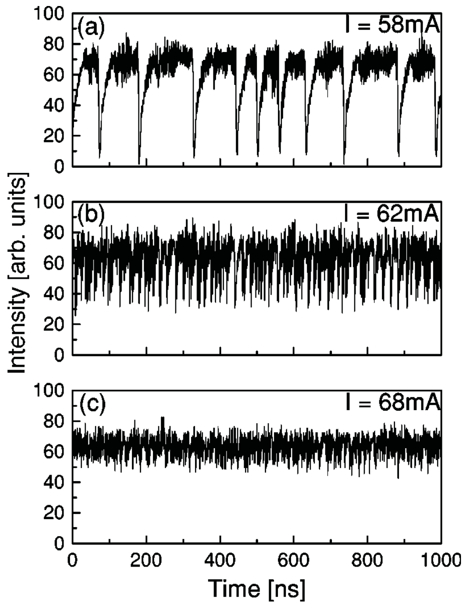

Figure 9.2: Intensity time series of a semiconductor laser subject to constant optical feedback and three different injection currents. Image from Heil *et al.* [138]. The time traces show typical LFF dynamics characterized by brutal power dropouts occurring at irregular intervals followed by slower recoveries. When the injection current increases (from (a) to (c)), the time intervals between dropouts shorten.

Fig.9.2 shows an experimental evolution of LFF in the case of a fixed conventional feedback ratio when varying the current [138]. In the case of phase-conjugate feedback LFF have been seen and studied experimentally [80], yet no satisfactory theoretical model capable to account for their origin has been formulated by contrast to the COF case. Moreover, to our knowledge there is no detailed analysis of the evolution of LFF in the case of PCF related to a variation of the feedback ratio. Therefore we study here in detail the LFF that occur in the case of PCF. We also report on an interesting new case of coherence resonance undergone by the laser when varying the feedback ratio and without any addition of external noise.

9.1 Experimental evidence

9.1.1 Conditions of occurrence

Generally, and as predicted by the theory, experiments that aim at showing low-frequency fluctuations work close to threshold. Indeed the LFF regime is expected to appear from a stable emission regime and to give way to a fully developed coherence collapse regime [80, 138, 140], as shown in Fig.9.3 in the case of COF. However it is also possible to see them for high current values.

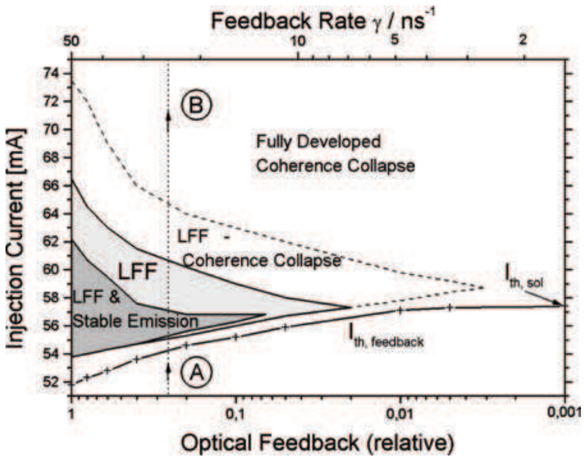

Figure 9.3: Dynamical behavior of a semiconductor laser subject to optical feedback in $feedback(\gamma) - current(I)$ space. The LFF regime is depicted in light gray. The dark-gray region embedded in the LFF regime corresponds to the region of coexistence of the stable emission state and the LFF state. The unshaded region encompassed by the dashed line corresponds to the continuous transition between the LFF regime and the fully developed coherence collapse regime. Image and description from Heil *et al.* [138].

In our experiment, we work at a fixed drive current value: $I = 60\, mA \Longleftrightarrow \frac{I}{I_{th}} \simeq 5$. Although LFF have been seen and theoretically predicted when the laser operates close to the threshold, the reason why we work at this high current value is the necessity of high beam powers to perform phase conjugation with a reasonable gain in the SPS crystal. The external cavity length is different from what it was in chapter 8. We have now $L_{cav} = 132\ cm$ with $L_1 = 32\ cm$ and $L_2 + L_3 + L_4 = 68\ cm$. The external cavity delay is $\tau = 4.5\ ns$. When we increase the mirror reflectivity value gradually from zero, the laser first exhibits self-pulsing external cavity modes as described in chapter 6. Then the system reaches the coherence collapse regime in which chaos shows features similar to what was reported in chapter 8 where the extreme events were studied. When further increasing R the dynamics qualitatively changes and starts resembling LFF. Indeed, the particular dynamics related to the LFF tends to impose itself upon the otherwise fully developed coherence collapse state. Therefore in our case LFF only appear for current values much higher than the laser threshold, once the laser is already operating in chaotic regime. This contrasts with some above-mentioned experiments in COF where LFF were seen as a transition to chaos. Moreover, in our reflectivity span, the LFF dynamics does not disappear nor does it give way to another dynamics –like a return to steady state– as could be expected from the literature. Fig.9.4 shows the evolution from fully developed chaos to the LFF regime seen in the time traces and the RF spectra.

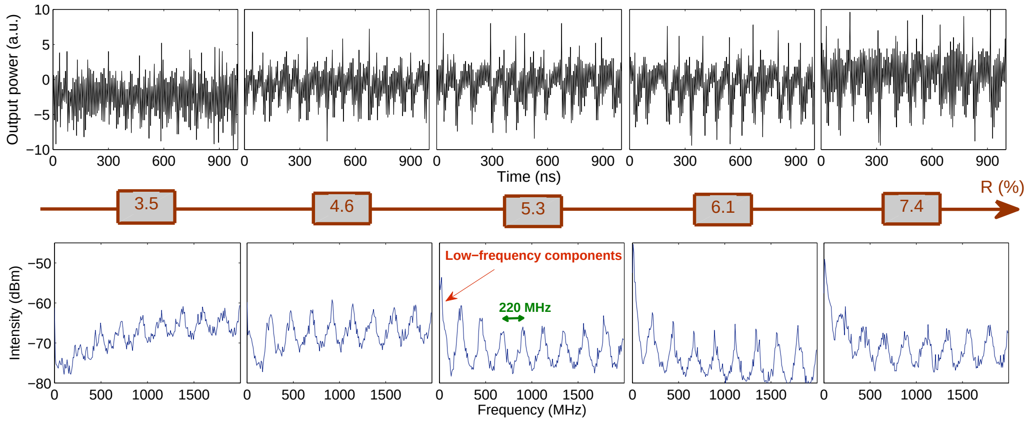

Figure 9.4: Birth of low-frequency fluctuations and qualitative evolution when R increases. The curves at the bottom are the RF spectra corresponding to the time series at the top.

One can see that when R increases, the laser power shows a transition from coherence collapse state ($R = 3.5\%$) to LFF dynamics characterized by the clearly visible abrupt power dropouts and the following slow recoveries. In the associated spectra this transition is easily spotted when the low-frequency components gain intensity comparatively to higher frequencies. The signature of the external cavity delay is strongly marked in the regular distribution of the frequency peaks. Indeed, the corresponding frequency interval is $\frac{1}{\tau} = 220\ MHz$. Depending on the feedback ratio, the regularity of the dropouts and the sharpness of the spectral peaks are altered. For instance, when $R = 6.1\%$, the power fluctuations appear to be more regular in time and the spectral peaks appear to be sharper than when $R = 4.6\%$.

9.1.2 Reflectivity range

Before moving to their detailed temporal and spectral analysis, the reflectivity range in which LFF are seen has to be discussed. We study the properties of the low-frequency fluctuations with reflectivities ranging up to 7.4%. This value is limited by the gain of the four-wave mixing in the phase conjugation process. Consequently we do not know how they evolve for higher reflectivity values. In Fig.9.4, LFF are seen for $R > 3.5\%$ even though they were never seen for the same values of reflectivities when studying extreme events in chapter 8. Indeed experimentally, for the same reflectivity values, there are times when the laser exhibits LFF and times when it does not show this transition and remains in a plain chaos dynamics as was the case in chapter 8.

Actually, the reason of this difference stems from the external cavity length. In the case of chapter 8, the time delay was 2.2 ns and no LFF was seen while now it is 4.5 ns. Hence the time delay is the parameter which controls the appearance of the LFF state. As was predicted in chapter 4, a longer time delay causes secondary bifurcations on ECMs to occur for smaller feedback values. Therefore, in the case of a longer external cavity, more complex chaotic dynamics are expected to be seen for smaller feedback values than in the case of a short cavity. This is why the transition to LFF was not seen in the study of the extreme events in chapter 8 and is seen now. Since our reflectivity range is limited to about 8%, it is strongly possible that the transition to LFF would have happened in the case of the short cavity for larger -but out of range- reflectivities. Indeed, what we call low-frequency fluctuations is merely a common chaotic state for which the contribution of the lowest frequencies of the laser power somehow become boosted up under the effect of the feedback. In other words, LFF state is a particular self-organization of the fluctuations constituting a chaotic trace in a slowly-varying enveloppe showing more or less regular power dropouts.

The time delay τ, through the external cavity length L_{cav}, is therefore a crucial parameter in the observation of the laser dynamics. According to its value, the laser exhibits totally different dynamics for the same range of feedback ratio.

9.2 An interplay between three time scales

The experimental conditions in this study of the LFF are $I = 60\ mA$ and $L_{cav} = 132\ cm$. This value of L_{cav} corresponds to the effective cavity length in the case when the grating within the crystal is a transmission grating, thus the path of the light takes into account one round-trip between the laser and the crystal –in this case 32 cm– plus the length of the ring cavity loop (68 cm).

One can see in Fig.9.4 that starting from a rather weak PCM reflectivity value ($R = 3.5\%$) for which the laser exhibits chaos, an increase of the reflectivity induces a modification of the time trace shape until power dropouts start to appear, characteristic of the LFF state. They are called low-frequency fluctuations due to the average time between dropouts ranging from about 30 to 200 ns, which is much longer than the laser relaxation oscillations period, remaining at about 150 ps. The power dropouts occur then with a frequency much lower than the relaxation oscillations: $f_{LFF} \simeq 10\ MHz \ll f_{RO} \simeq 7\ GHz$. Those LFF become distinguishable from the chaotic background only when operating above a certain value of PCM reflectivity. Furthermore, in our range of reflectivities, once the laser exhibits LFF, this dynamics does not disappear when further increasing R.

The RF spectra in Fig.9.4 show the frequency distribution of the signals. We first identify frequency peaks repeating themselves on a regular basis. They are the signature of the feedback time delay. Indeed in the spectrum those peaks are regularly distributed at a pace of $f_{cav} = 220\ MHz = \frac{c}{L_{cav}}$ which corresponds to the external cavity frequency. These peaks at $\frac{c}{L_{cav}}$ and multiples correspond to bifurcating self-pulsing dynamics at the external cavity frequency or, equivalently, indicate that the chaotic dynamics emerges from secondary bifurcations on a self-pulsing solution of the type of the ECMs. The characteristic feature related to the appearance of LFF is the relative intensity of the lowest frequencies of the signal with respect to the others. Indeed, in Fig.9.4, when $R = 3.5\%$ there is no visible LFF in the time trace since the contribution of the lowest frequencies in RF spectrum is weak. Then, when R in increased, the leftmost peaks in the RF spectra gain intensity and become much higher than the others (up to 20 dB more intense). This phenomenon happens along with the appearance of the power dropouts in the time traces to which it is equivalent. Since the leftmost peak in the spectrum is the one responsible for the low-frequency fluctuation dynamics, the higher its intensity the more distinguishable the LFF in the related time series.

As we mentioned, the LFF regime shows a competition between several time scales: the very fast relaxation oscillations $-f_{RO} \simeq 7\ GHz$–, the feedback time delay $-f_{cav} = 220\ MHz$– and the slow power dropout frequency $-f_{LFF} \simeq 10\ MHz$. In order to study the full details of the LFF we need to be able to see fluctuations within a bandwidth of about 10 GHz and at

the same time to do acquisitions of the traces in a time span long enough to see several low-frequency fluctuations and to study their distribution. This requires measurement devices with huge resolution and storage capabilities. Therefore we split the study of the LFF in two parts according to the working time span:
- In order to see the details of a single LFF package –relaxation oscillations and feedback time delay– we work with a 12-GHz-bandwidth LeCroy oscilloscope (40 GS/s) in a time span of about 500 ns.
- In order to see the evolution of the time distribution of the power dropouts at the LFF envelope time scale with many LFF packages repeating successively, we work with a 4-GHz-bandwidth oscilloscope in a time span of about 200 μs.

9.2.1 Detailed zoom on a single LFF package

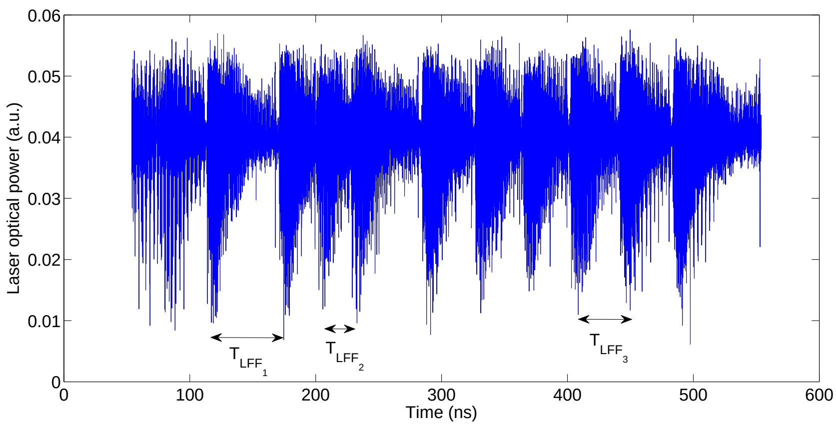

Figure 9.5: LFF in the laser time series with a 12-GHz bandwidth oscilloscope. The power dropouts are randomly distributed in time and the time between consecutive dropouts T_{LFF} has a great standard deviation. In this example, $T_{LFF_1} = 60\ ns$, $T_{LFF_2} = 30.2\ ns$ and $T_{LFF_3} = 43\ ns$.

Fig.9.5 shows a typical experimental time-trace of LFF chaotic dynamics seen with a 12-GHz bandwidth oscilloscope and observed for a mirror reflectivity of 5%. As typical in LFF dynamics [60] and as predicted theoretically in a model of a laser with PCF [51], the dynamics is made of successive significant power dropouts. As we will discuss later and as we can see in Fig.9.5, those power dropouts occur randomly in time but with an average time between dropouts much slower than both the laser internal time scale and the external cavity time delay.

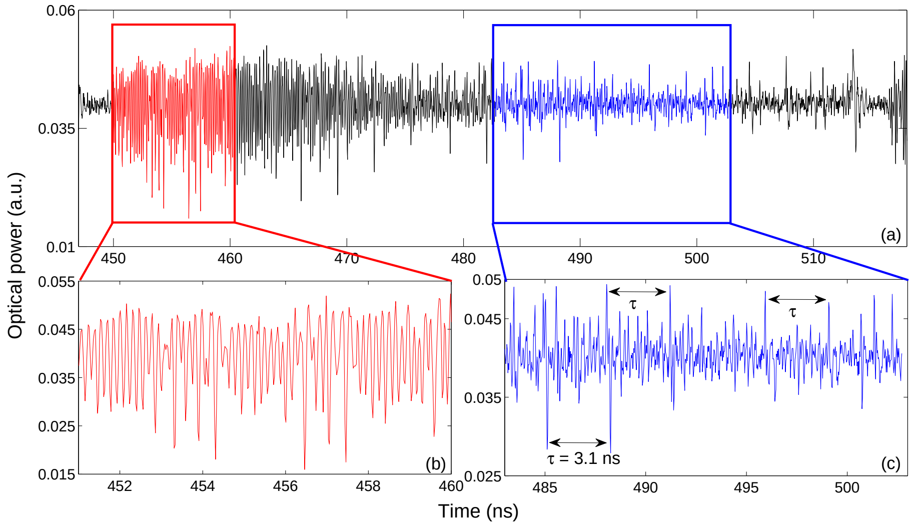

Figure 9.6: Detailed zoom on a single LFF package. Time series taken with a 12-GHz-bandwidth oscilloscope. The fast oscillations in red are the relaxation oscillations while the pulses in the blue trace are the signature of the external cavity delay. A LFF package is the dynamical superposition of those two time scales.

Fig.9.6 shows in detail the constitution of a single LFF package. We distinguish two regions in the package of qualitatively different dynamics. Indeed the first half (in red in Fig.9.6), contains mostly very fast fluctuations with a period of about 150 ps which we identify to be the relaxation oscillations. These oscillations quickly fade as off the second half of the package is reached, in which we mostly see pulses separated from the external cavity delay (in blue in Fig.9.6). A single LFF package sequence contains thus the signature of both the feedback delay and the relaxation oscillations' period. At the beginning of the LFF sequence, the relaxation oscillations are very intense and do not allow to see the pulses at the delay time scale. But when we move rightwards in the LFF package, the amplitude of the relaxation oscillations curbs and their damping ends up by unveiling pulses at the period of the time delay τ that were until then hidden in the fuzzy fast dynamics of the relaxation oscillations. To be more precise, the dynamics between two power dropouts is made of plateaus of damped relaxation oscillations which period is the time delay τ.

Note that the value of τ given in Fig.9.6 (3.1 ns) differs from the value given above (4.5 ns) because the experimental setup has been changed –the cavity length has been reduced– the day when the acquisition with the 12-

GHz-bandwidth oscilloscope was taken. But in all that follows in this chapter the external external time delay is $\tau = 4.5\ ns$.

9.2.2 Organization in successive packages

As we just saw, a LFF package shows particular dynamical properties due to a two-time-scale interplay between the relaxation oscillations frequency and the external cavity frequency. The last –and by far the most easily visible– temporal parameter in a time series exhibiting LFF is the time distribution of the packages T_{LFF}. As one can notice in Fig.9.5, all LFF packages do not have the same temporal extension, and T_{LFF} follows its own distribution policy. In order to see the distribution of the time between consecutive power dropouts, we take advantage of the fact that T_{LFF} is much larger than any other laser or feedback time scales, and therefore we filter out the time traces with a low-pass filter of 1-GHz bandwidth so that we keep only the frequency information on T_{LFF}.

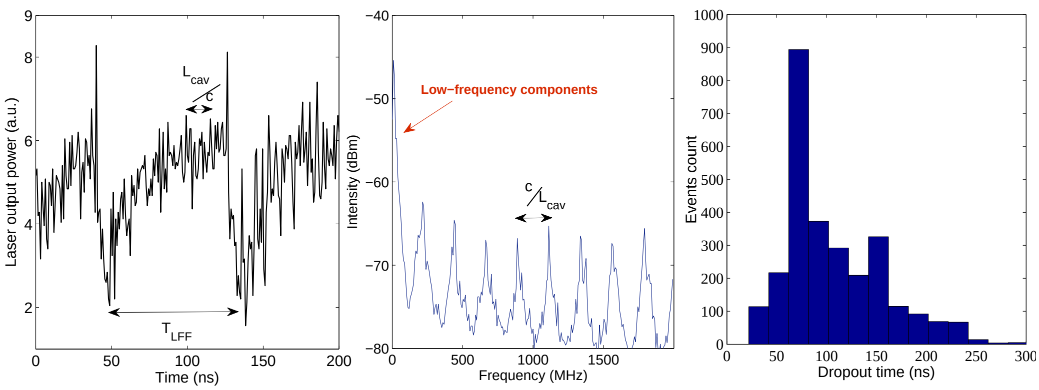

Figure 9.7: Consecutive LFF packages as typically seen in the laser power. The low fluctuation time T_{LFF} is distributed following the histogram at the right. The low-frequency components' peak in the RF spectrum in the middle is responsible for the power dropouts seen in the time series at the left.

A typical statistical distribution of T_{LFF} is shown in Fig.9.7 along with the corresponding time trace and the RF spectrum. Similarly to what has been reported for LFF dynamics in COF [55], the distribution shows no statistical event for times smaller than a given refractory time –here about 10 ns–, and then T_{LFF} follows a monotonously decreasing curve for larger times. The histogram in Fig.9.7 is the evidence that in the corresponding single time series –counting about 3,000 LFF packages–, the time distribution of these packages varies in a wide range from 10 ns to over 300 ns. What is interesting to study now is the evolution of this time distribution when the mirror reflectivity changes to see the influence of the feedback ratio on the temporal properties of the laser power.

9.3 Deterministic coherence resonance

9.3.1 Stochastic resonance and coherence resonance in dynamical systems

It is of common knowledge that the dynamics of a noise-driven nonlinear system can exhibit optimal response either to an external modulation or to one of the system's own time scale. The first case is called stochastic resonance and the resonance parameter stems from outside the system. Stochastic resonance was initially used in a climate model designed to explain the alternance of glacial and interglacial ages [141]. Later, stochastic resonance has also been reported in bistable noise-driven systems, such as in neuronal systems and solid-state physics [142]. In the field of optics, a pioneering experiment was performed using a bistable ring laser [143] and was later detailed using vertical-cavity surface-emitting lasers [144]. Stochastic resonance has also been seen in semi-conductor lasers exhibiting LFF by Buldú *et al.* in 2002 [145] where the action of both external noise and a modulation of the drive current leads the system to undergo resonance. This phenomenon is shown in Fig.9.8 where the standard deviation of the normalized dropout periods is shown for different noise intensities D.

A minimum of the standard deviation at noise intensity $D = 0.25\ ps$ is observed, showing a higher regularity in the dropouts. Moreover, the mean value of the dropout periods at this maximum regularity coincides with the modulation period $T = 70\ ns$ (in the upper trace). The indicator of the presence of resonance is usually the standard deviation. Indeed, a minimum value of the standard deviation is directly associated with a higher regularity of the system.

When the system, in presence of noise, shows optimal response to its own internal time scale, *i.e.* without the influence of external modulation, this phenomenon is called coherence resonance. Coherence resonance was found initially in noise-driven excitable nonlinear systems by Pikovsky and Kurths in 1997 [146]. Excitable systems are systems that can fire a pulse when given an appropriate perturbation above a certain threshold and that cannot fire

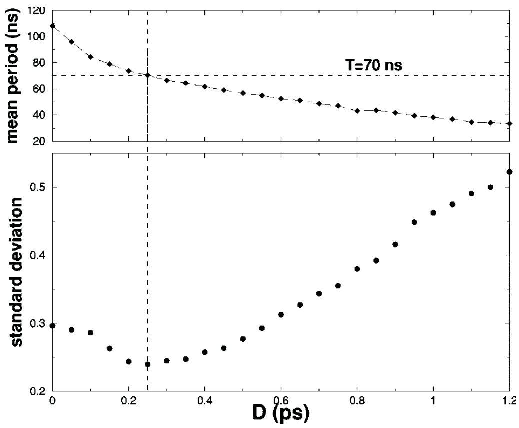

Figure 9.8: Mean value and relative standard deviation of the dropout periods versus noise intensity in a system showing LFF. Stochastic resonance is achieved for a particular value of the noise intensity. Figure from [145].

a second pulse until a given refractory time. They demonstrated that the normalized variance of the time between pulses may show a minimum value for a precise value of external noise amplitude as presented in Fig.9.9. Trace (a) can be seen as a sequence of pulses having durations t_p. In trace (b) is reported the normalized fluctuation of pulse duration $R = \frac{\sqrt{\sigma^2(t_p)}}{\langle t_p \rangle}$, where $\sigma^2(X)$ is the variance and $\langle X \rangle$ is the ensemble average of X. This quantity shows a minimum value when the noise amplitude D equals 0.07.

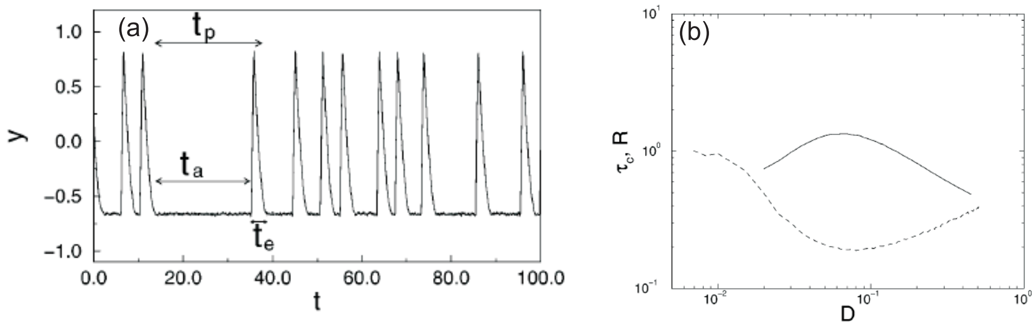

Figure 9.9: Coherence resonance in a Fitz Hugh-Nagumo system under external noisy driving. Trace (a) displays the amplitude of the emitted spikes y versus time. In trace (b), the normalized variance of the interspike time R (dashed curve) shows a minimum value for a specific noise amplitude ($D = 0.07$) while their correlation τ_c is maximum (solid curve). Figures from [146].

Examples of coherence resonance are typically found in the generation of nerve pulses in biology [147]. The first experimental demonstrations of coherence resonance have been reported in electronic circuits [148] and in a laser diode with optical feedback [56]. Both stochastic resonance and coherence resonance have today been demonstrated for a large class of dynamical systems, including in the random-like motion between chaotic attractors [149] and in bistable systems with time delay [150].

Both coherence and stochastic resonance have recently been shown in deterministic chaotic systems, *i.e.* without the addition of noise. Martinez Avila *et al.* [140] and Hong *et al.* [151] demonstrated that the increase of the drive current leads to an optimal regularity of the time between chaotic power dropouts in a laser diode. Buldú *et al.* reported that the chaotic fluctuations exhibit optimal entrainment to external modulation when the time period of this modulation is close to one of the multiples of the system's time scale [152]. As we are about to demonstrate, our experimental study of LFF dynamics also fits in the frame of coherence resonance. We will show in the following section that the laser exhibits optimal response to its own internal time scale for a specific value of the mirror reflectivity.

9.3.2 Delay-induced optimal dynamical regularity

As we saw before, the time distribution between power dropouts T_{LFF} in a time series showing LFF is sparse as recalled in Fig.9.10. We demonstrate here experimentally that when the mirror reflectivity varies, the distribution of T_{LFF} is affected and the system shows coherence resonance.

Fig.9.11 shows the evolution of the time series and the corresponding histograms of the distribution of T_{LFF}. Experimentally, with the increase of the mirror reflectivity, the LFF tend to gradually organize themselves in more and more regular power dropouts until a certain value of reflectivity. Here, the most regular traces are spotted when $R = 6.1\%$. For higher values this regularity is then gradually lost but due to the limitation on the PCM reflectivity in our setup at 7.4% we cannot observe what happens for higher reflectivity values.

This feature is also visible in the spectra in Fig.9.4. Indeed the regularity of the dropouts is related to the sharpness of the peaks distributed every 220 MHz. The sharper the peaks the smaller the frequency dispersion and thus the more regular the power dropouts. In Fig.9.4, the RF peaks are sharper when $R = 6.1\%$ than for any other reflectivity value.

Besides the qualitative observation of the time trace regularity and the RF spectra sharpness, another way to quantify the dispersion of T_{LFF} versus

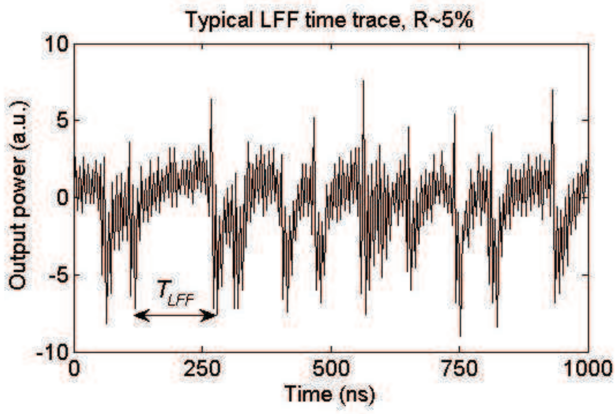

Figure 9.10: Consecutive LFF packages as typically seen in the laser power. The low fluctuation time T_{LFF} between two power dropouts is sparsely distributed in the time series.

R is to analyze the histograms of the time between dropouts as presented in Fig.9.11 for each time series. We find that an increase of the mirror reflectivity leads to a severe change of the statistical properties of T_{LFF}. First the average value of T_{LFF}, represented by the vertical red bars in the histograms, increases. Then there is an optimal value of R for which the dropout time distribution is narrower around its average value and therefore the standard deviation of T_{LFF} gets a minimum value (b). A further increase of the reflectivity leads to a statistical distribution (c) similar to case (a) but with a larger average value of T_{LFF}. This feature is further confirmed when looking at the corresponding time traces in Fig.9.11. Case (b) shows more regular power dropouts than (a) or (c) and corresponds to the optimal LFF regularity.

The fact that optimal regularity is achieved when $R = 6.1\%$ is confirmed by three indicators:
1/ The time series in Figs.9.11.(b) and 9.4 show higher regulatity when $R = 6.1\%$.
2/ The RF spectrum associated with the same time series in Fig.9.4 exhibits sharper peaks when $R = 6.1\%$.
3/ The histogram of the distribution of T_{LFF} in Fig.9.11.(b) has the smallest standard deviation.

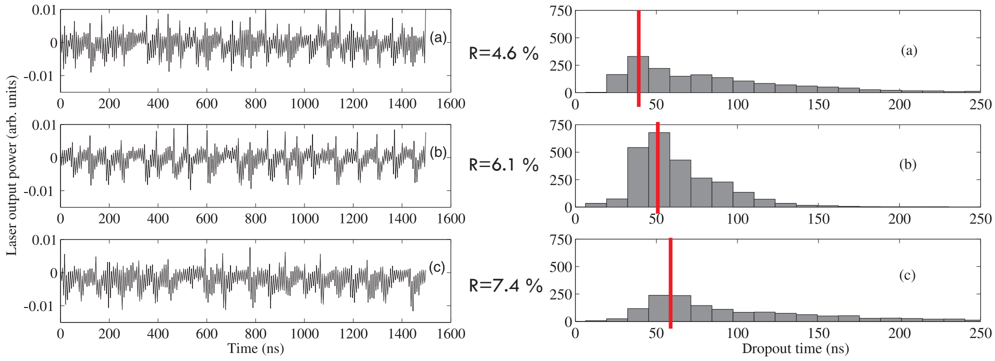

Figure 9.11: Evolution of the LFF time traces with the mirror reflectivity (left). The histograms at the right represent the statistical distribution of T_{LFF} for the related time trace. The red bars are the average values of T_{LFF} for each time trace.

9.3.3 Coherence resonance of LFF dynamics

The existence of an optimal regularity in the LFF time trace as a function of the PCM reflectivity is a potential signature of a coherence resonance. A common indicator for demonstrating coherence resonance is to check the evolution of the normalized variance defined by $V = \frac{\sigma_{T_{LFF}}}{<T_{LFF}>}$ –where $\sigma_{T_{LFF}}$ and $< T_{LFF} >$ are respectively the standard deviation and the average value of the dropout time T_{LFF}– as a function of the resonance parameter which is in our case the PCM reflectivity R. The resonance-like phenomenon is evidenced in Fig.9.12 which plots V as a function of the mirror reflectivity. This normalized variance V exhibits a clearly distinguishable minimum at a particular value of the mirror reflectivity that corresponds to case (b) of Fig.9.11 where the dropout time shows higher regularity and the time distribution shows smaller width. Like in the cases of [146] and [145], we conclude that the presence of this minimum is the signature of a resonance. The curve in Fig.9.12 shows three regions of qualitatively different features:

1/ For small mirror reflectivities, the laser exhibits a route to chaos from undamped relaxation oscillations, which leads to a chaotic dynamics with dominating high-frequency components at either the relaxation oscillation frequency or the multiples of the external cavity frequency. There is no distinguishable power dropout, and the dynamics shows a large dispersion of the times between chaotic pulses together with a small average time between pulses. As a consequence V is large.

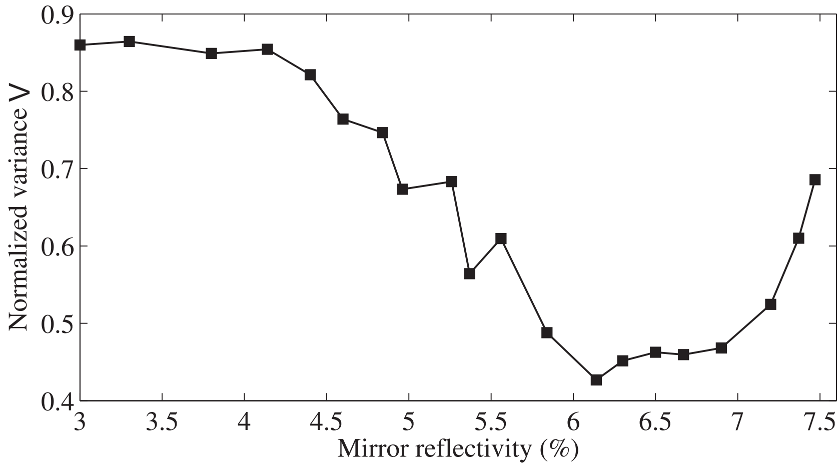

Figure 9.12: Evolution of $V = \frac{\sigma_{T_{LFF}}}{<T_{LFF}>}$ as a function of the PCM reflectivity R. A minimum is seen when $R = 6.1\%$, signature of a resonance.

2/ For a larger values of R, the low-frequency components –pulsing at frequencies ranging from 10 to 200 MHz– in the power spectrum gain intensity, which indicates the emergence of clearly distinguishable and slow power dropouts. The average time between dropouts increases with the increase of the mirror reflectivity, but this increase occurs more slowly than the decrease of the standard deviation of the time between dropouts. As a result, when R increases, V decreases down to a minimum value reached when $R = 6.1\%$. At that point the laser time series shows maximum regularity in the dropout times and coherence resonance is achieved.

3/ A further increase of the reflectivity leads to a more randomly-distributed sequence of power dropouts and $\sigma_{T_{LFF}}$ increases faster than $< T_{LFF} >$ with R. V increases again consequently.

Since the resonance occurs without external modulation –typically drive current [140] or external cavity length [152] modulation–, it is a coherence resonance. Moreover, by contrast to the well-known coherence resonance, in our case the resonance situation occurs without the need for any additional and optimal amount of noise. Therefore we call this phenomenon *delay-induced deterministic coherence resonance* where varying the amount of delayed feedback signal in a nonlinear system leads to an optimal response of the system to one of its own dynamical time scales without addition of noise.

An important difference between our experimental conditions and other demonstrations of coherence resonance is the fact that the resonance parameter is the feedback ratio only. More precisely we do not change the drive current value as has been done in [140] and [153]. Indeed changing the drive current induces a change in the relaxation oscillations frequency f_{RO}. Although we do not know the influence of f_{RO} on the resonance of the laser power dropouts, it is known that the competition between the dynamics at the relaxation oscillation frequency and the slow chaotic LFF at the time scale related to time delay is stronger when operating close to the laser threshold, where it also leads to locking of quasi-periodic dynamics known as synchronous LFF [154]. In our case we work at a fixed current level high above the threshold and only change the mirror reflectivity value. We claim that the resonance is purely delay-induced, *i.e.* that it is not related to or supported by current-dependent relaxation oscillation fluctuations. Therefore the mechanism that makes the laser undergo coherence resonance is totally different in the case when R is varied from the case when I is varied.

9.3.4 Independence of the resonance from the relaxation oscillations

Delay-induced coherence resonance is a phenomenon that does not require the relaxation oscillations' dynamics to be achieved. This claim is supported by simulations on a model from a much simpler laser system than the one used in the experiment: a class A laser with conventional optical feedback. By contrast to laser diodes or class B lasers, class A lasers like gas lasers do not exhibit relaxation oscillation-like dynamics because the carrier dynamics has been adiabatically removed. Thus the dynamics is made of a single equation for the optical field [18]. Taking into account the time delay, the class A laser model writes [155]:

$$\frac{dE}{dt} = \mu(1+i\alpha)E - b(1+i\beta)|E|^2E + a(1+i\epsilon)E(t-T_r) \tag{9.1}$$

In this equation, t is the time measured in units of $1/\gamma_\perp$. $\gamma_\perp$ is the polarization decay rate, E is the complex electric field, μ is a dimensionless gain coefficient and b a saturation coefficient. α is a detuning coefficient that is function of Δ and δ, where Δ is the detuning between the cavity frequency and the laser frequency and δ is the detuning between the atomic center frequency and the laser frequency. β is a detuning coefficient, function of δ. T_r is the normalized delay time. $a = (1-R_2)\sqrt{R_2R_3}/[R_2\sqrt{(1+\epsilon^2)}\gamma_\perp\tau_{in}]$ is the normalized delayed feedback ratio, where τ_{in} is the internal laser cavity

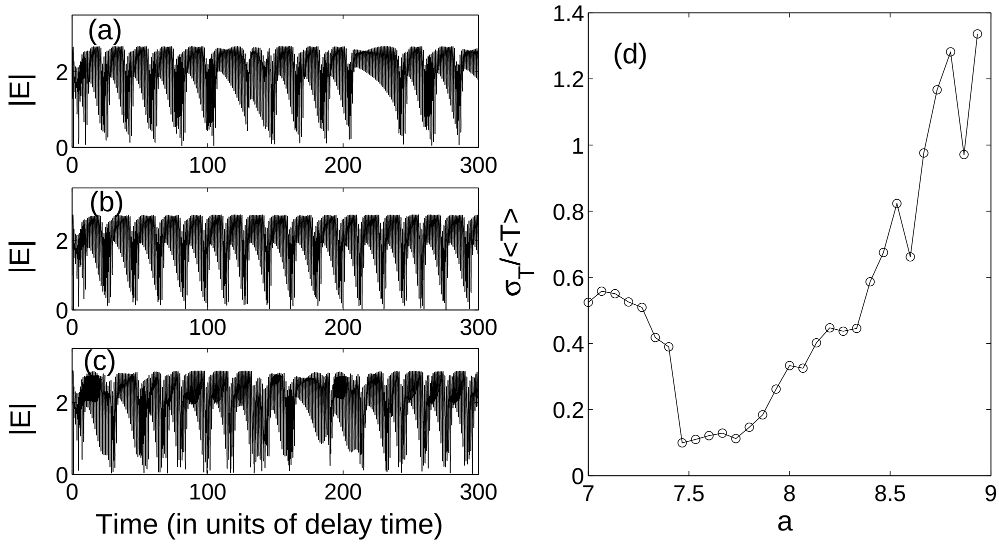

Figure 9.13: Simulations of equation 9.1. Traces (a)-(c): low-frequency power dropouts for $a = 7.2$, $a = 7.5$, $a = 8.3$, respectively. Diagram (d) shows the ratio of standard deviation to mean value of the time between drops (T) as a function of a. A minimum in the curve of the normalized variance (d) is again the signature of a resonance, like in our experiment.

round-trip time, R_2 is the power reflectivity of the laser output mirror and R_3 the power reflectivity of the external mirror. $(1 + i\epsilon)$ is the phase shift induced by optical feedback. We have simulated the dynamics of E for increasing values of a and the other parameters fixed as follows: $\mu = 0$ (laser pumped at threshold), $\alpha = 1.4$, $b = 1$, $\beta = 3$, $\epsilon = 0$ (the feedback phase is not taken into account), $T_r = 1$.

Samples of chaotic time series are shown in fig.9.13 for increasing values of a, with the time scale being normalized by the delay time T_r. One can observe fast pulsations of the laser output at a period close to T_r and dropouts that occur at random time intervals and with a much slower time scale, of the order of $20T_r$ or even more. As shown in fig.9.13, the time interval between successive power dropouts gets an optimal regularity for an intermediate value of the feedback ratio (b), if compared to the situation at smaller (a) or larger (c) feedback ratios. This conclusion is confirmed by a plot of the ratio between standard deviation and mean value of the time between power dropouts $\frac{\sigma_T}{<T>}$ as a function of the feedback ratio a (d).

This delay-induced resonance of chaotic dynamics is qualitatively similar to the one seen in our experiment, even though the dynamical system exhibits no relaxation oscillation or internal dynamics faster than the delay time-scale. Since class A lasers are dynamical systems of higher simplicity than laser diodes (no relaxation oscillations) we claim that the conclusion about the coherence resonance shown in the simulation can be extended to a much wider category of time-delayed optical systems.

9.4 Simulated illustration of LFF

Although low-frequency fluctuations in laser diodes have been largely studied experimentally, there are very few reports of simulated LFF in the case of phase-conjugate feedback. Moreover, the cascade of bifurcations leading to LFF state is still unknown. A pioneering simulated evidence of LFF dynamics has been led by O'Brien *et al.* by simulation of the same Lang-Kobayashi system of equations for PCF as analyzed in this manuscript [51].

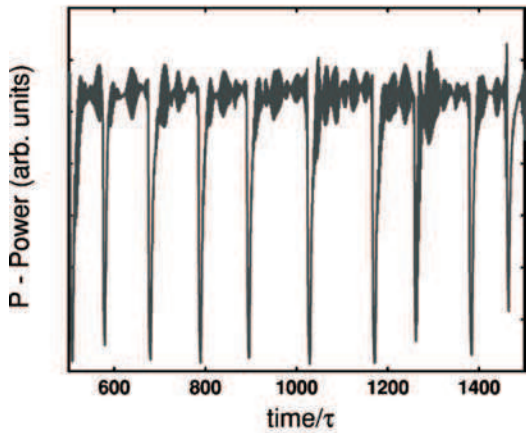

Figure 9.14: Simulated low-frequency fluctuations dynamics seen in the laser power filtered at the round-trip time τ. Picture from [51].

An illustration of LFF dynamics is presented in Fig.9.14. Yet LFF are seen for values of parameters out of physical range since the feedback ratio value corresponding to the trace in Fig.9.14 is $\gamma = 5$. Indeed, as we explained in chapter 4, 100% PCM reflectivity is reached for $\gamma = 0.256$.

We show here that a transition to LFF dynamics is also expected from the theory within a range of parameters closer to our experimental conditions. In the continuity of the simulations shown in the theoretical model in chapter 4, Fig.9.15 shows bifurcation diagrams in which we identify LFF dynamics.

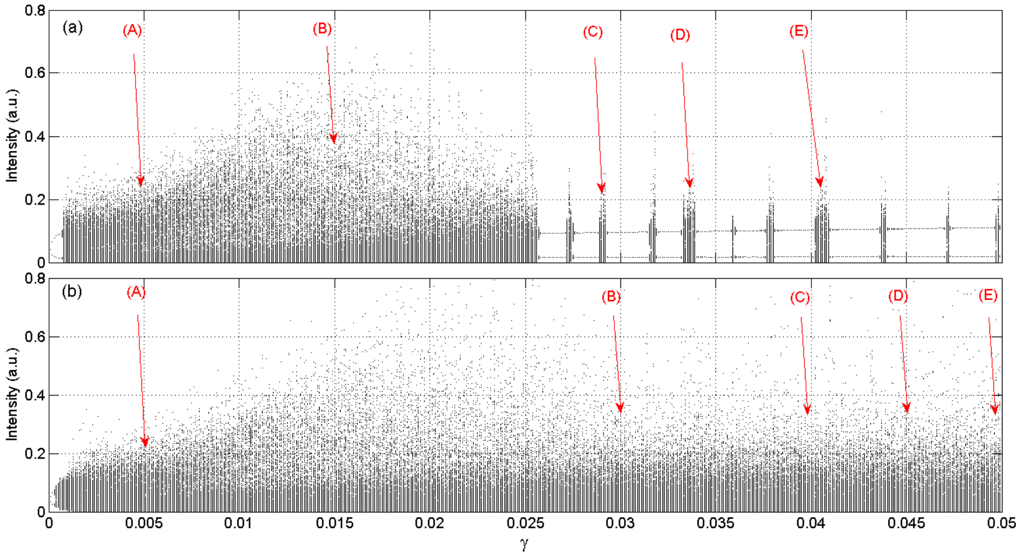

Figure 9.15: Bifurcation diagrams in which LFF dynamics are seen. The simulation parameters for diagram (a) are $P = 0.0417$, $T = 1428$, $\alpha = 3$ and $\theta = 3200$. In diagram (b), $P = 0.0417$, $T = 1428$, $\alpha = 5$ and $\theta = 3200$.

Diagram (a) in Fig.9.15 is calculated for the same parameters as Fig.4.1 except θ which has been changed to fit to the experimental time delay: $\theta = 3200 \Leftrightarrow \tau \simeq 4.5\ ns$. The related time traces and spectra –tagged from (A) to (E)– are presented in Fig.9.16 and show a transition to LFF dynamics when the feedback ratio increases. The time traces have been filtered at the delay θ. The transition to LFF is seen for reasonable values of γ. Indeed, the developed coherence collapse state displayed in trace (A) gives way to the first visible LFF dynamics (B) as γ reaches 0.015. Then, when the feedback ratio increases, the power dropouts dominate the laser dynamics and the time interval between consecutive dropouts gets larger (C), (D) and (E). The general shape of the time traces show the dynamical properties of typical LFF regime. Besides, we can see in the corresponding RF spectra the increase of the level of the low-frequency components, which are responsible for the transition from the coherence collapse state to sharp power dropouts. This trend is in accordance with the experimental traces of LFF that were presented in Fig.9.11.

The simulations however show a particular feature in comparison to the experiment. The comparison between Fig.9.4 (bottom) and Fig.9.16 (middle) shows that in the experiment the RF spectrum is made of peaks separated by 200 MHz (equivalent to $\frac{1}{\tau}$) while in the simulations the RF spectrum peaks are separated by 110 MHz (equivalent to $\frac{1}{2\tau}$). Although solutions pulsing at frequencies corresponding to double round-trip conditions have been theoretically predicted in PCF from an analysis of the standing waves [71, 90], such solutions are not possible in our Lang-Kobayashi equations that only account for single round-trip solutions. The reason is most probably to be found in a period-doubling bifurcation on the ECM solution before it bifurcates to chaotic LFF. However, a clear confirmation of this feature would require an analysis of the ECM bifurcations, *e.g.* with continuation techniques like in chapter 5.

Moreover, in contrast to the experiment, as displayed in Fig.9.15.(a), the LFF regime in simulations is seen within chaos bubbles interspaced by external cavity modes. This means that within each bubble of chaos a transition from the self-pulsing state characteristic of the ECM is destabilized in a chaotic dynamics with the properties of LFF dynamics presented in Fig.9.16. Experimentally, when LFF dynamics is observed, the laser operates in a continuous region of chaos without being interrupted by windows of ECMs.

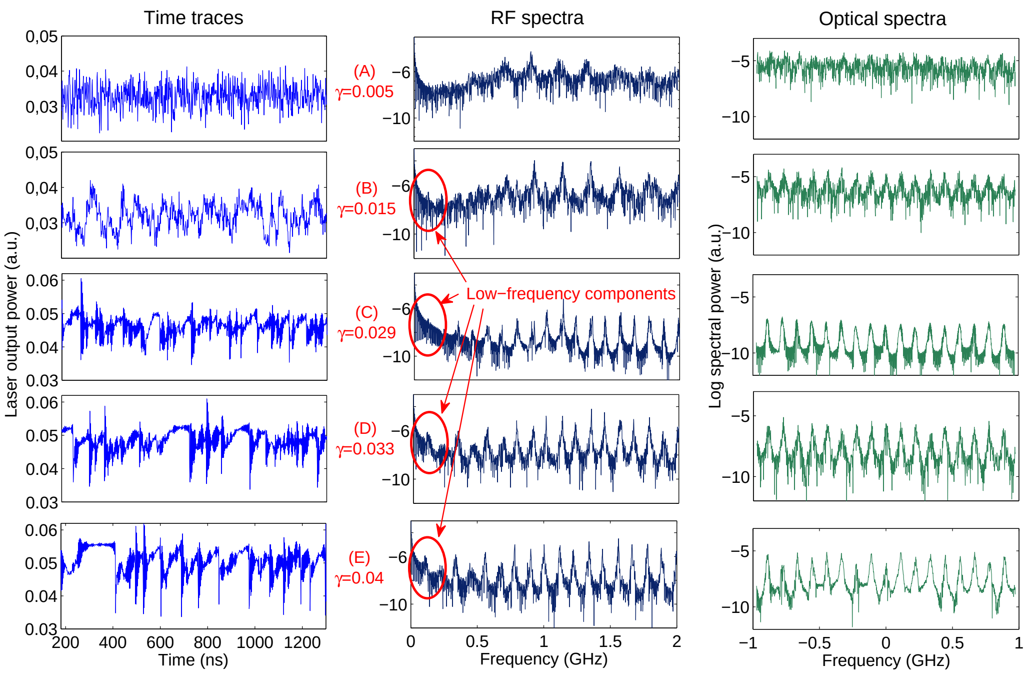

Figure 9.16: Simulated transition to LFF obtained for $P = 0.0417$, $T = 1428$, $\alpha = 3$ and $\theta = 3200$. Traces A to E refer to the tags in Fig.9.15.(a).

The bifurcation diagram in Fig.9.15.(b) brings theoretical illustration of

LFF dynamics closer to the experimental observation conditions. Indeed, by contrast to diagram (a), chaos is now extended to the whole feedback span. Therefore, it shows a transition to LFF in a continuous chaotic state without interruptions due to recoveries to pulsing ECMs. Diagram (b) is obtained by increasing α up to 5, compared to diagram (a). The corresponding transition to LFF is presented in Fig.9.17.

In the associated time traces and spectra, the transition from coherence collapse state to LFF dynamics is shown to occur for a value of γ larger than in the case of Fig.9.16 where $\alpha = 3$. Indeed, the transition becomes clear in trace B when $\gamma = 0.03$. The same dynamical properties as discussed in Fig.9.16 are visible: the fluctuations get stronger and the interval time between power dropouts gets larger when γ increases. Yet due to a higher value of α, dropouts are less sharp and the dynamics show more fuzzy fluctuations. The main spectral properties such as the increase in the level of the low-frequency components and the frequency spacing of the peaks are similar to the previous case.

This set of simulated parameters illustrates with good qualitative accordance the transition to LFF as seen experimentally. Indeed this transition occurs for physically reachable feedback ratios and the LFF are seen in a region of continuous chaos, without windows of periodic states.

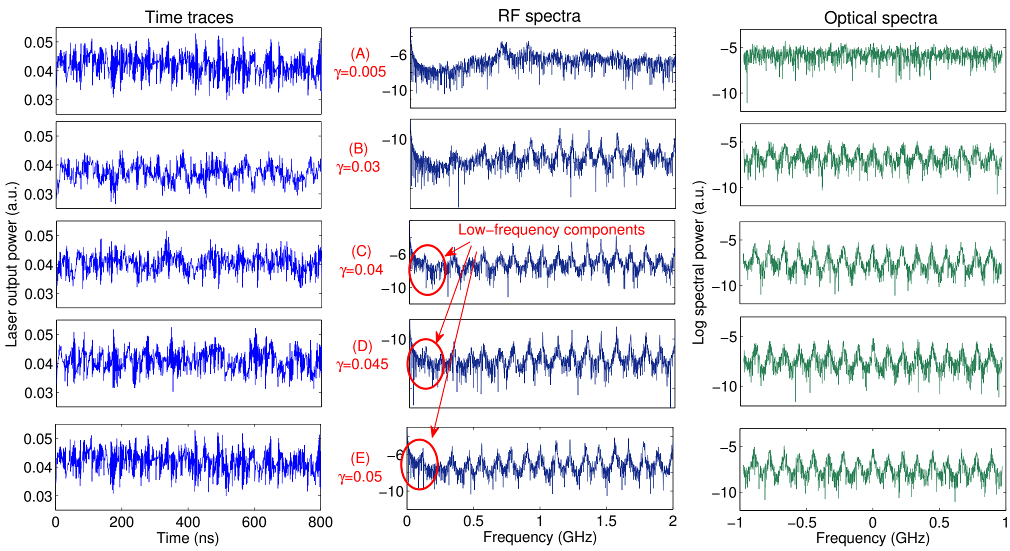

Figure 9.17: Simulated transition to LFF obtained for $P = 0.0417$, $T = 1428$, $\alpha = 5$ and $\theta = 3200$. Traces A to E refer to the tags in Fig.9.15.(b).

Those simulations aim at showing that there are configurations of parameters for which a theoretical prediction of LFF dynamics is possible. The main parameter that allows to see the LFF is the time delay. According to the value of θ, the simulations predict different dynamical states which support the experimental observations done for different external cavity lengths.

Since LFF dynamics can be observed in the simulation, it could be of interest to carry out a study about the deterministic delay-induced coherence resonance of LFF in the theoretical model as we reported in the experiment. However, the short range of parameters in which LFF are seen in our simulations does not allow such a relevant study. Our aim here is limited to show that this particular dynamics observed in the experiment is justified by a theoretical background using a set of parameters reasonably close to the physical ones.

9.5 Inverted LFF and burstups

Besides the common LFF state showing power dropouts, an inverted LFF dynamics, showing brutal power increases followed by gradual decreasing recoveries can also be observed. Yet these inverted LFF are very scarce and accounts in the literature are in very short supply. Pan *et al.* saw them in a semiconductor laser subject to moderate and strong conventional optical feedback in 1996 [49]. They have also been spotted in asymmetric laser diodes with different reflectivities in both facets [48]. Numerical calculations also predicted them in laser diodes with frequency-selective optical feedback [156], in multimode lasers with anticorrelated LFF dynamics [157] and in the power VCSELs of different polarization states [54]. In our experiment we also see evidence of this particular kind of LFF as shown in Fig.9.18. Yet this switching has been operated without any changes in the experiment compared to the previous study of the LFF.

The dynamics is pretty much the same as in the case of the common power dropouts: the shape and the time scale of the LFF packages show no difference except the fact that instead of brutal power dropouts, the laser power shows brutal power increases. However, a particular feature makes the transformation of inverted LFF into common LFF by a mere upside-down shifting operation impossible. Indeed in both cases the brutal power variations (either dropouts or increases) occur along with very intense power burstups. Those power burstups are made of very short pulses – therefore they need a high resolution scope to be detected– that appear along with each LFF package whether it be a power dropout or a power increase. These high-amplitude peaks preceding power bursts or dropouts are emphasized in Fig.9.19.

Compared to the standard LFF package, the inverted one (Fig.9.19.(b))

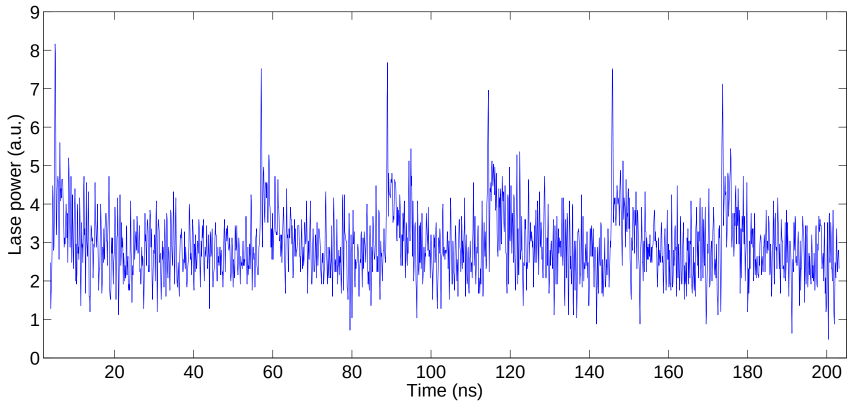

Figure 9.18: Experimental evidence of an inverted LFF time series.

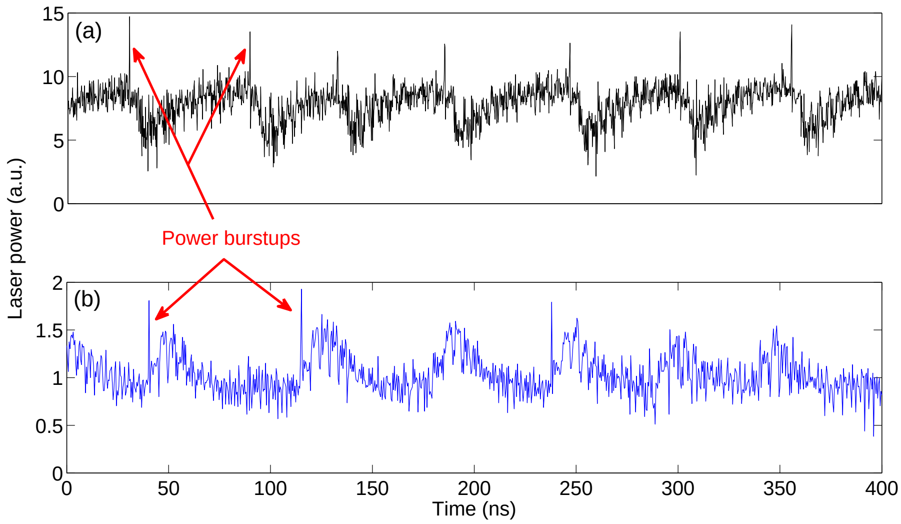

Figure 9.19: Comparison of the two kinds of LFF states. (a) is the common LFF trace showing power dropouts while (b) is the inverted LFF state showing power increases. In both cases the LFF packages show sharp and intense power burstups.

shows the same very short power burstup pulse with an inverted pulse package. An interesting feature could be the study of the burstups' occurrences. There is to our knowledge no account for their presence and for the scenario of bifurcations giving birth to them. Although we believe they always come along with the LFF packages, they might not have been spotted before due to the high temporal resolution required to see them. Indeed we measured the average HWHM of those burstups at about 300 ps.

9.6 Discussion

We have demonstrated here purely delay-induced and deterministic coherence resonance in the precise case of the chaotic low-frequency fluctuations (LFF) in a semiconductor laser with phase-conjugate feedback. This observation of low-frequency fluctuations is in good accordance with the simulations showing that the theory expects the laser to exhibit LFF dynamics. This is, to our knowledge, the first simulated evidence of low-frequency fluctuations for reasonable values of feedback. Yet a thorough theoretical study of LFF would be of great interest since the cascade of bifurcations leading to LFF and their evolution with the feedback ratio remain unexplored.

This experimental evidence of the appearance of low-frequency fluctuations in a chaotic laser with phase-conjugate feedback along with the study of the statistics of the time between power dropouts led to the demonstration of a new kind of coherence resonance. The originality of this study is that coherence resonance occurs without noise addition and also that the resonance parameter is the PCF ratio only, all other parameters such as the driving current are kept constant. Indeed, we saw that for an optimal amount of feedback ratio, the laser diode exhibits an optimal regularity of the time between slow power dropouts. This further confirms that the resonance is induced by the feedback strength only and is not related to any appropriate relationship between the system's time scale and the time delay.

We also saw that low-frequency fluctuations are not always characterized by power dropouts but can also show rapid power increases followed by slower decreases. This inverted LFF state appears much more scarcely and it was not possible to us to see them many times or to do a similar study as for the regular LFF with power dropouts. However when we saw inverted LFF they were not as easily destabilized as an external cavity mode could be. Indeed, changing the mirror reflectivity or the drive current would keep them still present at the scope. Indeed, they behave exactly as counterparts showing power dropouts. Thus they cannot be identified to mere transient oddities or noise-driven instabilities. The reason why sometimes inverted LFF appear instead of the regular ones is unknown to us. Under apparently identical experimental conditions they could show up and then never turn up again for a long time. To our knowledge there is no theoretical explanation to their appearance.

As we already mentioned previously in this chapter, we studied the LFF in the same range of reflectivities for which we studied the extreme events of chapter 8 and in which LFF were never seen. This is because the transition from fully developed chaos –which is the state in which we tackled the detection of extreme events– to the LFF state does not only depend on the feedback ratio but also on the effective external cavity length. Since L_{cav} is larger here (132 cm) than in chapter 8 (66 cm), our small reflectivity range –limited at about 7.5%– is enough to see the transition to LFF state. Yet, we have no experimental evidence of how this LFF state could evolve for higher values of R, even with this long cavity configuration.

Chapter 10
Conclusion and perspectives

What is a scientist after all? It is a curious man looking through a keyhole, the keyhole of nature, trying to know what's going on. Jacques-Yves Cousteau

Our study of nonlinear dynamics in laser diode subject to phase-conjugate feedback has unveiled several new theoretical and experimental results. We discuss here the resulting conclusions and perspectives for a further continuation of our work.

10.1 Summary of the results

The first main point was to design the experimental setup on which all our observations and measurements were based. We performed phase-conjugate feedback generation in a photorefractive semiconductor SPS crystal through both reflection and transmission gratings. PCM reflectivities up to about 8% are achieved with a laser diode power of 50 mW and with a build-up time of some milliseconds. The effects of very small values of PCF ratio on the laser properties have been evidenced in a reduction of the laser spectral width and of its current threshold.

We tackled then the theoretical study of the nonlinear laser dynamics through the exploitation of the Lang-Kobayashi system of equations adapted for the PCF case. After demonstrating accordance with other simulations carried out with different models, we extended the analysis of the laser dynamics to longer feedback ratio values. We showed that the laser may exhibit chaos crisis, characterized by a gradual shrinkage of the regions of chaos as the feedback ratio increases, resulting in chaos suppression. This phenomenon is also at the origin of bistability between external cavity modes that are self-pulsing solutions which frequency can possibly reach several tens of GHz when increasing the feedback ratio.

For small values of the external cavity length, we showed evidence of self-pulsing external cavity modes along with the bifurcation cascade that stabilize and destabilize them. The spectral signature of the delay initiates the transition from chaos to a stable ECM which further undergoes period multiplying and gives way to the next stable ECM. Moreover, the frequency detuning between consecutive ECMs equals the external cavity frequency.

If the feedback rate is further increased, the dynamics qualitatively changes making the self-pulsing ECMs unstable and transition to chaos occur. In this chaotic dynamics we have identified and characterized the presence of extreme events in the laser power. Extreme events are of two kinds: lone peaks (group I) and bunches of pulses at the delay time scale (group II). As the phase-conjugate mirror reflectivity increases, the ratio of extreme events is modified, showing a higher impact of the time scale of the delayed feedback on the elapsed time between successive extreme events. The mirror reflectivity controls the evolution of the extreme events, from their birth until their transition to another dynamical solution.

The transition to the low-frequency fluctuation regime is triggered by the feedback ratio. The chaotic fluctuations of the laser corresponding to a fully coherence collapse state organize themselves in power dropouts at a frequency much smaller than the external cavity frequency. Under the effect of the feedback ratio, the power dropouts undergo coherence resonance, *i.e.* the property to show optimal response to the system's own time scale. This resonance is achieved under the sole effect of the feedback ratio without current or external noise modulation. As a consequence we termed this phenomenon "feedback-induced deterministic coherence resonance".

Fig.10.1 summarizes in a bifurcation diagram the intervals of feedback in which the various dynamics can be seen. Experimentally, the transition between dynamics of qualitatively different dynamics are enabled by a variation of the feedback ratio. Yet we also insisted in the importance of the feedback delay which is a parameter that can be tuned as well as the feedback ratio in order to favor the stabilization of a particular dynamics, especially when working with a physically limited feedback range.

10.2 Consequences and novel contributions

In chapters 4 and 6, the theoretical studies have both confirmed and extended the Lang-Kobayashi system of rate equations adapted for PCF –equations (4.1)– for the analysis of a laser subject to PCF. The extension to higher feedback values unveiled a route to chaos suppression and ECM bistability.

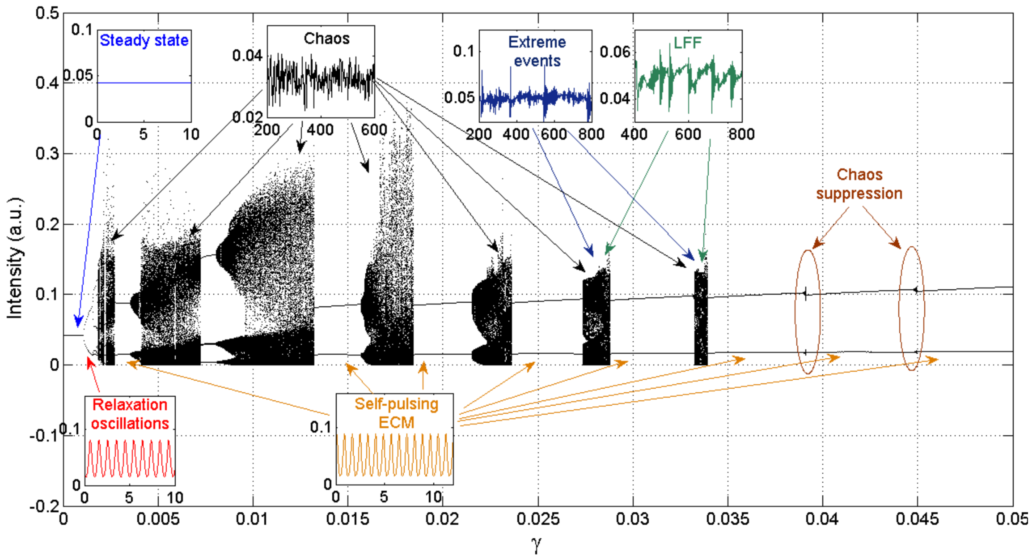

Figure 10.1: Bifurcation diagram summarizing the repartition of the dynamical states. The simulation parameters are $P = 0.0417$, $T = 1428$, $\alpha = 3$ and $\theta = 476$.

In addition to this, the experiment has also shown main novelties. First, the generation of phase-conjugate feedback with a SPS crystal in a self-pumped ring cavity in order to exhibit nonlinear dynamics in a laser diode is a new configuration. Then, we showed the first experimental observation of self-pulsing external cavity modes at different frequencies. This brings a major illustration and confirmation of the theoretical predictions carried out for years in this field.

We also have highlighted main differences compared to the conventional optical feedback case. Indeed the presence self-pulsing external cavity modes at frequencies multiples of f_{cav} is a characteristic of the PCF dynamics that cannot be seen in the COF case. The theoretical study extended to higher values of feedback which predicts chaos suppression and the resulting ECM bistability is also a major difference with the COF case. More specifically, we pointed out the crucial importance of the feedback rate and the feedback delay. A judicious configuration of those two parameters allows the laser to switch from one dynamical state to another. This property is a step towards control of chaos and self-pulsing laser tunability.

In chapter 7 the comparative presentation of the four possible pulsing states in a laser diode (undamped relaxation oscillations, mode locking, beating between ECMs in the case of COF and self-pulsing ECMs in PCF) led us to an interesting result. Each pulsing state has its own spectral characteristic and is discriminated by the signature of the external cavity delay in the optical spectrum. We identified the fundamental differences between these pulsing states and therefore we emphasized that the self-pulsing dynamics obtained with PCF is fundamentally different from any previously reported case of self pulsation in a laser diode with optical feedback.

A laser diode with phase-conjugate feedback is a delayed nonlinear system in which the dynamics is ruled by two fundamental parameters that determine the operating point. The feedback delay through the external cavity length and the feedback ratio through the phase-conjugate mirror reflectivity are the two parameters that decide of the operating state of the laser. Fig.10.2 displays in a 3-dimension mapping the evolution of the bifurcation diagram as γ and θ vary.

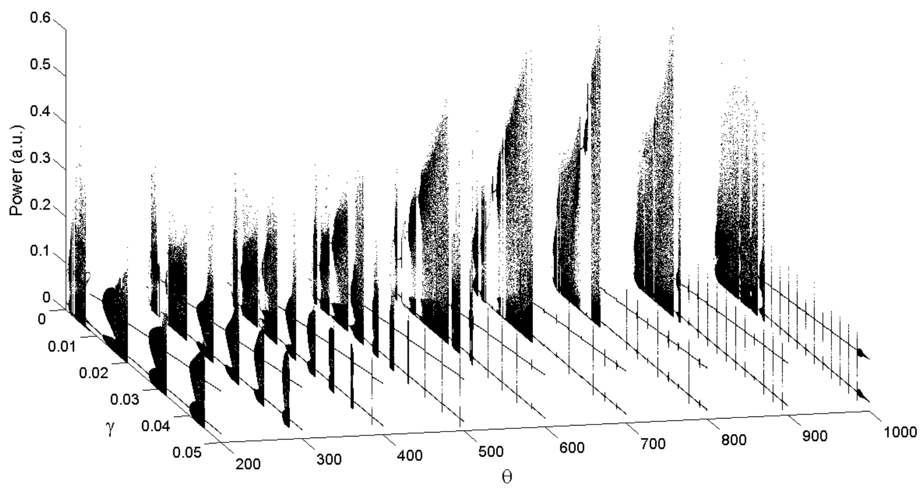

Figure 10.2: Cascade of bifurcations and dynamical operating states as a function of γ and θ. The simulation parameters are $P = 0.0417$, $T = 1428$ and $\alpha = 3$. For a given value of θ, if γ varies, the usual bifurcation cascade through a succession of self-pulsing ECMs and chaos is observed. Then, if θ increases, the bifurcation points drift towards the smaller values of γ.

With a simple theoretical model, we had the opportunity to account for many dynamical operating states. Moreover, the simulations that we present always show good qualitative accordance with the experimental observations.

This experiment also proved that generating a phase-conjugate feedback from a SPS crystal in a ring cavity loop is possible and suitable to the study of the nonlinear dynamics of semiconductor lasers. This material shows sufficient gain properties to be fruitfully used to generate PCF without the need for an external electric field.

10.3 Perspectives for a future work

There are still several points of interest to be addressed, though. They concern both theoretical extension of the model and experimental characterizations.

Thorough theoretical study of the extreme events and coherence resonance of LFF

In chapters 8 and 9, we showed simulated evidence of extreme events and low-frequency fluctuations. Yet, we did not go further in the analysis of the bifurcation cascade that unveils those dynamics and their evolution. Showing that the model predicts the existence of those two particular dynamical states is sufficient to bring legitimate confirmation to our experiment. Yet, studying the evolution of the extreme events and LFF with γ could result in the discovery of the bifurcation mechanisms that give birth to them. Moreover we expect that the experimental behaviors that we identified such as the evolution of extreme events of group I and II and the signature of a coherence resonance of LFF dynamics could be unveiled with a detailed theoretical study. Continuation methods may prove appropriate to identify the transitions to these dynamics.

Taking into account the finite mirror response in the model

As we mentioned in chapter 4, our simple simulated model of the Lang-Kobayashi system of equations does not take the PCF build-up time into account, considering that the PCM has instantaneous response time. Since it allows to work with much simpler equations that have until now shown good accordance with experimental results, few publications have addressed the question of integrating the mirror response time. However, we believe that taking into account the PCF build-up time scale in the equations could unveil different bifurcation scenarios according to the response time. In particular the values of feedback ratios for which the bifurcations occur could show better accordance with experimental values and the transition from a short-cavity configuration to a long-cavity configuration could be better understood.

Along with the theoretical study of the influence of the mirror response time, its experimental counterpart also deserves attention. The research of new materials to perform phase conjugation showing new build-up time scales and gain properties could also be motivated by a developing theoretical research in the field. A mapping of the various suitable media to generate PCF with their properties could bring a solid foundation to the state of the art of the phase-conjugation generation techniques.

Experimental traces still unclarified

Among the wealthy dynamical states that were observed in our experiment, there are still some to which we could bring no physical explanation about their origin due to either uncertain experimental observation conditions or to a too quick transition to a different dynamics. We present in Fig.10.3 two samples of periodic states exhibiting short pulses or groups of pulses.

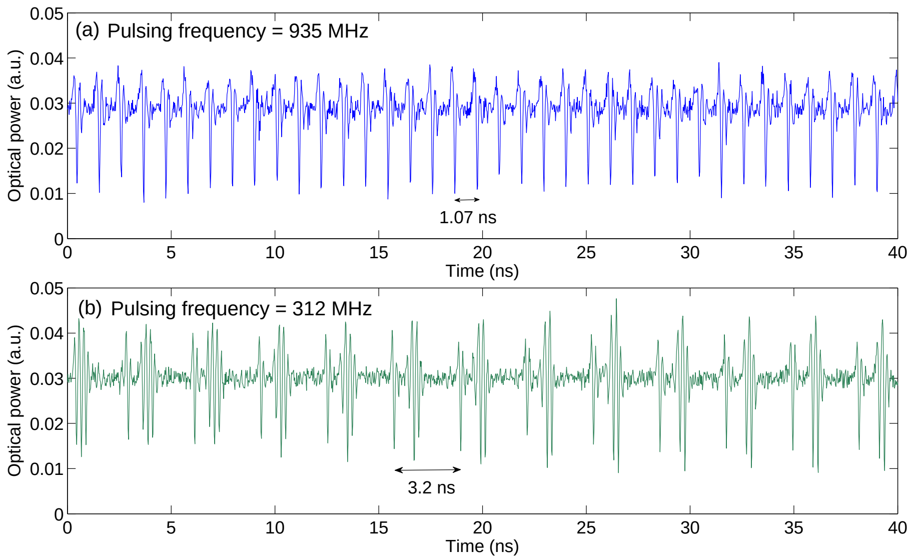

Figure 10.3: Pulsing states observed in the experiment. Trace (a) pulsing at 935 MHz and (b) at 312 MHz were seen for the same experimental configuration as the traces presented in Fig.6.8.

Traces (a) and (b) were seen for the same experimental conditions as the traces displayed in Fig.6.8. Although we are not sure of the mechanism that led to those traces due to a lack of experimental repeatability, a careful look into the two traces suggests that trace (b) in Fig.10.3 could be originated from a period tripling operated upon trace (a). Yet, the shape of the pulses are not the same as the ones presented in Fig.6.8. Indeed the pulses in Fig.6.8 were centered on the mean power value –with power burstups as intense as dropouts– while the pulses presented in Fig.10.3 show mostly power dropouts. Therefore we cannot conclude on an potential scenario of bifurcation leading to trace (b). It might also be totally independent from trace (a). At first look, both traces resemble excitable pulse trains, either of the simple pulse or the multiple pulse types that have been largely discussed in the case of laser diodes with optical injection. Excitable pulses have been theoretically predicted by Wieczorek *et al.* [158] in the PCF case and our experiment might have resolved one of such excitable dynamics.

Control of chaos and applications

Chaos applications such as optical cryptography and random number generation are up-to-date applications using laser diodes with optical feedback. Through our study of the nonlinear dynamics of a laser diode with phase-conjugate feedback we have made a further step in the direction of chaos control. Indeed, with the experimental reports on self-pulsing ECMs that follow the trend predicted by the simulated model one may think of performing generation of optical frequency-tunable pulsing states. We can imagine to design a tunable source of optical pulses at high frequencies where, by merely changing the feedback ratio, the frequency selection could be operated. And naturally, the physical origin of the pulses would be then the excitation of self-pulsing external cavity modes of a laser diode with phase-conjugate feedback.

By contrast to the techniques using electrical modulation, an accurate control of the PCF delay and ratio can make the laser exhibit either harmonic oscillations or train of pulses at high frequencies. The challenge is to be able to master the laser dynamical states in order to change it into a tunable optical source at frequencies much higher that the boundary imposed by the relaxation oscillations which restricts the electrical modulation frequency, hardly reaching 10 GHz. High-speed applications in the field of optical communications motivate the research in this field.

Bibliography

[1] T.H. Maiman, "Stimulated optical radiation in ruby", *Nature*, vol. 187, pp. 493–494, 2002.

[2] J. Gleick, *Chaos: Making a New Science*, Vintage, 1987.

[3] H. Kroemer, "A proposed class of hetero-junction injection lasers", *Proceedings of the IEEE*, vol. 51, pp. 1782–1783, 1963.

[4] A. Yariv, *Quantum Electronics*, Wiley, 1988.

[5] A.K. Dutta, H. Kosaka, K. Kurihara, Y. Sugimasa, and K. Kasahara, "High-speed VCSEL of modulation bandwidth over 7.0 GHz and its application to 100 m PCF datalink", *Journal of Lightwave Technology*, vol. 16, pp. 870–875, 1998.

[6] G.T. Liu, A. Stintz, H. Li, K.J. Malloy, and L.F. Lester, "Extremely low room-temperature threshold current density diode lasers using InAs dots in $\mathrm{I}n_{0.15}\mathrm{G}a_{0.85}\mathrm{A}s$ quantum well", *Electronics Letters*, vol. 35, pp. 1163–1165, 1999.

[7] M.T. Crowley, N.A. Naderi, H. Su, F. Grillot, and L.F. Lester, "Gaas-based quantum dot lasers", *Semiconductors and Semimetals: Advances in Semiconductor Lasers*, vol. 86, pp. 371–417, 2012.

[8] O. Svelto, *Principles of Lasers*, Springer, 2010.

[9] O. Hess, S.W. Koch, and J.V. Moloney, "Filamentation and beam propagation in broad-area semiconductor lasers", *IEEE Journal of Quantum Electronics*, vol. 31, pp. 35–43, 1995.

[10] J.R. Marciante and G.P. Agrawal, "Nonlinear mechanisms of filamentation in broad-area semiconductor lasers", *IEEE Journal of Quantum Electronics*, vol. 32, pp. 590–596, 1996.

[11] J.H. Gurian, H. Maeda, and T.F. Gallagher, "Kilohertz dye laser system for high resolution laser spectroscopy", *Review of Scientific Instruments*, vol. 81, pp. 073111, 2010.

[12] D.M. Kane and K.A. Shore, *Unlocking dynamical diversity*, Wiley, 2005.

[13] M. Lax, "Classical noise. v. noise in self-sustained oscillators", *Physical Review*, vol. 16, pp. 290–307, 1967.

[14] C.H. Henry, "Theory of the linewidth of semiconductor lasers", *IEEE Journal of Quantum Electronics*, vol. 18, pp. 259–264, 1982.

[15] C. Masoller, "Implications of how the linewidth enhancement factor is introduced on the Lang and Kobayashi model", *IEEE Journal of Quantum Electronics*, vol. 33, pp. 793–803, 1997.

[16] J. Ohtsubo, *Semiconductor Lasers: Stability, Instability and Chaos*, Springer Series in Optical Sciences, 2006.

[17] F.T. Arecchi, G.L. Lippi, G.P. Puccioni, and J.R. Tredicce, "Deterministic chaos in laser with injected signal", *Optics Communications*, vol. 51, pp. 308–314, 1984.

[18] J.R. Tredicce, F.T. Arecchi, G.L. Lippi, and G.P. Puccioni, "Instabilities in lasers with an injected signal", *Journal of the Optical Society of America B*, vol. 2, pp. 173–183, 1985.

[19] G.H.M van Tartwijk and D. Lenstra, "Semiconductor lasers with optical injection and feedback", *Quantum Semiclassical Optics*, vol. 7, pp. 87, 1995.

[20] K. Petermann, "External optical feedback phenomena in semiconductor lasers", *IEEE J. Sel. Top. Quantum Electron.*, vol. 1, pp. 480–489, 1995.

[21] L. Goldberg, H.F. Taylor, A. Dandridge, J.F. Weller, and R.O. Miles, "Spectral characteristics of semiconductor lasers with optical feedback", *IEEE Transactions on Microwave Theory and Techniques*, vol. 30, pp. 401–410, 1982.

[22] J. Osmundsen and N. Gade, "Influence of optical feedback on laser frequency spectrum and threshold conditions", *IEEE Journal of Quantum Electronics*, vol. 19, pp. 465–469, 1983.

[23] D.R. Hjelme, A.R. Mickelson, and R.G. Beausoleil, "Semiconductor laser stabilisation by external optical feedback", *IEEE Journal of Quantum Electronics*, vol. 27, pp. 352–372, 1991.

[24] M.W. Fleming and A. Mooradian, "Spectral characteristics of external-cavity controlled semiconductor lasers", *IEEE Journal of Quantum Electronics*, vol. 17, pp. 44–59, 1981.

[25] F. Favre, D. Le Guen, and J. Simon, "Optical feedback effects upon laser diode oscillation field spectrum", *IEEE Journal of Quantum Electronics*, vol. 18, pp. 1712–1717, 1982.

[26] S. Sampei, H. Tsuchida, M. Ohtsu, and T. Tako, "Frequency stabilization of $AlGaAs$ semiconductor lasers with external grating feedback", *Japanese Journal of Applied Physics*, vol. 22, pp. 258–260, 1983.

[27] H.R. Telle, "Narrow linewidth laser diodes with broad continuous tuning range", *Applied Physics B*, vol. 49, pp. 217–226, 1989.

[28] R.W. Tkach and A.R. Chraplyvy, "Regimes of feedback effects in 1.5 μm distributed feedback lasers", *Journal of Lightwave Technology*, vol. 4, pp. 1655–1661, 1986.

[29] J. Mørk, M. Semkow, and B. Tromborg, "Measurement and theory of mode hopping in external cavity lasers", *Electronics Letters*, vol. 26, pp. 609–610, 1990.

[30] J. Wang and K. Petermann, "Noise analysis of semiconductor lasers within the coherence collapse regime", *IEEE Journal of Quantum Electronics*, vol. 27, pp. 3–9, 1991.

[31] O. Hirota and Y. Suematsu, "Noise properties of injection lasers due to reflected waves", *IEEE Journal of Quantum Electronics*, vol. 15, pp. 142–149, 1979.

[32] K.E. Stubkjaer and M.B. Small, "Noise properties of semiconductor lasers due to optical feedback", *IEEE Journal of Quantum Electronics*, vol. 20, pp. 472–478, 1984.

[33] P. Spano, S. Piazzolla, and M. Tamburrini, "Theory of noise in semiconductor lasers in the presence of optical feedback", *IEEE Journal of Quantum Electronics*, vol. 20, pp. 350–357, 1984.

[34] T. Kanada and K. Nawata, "Injection laser characteristics due to reflected optical power", *IEEE Journal of Quantum Electronics*, vol. 15, pp. 559–565, 1979.

[35] A.P. Bogatov, P.G. Eliseev, L. Ivanov, A.S. Logginov, M.A. Manko, and K. Senatorov, "Study of the single-mode injection laser", *IEEE Journal of Quantum Electronics*, vol. 9, pp. 392–394, 1973.

[36] C. Voumard, R. Salathé, and H. Weber, "Resonance amplifier model describing diode lasers coupled to short external resonators", *Applied Physics*, vol. 12, pp. 369–378, 1977.

[37] L. Goldberg, H.F. Taylor, A. Dandridge, J.F. Weller, and R.O. Miles, "Spectral characteristics of semiconductor lasers with optical feedback", *IEEE Journal of Quantum Electronics*, vol. 18, pp. 555–564, 1982.

[38] G.P. Agrawal, "Line narrowing in a single mode injection laser due to external optical feedback", *IEEE Journal of Quantum Electronics*, vol. 20, pp. 468–471, 1984.

[39] Y.C. Chen, "Phase noise characteristics of single mode semiconductor lasers with optical feedback", *Applied Physics Letters*, vol. 44, pp. 10–12, 1984.

[40] J. Mørk, B. Tromborg, and J. Mark, "Chaos in semiconductor lasers with feedback: theory and experiment", *IEEE Journal of Quantum Electronics*, vol. 28, pp. 93–108, 1992.

[41] H. Li, J. Ye, and J.G. McInerney, "Detailed analysis of coherence collapse in semiconductor lasers", *IEEE Journal of Quantum Electronics*, vol. 29, pp. 2421–2432, 1993.

[42] J.S. Cohen, R.R. Drenten, and B.H. Verbeeck, "The effect of optical feedback on the relaxation oscillation in semiconductor lasers", *IEEE Journal of Quantum Electronics*, vol. 24, pp. 1989–1995, 1988.

[43] C.H. Henry and R.F. Kazarinov, "Instability of semiconductor lasers due to optical feedback from distant reflectors", *IEEE Journal of Quantum Electronics*, vol. 22, pp. 294–301, 1986.

[44] H. Sato, T. Fujita, and K. Fujito, "Intensity fluctuation in semiconductor lasers coupled to external cavity", *IEEE Journal of Quantum Electronics*, vol. 21, pp. 46–51, 1985.

[45] B. Tromborg, J. Osmundsen, and H. Olesen, "Stability analysis for a semiconductor laser in an external cavity", *IEEE Journal of Quantum Electronics*, vol. 20, pp. 1023–1032, 1984.

[46] D. Lenstra, B. Verbeek, and A. Den Boef, "Coherence collapse in single-mode semiconductor lasers due to optical feedback", *IEEE Journal of Quantum Electronics*, vol. 21, pp. 674–679, 1985.

[47] J. Py O. Gauthier-Lafaye V. Voiriot F. Grillot, B. Thedrez and J.L. Lafragette, "2.5-gb/s transmission characteristics of 1.3μ m dfb lasers with external optical feedback", *IEEE Photonics Technology Letters*, vol. 14, pp. 101–103, 2002.

[48] F. de Tomasi, E. Cerboneschi, and E. Arimondo, "Asymmetric pulse shape in the LFF instabilities of a semiconductor laser with optical feedback", *IEEE Journal of Quantum Electronics*, vol. 30, pp. 2277–2280, 1994.

[49] M-W. Pan, B-P. Shi, and G.R. Gray, "Semiconductor laser dynamics subject to strong optical feedback", *Optics Letters*, vol. 22, pp. 166–168, 1997.

[50] G.H.M. van Tartwijk, A.M. Levine, and D. Lenstra, "Sisyphus effect in semiconductor lasers with optical feedback", *IEEE Journal of Quantum Electronics*, vol. 1, pp. 466–472, 1995.

[51] D. O'Brien, G. Huyet, and J.G. McInerney, "Low-frequency fluctuations in a semiconductor laser with phase conjugate feedback", *Physical Review A*, vol. 64, pp. 025802, 2001.

[52] T. Heil, I. Fischer, W. Elsäßer, and A. Gavrielides, "Dynamics of semiconductor lasers subject to delayed optical feedback: The short cavity regime", *Physical Review Letters*, vol. 87, pp. 243901, 2001.

[53] A. Tabaka, K. Panajotov, I. Veretennicoff, and M. Sciamanna, "Bifurcation study of regular pulse packages in laser diodes subject to optical feedback", *Physical Review E*, vol. 70, pp. 036211, 2004.

[54] M. Sciamanna, C. Masoller, N.B. Abraham, F. Rogister, P. Mégret, and M. Blondel, "Different regimes of low-frequency fluctuations in vertical-cavity surface-emitting lasers", *Journal of the Optical Society of America B*, vol. 20, pp. 37–44, 2003.

[55] A.M Yacomotti, M.C. Eguia, J. Aliaga, O.E. Martinez, G.B. Mindlin, and A. Lipsich, "Interspike time distribution in noise driven excitable systems", *Physical Review Letters*, vol. 83, pp. 292–295, 1999.

[56] G. Giacomelli, M. Giudici, S. Balle, and J. Tredicce, "Experimental evidence of coherence resonance in an optical system", *Physical Review Letters*, vol. 84, pp. 3298–3301, 2000.

[57] R. Lang and K. Kobayashi, "External optical feedback effects on semiconductor injection laser properties", *IEEE Journal of Quantum Electronics*, vol. 16, pp. 347–355, 1980.

[58] B.J. Thedrez and C.H. Lee, "A reassessment of standard rate equations for low facet reflectivity semiconductor lasers using travelling wave equations", *IEEE Journal of Quantum Electronics*, vol. 28, pp. 2706–2713, 1992.

[59] V. Annovazzi-Lodi, S. Donati, and M. Manna, "Chaos and locking in a semiconductor laser due to external injection", *IEEE Journal of Quantum Electronics*, vol. 30, pp. 1537–1541, 1994.

[60] A. Hohl and A. Gavrielides, "Bifurcation cascade in a semiconductor laser subject to optical feedback", *Physical Review Letters*, vol. 82, pp. 1148–1151, 1999.

[61] J. Ohtsubo, "Feedback induced instability and chaos in semiconductor lasers and their applications", *Optical Review*, vol. 6, pp. 1–15, 1999.

[62] T. Erneux, A. Gavrielides, and M. Sciamanna, "Stable microwave oscillations due to external-cavity-mode beating in laser diodes subject to optical feedback", *Physical Review A*, vol. 66, pp. 33809, 2002.

[63] M. Sciamanna, *Nonlinear dynamics and polarization properties of externally driven semiconductor lasers*, PhD thesis, Faculté Polytechnique de Mons, Mons, Belgium, 2004.

[64] S. Sivaprakasam, R. Saha, P.A. Lakshmi, and R. Singh, "Mode hopping in external-cavity diode lasers", *Optics Letters*, vol. 21, pp. 411–413, 1996.

[65] J. Mørk, J. Mark, and B. Tromborg, "Route to chaos and competition between relaxation oscillations for a semiconductor laser with optical feedback", *Physical Review Letters*, vol. 65, pp. 1999–2002, 1990.

[66] G.R. Gray, D. Huang, and G.P. Agrawal, "Chaotic dynamics of semiconductor lasers with phase-conjugate feedback", *Physical Review A*, vol. 49, pp. 2096–2105, 1994.

[67] P. Yeh, *Introduction to Photorefractive Nonlinear Optics*, Wiley, 1993.

[68] R.C. Lind and D.G. Steel, "Demonstration of the longitudinal modes and aberration-correction properties of a continuous-wave dye laser

with a phase-conjugate mirror", *Optics Letters*, vol. 6, pp. 554–556, 1981.

[69] J. Feinberg, "Self-pumped, continuous-wave conjugator using internal reflection", *Optics Letters*, vol. 7, pp. 486–488, 1982.

[70] G.H.M. van Tartwijk, H.J.C. van der Linden, and D. Lenstra, "Theory of a diode laser with phase-conjugate feedback", *Optics Letters*, vol. 17, pp. 1590–1592, 1992.

[71] E. Bochove, "Theory of a semiconductor laser with phase-conjugate optical feedback", *Physical Review A*, vol. 55, pp. 3891–3899, 1997.

[72] B. Krauskopf, G.R. Gray, and D. Lenstra, "Semiconductor laser with phase-conjugate feedback: dynamics and bifurcations", *Physical Review E*, vol. 58, pp. 7190–7197, 1998.

[73] D.H. DeTienne, G.R. Gray, G.P. Agrawal, and D. Lenstra, "Semiconductor laser dynamics for feedback from a finite-penetration-depth phase-conjugate mirror", *IEEE Journal of Quantum Electronics*, vol. 33, pp. 838–844, 1997.

[74] W.A. van der Graaf, L. Pesquera, and D. Lenstra, "Stability of a diode laser with phase-conjugate feedback", *Optics Letters*, vol. 23, pp. 256–258, 1998.

[75] T. Erneux, A. Gavrielides, K. Green, and B. Krauskopf, "External cavity modes of semiconductor lasers with phase-conjugate feedback", *Physical Review E*, vol. 68, pp. 066205, 2003.

[76] T. Bach, M. Jazbinšek, G. Montemezzani, P. Günter, A.A. Grabar, I.M. Stoika, and Y.M. Vysochanskii, "Enhanced near-infrared photorefractive properties of Te-doped $Sn_2P_2S_6$", in *Proceedings of SPIE*, 2006, pp. 625208–1.

[77] M. Jazbinšek, D. Haertle, G. Montemezzani, P. Günter, A.A. Grabar, I.M. Stoika, and Y.M. Vysochanskii, "Wavelength dependence of visible and near-infrared photorefraction and phase conjugation in $Sn_2P_2S_6$", *Journal of the Optical Society of America B*, vol. 22, pp. 2459–2467, 2005.

[78] M. Cronin-Golomb and C.D. Brandle, "Ring self-pumped phase conjugator using total internal reflection in photorefractive strontium barium niobate", *Optics Letters*, vol. 14, pp. 462–464, 1989.

[79] O.K. Andersen, A.P.A. Fischer, I.C. Lane, E. Louvergneaux, S. Stolte, and D. Lenstra, "Experimental stability diagram of a diode laser subject to weak phase-conjugate feedback from a rubidium vapor cell", *IEEE Journal of Quantum Electronics*, vol. 35, pp. 577–582, 1999.

[80] J.S. Lawrence and D.M Kane, "Contrasting conventional optical and phase-conjugate feedback in laser diodes", *Physical Review A*, vol. 63, pp. 033805, 2001.

[81] K. Green and B. Krauskopf, "Bifurcation analysis of a semiconductor laser subject to non-instantaneous phase-conjugate feedback", *Optics Communications*, vol. 231, pp. 383–393, 2004.

[82] M. Virte, A. Karsaklian Dal Bosco, M. Sciamanna, and D. Wolfersberger, "Chaos crisis and bistability of self-pulsing dynamics in a laser diode with phase-conjugate feedback", *Physical Review A*, vol. 84, pp. 043836, 2011.

[83] M. Cronin-Golomb, K.Y. Lau, and A. Yariv, "Infrared photorefractive passive phase conjugation with $BaTiO_3$: Demonstrations with $GaAlAs$ and 1.09-μm Ar^+ lasers", *Applied Physics Letters*, vol. 47, pp. 567–569, 1985.

[84] G.R. Gray, D.H. DeTienne, and G.P. Agrawal, "Mode locking in semiconductor lasers by phase-conjugate optical feedback", *Optics Letters*, vol. 20, pp. 1295–1297, 1995.

[85] E. Miltényi, M.O. Ziegler, M. Hofmann, J. Sacher, W. Elsäßer, E.O. Göbel, and D.L. MacFarlane, "Long-term stable mode locking of a visible diode laser with phase-conjugate feedback", *Optics Letters*, vol. 20, pp. 734–736, 1995.

[86] G. Klose and A. Siahmakoun, "External mode locking with feedback from a self-pumped phase-conjugator $BaTiO_3$ mirror", *Optical Engineering*, vol. 35, pp. 2983–2988, 1996.

[87] P. Kürz and T. Mukai, "Frequency stabilization of a semiconductor laser by external phase-conjugate feedback", *Optics Letters*, vol. 21, pp. 1369–1371, 1996.

[88] A. Shiratori and M. Obara, "Wavelength-stable, narrow-spectral-width oscillation of an algainp diode laser coupled to a $BaTiO_3 : Co$ stimulated photorefractive backscattering phase conjugator", *Applied Physics B*, vol. 65, pp. 329–333, 1997.

[89] N. Cyr, M. Breton, M. Têtu, and S. Thériault, "Laser diode frequency control by resonant phase-conjugate reflection from an atomic vapour", *Optics Letters*, vol. 16, pp. 1298–1300, 1991.

[90] L. Petersen, U. Gliese, and T.N. Nielsen, "Phase noise reduction by self-phase locking in semiconductor lasers using phase conjugate feedback", *IEEE Journal of Quantum Electronics*, vol. 30, pp. 2526–2533, 1994.

[91] B.W. Liby and D. Statman, "Controling the linewidth of a semiconductor laser with photorefractive phase conjugate feedback", *IEEE Journal of Quantum Electronics*, vol. 32, pp. 835–838, 1996.

[92] M. Ohtsu, I. Koshiishi, and Y. Teramachi, "A semiconductor laser as a stable phase conjugate mirror for linewidth reduction of another semiconductor laser", *Japanese Journal of Applied Physics*, vol. 29, pp. 2060–2062, 1990.

[93] K. Vahala, K. Kyuma, A. Yariv, S-K. Kwong, M. Cronin-Golomb, and K.Y. Lau, "Narrow linewidth, single frequency semiconductor laser with a phase conjugate external cavity mirror", *Applied Physics Letters*, vol. 49, pp. 1563–1565, 1986.

[94] A. Shiratori and M. Obara, "Frequency stable, narrow linewidth oscillation of a red diode laser with phase conjugate feedback using stimulated photorefractive backscattering", *Applied Physics Letters*, vol. 69, pp. 1515–1516, 1996.

[95] G.P. Agrawal and J.T. Klaus, "Effect of phase-conjugate feedback on semiconductor laser dynamics", *Optics Letters*, vol. 16, pp. 1325–1327, 1991.

[96] W.A. Kuperman, W.S. Hodgkiss, H.C. Song, T. Akal, C. Ferla, and D.R. Jackson, "Phase conjugation in the ocean: Experimental demonstration of an acoustic time-reversal mirror", *Journal of the Acoustical Society of America*, vol. 103, pp. 25–40, 1998.

[97] M. Lucente, G.M. Carter, and J.G. Fujimoto, "Nonlinear mixing and phase conjugation in broad-area diode lasers", *Applied Physics Letters*, vol. 53, pp. 467–469, 1988.

[98] P. Kürz, R. Nagar, and T. Mukai, "Highly efficient phase conjugation using spatially nondegenerate four-wave mixing in a broad-area laser diode", *Applied Physics Letters*, vol. 68, pp. 1180–1182, 1996.

[99] P.P. Vasil'ev and I.H. White, "Phase-conjugation broad area twin-contact semiconductor laser", *Applied Physics Letters*, vol. 71, pp. 40–42, 1997.

[100] I. Park, I. Fischer, and W. Elsäßer, "Highly nondegenerate four-wave mixing in a tunable dual-mode semiconductor laser", *Applied Physics Letters*, vol. 84, pp. 5189–5191, 2004.

[101] J.E. Millerd, E.M. Garmire, and M.B. Klein, "Self-pumped phase conjugation in $InP : Fe$ using band-edge resonance and temperature stabilization: theory and experiments", *Optics Letters*, vol. 17, pp. 100–102, 1992.

[102] R.B. Bylsma, A.M. Glass, D.H. Olson, and M. Cronin-Golomb, "Self-pumped phase conjugation in $InP : Fe$", *Applied Physics Letters*, vol. 54, pp. 1968–1970, 1989.

[103] M. Jazbinšek, G. Montemezzani, P. Günter, A.A. Grabar, I.M. Stoika, and Y.M. Vysochanskii, "Fast near-infrared self-pumped phase conjugation with photorefractive $Sn_2P_2S_6$", *Journal of the Optical Society of America B*, vol. 20, pp. 1241–1246, 2003.

[104] M. Cronin-Golomb, B. Fischer, J.O. White, and A. Yariv, "Theory and applications of four-wave mixing in photorefractive media", *IEEE Journal of Quantum Electronics*, vol. 20, pp. 12–30, 1984.

[105] N. Huot, J.M.C. Jonathan, G. Roosen, and D. Rytz, "Characterization and optimization of a ring self-pumped phase-conjugate mirror at 1.06 μm with $BaTiO_3 : Rh$", *Journal of the Optical Society of America*, vol. 15, pp. 1992–1999, 1998.

[106] C. Mailhan, *Optimisation du double miroir à conjugaison de phase dans $BaTiO_3$*, PhD thesis, Université Paul Verlaine, Metz, France, 2000.

[107] A.A. Grabar, R.I. Muzhikash, A.D. Kostyuk, and Y.M. Vysochanskii, "Investigation of the switching processes in the domain structure of ferroelectric $Sn_2P_2S_6$ by the dynamic holography method", *Soviet physics. Solid State*, vol. 33, pp. 1314–1316, 1991.

[108] S.G. Odoulov, A.N. Shumelyuk, U. Hellwig, R.A. Rupp, A.A. Grabar, and I.M. Stoyka, "Photorefraction in tin hypothiodiphosphate in the near infrared", *Journal of the Optical Society of America B*, vol. 13, pp. 2352–2360, 1996.

[109] S.G. Odoulov, A.N. Shumelyuk, U. Hellwig, R.A. Rupp, and A.A. Grabar, "Photorefractive beam coupling in tin hypothiodiphosphate in the near infrared", *Optics Letters*, vol. 21, pp. 752–754, 1996.

[110] J. Feinberg, "Asymmetric self-defocusing of an optical beam from the photorefractive effect", *Journal of the Optical Society of America*, vol. 72, pp. 46–51, 1982.

[111] V.A. D'yakov, S.A. Korol'kov, A.V. Mamaev, V.V. Shkunov, and A.A. Zozulya, "Reflection-grating photorefractive self-pumped ring mirror", *Optics Letters*, vol. 16, pp. 1614–1616, 1991.

[112] J.S. Lawrence and D.M. Kane, "Determination of external cavity coupling-coefficient for diode laser with phase-conjugate feedback", *Electronics Letters*, vol. 36, pp. 535–537, 2000.

[113] J.S. Lawrence, *Diode Lasers with Optical-Feedback, Optical-Injection, and Phase-Conjugate Feedback*, PhD thesis, Macquarie University, Sydney, Australia, 2000.

[114] K. Green and B. Krauskopf, "Bifurcation analysis of frequency locking in a semiconductor laser with phase-conjugate feedback", *International Journal of Bifurcation Chaos*, vol. 13, pp. 2589–2601, 2003.

[115] A. Murakami, J. Ohtsubo, and Y. Liu, "Stability analysis of semiconductor laser with phase-conjugate feedback", *IEEE Journal of Quantum Electronics*, vol. 33, pp. 1825–1831, 1997.

[116] K. Green, B. Krauskopf, and K. Engelborghs, "Bistability and torus break-up in a semiconductor laser with phase-conjugate feedback", *Physica D: Nonlinear Phenomena*, vol. 173, pp. 114–129, 2002.

[117] K. Engelborghs, T. Luzyanina, and G. Samaey, *DDE-BIFTOOL v. 2.00: a Matlab package for bifurcation analysis of delay differential equations*, Report TW330, Department of Computer Science, K.U.Leuven, 2001.

[118] M. Sciamanna, P. Mégret, and M. Blondel, "Hopf bifurcation cascade in small-α laser diodes subject to optical feedback", *Physical Review E*, vol. 69, pp. 046209, 2004.

[119] A.A. Tager and K. Petermann, "High-frequency oscillations and self-mode locking in short external-cavity laser diodes", *IEEE Journal of Quantum Electronics*, vol. 30, pp. 1553, 1994.

[120] J-M. Liu, *Photonic Devices*, Cambridge, 2005.

[121] J. Mulet, M. Kroh, and J. Mørk, "Pulse properties of external-cavity mode-locked semiconductor lasers", *Optics Express*, vol. 14, pp. 1119–1124, 2006.

[122] D. Pieroux, T. Erneux, B. Haegeman, K. Engelborghs, and D. Roose, "Bridges of periodic solutions and tori in semiconductor lasers subject to delay", *Physical Review Letters*, vol. 87, pp. 193901, 2001.

[123] M. Sciamanna, T. Erneux, F. Rogister, O. Deparis, P. Mégret, and M. Blondel, "Bifurcation bridges between external-cavity modes lead to polarization self-modulation in vertical-cavity surface-emitting lasers", *Physical Review A*, vol. 65, pp. 041801, 2002.

[124] C. Kharif, E. Pelinovsky, and A. Slunyaev, *Rogue waves in the ocean*, Springer, 2013.

[125] S. Residori, U. Bortolozzo, A. Montina, F. Lenzini, and F.T. Arecchi, "Rogue waves in spatially extended optical systems", *Fluctuation and Noise Letters*, vol. 11, pp. 1240014, 2012.

[126] J. Gemmrich and C. Garrett, "Unexpected waves", *Journal of Pysical Oceanography*, vol. 38, pp. 2330–2336, 2008.

[127] S.K. El-Labany, W.M. Moslem, N.A. El-Bedwehy, R. Sabry, and H.N. Abd El-Razek, "Rogue wave in Titan's atmosphere", *Astrophysics and Space Science*, vol. 338, pp. 3–8, 2012.

[128] R. Höhmann, U. Kuhl, H-J. Stöckmann, L. Kaplan, and E.J. Heller, "Freak waves in the linear regime: A microwave study", *Physical Review Letters*, vol. 104, pp. 093901, 2010.

[129] H. Bailung, S.K. Sharma, and Y. Nakamura, "Observation of peregrine solitons in a multicomponent plasma with negative ions", *Physical Review Letters*, vol. 107, pp. 255005, 2011.

[130] D.R. Solli, C. Ropers, P. Koonath, and B. Jalali, "Optical rogue waves", *Nature*, vol. 450, pp. 1054–1057, 2007.

[131] J.M. Dudley, G. Genty, and B.J. Eggleton, "Harnessing and control of optical rogue waves in supercontinuum generation", *Optics Express*, vol. 16, pp. 3644, 2008.

[132] N. Akhmediev, A. Ankiewicz, and M. Taki, "Waves that appear from nowhere and disappear without a trace", *Physics Letters A*, vol. 373, pp. 675, 2009.

[133] J.M. Soto-Crespo, Ph. Grelu, and N. Akhmediev, "Dissipative rogue waves: Extreme pulses generated by passively mode-locked lasers", *Physical Review E*, vol. 84, pp. 016604, 2011.

[134] M.G. Kovalsky, A.A. Hnilo, and J.R. Tredicce, "Extreme events in the Ti:sapphire laser", *Optics Letters*, vol. 36, pp. 4449, 2011.

[135] C. Bonatto, M. Feyereisen, S. Barland, M. Giudici, C. Masoller, J.R. Rios Leite, and J.R. Tredicce, "Deterministic optical rogue waves", *Physical Review Letters*, vol. 107, pp. 053901, 2011.

[136] K. Schires, A. Hurtado, I.D. Henning, and M.J. Adams, "Rare disruptive events in polarisation-resolved dynamics of optically injected 1550 nm VCSELs", *Electronics Letters*, vol. 48, pp. 872, 2012.

[137] P. Sibani, "Extremal noise events, intermittency and log-poisson statistics in non-equilibrium aging of complex systems", in *Proc. SPIE 5845, Noise in Complex Systems and Stochastic Dynamics III*, 2005, p. 271.

[138] T. Heil, I. Fischer, and W. Elsäßer, "Coexistence of low-frequency fluctuations and stable emission on sigle high-gain mode in semiconductor lasers with external optical feedback", *Physical Review A*, vol. 58, pp. 2672–2675, 1998.

[139] C. Risch and C. Voumard, "Self-pulsation in the output intensity and spectrum of GaAs-AlGaAs cw diode lasers coupled to a frequency-selective external optical cavity", *Journal of Applied Physics*, vol. 48, pp. 2083–2085, 1977.

[140] J.F. Martinez Avila, H.L.D.de S. Cavalcante, and J.R. Rios Leite, "Experimental deterministic coherence resonance", *Physical Review Letters*, vol. 93, pp. 144101, 2004.

[141] R. Benzi, G. Parisi, A. Sutera, and A. Vulpiani, "Stochastic resonance in climatic change", *Tellus*, vol. 34, pp. 10–16, 1982.

[142] L. Gammaitoni, P. Hänggi, P. Jung, and F. Marchesoni, "Stochastic resonance", *Reviews of Modern Physics*, vol. 70, pp. 223–287, 1998.

[143] B. McNamara, K. Wiesenfeld, and R. Roy, “Observation of stochastic resonance in a ring laser”, *Physical Review Letters*, vol. 60, pp. 2626–2629, 1988.

[144] G. Giacomelli, F. Marin, and I. Rabbiosi, “Stochastic and bona fide resonance: an experimental investigation”, *Physical Review Letters*, vol. 82, pp. 675–678, 1999.

[145] J.M. Buldú, J. García-Ojalvo, C.R. Mirasso, and M.C. Torrent, “Stochastic entrainment of optical power dropouts”, *Physical Review E*, vol. 66, pp. 021106, 2002.

[146] A.S. Pikovsky and J. Kurths, “Coherence resonance in a noise-driven excitable system”, *Physical Review Letters*, vol. 78, pp. 775–778, 1997.

[147] B. Lindner, J. García-Ojalvo, A. Neiman, and L. Schimansky-Geier, “Effects of noise in excitable systems”, *Physics Reports*, vol. 392, pp. 321–424, 2004.

[148] D.E. Postnov, S.K. Han, T.G. Yim, and O.V. Sosnovtseva, “Experimental observation of coherence resonance in cascaded excitable systems”, *Physical Review E*, vol. 59, pp. 3791–3794, 1999.

[149] C. Masoller, “Noise-induced resonance in delayed feedback systems”, *Physical Review Letters*, vol. 88, pp. 034102, 2002.

[150] M.A. Arteaga, M. Valencia, M. Sciamanna, H. Thienpont, M. Lo’pez-Amo, and K. Panajotov, “Experimental evidence of coherence resonance in a time-delayed bistable system”, *Physical Review Letters*, vol. 99, pp. 023903, 2007.

[151] Y. Hong and K.A. Shore, “Influence of optical feedback time-delay on power-drops in vertical-cavity surface-emitting lasers”, *IEEE Journal of Quantum Electronics*, vol. 41, pp. 1054, 2005.

[152] J.M. Buldú, J. García-Ojalvo, and M.C. Torrent, “Delay-induced resonances in an optical system with feedback”, *Physical Review Letters*, vol. 69, pp. 046207, 2004.

[153] J.F. Martinez Avila, H.L.D.de S. Cavalcante, and J.R. Rios Leite, “Coarse grained variables and deterministic chaos in an excitable system”, *Physical Review Letters*, vol. 100, pp. 044101, 2008.

[154] A. Gavrielides, T.C. Newell, V. Kovanis, R.G. Harrison, N. Swanston, D. Yu, and W. Lu, "Synchronous Sisyphus effect in diode lasers subject to optical feedback", *Physical Review A*, vol. 60, pp. 1577–1581, 1999.

[155] F. Kuwashima, I. Kitazima, and H. Iwasawa, "Theory of chaotic dynamics on class a laser with optical delayed feedback", *Japanese Journal of Applied Physics*, vol. 40, pp. 601, 2001.

[156] F. Rogister, M. Sciamanna, O. Deparis, P. Mégret, and M. Blondel, "Low-frequency fluctuation regime in a multimode semiconductor laser subject to a mode-selective optical feedback", *Physical Review A*, vol. 65, pp. 015602, 2001.

[157] D. Yu, I. Wallace, R.G. Harrison, and A. Gavrielides, "Low frequency fluctuations and locked states in a multi-mode semiconductor laser with external feedback", *Optics Communications*, vol. 195, pp. 249–258, 2001.

[158] S. Wieczorek, B. Krauskopf, and D. Lenstra, "Multipulse excitability in a semiconductor laser with optical injection", *Physical Review Letters*, vol. 88, pp. 063901, 2002.

Résumé en français
Summary in French

Chaos et auto-pulsations à haute fréquence dans une diode laser soumise à rétroaction optique à conjugaison de phase

Table des matières

Chapitre 1
Introduction

L'acronyme LASER signifie "Light Amplification by Stimulated Emission of Radiation". Le premier laser fut inventé en 1960 par Theodore Maiman qui utilisa un cristal de rubis pour générer de la lumière rouge. Les lasers à semi-conducteurs, ou diodes laser, apparurent dès 1962 et ont pris depuis lors une place de plus en plus importantes dans nos vies quotidiennes. On trouve des applications aux diodes laser dans de nombreux domaines de la technologie, l'ingénierie et la recherche tels que les télécommunications, la métrologie, le stockage de données et la médecine. Leur faibles coût et dimensions, la possibilité de les produire à grandes échelle ainsi que leur capacité à couvrir un large spectre de longueur d'onde ont rapidement permis de les intégrer à tous domaines d'activité. Les lasers ont la particularité de générer des faisceaux cohérents monochromatiques, particulièrement adaptés aux applications d'interférométrie et de spectrométrie.

Nous nous intéressons dans cette thèse à l'étude de la dynamique d'une diode laser lorsqu'elle est soumise à de la rétroaction optique. On parle de rétroaction optique lorsqu'une partie du faisceau émis par le laser lui est redirigé vers sa cavité après réflexion partielle sur un miroir. La rétroaction est connue pour créer des instabilités dans le laser. C'est précisément dans quelle mesure la présence d'une rétroaction optique à conjugaison de phase perturbe le laser que nous nous proposons d'étudier dans ce manuscrit. Il s'agit donc d'une étude de la dynamique non linéaire du laser pilotée par une rétroaction optique à conjugaison de phase.

Les systèmes non linéaires sont inhérents à la nature, les plus connus étant les comportements atmosphériques et la dynamique des fluides. Les équations régissant ce type de systèmes sont très difficiles à résoudre et sont à l'origine de phénomènes particuliers comme le chaos. La théorie du chaos fut initiée à la fin du XIX^{e} siècle par Henri Poincaré avec l'étude du problème à trois corps. Les systèmes chaotiques sont déterministes et montrent une grande sensibilité aux conditions initiales car une légère modification des conditions initiales pour un même système peut mener à des évolutions à long terme totalement différentes.

Par conséquent, nous combinons par cette étude les domaines de la dynamique de systèmes non linéaires et de l'optique non linéaire. Une diode laser avec rétroaction optique peut être vue comme un oscillateur non linéaire régi par des des paramètres intérieurs et extérieurs au système. En effet, en absence de rétroaction, la dynamique du laser est gouvernée par ses oscillations de relaxation à la période bien définie. L'ajout de la rétroaction fait intervenir une deuxième échelle de temps liée à son retard temporel. Le laser va en conséquence suivre une successions de bifurcations aux dynamiques particulières sous l'effet du taux de rétroaction. La configuration utilisant la conjugaison de phase rajoute une troisième échelle de temps qui est celle du temps de génération de la rétroaction. La dynamique du laser et ses points de fonctionnement dépendent donc fortement de l'interaction entre ces trois échelles de temps dont les caractéristiques sont visibles temporellement et spectralement.

Nous apportons ici une contribution théorique et expérimentale sur la dynamique d'une diode laser soumise à rétroaction optique par conjugaison de phase. Nous discuterons les différences fondamentales qui y sont attendues par rapport au cas de la rétroaction conventionnelle. Au-delà de l'intérêt applicatif du système, il s'agit aussi de la compréhension fondamentale d'un système non linéaire montrant une rétroaction à retard. Bien que ce type de système ait été étudié depuis plusieurs décennies, il reste de nombreux comportements à élucider ainsi que des phénomènes à découvrir.

Nous commencerons cette étude avec un bref rappel de l'état de l'art des diodes laser à rétroaction optique puis nous présenterons le dispositif expérimental permettant l'étude de la dynamique du laser. Nous définirons aussi la rétroaction à conjugaison de phase ainsi que le retard associé. L'étude théorique présente le modèle utilisé pour simuler les comportements du laser ainsi que les prévisions des routes vers le chaos et des influences de plusieurs paramètres. Nous mettrons en évidence les phénomènes de bistabilité entre solutions pulsées, ainsi que la crise chaotique et la suppression de chaos résultantes. Une manifestation expérimentale de solutions auto-pulsées et leurs processus de stabilisation et de déstabilisation associés seront ensuite présentés ainsi qu'une confirmation qualitative obtenue par simulation. L'évolution de la dynamique du laser alors que la force de la rétroaction augmente sera ensuite présentée et illustrée par la visualisation expérimentale d'événements extrêmes et d'une résonance cohérente déterministe en régime de fluctuations à basse fréquence. Nous terminerons enfin avec un rappel des points abordés et une ouverture sur les pistes de recherche dans ce domaine.

Chapitre 2
Contexte et motivations

2.1 Diodes lasers soumises à rétroaction optique

2.1.1 Rétroaction conventionnelle

La génération d'une rétroaction optique est en général simplement réalisée en insérant un miroir sur le trajet du faisceau émis afin d'en renvoyer une partie à l'intérieur de la cavité laser. La distance L entre le miroir et le laser est habituellement de plusieurs centimètres. La figure 2.1 présente la réalisation d'une rétroaction dite conventionnelle (notée COF : Conventional Optical Feedback), c'est-à-dire où le miroir est un miroir classique. La présence de cette rétroaction a de nombreux effets sur la dynamique du laser en fonction de sa force. La proportion de rétroaction retournant dans le laser est définie comme étant le rapport entre les puissances réfléchie par le miroir et émise par le laser : $R = \frac{P_{\text{rétroaction}}}{P_{\text{émis}}}$. La rétroaction optique peut être source de désavantages car elle peut changer totalement les propriétés du laser et y causer des instabilités tout comme elle peut être utilisée au contraire pour en améliorer des propriétés et contribuer à la suppression de modes secondaires, l'affinement spectral, l'accordabilité ou la stabilité en fréquence [1–9].

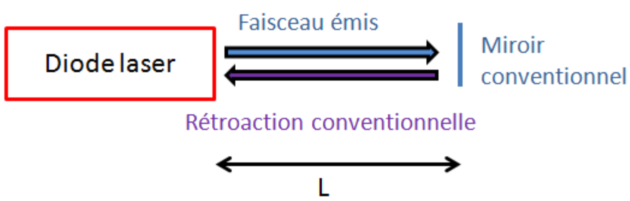

Figure 2.1 – Diode laser soumise à une rétroaction conventionnelle : un miroir renvoie une partie du faisceau émis dans la cavité laser.

Sous l'effet d'une telle rétroaction, le laser peut montrer des transitions entre points de fonctionnement (ou régimes) qui ont été identifiées par Tkach et Chraplyvy en 1986, rappelés en figure 2.2.

Le régime 1 correspond aux valeurs de rétroaction les plus faibles ($R < 0.01\%$). Le laser montre de l'affinement ou de l'élargissement spectral selon le

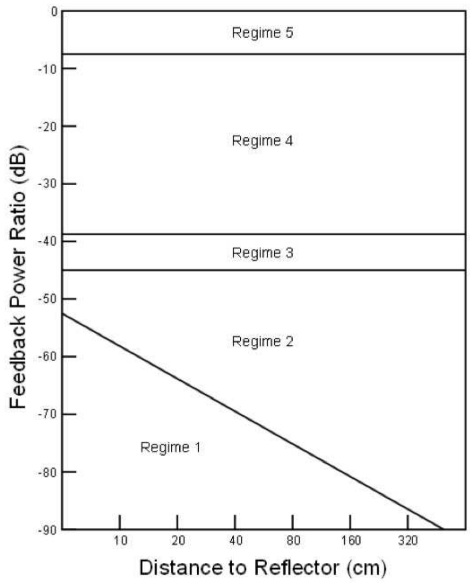

FIGURE 2.2 – Les cinq régimes pouvant se manifester dans une diode laser soumise à rétroaction conventionnelle. La proportion de rétroaction et la distance au miroir déterminent le régime. Figure provenant de [10].

déphasage du faisceau de rétroaction, c'est-à-dire selon la distance au miroir. Le régime 2 est atteint pour des valeurs de R atteignant 0.1%. Des sauts entre modes de cavité externe induits par la rétroaction y sont possibles. Ces modes de cavité externe correspondent aux modes formés dans la cavité délimitée par la facette émettrice du laser et le miroir extérieur.
Le régime 3 n'existe que pour une faible gamme de rétroaction (proche de 1%) et est caractérisé par de l'affinement spectral.
Dans le régime 4, la proportion de rétroaction est modérée ($R \simeq 1\%$). Le spectre laser montre des modes secondaires naissant à des intervalles de fréquence de part et d'autre du mode principal définis par la fréquence des oscillations de relaxation. Les oscillations de relaxation représentent l'échange d'énergie entre les photons et les porteurs de charge dans la cavité laser. Leur échelle de fréquence est habituellement de 5 à 8 GHz. Le spectre laser s'élargit en conséquence. De plus, le laser est susceptible de montrer des oscillations et du chaos.
Le régime 5 est atteint pour des valeurs de rétroaction très élevées ($R > 10\%$). La cavité externe se comporte alors comme un prolongement de la cavité interne et le système est équivalent à un court milieu amplificateur (la diode laser) dans une très longue cavité. Le laser émet alors un faisceau monomode

avec une grande finesse spectrale.

Les recherches dans la dynamique des diodes lasers soumises à rétroaction conventionnelle ont montré des phénomènes d'hystérésis et de multistabilité [11], d'oscillations de relaxation non amorties [12–14], de régimes pulsés [15–17], de fluctuations à basse fréquence [18–21] ainsi que d'excitabilité [22] et de résonance cohérente pilotée par du bruit [23].

2.1.2 Rétroaction optique à conjugaison de phase (PCF)

Nous nous intéressons plus spécifiquement à un type particulier de rétroaction appelé rétroaction à conjugaison de phase (ou PCF : Phase-Conjugate Feedback). Cette rétroaction est générée à partir d'un miroir à conjugaison de phase qui est un milieu dans lequel des interactions non linéaires entre différents faisceaux ont pour conséquence la création d'un faisceau conjugué par rapport au faisceau émis, comme schématisé en figure 2.3.

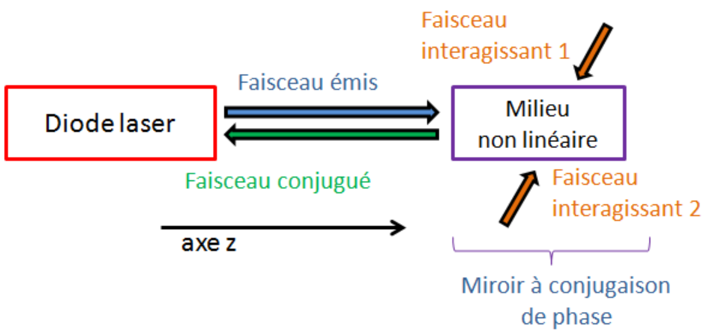

FIGURE 2.3 – Laser soumis à rétroaction à conjugaison de phase. La génération de la rétroaction est basée sur des interactions entre le faisceau émis par le laser et deux autres faisceaux interférant dans un milieu non linéaire. Dans ce cas-ci, la conjugaison de phase est créée par mélange à quatre ondes (Four-Wave Mixing (FWM) [25]).

Les effets d'une rétroaction à conjugaison de phase sont similaires au cas de la rétroaction conventionnelle. En effet, la laser montre des instabilités et une route vers le chaos à travers des régimes oscillants. Cependant, en regardant dans le détail comment s'opèrent les transitions entre dynamiques et les natures-mêmes de celles-ci, on se rend rapidement compte que des différences fondamentales existent. En conséquence, dans le cas de la conjugaison de phase, la séquence de bifurcations vers le chaos fait intervenir des dynamiques inexistantes dans le cas de la rétroaction conventionnelle [24]. La dynamique des diodes laser avec PCF a été l'objet de nombreuses études théoriques. De plus, d'un point de vue expérimental, les propriétés de la génération de la conjugaison de phase font que l'onde conjuguée créée et le faisceau incident sont auto-alignés, ce qui a l'avantage à la fois d'augmenter le facteur de couplage des faisceaux et de s'affranchir de l'alignement manuel nécessaire dans le cas du COF.

Une onde plane électromagnétique d'amplitude E, de pulsation ω se propageant suivant l'axe z s'écrit $E(x,y,z,t) = E_0 cos(\omega t - kz - \phi(x,y,z))$. Après réflexion sur le miroir à conjugaison de phase, l'onde correspondante s'écrit $E_{conj}(x,y,z,t) = rE_0 cos(\omega t + kz + \phi(x,y,z))$. r est le coefficient de réflexion en amplitude du miroir. En réalité ces deux expressions représentent la même onde mais la composante longitudinale du vecteur d'onde k et la phase ϕ sont de signe opposé.

Les études théoriques d'un laser avec PCF prévoient une grande richesse dynamique [26–28]. Des comparaisons ont été établies confrontant le COF au PCF. La principale différence qui nous intéresse ici est présentée en figure 2.4. Il s'agit de la nature des modes de cavité externe. Dans le cas du PCF, lorsque le taux de rétroaction augmente, une fois la première transition vers le chaos effectuée, le système ne retrouve jamais de solution stationnaire. Cependant, dans le cas du COF, les régions de chaos sont entrecoupées de solutions stationnaires appelées modes de cavité externe dans le cas du COF qui sont représentés par des régions ne présentant aucun point. Dans un système avec PCF, les régions de chaos sont entrecoupées de solutions pulsées périodiques appelées modes de cavité externe dans le cas du PCF, représentées par des régions constituées de lignes continues. Comme nous le discuterons plus loin, les fréquences de pulsation de ces solutions sont parfaitement définies par le retard de la rétroaction. Dans ce cas, le champ électrique complexe du faisceau laser peut s'exprimer $E_0(t) = A_1 exp(i\omega t) + A_2 exp(-i\omega t)$ où A_1 et A_2 sont des constantes scalaires [29]. ω est la pulsation qui est rattachée à la longueur de la cavité externe par $\omega = 2\pi \frac{c}{2L_{cav}}$, c étant la vitesse de la lumière et L_{cav} la longueur de la cavité externe.

Malgré de nombreuses études théoriques menées sur le sujet, les études expérimentales de la dynamique de diodes laser avec rétroaction à conjugaison de phase demeurent peu nombreuses. Il est cependant documenté dans la littérature une route vers le chaos à travers un régime d'oscillations de relaxation non amorties [30], ainsi que des évolutions de propriétés spectrales et une mise en évidence d'un régime de fluctuations à basse fréquence [31].

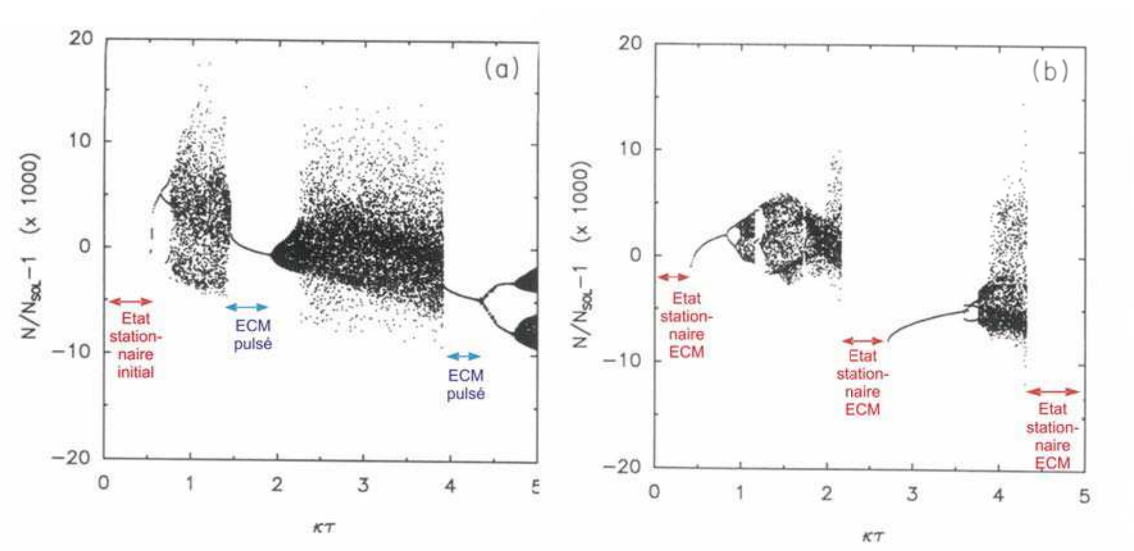

FIGURE 2.4 – Diagrammes de bifurcation dans le cas de PCF (a) et du COF (b) pour les mêmes valeurs de paramètres. N est la population électronique et N_{sol} sa valeur à l'état stationnaire en absence de rétroaction. κ représente la proportion de rétroaction et τ le retard de la rétroaction : temps d'aller-retour dans la cavité externe. Figure adaptée de [24].

2.2 Pourquoi l'étude de diodes laser avec PCF ?

Les diodes laser soumises à rétroaction optique à conjugaison de phase présentent encore des propriétés inexploitées ou peu connues jusqu'à aujourd'hui. Nous apportons ici une extension de l'étude des modes de cavité externe en en montrant la première illustration expérimentale. Puis nous étudierons aussi l'influence du retard, par le biais de la longueur de la cavité externe, sur les dynamiques observables en montrant des transitions vers le chaos dans lesquelles des événements extrêmes peuvent être détectés ainsi qu'un forme particulière de résonance cohérente en régime de fluctuations à basse fréquence. Sur le plan théorique, nous apportons aussi une explication aux phénomènes de crise chaotique et bistabilité de solutions auto-pulsées, attendues pour des taux de rétroaction plus élevés que ceux étudiés jusqu'à présent. Nous mentionnerons également dans les perspectives d'autres pistes de recherche que nous ne développerons pas dans cette thèse.

Chapitre 3

Dispositif expérimental

Nous présentons ici le montage expérimental qui permet de réaliser la conjugaison de phase puis d'étudier la dynamique du laser avec rétroaction à conjugaison de phase ainsi que les différents appareils de mesure associés à l'acquisition des données.

Notre diode laser est un laser à semi-conducteur à émission latérale monomode (JDS Uniphase DL-SDL-5400). La couche active est faite de puits quantiques dans de l'$AlGaAs$ et la longueur d'onde est $\lambda = 852 \pm 4\ nm$. Le courant d'alimentation est fixé à 60 mA, ce qui correspond à une puissance disponible en sortie de 45 mW. Ce type de diode laser est couramment utilisé dans les communications par fibre optique dans le proche infrarouge, dans les imprimantes laser et dans les lecteurs de disques.

3.1 Rétroaction à conjugaison de phase

La première étude expérimentale d'une diode laser avec rétroaction provenant d'un miroir à conjugaison de phase remonte aux expériences de Cronin-Golomb *et al.* en 1985 [32]. La conjugaison de phase est une technique utilisée pour corriger les distortions de front d'onde, stabiliser un laser par mode-locking, réduire le bruit et améliorer sa finesse spectrale [33–44].

Contrairement au cas du COF, le PCF a la particularité d'être une rétroaction auto-alignée et auto-corrigée [45]. Par conséquent, tout déphasage acquis par le faisceau à l'aller est compensé par un déphasage opposé acquis lors du trajet retour vers le laser de telle sorte que le front d'onde retour soit en tout point du trajet retour identique à ce qu'il était lors du trajet aller. Cette propriété est illustrée sur la figure 3.1.

Les milieux adaptés à la réalisation d'un miroir à conjugaison de phase sont nombreux. On y dénombre les milieux à effet Kerr pouvant avoir des temps de réponse de l'ordre de la femtoseconde [46], les cristaux photoréfractifs dont le temps de réponse va de la miliseconde à plusieurs secondes [33,47] ou encore les diodes laser répondant à la nanoseconde [37,48–51]. Dans notre

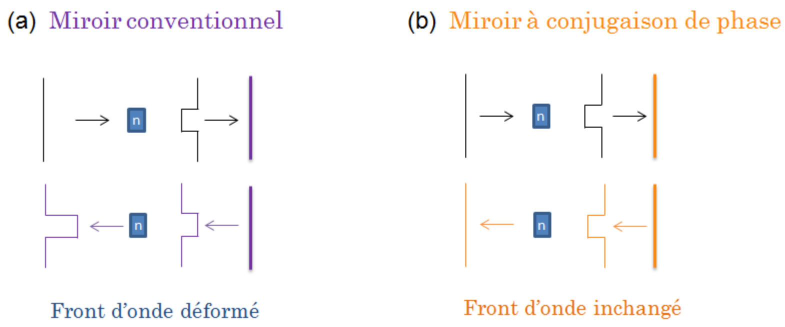

FIGURE 3.1 – Miroir à conjugaison de phase et miroir conventionnel. Le front d'onde dans le cas du COF subi une double distortion après un aller-retour dans la cavité contenant un milieu d'indice de réfraction n (a) alors que dans le cas du PCF le front d'onde est inchangé (b).

expérience, nous utilisons un cristal semi-conducteur photoréfractif d'hypothiodiphosphate d'étain dopé tellure : $Sn_2P_2S_6 : Te$ (1%) que nous appellerons plus simplement SPS. Ce matériau présente plusieurs avantages : il est particulièrement adapté au proche infrarouge pour lequel il présente des taux d'absorption faible et de gain élevé [52], ainsi qu'un court temps de réponse comparé aux autres cristaux photoréfractifs. En effet nous avons mesuré son temps de réponse à environ 3.8 ms alors que l'ordre de grandeur habituel est entre plusieurs centaines de millisecondes (SBN [47]), et plusieurs secondes ($BaTiO_3$ [33]).

Il existe plusieurs configurations utilisant les cristaux photoréfractifs pour créer de la conjugaison de phase. Nous travaillons dans une configuration en anneau auto-pompée dans laquelle les trois faisceaux intervenant dans le mélange à quatre ondes proviennent du même laser. Cette configuration en anneau est présentée en figure 3.2.

Le principe de la conjugaison de phase est le suivant. Deux faisceaux pompes interagissent dans le cristal créant ainsi un réseau d'indice de réfraction au sein du cristal. La diffraction d'un troisième faisceau sur ce réseau a pour conséquence d'engendrer la création du quatrième faisceau : la rétroaction conjuguée en phase. Une formulation mathématique a été proposée par Cronin-Golomb *et al.* et appliquée à la caractérisation de miroirs à conjugaison de phase [53, 54]. Dans cette configuration, il est en réalité possible de réaliser deux réseaux d'indices de natures différentes. En effet, selon quels faisceaux jouent le rôle de pompes et de signaux, il se peut que le réseau créé soit soit un réseau de transmission soit un réseau de réflexion. La pos-

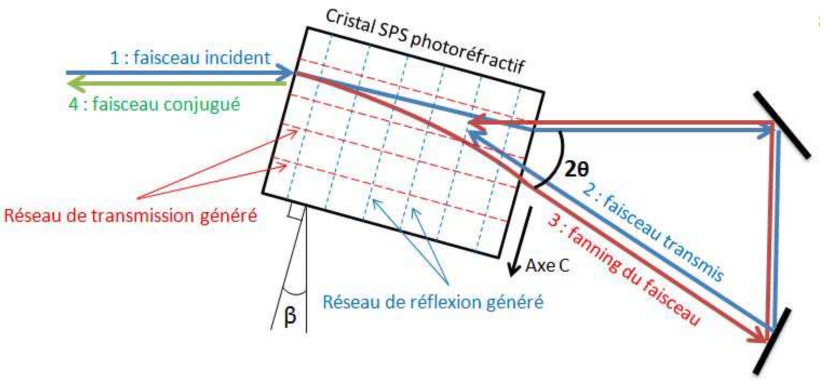

FIGURE 3.2 – Principe du miroir à conjugaison de phase : mélange à quatre ondes dans un cristal photoréfractif SPS présentant des réseaux de réflexion (bleu) et de transmission (rouge).

sibilité de pouvoir sélectionner l'un ou l'autre de ces deux réseaux présente un avantage considérable qui sera discuté plus loin en termes de dynamiques observables dans le laser.
Sur le schéma de la figure 3.2, les angles $\beta = 26^o$ et $2\theta = 30^o$ ont été ajustés pour optimiser le gain du processus de mélange à quatre ondes et éviter au maximum les pertes par réflexion de Fresnel à l'entrée du cristal. Étant donnée la géométrie de la configuration, nous sommes certains qu'aucune rétroaction conventionnelle n'est renvoyée vers le laser et, d'après la théorie de la génération de l'onde conjuguée qui est auto-alignée sur le faisceau incident, seule la rétroaction à conjugaison de phase est redirigée vers la cavité laser. Le montage complet est présenté en figure 3.3.

3.2 Visualisation de la dynamique du laser

La proportion de rétroaction contrôlée à l'aide d'un atténuateur variable inséré dans la boucle de la cavité en anneau qui influe sur le gain du mélange à quatre ondes. Avec les notations de la figure 3.2, la réflectivité du miroir est définie par $R = \frac{\text{Puissance du faisceau 4}}{\text{Puissance du faisceau 1}}$. Nous parvenons à obtenir une réflectivité maximale de 9% avec notre montage.

Le retard temporel de la rétroaction est défini par son temps de propagation dans la cavité extérieure. Si L_{cav} est la distance totale parcourue par le faisceau dans la cavité, le retard associé s'écrit $\tau = \frac{c}{L_{cav}}$. Nous avons vu que deux types de réseaux sont possibles, comme rappelé en figure 3.4. Or

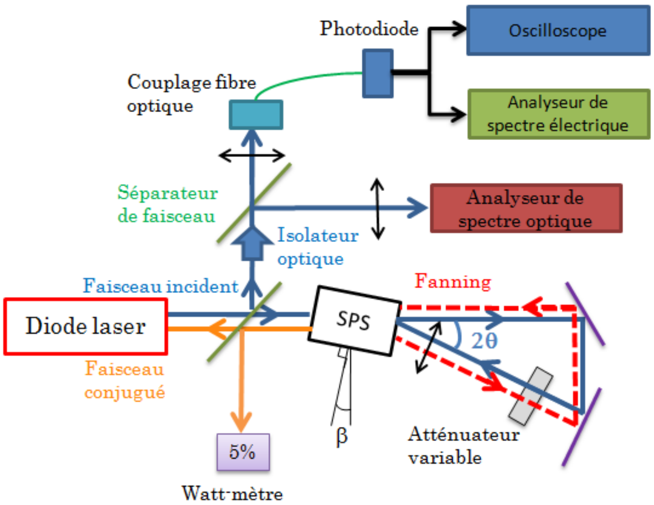

FIGURE 3.3 – Montage complet. Des appareils de mesure et un watt-mètre indiquant la puissance de l'onde conjuguée générée sont introduits afin de mesurer et quantifier la dynamique du laser soumis à la rétroaction optique.

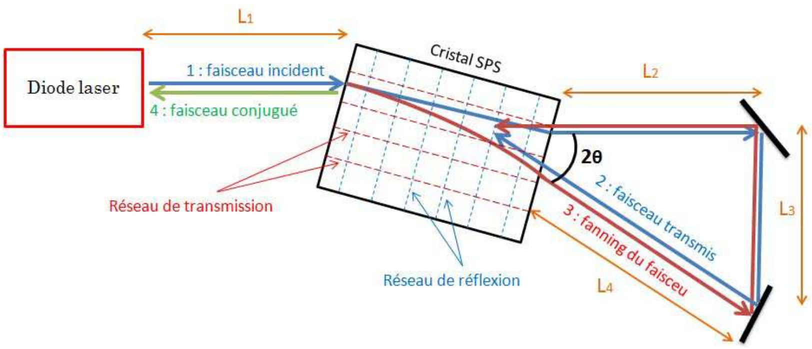

FIGURE 3.4 – Dépendance de la longueur de cavité équivalente en fonction des réseaux. $L_{cav_{reflexion}} = 2L_1$ alors que $L_{cav_{transmission}} = 2L_1 + L_2 + L_3 + L_4$. La propagation à l'intérieur du cristal n'est pas prise en compte ici.

chacun est associé à une distance parcourue différente. En effet, dans le cas d'un réseau de réflexion, le cristal se comporte comme un miroir classique et la propagation dans la cavité en anneau n'est pas prise en compte. Le retard est alors simplement égal au temps l'aller-retour dans l'espace séparant le laser du cristal et la distance parcourue équivalente est $L_{cav_{reflexion}} = 2L_1$. Dans le cas où la génération de l'onde conjuguée se fait au moyen d'un réseau de transmission, le retard prend en compte la propagation dans la cavité en anneau et la distance parcourue est $L_{cav_{transmission}} = 2L_1 + L_2 + L_3 + L_4$. La capacité à passer d'un réseau à l'autre permet de changer la longueur de la cavité vue par le laser, ou en d'autre termes, de changer le retard temporel de la rétroaction.

Les appareils de mesure donnent simultanément plusieurs informations complémentaires. Les données temporelles sont fournies par un oscilloscope Tektronix CSA 7404, 20 GS/s avec une bande passante de 4 GHz. Les données spectrales sont fournies par un analyseur de spectre électrique Rohde & Schwarz FSP30, avec une bande passante de 9 kHz-30 GHz et une résolution de 6 MHz ainsi qu'un analyseur de spectre optique confocal Thorlabs SA210-8B avec une finesse de 150. Afin de voir les différentes dynamiques du laser, on maintient généralement le courant d'alimentation fixé à 60 mA et on fait varier la réflectivité du miroir au moyen de l'atténuateur optique variable.

Chapitre 4

Modèle théorique et scénario simulé

4.1 Système d'équations de Lang-Kobayashi

Le modèle théorique sur lequel nous nous basons pour l'étude de la dynamique non linéaire du laser est le système d'équations de Lang-Kobayashi adapté dans le cas de la conjugaison de phase, fréquemment utilisé pour modéliser ce système [24, 28, 29, 55]. Les équations s'écrivent comme suit :

$$\begin{cases} \dfrac{dE}{dt}(t) = (1 + i\alpha)N(t)E(t) + \gamma E^*(t - \theta) \\ T\dfrac{dN}{dt}(t) = P - N(t) - (1 + 2N(t))|E(t)|^2 \end{cases} \tag{4.1}$$

θ est le retard de la rétroaction normalisé par le temps de vie des photons τ_p, pris égal à $\tau_p = 1.4\ ps$, d'après la référence [29]. D'où $\theta = \frac{\tau}{\tau_p}$. Le lien physique avec la longueur de la cavité est $\tau = \frac{L_{cav}}{c}$. α est le facteur d'élargissement spectral et T le rapport du temps de vie des électrons sur celui des photons. E est l'enveloppe complexe du champ électrique, N l'inversion de population et P le courant d'alimentation normalisé au-dessus du seuil : $P = \frac{I - I_{th}}{I_{th}}$ où I_{th} est le courant de seuil. γ est le taux de rétroaction normalisé : $\gamma = \tau_p \kappa$ où $\kappa = \frac{1-R_m}{\tau_L}\sqrt{\eta_c \frac{R}{R_m}}$. R_m est le coefficient de réflexion des facettes du laser, η_c le coefficient de couplage et R la réflectivité du miroir à conjugaison de phase. τ_L est le temps d'aller-retour des photons dans la cavité laser : $\tau_L = \frac{2nL_{cavit\ laser}}{c}$ où n est l'indice de réfraction du matériau semi-conducteur dans lequel est construite la cavité laser. Pour un courant d'alimentation fixé, on peut considérer que γ est proportionnel à la racine carrée de la réflectivité du miroir à conjugaison de phase R. Pour indication, $R = 100\%$ correspond à $\gamma = 0.256$ avec $\eta_c = 1$, $\tau_L = 7\ ps$, $R_m = 0.3$ et $\tau_p = 1.4\ ps$.

Ce modèle assez simple traduit dans la première équation l'équilibre entre la génération de photons et les pertes dans la cavité laser et dans la deuxième équation la dynamique des porteurs de charge. Les dynamiques prédites par ce système alors que γ varie on été étudiées par Krauskopf *et al.* en 1998 [28] qui documentèrent de façon détaillée l'évolution des diagrammes de bifurcation et des routes vers le chaos pour des faibles valeurs de γ en identifiant les premières "bulles de chaos".

4.2 Évolution de la dynamique pour γ modéré

Un diagramme de bifurcation typique d'une diode laser avec PCF est présenté en figure 4.1 dont les paramètres pris pour la simulation sont les mêmes que ceux de la référence [28]. On y distingue les régions de chaos apparaissant sous formes de bulles entrecoupées de solutions périodiques.

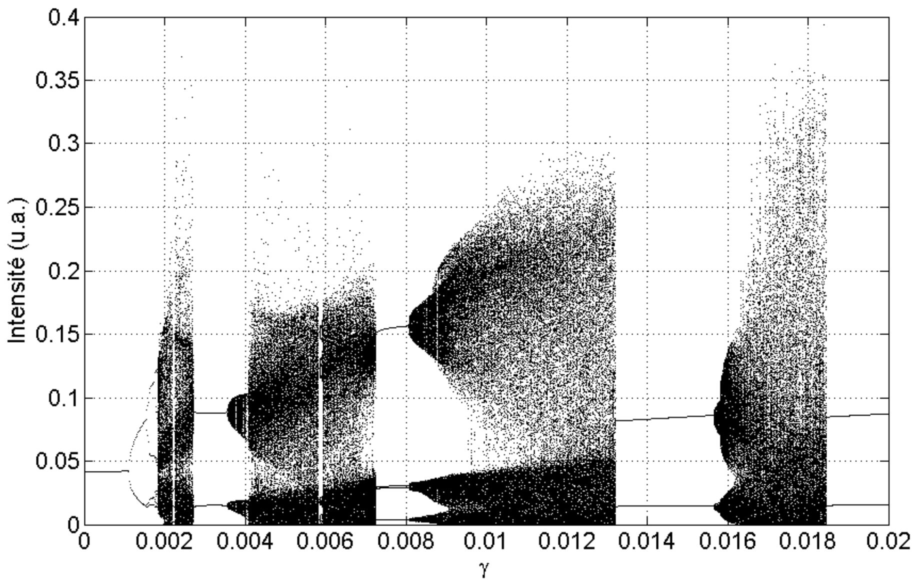

FIGURE 4.1 – Diagramme de bifurcation calculé pour θ=476, P=0.0417, T=1428 et $\alpha = 3$.

La première bulle de chaos est en fait la transition entre l'état stationnaire initial et la première solution périodique auto-pulsée à une fréquence liée à la longueur de la cavité externe. Ses principales dynamiques sont représentées en figure 4.2. On y voit d'abord le cycle limite des oscillations de relaxation non amorties (A) oscillant à 1.036 GHz. Puis, alors que γ croît, le laser subit des doublements de période (B) jusqu'à ce qu'un attracteur chaotique soit créé (C) et que le laser montre des dynamiques chaotiques (D) et (F) qui finissent par se restabiliser en des cycles limites correspondant à des modes de cavité externe auto-pulsés (ECM) à la fréquence de la cavité externe 1.36 GHz (H).

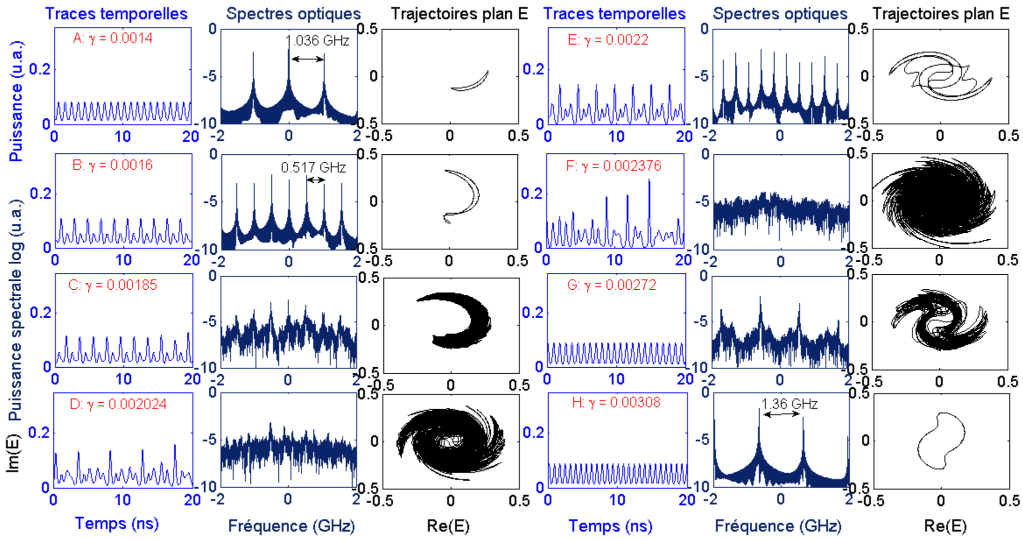

FIGURE 4.2 – Traces temporelles, spectres et représentations dans le plan complexe de l'évolution du laser au travers de la première bulle de chaos.

L'évolution du laser au travers de la deuxième bulle de chaos est présentée en figure 4.3. Alors que le laser vient de quitter la première bulle de chaos et oscille à la fréquence de la cavité externe, une bifurcation vient changer ce cycle limite en tore (B) puis en un attracteur chaotique (C) et (E). À nouveau, le laser finit par se restabiliser en une solution périodique (G) qui n'est cependant pas une sinusoïde pure, contrairement à ce qui se produit en fin de bulle 1. Cette solution n'est donc pas un mode de cavité externe bien que la fréquence fondamentale soit au double de celle de la trace (H) de la figure 4.2.

Enfin la troisième bulle, dont les dynamiques sont représentées en figure 4.4, montre à nouveau une déstabilisation du cycle limite issu de la bulle 2 menant vers du chaos (B), (C) et (D). En fin de bulle 3, le système recouvre un cycle limite symétrique correspondant au troisième mode de cavité externe (F), pulsant à 4.1 GHz.

Ces simulations sont en très bon accord avec les travaux de la référence [28] et permettent donc de confirmer le code servant à modéliser la dynamique du laser ainsi que les outils d'analyse que nous utiliserons dans

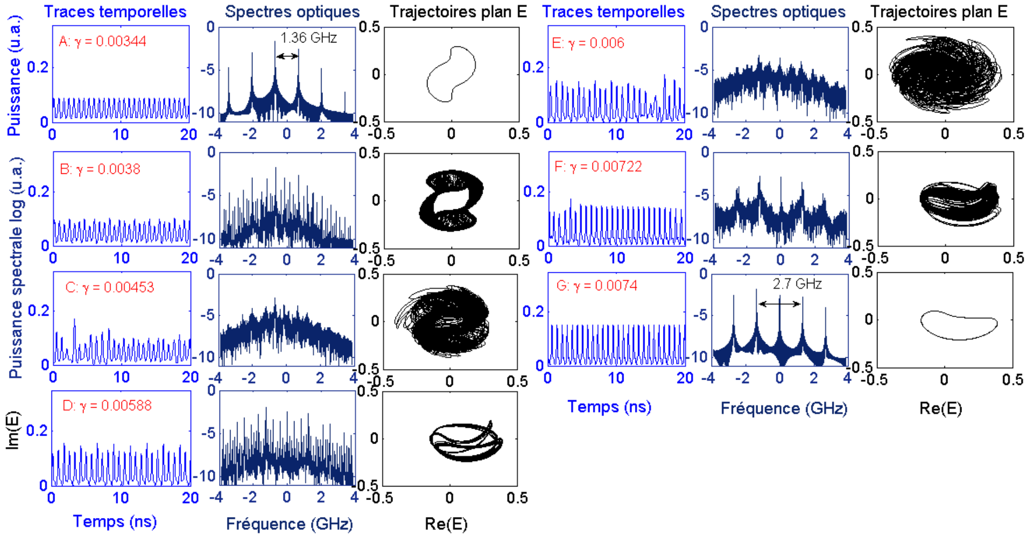

FIGURE 4.3 – Traces temporelles, spectres et représentations dans le plan complexe de l'évolution du laser au travers de la deuxième bulle de chaos.

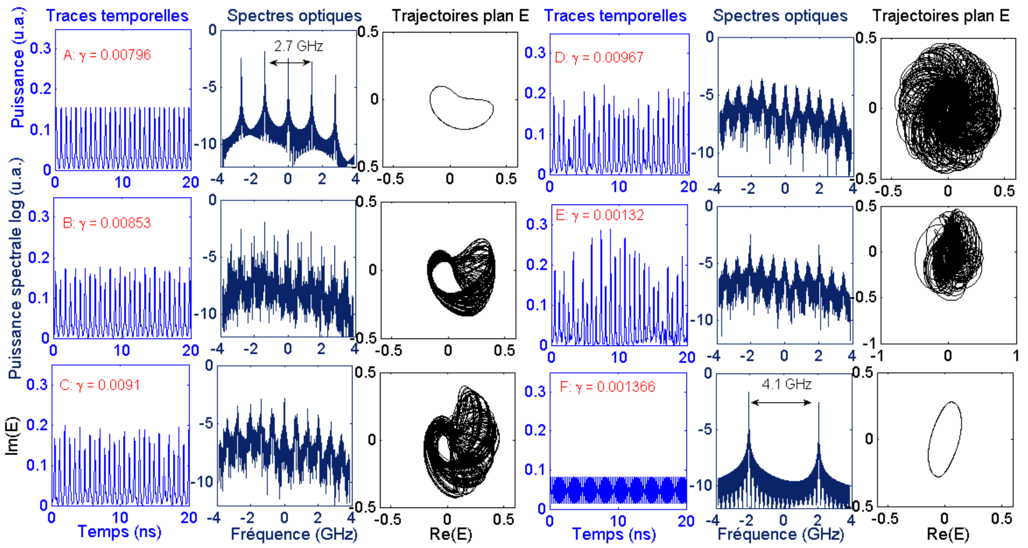

FIGURE 4.4 – Traces temporelles, spectres et représentations dans le plan complexe de l'évolution du laser au travers de la troisième bulle de chaos.

le suite pour étendre l'étude aux valeurs de γ plus élevées.

4.3 Évolution de la dynamique pour γ élevé

Nous poursuivons ici les travaux menés dans les références [28,29,55] pour des valeurs de γ plus élevées. Le diagramme de bifurcation présenté en figure 4.5 est l'extension de celui de la figure 4.1 pour des taux de rétroaction plus élevés. On y voit que les régions de chaos disparaissent et que, pour des valeurs de γ supérieures à 0.035, seules des solutions pulsées (modes de cavité externe) sont visibles. Le laser semble demeurer dans une succession d'états pulsés sans jamais bifurquer vers le chaos à nouveau. Afin de comprendre ce phénomène qui fait se réduire les intervalles de régions chaotique (crise chaotique) jusqu'à les faire disparaître (suppression de chaos), nous faisons appel à une méthode de continuation dans l'objectif de localiser les points de bifurcation responsables de la stabilisation et de la déstabilisation des modes de cavité externe.

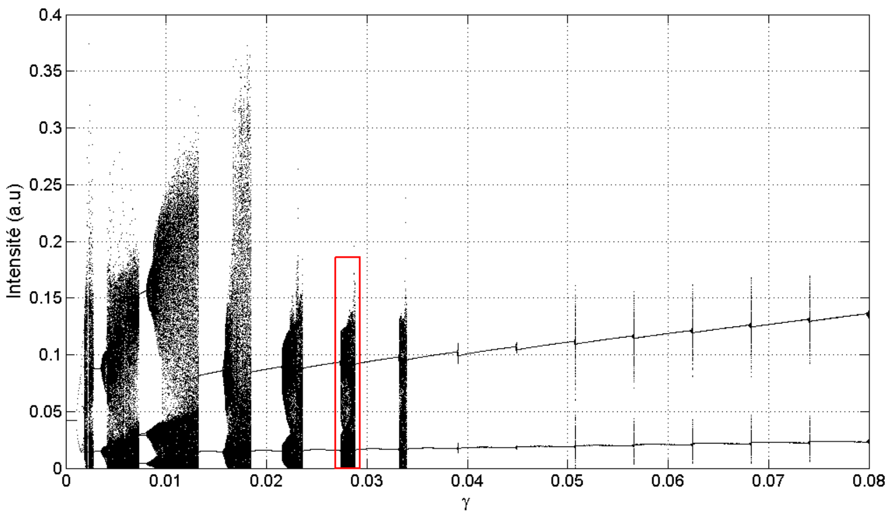

FIGURE 4.5 – Diagramme de bifurcation pour θ=476, P=0.0417, T=1428 et α=3. Identique à celui en figure 4.1 mais pour des valeurs de rétroaction plus élevées. On y compte sept régions chaotiques de plus en plus fines et qui finissent par disparaître alors que γ augmente.

La figure 4.6 montre le même diagramme de bifurcation qu'en figure 4.5 sur lequel la position des bifurcations a été superposée avec les branches de chaque ECM. Le mécanisme de crise chaotique et de suppression de chaos peut s'expliquer de la manière suivante. Quand γ augmente, les intervalles de taux de rétroaction sur lesquels les ECMs sont stables (représentés par les lignes jaunes épaisses délimitées par les bifurcations en selle qui les stabilisent et les bifurcations en tore qui les déstabilisent) s'allongent. Les régions de chaos s'amincissent en conséquence, causant ainsi une crise chaotique. Pas ailleurs, pour les plus hautes valeurs de γ, on voit que le processus de stabilisation de l'ECM_{n+1} peut se produire avant, (en termes de valeurs de γ), que le processus de déstabilisation de l'ECM_n ne soit accompli. Par conséquent, lorsque le laser atteint la fin de l'ECM_n, il a la possibilité de "sauter" directement sur l'ECM_{n+1} sans bifurquer vers le chaos. Il existe donc des intervalles de γ pour lesquels deux ECMs consécutifs sont stables. Cette bistabilité de modes de cavité externe est à l'origine de la suppression de chaos.

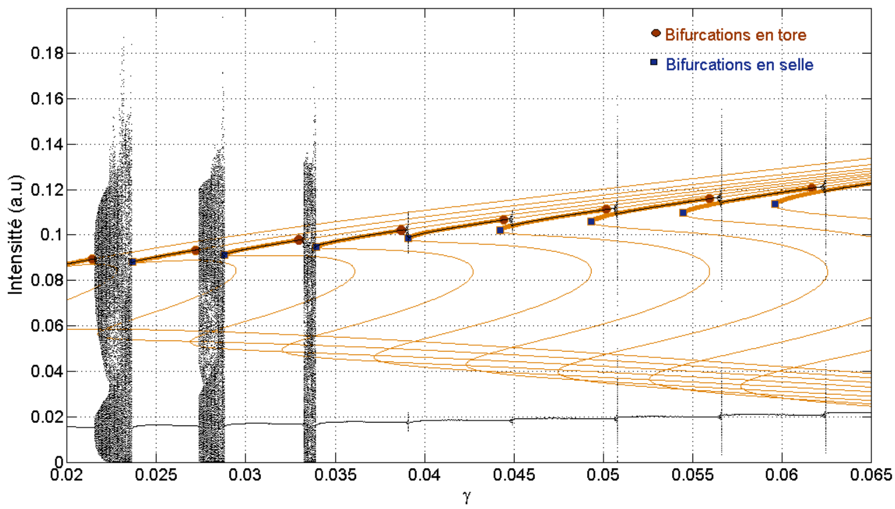

FIGURE 4.6 – Méthode de continuation appliquée au diagramme de bifurcation. Les branches stables des ECMs sont représentées par des lignes jaunes épaisses et les branches instables par des lignes jaunes fines. Quand γ augmente, les régions de stabilité des ECMs s'élargissent aux dépens des régions de chaos développé.

La figure 4.7 montre la distribution fréquentielle des ECMs. On voit que dans les régions de bistabilité le laser a le choix entre deux solutions pulsées à des fréquences différentes, dont l'écart correspond en réalité à la fréquence fondamentale de la cavité externe f_{cav} (soit l'inverse du retard $\tau = \frac{L_{cav}}{c}$). De façon générale, les valeurs de fréquence auxquelles peuvent pulser les modes de cavité externe successifs sont réparties sur la base de la fréquence f_{cav} et sont toutes des multiples de cette fréquence f_{cav}. On appelle alors ECM_n le mode de cavité externe dont la fréquence est égale à nf_{cav}.

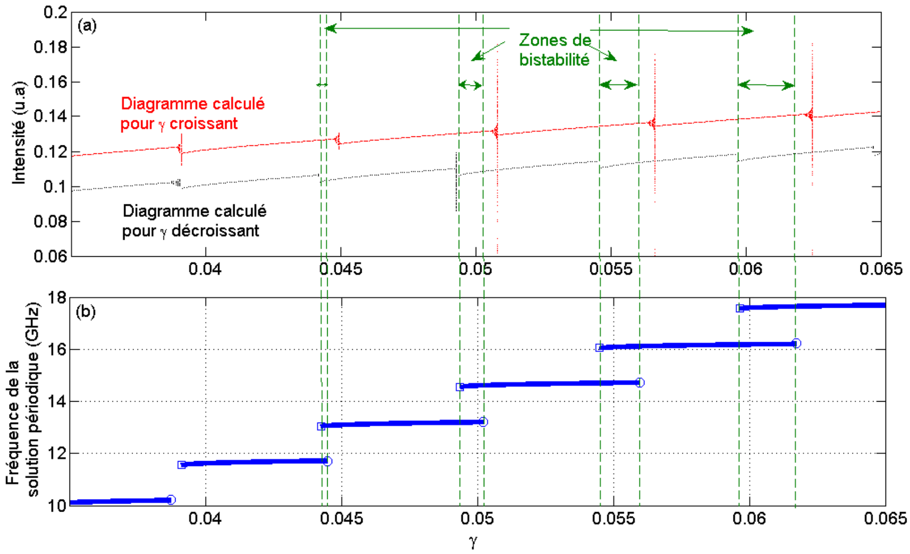

FIGURE 4.7 – Régions de bistablilité. La figure (a) montre en rouge le diagramme de bifurcation calculé pour des valeurs de γ croissantes et en noir pour des valeurs décroissantes. Les diagrammes sont décalés verticalement pour une meilleure lisibilité. La figure (b) montre les solutions auto-pulsées et leurs fréquences respectives. Les domaines de bistabilité (délimités par les lignes interrompues verticales vertes) correspondent à des intervalles de γ sur lesquels deux solutions pulsées (ECMs) sont stables.

Il et aussi intéressant d'étudier l'influence des différents paramètres de simulation (T, P, α et θ) sur l'allure du diagramme de bifurcation en termes de points de bifurcation et stabilité des dynamiques observables. Il apparaît qu'une variation de T influe peu sur l'aspect général. On observe cependant que lorsque T est grand une légère stabilisation due au rétrécissement des régions chaotiques est constatée. P et α agissent tout deux dans le même sens dans la mesure où quand leurs valeurs sont plus élevées, le laser se déstabilise plus vite en faisant que les régions correspondant aux ECMs stables diminuent au profit des zones de chaos. θ est un paramètre dont les effets sont plus visibles. En effet, un retard plus court décale les points de bifurcations vers les valeurs de γ plus élevées, révélant des ECMs stables sur de longs intervalles de taux de rétroaction. Pour des valeurs de θ élevées, les bifurcations se rapprochent et le diagramme semble ne montrer que du chaos en continu sur un grand intervalle de γ. Cependant la crise chaotique et la suppression de chaos sont toujours observées pour des valeurs de γ suffisamment grandes.

Chapitre 5

Modes de cavité externe auto-pulsés

5.1 Visualisation expérimentale

Nous présentons dans ce chapitre le résultat expérimental majeur de ce travail sur la dynamique des diodes laser avec PCF : la première observation expérimentale de modes de cavité externe auto-pulsés dans une diode laser. Nous avons vu dans les prévisions théoriques que ces ECMs sont censés avoir une répartition fréquentielle particulière et totalement dépendante de la longueur de la cavité externe : $f_{ECM\ n} = \frac{nc}{L_{cav}}$. Nous révélons ici des pulsations à deux de ces fréquences ainsi que les transitions vers ces ECMs et leur déstabilisation vers le chaos.

La figure 5.1 montre l'évolution de la trace temporelle et des spectres du laser depuis l'état stationnaire vers le chaos en manifestant deux ECMs se stabilisant et de déstabilisant. La trace (a) représente l'état stationnaire puis, alors que R augmente, le laser montre la trace (b) sur laquelle la signature du retard (à la fréquence fondamentale de la cavité externe $f_{cav} = 680\ MHz$) est visible, notamment sur les spectres. Elle marque en réalité la fin d'un attracteur chaotique sur lequel l'influence du retard se dénote avant de bifurquer vers un cycle limite (trace c), à l'évolution harmonique dont la fréquence de 1360 MHz correspond au double de la fréquence de la cavité externe : $1360\ MHz = 2f_{cav}$. La même dynamique est remarquée sur la trace (d) qui, elle, pulse à 2064 MHz, soit $3f_{cav}$. Nous pouvons donc identifier les traces (c) et (d) comme étant respectivement les deuxième et troisième modes de cavité externe de l'expérience. La transition entre l'ECM2 et l'ECM3 fut expérimentalement très rapide, et il ne fut possible de la suivre. Cependant, la déstabilisation de l'ECM3 montre une route vers le chaos par triplement de période (trace e) suivi encore d'une multiplication de période (f) avant de ne montrer que du chaos développé sans qu'il n'y soit plus possible d'y distinguer le présence du retard.

Nous remarquerons que toute cette succession de stabilisation et de déstabilisation d'ECMs et route vers le chaos se produit sur un intervalle de taux de rétroaction réduit : pour $R > 1\%$, le laser ne montre plus que du chaos. Notons aussi que le premier ECM, celui que l'on s'attendrait à voir pulser à 680 MHz, ne fut pas visible dans l'expérience. Il est possible que son intervalle de stabilité soit trop court ou même noyé dans une région de chaos.

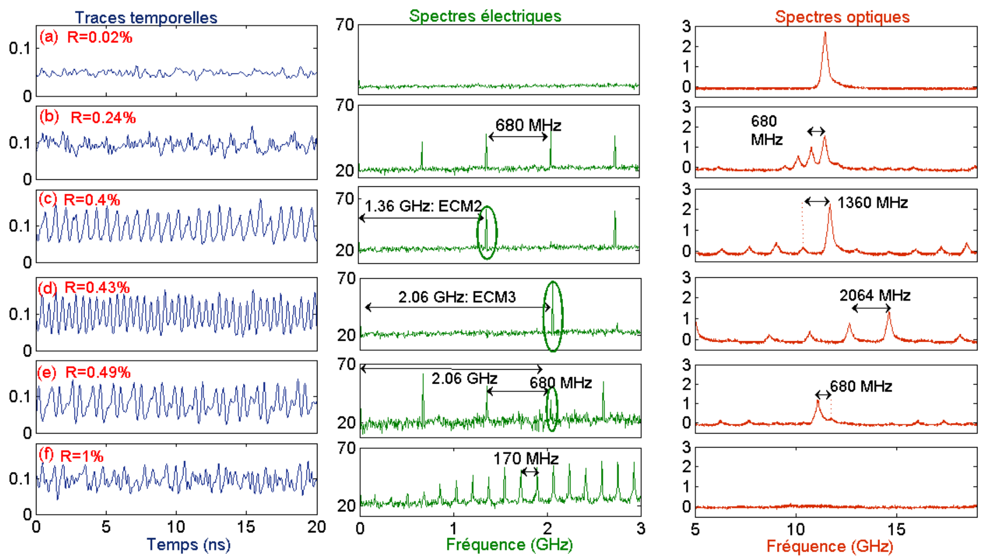

FIGURE 5.1 – Évolution temporelle et spectrale quand R augmente. L'axe des ordonnées est en unités arbitraires, l'échelle est linéaire pour les traces temporelles et logarithmique pour les spectres.

Remarquons que la valeur de la fréquence fondamentale de la cavité externe $f_{cav} = 680\ MHz$ correspond à une distance équivalente parcourue dans la cavité de $L_{cav} = 44\ cm$. Nous avons, pour cette visualisation des ECMs, travaillé avec une génération de faisceau conjugué opéré par un réseau de réflexion dans le cristal afin de minimiser le retard. En effet, ces 44 cm correspondent à la distance aller-retour entre le laser et le cristal. L'avantage de pouvoir travailler avec un réseau de réflexion au lieu d'un réseau de transmission est de raccourcir le retard, ne prenant ainsi pas en compte la propagation dans la cavité en anneau, afin de pouvoir avoir une meilleure chance d'observer les premiers ECMs. En effet, comme prédit par la théorie, et confirmé expérimentalement, un retard plus court déplace les bifurcations vers les plus hautes valeurs de taux de rétroaction, laissant ainsi les intervalles de stabilité des ECMs plus longs.

5.2 Confirmation théorique

Nous avons cherché à trouver un jeu de paramètres pour lesquels il serait possible d'obtenir en simulation la même évolution de dynamiques que celle présentée expérimentalement sur la figure 5.1. Nous cherchons donc un scénario où l'on verrait les ECMs 2 et 3 (mais pas l'ECM1), suivis d'une route vers le chaos par multiplication de période. Ce scénario est visible sur les traces simulées présentées en figure 5.3, correspondant au diagramme de bifurcation de la figure 5.2. Les paramètres de la simulation sont : $P = 0.04$, $T = 1000$, $\alpha = 2.2$ et $\theta = 1050$. Cette valeur de θ correspond au retard physique de l'expérience : $\theta = 1050 \Leftrightarrow f_{cav} \simeq 680\ MHz$.

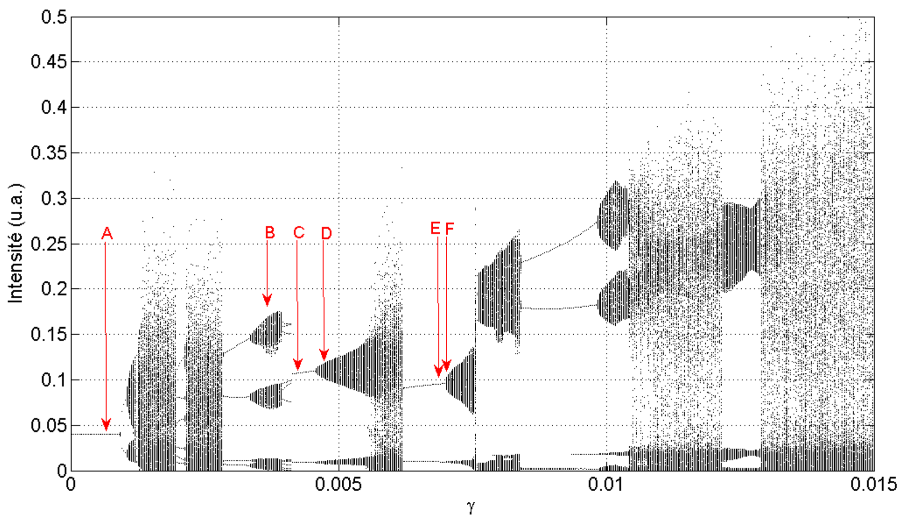

FIGURE 5.2 – Diagramme de bifurcation pour $\theta = 1050$, $P = 0.04$, $T = 1000$, et $\alpha = 2.2$.

On retrouve sur la figure 5.3 le même enchaînement de dynamiques que présenté expérimentalement en figure 5.1. Le scénario débute avec la trace (A) correspondant à l'état stationnaire puis, pour γ plus élevé, on voit des fluctuation irrégulières portant la signature du retard (B), dont la fréquence est d'environ 650 MHz. Les traces (C) et (E) sont les ECMs 2 et 3. On voit ici le processus de déstabilisation de l'ECM2 avant de donner l'ECM3 par triplement de période (D), en suivant le même procédé que la route vers le chaos amorcée par l'ECM3 expérimentalement. Ensuite, si γ augmente encore, le système bifurque vers un état de chaos développé (F).

Cette confrontation entre résultats expérimentaux et théoriques apporte

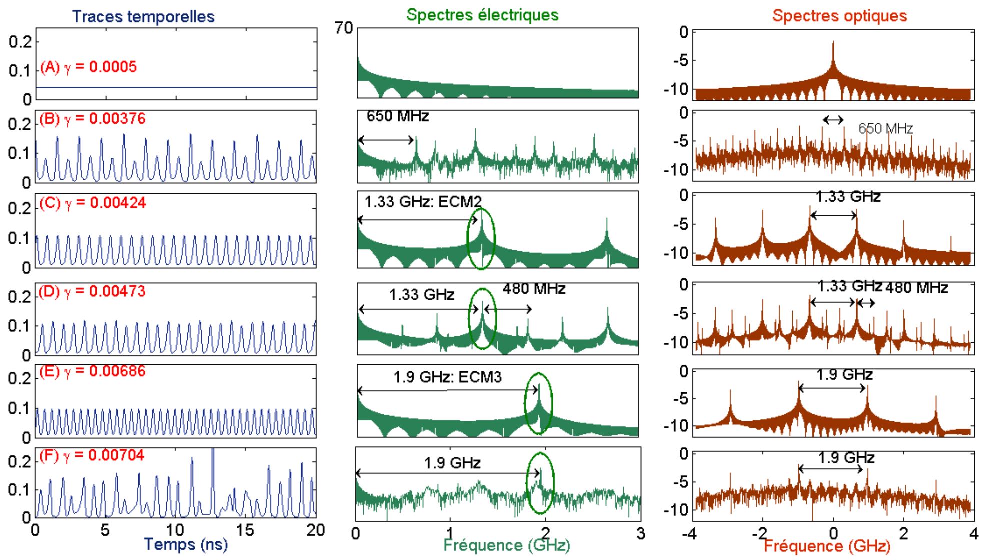

FIGURE 5.3 – Traces temporelles et spectres simulés correspondant aux dynamiques A à F du diagramme de la figure 5.2. L'axe des ordonnées est en unités arbitraires, l'échelle est linéaire pour les traces temporelles et logarithmique pour les spectres.

un très bon accord qualitatif quant aux ECMs qui sont visibles ainsi qu'à leurs fréquences de pulsation et leurs processus de stabilisation et déstabilisation. La transition entre modes de cavités auto-pulsés successifs se fait donc par multiplication de période et quasi-périodicité mettant en jeu la fréquence de la cavité externe et ses multiples.

Nous avons ainsi apporté la première preuve expérimentale de modes de cavité auto-pulsés à des fréquences multiples de la fréquence de la cavité dans une diode laser soumise à rétroaction à conjugaison de phase. Nous avons aussi documenté leurs transitions et apporté une confirmation de leurs dynamiques relatives par simulation.

Chapitre 6
Événements extrêmes

Ce chapitre traite de l'apparition d'événements extrêmes dans la puissance du laser pouvant survenir sans prévenir sous l'effet du taux de rétroaction. Ces événements particuliers, aussi appelés rogue waves, événements rares, ou vagues scélérates sont caractérisés par leur grande amplitude, par rapport aux aux autres événements se produisant dans le système, ainsi que par la déformation de la distribution d'énergie du système.

6.1 Définition et visualisation

Les événements extrêmes sont étudiés dans de nombreux domaines de la physique comme l'océanographie, la physique des plasmas et l'électromagnétisme [56–58]. En optique, ces événements extrêmes ont aussi été documentés dans des fibres optiques à miscrostructures [59], dans des lasers montrant du mode-locking [60, 61] et dans les diodes à injection optique [62, 63].

Dans notre système de laser à retard, nous nous intéressons à la possibilité d'occurrence de ces événements rares sous l'effet de la force de la rétroaction. Nous considérons que chaque pic dans la puissance optique émise par le laser est un événement. Elle est par conséquent constituée d'une succession d'événements. Chacun de ces pics est potentiellement un événement extrême. Pour discriminer les événements pouvant être considérés comme extrêmes de ceux qui ne le sont pas, nous utilisons deux critères de sélection. Le premier est un critère sur l'amplitude, connu sur le nom d'indice d'anormalité noté AI (Abnormality Index) et consiste en un seuil dont la valeur dépend des amplitudes de tous les événements du signal comme défini dans la référence [64]. Un pic de puissance vérifiant $AI > 2$ pourra être considéré comme étant un événement extrême si le second critère est vérifié. Ce second critère porte sur la distribution en puissance du signal sur l'ensemble de ses événements. Conformément à la référence [65], les événements extrêmes doivent induire une déformation de la distribution de la puissance en faisant apparaître un allongement pour les hautes valeurs de puissance. Ainsi, les événements vérifiant à la fois la condition sur l'indice d'anormalité et sur la déformation de la distribution seront considérés dans notre cas comme des événements extrêmes.

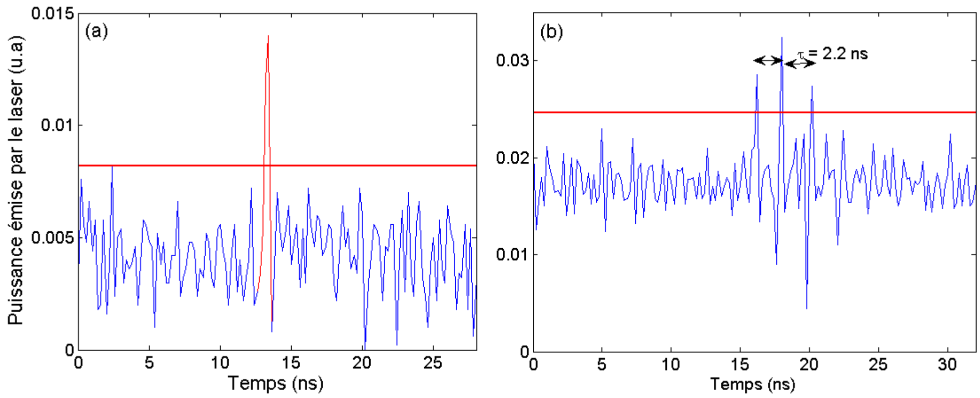

FIGURE 6.1 – Événements extrêmes visibles dans la puissance du laser : soit sous forme de pics isolés (a) soit sous la forme de groupes de pics séparés par le retard τ (b). Les lignes rouges sont les seuils $AI = 2$.

En analysant en détails la trace temporelle du laser soumis au PCF, il apparaît que les événements extrêmes peuvent apparaître sous deux formes : soit sous forme de pics isolés sans lien apparent les uns avec les autres (formant le groupe I) soit sous la forme de groupes de quelques pics très rapprochés, et, plus précisément, séparés les uns des autres par un intervalle de temps proche du retard temporel (τ =2.2 ns sous les conditions expérimentales avec lesquelles les événements extrêmes sont observés), formant le groupe II. La figure 6.1 présente ces deux types d'événements extrêmes.

L'évolution de l'apparition d'événements extrêmes dans la puissance du laser en fonction de la réflectivité du miroir à conjugaison de phase est présentée en figure 6.2. On y voit que plus R augmente, plus le nombre d'événements franchissant le seuil $AI = 2$ augmente aussi. En effet, pour les plus faibles valeurs de R, aucun événement extrême n'est présent, jusqu'à ce que 1.8 % des événements soient des événements extrêmes pour R=7 %. De plus, l'évolution de l'enveloppe de ces histogrammes, représentant la distribution de l'amplitude des événements présentée en figure 6.3 illustre clairement le déviation de la distribution gaussienne existant en l'absence d'événements extrêmes causée par l'émergence de ceux-ci quand R croît.

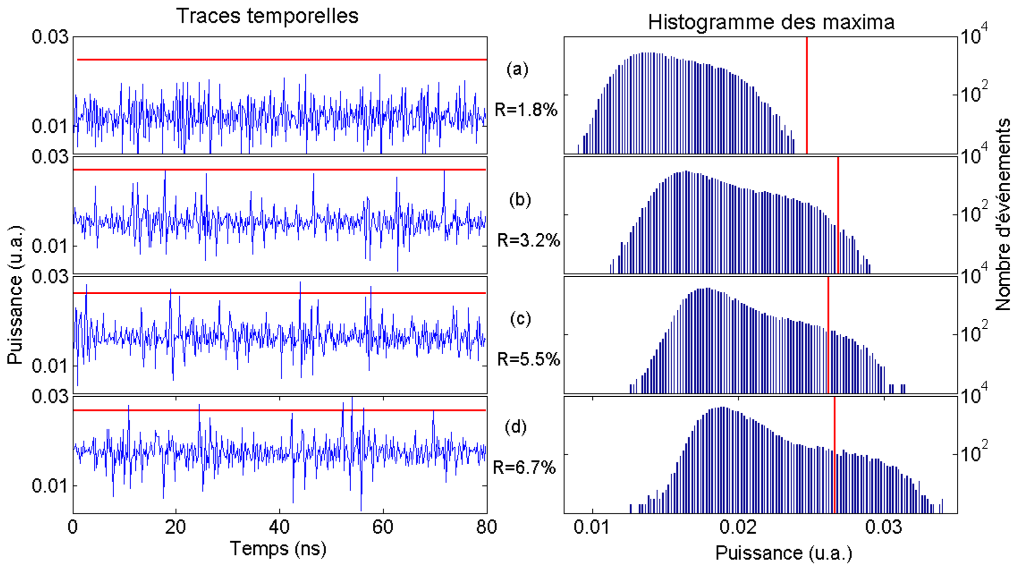

FIGURE 6.2 – Traces temporelles et histogrammes des pics d'intensité pour des valeurs de R croissantes. Les lignes rouges verticales et horizontales représentent les seuils correspondant à $AI = 2$.

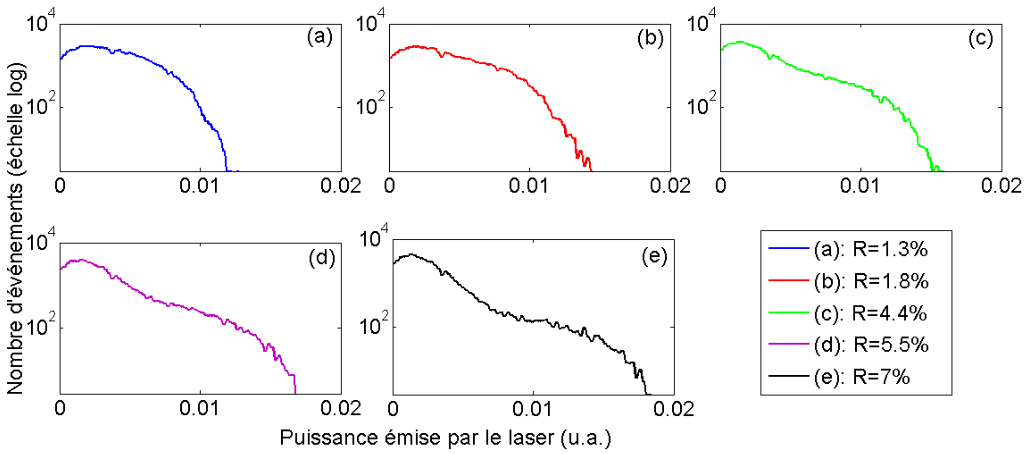

FIGURE 6.3 – Distortion de la distribution des amplitudes des pics dans la puissance du laser pour R (de (a) à (e)) croissant. L'apparition d'une nouvelle concavité grandissante témoigne de la présence des événements extrêmes.

6.2 Distribution temporelle

Une propriété remarquable des événements extrêmes visibles dans la trace temporelle du laser est leur répartition en fonction du temps, ainsi que l'influence de la force de la rétroaction sur cette répartition. L'effet de cette rétroaction est visible sur la figure 6.4 où les intervalles de temps entre événements extrêmes consécutifs sont représentés pour $R = 4.4\%$ et $R = 7\%$. Conformément à ce qui est attendu d'après l'étude d'événements extrêmes dans d'autres systèmes optiques comme la référence [65], on voit que la statistique suit une distribution poissonienne, représentée ici en échelle logarithmique par une droite sur le graphique (a) où le taux de rétroaction est faible. Cependant, dans le cas (b) où la réflectivité du miroir est plus forte ($R = 7\%$), la distribution des temps entre événements extrêmes dévie de la simple droite et montre en réalité deux droites aux pentes différentes. Il est intéressant de constater que l'échelle de temps pour laquelle cette déviation de la droite initiale est significative est proche de l'échelle de temps du retard. Sous l'effet d'une rétroaction grandissante, les événements extrêmes sont en quelque sorte incités à se produire plus souvent (donc à être plus nombreux) mais aussi à se produire préférentiellement à des échelles de temps proches de celle du retard lui-même qui impose de cette façon sa dynamique temporelle sur le système.

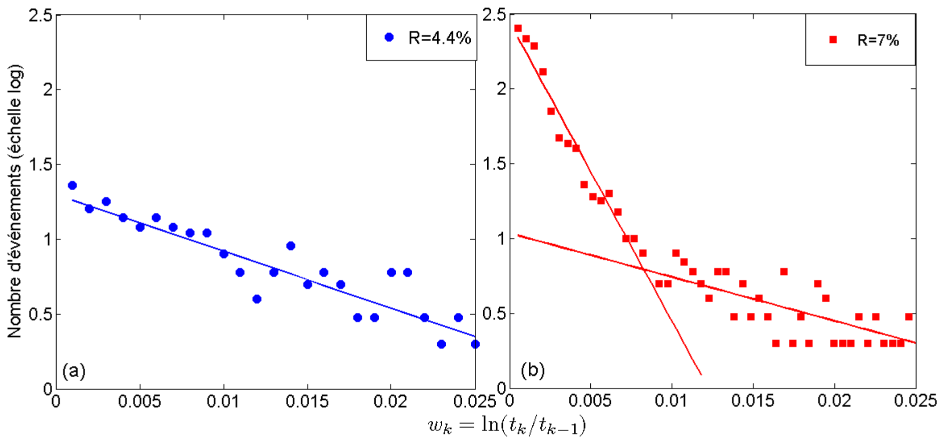

FIGURE 6.4 – Distribution temporelle statistique des temps entre événements extrêmes pour $R = 4.4\%$ (a) et $R = 7\%$ (b). On note t_k l'instant où se produit l'événement extrême k.

Une rapide simulation du système montre également que les événements extrêmes sont attendus par la théorie, bien que nous n'ayons pas identifié le scénario de bifurcations qui les fait se produire.

CHAPITRE 7

Fluctuations à basse fréquence

Ce chapitre s'intéresse à la visualisation de fluctuations à basse fréquence dans la trace temporelle du laser. Nous étudions aussi leur évolution quand la réflectivité du miroir augmente et mettons en évidence une résonance cohérente déterministe induite par le retard de la rétroaction.

7.1 Définition et évolution avec R

Les fluctuations à basse fréquence (aussi connues sous le nom de LFF pour Low-Frequency Fluctuations) se produisent quand le laser est en régime chaotique et sont caractérisées par des chutes soudaines de puissance suivies de retour plus lents au niveau initial. L'échelle de temps sur laquelle ces chutes se produisent est très grande ($\simeq 100\ ns$) devant l'échelle de temps des oscillations du laser ($\simeq 10\ ps$), d'où l'appellation de fluctuations à basse fréquence. Depuis leur première mise en évidence expérimentale par Risch et Voumard en 1977 [66], elles furent étudiées avec le modèle de Lang-Kobayashi dans le cas du COF où elles ont été identifiées comme provenant d'une séquence de bifurcations sur un grand nombre de modes de cavité externe. Dans le cas du PCF, leur existence est documentée expérimentalement [31] bien qu'aucune explication théorique quant à leur origine n'ait été développée jusqu'à présent.

La figure 7.1 présente comment apparaissent et évoluent les LFF dans notre expérience. On y voit que lorsque R augmente, le laser montre une transition depuis un état de chaos développé vers une dynamique caractéristique de ces chutes de puissances soudaines suivies de retours plus lents au niveau initial de puissance ($R = 3.5\%$). Dans les spectres associés, cette transition est facilement visible par l'apparition de composantes fréquentielles pour les fréquences les plus faibles qui naissent et gagnent en intensité par rapport au reste du spectre. La signature du retard est visible dans la répartition parfaitement régulière des pics de fréquence à des intervalles égaux à $\frac{1}{\tau} = 220\ MHz$. En effet, la longueur de la cavité externe est dans ce cas de 132 cm, ce qui correspond à $f_{cav} = 220\ MHz$. En fonction du taux de rétroaction, la régularité des chutes de puissance et le finesse des pics de fréquence

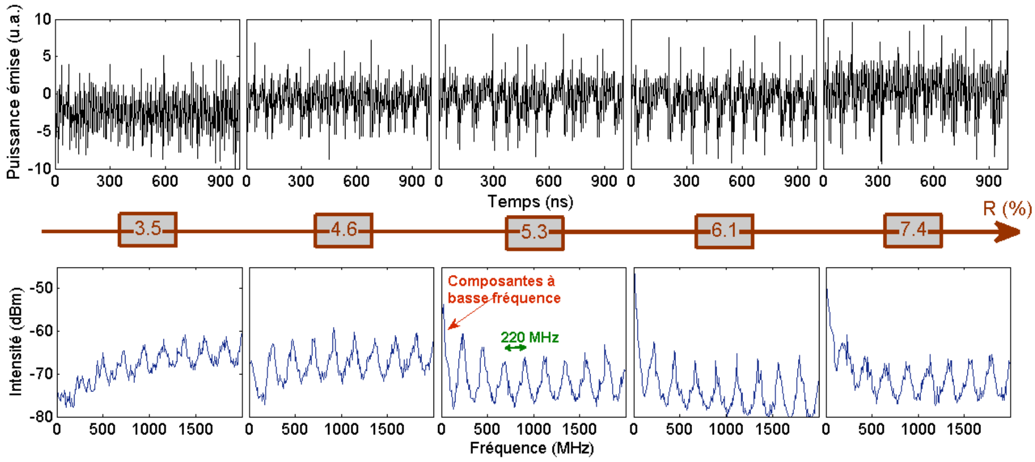

FIGURE 7.1 – Naissance des fluctuations à basse fréquence et évolution qualitative quand R augmentes. Les traces du bas représentent les spectres électriques associés aux traces temporelles du haut.

varie.

7.2 Cohérence résonante induite par le retard

Il est commun de trouver le phénomène de résonance dans divers systèmes physiques soumis ou non à des signaux externes dans lesquels la réponse du système à une excitation est optimale. Lorsqu'un système non linéaire montre une réponse optimale à sa propre échelle de temps en présence de bruit, on parle de résonance cohérente. La résonance cohérente fut d'abord mise en évidence par Pikovsky et Kurths en 1997 [67] dans un système excitable.

Des exemples de résonance cohérente en optique peuvent être trouvés dans divers systèmes dynamiques [68], des diodes laser soumises à de la rétroaction [23] ou des systèmes bistables [69]. Nous nous intéressons ici au phénomène de résonance cohérente dans la distribution des chutes de puissances vues en régime de LFF.

La figure 7.2 montre l'évolution des traces temporelles et des histogrammes des temps entre chutes de puissance (notés T_{LFF}) associés. Expérimentalement, lorsque la réflectivité du miroir augmente, les LFF ont tendance à s'organiser en des chutes de puissance de plus en plus régulières jusqu'à une certaine valeur de réflectivité. Là, les traces les plus régulières, c'est-à-dire celles qui montrent les spectres les plus fins et les histogrammes les moins larges, sont observées. Dans notre expérience, cela se produit pour $R = 6.1\%$. Pour des valeurs de R supérieures, cette régularité est progressivement perdue.

En plus de l'observation qualitative de la régularité des traces temporelles et de la finesse des spectres, un moyen de quantifier la dispersion de T_{LFF} est d'analyser les histogrammes des temps entre chutes de puissance. En effet, la figure 7.2 montre la déformation de la distribution des temps entre chutes alors que R augmente. On y voit à nouveau qu'il existe une valeur de R optimale pour laquelle la distribution est plus fine et plus regroupée autour de sa valeur moyenne, indiquant ainsi une dispersion plus faible du temps entre chutes. Une augmentation de la réflectivité résulte en une perte de cette régularité maximale.

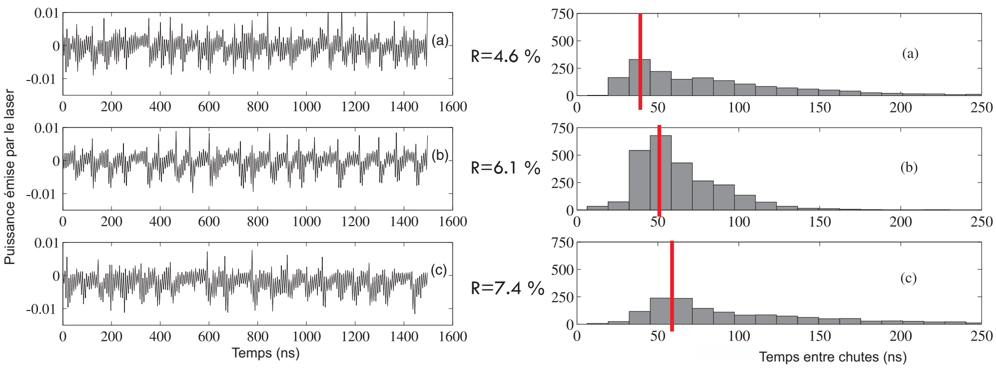

FIGURE 7.2 – Évolution des LFF en fonction de la réflectivité du miroir vues sur les traces temporelles (à gauche). Les distributions des temps entre chutes de puissance T_{LFF} associées sont représentées à droite. Les barres rouges marquent les valeurs moyennes de T_{LFF} pour chaque cas.

Le fait que l'optimum de régularité soit atteint pour $R = 6.1\%$ dans notre cas est confirmé par trois indicateurs :
1/ La trace temporelle da la figure 7.2.(b) est la plus régulière.
2/ Le spectre électrique associé à cette même trace temporelle sur la figure 7.1 présente des pics de fréquence plus fins lorsque $R = 6.1\%$.
3/ La distribution de T_{LFF} sur la figure 7.2.(b) présente la dispersion la plus faible.

L'existence de cette régularité optimale pour une valeur particulière de réflectivité démontre un phénomène de résonance cohérente induite par le taux de rétroaction. La figure 7.3 montre l'évolution de la déviation normalisée

$V = \frac{\sigma_{T_{LFF}}}{<T_{LFF}>}$ des temps entre chutes pour R croissant où $\sigma_{T_{LFF}}$ et $< T_{LFF} >$ sont respectivement l'écart-type et la moyenne des temps entre chutes T_{LFF}. On y distingue clairement un minimum pour V lorsque $R = 6.1\%$, témoignant de la régularité optimale des temps entre chutes et donc de la réponse optimale du laser à la rétroaction pour cette valeur de réflectivité particulière. Tout comme dans les cas des références [67] et [70], nous pouvons conclure que la présence de ce minimum est la signature d'une résonance cohérente.

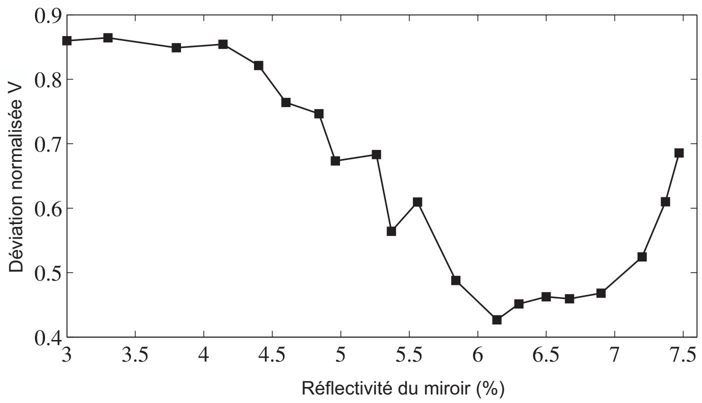

FIGURE 7.3 – Évolution de $V = \frac{\sigma_{T_{LFF}}}{<T_{LFF}>}$ en fonction de la réflectivité du miroir à conjugaison de phase R. Un minimum est constaté lorsque $R = 6.1\%$, signature d'une résonance.

Puisque notre système évolue en l'absence de modulation externe (comme souvent appliqué à l'aide du courant d'alimentation [71] ou d'une variation de la longueur de la cavité externe [72]), il s'agit d'une résonance cohérente. De plus, contrairement aux cas de résonances cohérentes courantes, cette résonance se produit sans la nécessité d'apporter un bruit quelconque. Par conséquent, nous dénommons ce type de résonance cohérente une résonance cohérente déterministe induite par la rétroaction à retard. En effet, c'est un système dans lequel la résonance a lieu en changeant le taux de rétroaction sans addition de bruit externe.

Une simulation menée sur un laser de classe A, donc ne présentant pas de phénomène d'oscillations de relaxation, montre que le même phénomène de résonance cohérente se produit pour une certaine valeur de taux de rétroaction. Ceci indique que ce résultat expérimental sur la résonance cohérente n'est pas limité au cas des diodes laser mais peut être généralisée à un champ de systèmes optiques à retard plus large.

D'autres simulations sur le modèle théorique montrent des transitions depuis le chaos développé vers le régime de LFF, ce qui apporte une confirmation théorique aux observations expérimentales. Cependant nous n'avons pas cherché à mettre en évidence une résonance cohérente ou la cascade de bifurcations menant au régime de LFF.

Chapitre 8

Conclusion et perspectives

8.1 Résumé des résultats

Cette étude de la dynamique non linéaire d'une diode laser soumise à rétroaction optique par conjugaison de phase nous a amenés à nous intéresser à différents points.

Le premier fut la conception d'un banc expérimental permettant l'étude de ce système, en générant de la conjugaison de phase au moyen d'un mélange à quatre ondes dans un cristal photoréfractif de SPS. Puis nous nous sommes intéressés à l'étude théorique de la dynamique du système en mettant en évidence les bifurcations vers le chaos, les phénomènes de crise chaotique, bistabilité entre ECMs et suppression de chaos. Les résultats expérimentaux montrèrent pour la première fois dans un système laser avec PCF une transition vers des solutions auto-pulsées à des fréquences multiples de la fréquence de la cavité externe : les modes de cavité externe (ECMs). Nous avons aussi rendu compte du processus de stabilisation et de déstabilisation de ces ECMs. Nous avons ensuite vu, pour des valeurs de réflectivités et de tailles de cavité externe supérieures que le laser pouvait montrer des événements extrêmes caractérisés par leur haute amplitude et la déformation de la statistique qu'ils engendrent. L'influence de la rétroaction sur leur distribution temporelle fut aussi démontrée. Enfin, le régime de fluctuations à basse fréquence (LFF) avec le phénomène de résonance cohérente induit par la rétroaction fut aussi caractérisé dans notre système.

La figure 8.1 résume en un seul diagramme de bifurcation les intervalles de taux de rétroaction sur lesquels les différentes dynamiques mentionnées et étudiées dans cette thèse sont observables. Expérimentalement, les transitions entre dynamiques sont causées par une variation du taux de rétroaction, via la réflectivité du miroir à conjugaison de phase. Mais pour une analyse systématique d'une dynamique particulière, il existe des conditions expérimentales plus propices que d'autres, en particulier en termes de valeur du retard, via la longueur de la cavité externe. Ces deux paramètres (force et retard de la rétroaction) sont fondamentaux et conditionnent totalement le

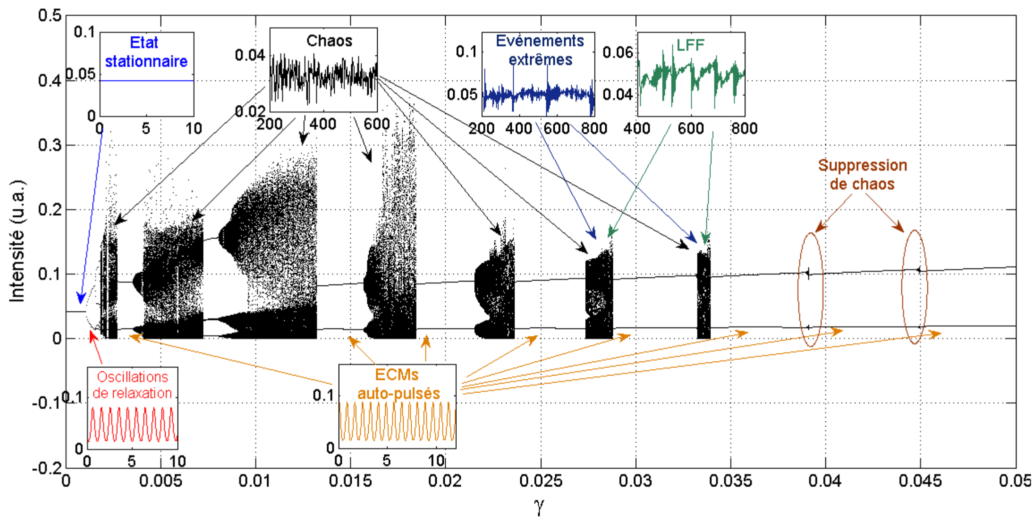

FIGURE 8.1 – Diagramme de bifurcation résumant la répartition des dynamiques. Les paramètres pris pour la simulation sont $P = 0.0417$, $T = 1428$, $\alpha = 3$ et $\theta = 476$.

point de fonctionnement dynamique du laser.

8.2 Contributions personnelles

Au-delà de l'intérêt théorique de la poursuite de l'étude de ce système pour des gammes de paramètres encore inexploités, comme lors de l'étude de la crise chaotique et de la suppression de chaos, l'apport de cette thèse est essentiellement expérimental. Et c'est dans l'identification des modes de cavité externe auto-pulsés que notre contribution est la plus importante. La démonstration expérimentale des solution harmoniques aux fréquences multiples de la fréquence de la cavité externe, depuis longtemps prédites par la théorie mais jusqu'alors jamais vues, ouvre la voie vers des applications de génération tout optique de signaux périodiques à haute fréquence. En effet, nous avons montré que ces solutions s'échelonnent en fréquences multiples de f_{cav} : $f_{ECMn} = nf_{cav}$. Avec un meilleur contrôle de la stabilité de ces solutions, il serait possible d'atteindre des valeurs de n élevées et par conséquent de pulser à plusieurs dizaines de GHz, sans modulation électrique extérieure.

Nous soulignons aussi l'importance cruciale du retard et du taux de rétroaction qui décident conjointement des régions de stabilité des différentes dynamiques visibles dans le laser. Nous sommes convaincus d'avoir franchi un pas dans le contrôle de chaos dans les lasers et leur accordabilité.

À l'aide du simple modèle des équations de Lang-Kobayashi adaptées au cas du PCF, nous avons pu apporter diverses confirmations théoriques aux comportements expérimentaux observées avec une bonne fidélité qualitative.

8.3 Perspectives

Pour aller plus loin dans l'étude de ce système, nous proposons quelques pistes d'analyse dans la continuité immédiate de notre étude :

1/ Il serait intéressant de mener une étude théorique plus poussée sur l'apparition des événements extrêmes ainsi que des LFF dans le cas du PCF et a fortiori de mettre en évidence une résonance cohérente déterministe comme dans l'expérience.

2/ La prise en compte du temps de réponse du miroir dans le modèle théorique, lié aux interactions non linéaires dans le cristal photoréfractif pourrait mener à un scénario plus proche de celui observé expérimentalement, avec un meilleur accord qualitatif.

3/ Sur l'étude des ECMs auto-pulsés, la recherche de solutions à des multiples de la fréquence de la cavité externe d'ordres plus élevés serait aussi une grande avancée dans la génération de signaux tout optique à haute fréquence. D'après ce qui a été vu ici, cette recherche serait probablement facilitée en travaillant dans des configurations de cavités externes courtes.

Bibliographie

[1] G.H.M van Tartwijk and D. Lenstra, “Semiconductor lasers with optical injection and feedback”, *Quantum Semiclassical Optics*, vol. 7, pp. 87, 1995.

[2] K. Petermann, “External optical feedback phenomena in semiconductor lasers”, *IEEE J. Sel. Top. Quantum Electron.*, vol. 1, pp. 480–489, 1995.

[3] L. Goldberg, H.F. Taylor, A. Dandridge, J.F. Weller, and R.O. Miles, “Spectral characteristics of semiconductor lasers with optical feedback”, *IEEE Transactions on Microwave Theory and Techniques*, vol. 30, pp. 401–410, 1982.

[4] J. Osmundsen and N. Gade, “Influence of optical feedback on laser frequency spectrum and threshold conditions”, *IEEE Journal of Quantum Electronics*, vol. 19, pp. 465–469, 1983.

[5] D.R. Hjelme, A.R. Mickelson, and R.G. Beausoleil, “Semiconductor laser stabilisation by external optical feedback”, *IEEE Journal of Quantum Electronics*, vol. 27, pp. 352–372, 1991.

[6] M.W. Fleming and A. Mooradian, “Spectral characteristics of external-cavity controlled semiconductor lasers”, *IEEE Journal of Quantum Electronics*, vol. 17, pp. 44–59, 1981.

[7] F. Favre, D. Le Guen, and J. Simon, “Optical feedback effects upon laser diode oscillation field spectrum”, *IEEE Journal of Quantum Electronics*, vol. 18, pp. 1712–1717, 1982.

[8] S. Sampei, H. Tsuchida, M. Ohtsu, and T. Tako, “Frequency stabilization of $AlGaAs$ semiconductor lasers with external grating feedback”, *Japanese Journal of Applied Physics*, vol. 22, pp. 258–260, 1983.

[9] H.R. Telle, “Narrow linewidth laser diodes with broad continuous tuning range”, *Applied Physics B*, vol. 49, pp. 217–226, 1989.

[10] R.W. Tkach and A.R. Chraplyvy, “Regimes of feedback effects in 1.5 μm distributed feedback lasers”, *Journal of Lightwave Technology*, vol. 4, pp. 1655–1661, 1986.

[11] J. Wang and K. Petermann, “Noise analysis of semiconductor lasers within the coherence collapse regime”, *IEEE Journal of Quantum Electronics*, vol. 27, pp. 3–9, 1991.

[12] J. Mørk, B. Tromborg, and J. Mark, “Chaos in semiconductor lasers with feedback : theory and experiment”, *IEEE Journal of Quantum Electronics*, vol. 28, pp. 93–108, 1992.

[13] H. Li, J. Ye, and J.G. McInerney, "Detailed analysis of coherence collapse in semiconductor lasers", *IEEE Journal of Quantum Electronics*, vol. 29, pp. 2421–2432, 1993.

[14] J.S. Cohen, R.R. Drenten, and B.H. Verbeeck, "The effect of optical feedback on the relaxation oscillation in semiconductor lasers", *IEEE Journal of Quantum Electronics*, vol. 24, pp. 1989–1995, 1988.

[15] C.H. Henry and R.F. Kazarinov, "Instability of semiconductor lasers due to optical feedback from distant reflectors", *IEEE Journal of Quantum Electronics*, vol. 22, pp. 294–301, 1986.

[16] H. Sato, T. Fujita, and K. Fujito, "Intensity fluctuation in semiconductor lasers coupled to external cavity", *IEEE Journal of Quantum Electronics*, vol. 21, pp. 46–51, 1985.

[17] B. Tromborg, J. Osmundsen, and H. Olesen, "Stability analysis for a semiconductor laser in an external cavity", *IEEE Journal of Quantum Electronics*, vol. 20, pp. 1023–1032, 1984.

[18] F. de Tomasi, E. Cerboneschi, and E. Arimondo, "Asymmetric pulse shape in the LFF instabilities of a semiconductor laser with optical feedback", *IEEE Journal of Quantum Electronics*, vol. 30, pp. 2277–2280, 1994.

[19] M-W. Pan, B-P. Shi, and G.R. Gray, "Semiconductor laser dynamics subject to strong optical feedback", *Optics Letters*, vol. 22, pp. 166–168, 1997.

[20] G.H.M. van Tartwijk, A.M. Levine, and D. Lenstra, "Sisyphus effect in semiconductor lasers with optical feedback", *IEEE Journal of Quantum Electronics*, vol. 1, pp. 466–472, 1995.

[21] D. O'Brien, G. Huyet, and J.G. McInerney, "Low-frequency fluctuations in a semiconductor laser with phase conjugate feedback", *Physical Review A*, vol. 64, pp. 025802, 2001.

[22] A.M Yacomotti, M.C. Eguia, J. Aliaga, O.E. Martinez, G.B. Mindlin, and A. Lipsich, "Interspike time distribution in noise driven excitable systems", *Physical Review Letters*, vol. 83, pp. 292–295, 1999.

[23] G. Giacomelli, M. Giudici, S. Balle, and J. Tredicce, "Experimental evidence of coherence resonance in an optical system", *Physical Review Letters*, vol. 84, pp. 3298–3301, 2000.

[24] G.R. Gray, D. Huang, and G.P. Agrawal, "Chaotic dynamics of semiconductor lasers with phase-conjugate feedback", *Physical Review A*, vol. 49, pp. 2096–2105, 1994.

[25] P. Yeh, *Introduction to Photorefractive Nonlinear Optics*, Wiley, 1993.

[26] G.H.M. van Tartwijk, H.J.C. van der Linden, and D. Lenstra, “Theory of a diode laser with phase-conjugate feedback”, *Optics Letters*, vol. 17, pp. 1590–1592, 1992.

[27] E. Bochove, “Theory of a semiconductor laser with phase-conjugate optical feedback”, *Physical Review A*, vol. 55, pp. 3891–3899, 1997.

[28] B. Krauskopf, G.R. Gray, and D. Lenstra, “Semiconductor laser with phase-conjugate feedback : dynamics and bifurcations”, *Physical Review E*, vol. 58, pp. 7190–7197, 1998.

[29] T. Erneux, A. Gavrielides, K. Green, and B. Krauskopf, “External cavity modes of semiconductor lasers with phase-conjugate feedback”, *Physical Review E*, vol. 68, pp. 066205, 2003.

[30] O.K. Andersen, A.P.A. Fischer, I.C. Lane, E. Louvergneaux, S. Stolte, and D. Lenstra, “Experimental stability diagram of a diode laser subject to weak phase-conjugate feedback from a rubidium vapor cell”, *IEEE Journal of Quantum Electronics*, vol. 35, pp. 577–582, 1999.

[31] J.S. Lawrence and D.M Kane, “Contrasting conventional optical and phase-conjugate feedback in laser diodes”, *Physical Review A*, vol. 63, pp. 033805, 2001.

[32] M. Cronin-Golomb, K.Y. Lau, and A. Yariv, “Infrared photorefractive passive phase conjugation with $\mathrm{B}a\mathrm{T}i\mathrm{O}_3$: Demonstrations with $\mathrm{G}a\mathrm{A}l\mathrm{A}s$ and 1.09-μm $\mathrm{A}r^+$ lasers”, *Applied Physics Letters*, vol. 47, pp. 567–569, 1985.

[33] J. Feinberg, “Self-pumped, continuous-wave conjugator using internal reflection”, *Optics Letters*, vol. 7, pp. 486–488, 1982.

[34] G.R. Gray, D.H. DeTienne, and G.P. Agrawal, “Mode locking in semiconductor lasers by phase-conjugate optical feedback”, *Optics Letters*, vol. 20, pp. 1295–1297, 1995.

[35] E. Miltényi, M.O. Ziegler, M. Hofmann, J. Sacher, W. Elsäßer, E.O. Göbel, and D.L. MacFarlane, “Long-term stable mode locking of a visible diode laser with phase-conjugate feedback”, *Optics Letters*, vol. 20, pp. 734–736, 1995.

[36] G. Klose and A. Siahmakoun, “External mode locking with feedback from a self-pumped phase-conjugator $\mathrm{B}a\mathrm{T}i\mathrm{O}_3$ mirror”, *Optical Engineering*, vol. 35, pp. 2983–2988, 1996.

[37] P. Kürz and T. Mukai, “Frequency stabilization of a semiconductor laser by external phase-conjugate feedback”, *Optics Letters*, vol. 21, pp. 1369–1371, 1996.

[38] A. Shiratori and M. Obara, "Wavelength-stable, narrow-spectral-width oscillation of an algainp diode laser coupled to a $BaTiO_3 : Co$ stimulated photorefractive backscattering phase conjugator", *Applied Physics B*, vol. 65, pp. 329–333, 1997.

[39] N. Cyr, M. Breton, M. Têtu, and S. Thériault, "Laser diode frequency control by resonant phase-conjugate reflection from an atomic vapour", *Optics Letters*, vol. 16, pp. 1298–1300, 1991.

[40] L. Petersen, U. Gliese, and T.N. Nielsen, "Phase noise reduction by self-phase locking in semiconductor lasers using phase conjugate feedback", *IEEE Journal of Quantum Electronics*, vol. 30, pp. 2526–2533, 1994.

[41] B.W. Liby and D. Statman, "Controling the linewidth of a semiconductor laser with photorefractive phase conjugate feedback", *IEEE Journal of Quantum Electronics*, vol. 32, pp. 835–838, 1996.

[42] M. Ohtsu, I. Koshiishi, and Y. Teramachi, "A semiconductor laser as a stable phase conjugate mirror for linewidth reduction of another semiconductor laser", *Japanese Journal of Applied Physics*, vol. 29, pp. 2060–2062, 1990.

[43] K. Vahala, K. Kyuma, A. Yariv, S-K. Kwong, M. Cronin-Golomb, and K.Y. Lau, "Narrow linewidth, single frequency semiconductor laser with a phase conjugate external cavity mirror", *Applied Physics Letters*, vol. 49, pp. 1563–1565, 1986.

[44] A. Shiratori and M. Obara, "Frequency stable, narrow linewidth oscillation of a red diode laser with phase conjugate feedback using stimulated photorefractive backscattering", *Applied Physics Letters*, vol. 69, pp. 1515–1516, 1996.

[45] G.P. Agrawal and J.T. Klaus, "Effect of phase-conjugate feedback on semiconductor laser dynamics", *Optics Letters*, vol. 16, pp. 1325–1327, 1991.

[46] R.C. Lind and D.G. Steel, "Demonstration of the longitudinal modes and aberration-correction properties of a continuous-wave dye laser with a phase-conjugate mirror", *Optics Letters*, vol. 6, pp. 554–556, 1981.

[47] M. Cronin-Golomb and C.D. Brandle, "Ring self-pumped phase conjugator using total internal reflection in photorefractive strontium barium niobate", *Optics Letters*, vol. 14, pp. 462–464, 1989.

[48] M. Lucente, G.M. Carter, and J.G. Fujimoto, "Nonlinear mixing and phase conjugation in broad-area diode lasers", *Applied Physics Letters*, vol. 53, pp. 467–469, 1988.

[49] P. Kürz, R. Nagar, and T. Mukai, "Highly efficient phase conjugation using spatially nondegenerate four-wave mixing in a broad-area laser diode", *Applied Physics Letters*, vol. 68, pp. 1180–1182, 1996.

[50] P.P. Vasil'ev and I.H. White, "Phase-conjugation broad area twin-contact semiconductor laser", *Applied Physics Letters*, vol. 71, pp. 40–42, 1997.

[51] I. Park, I. Fischer, and W. Elsäßer, "Highly nondegenerate four-wave mixing in a tunable dual-mode semiconductor laser", *Applied Physics Letters*, vol. 84, pp. 5189–5191, 2004.

[52] T. Bach, M. Jazbinšek, G. Montemezzani, P. Günter, A.A. Grabar, I.M. Stoika, and Y.M. Vysochanskii, "Enhanced near-infrared photorefractive properties of Te-doped $Sn_2P_2S_6$", in *Proceedings of SPIE*, 2006, pp. 625208–1.

[53] M. Cronin-Golomb, B. Fischer, J.O. White, and A. Yariv, "Theory and applications of four-wave mixing in photorefractive media", *IEEE Journal of Quantum Electronics*, vol. 20, pp. 12–30, 1984.

[54] N. Huot, J.M.C. Jonathan, G. Roosen, and D. Rytz, "Characterization and optimization of a ring self-pumped phase-conjugate mirror at 1.06 μm with $\mathrm{B}aTiO_3 : \mathrm{R}h$", *Journal of the Optical Society of America*, vol. 15, pp. 1992–1999, 1998.

[55] K. Green and B. Krauskopf, "Bifurcation analysis of frequency locking in a semiconductor laser with phase-conjugate feedback", *International Journal of Bifurcation Chaos*, vol. 13, pp. 2589–2601, 2003.

[56] J. Gemmrich and C. Garrett, "Unexpected waves", *Journal of Pysical Oceanography*, vol. 38, pp. 2330–2336, 2008.

[57] S.K. El-Labany, W.M. Moslem, N.A. El-Bedwehy, R. Sabry, and H.N. Abd El-Razek, "Rogue wave in Titan's atmosphere", *Astrophysics and Space Science*, vol. 338, pp. 3–8, 2012.

[58] R. Höhmann, U. Kuhl, H-J. Stöckmann, L. Kaplan, and E.J. Heller, "Freak waves in the linear regime : A microwave study", *Physical Review Letters*, vol. 104, pp. 093901, 2010.

[59] D.R. Solli, C. Ropers, P. Koonath, and B. Jalali, "Optical rogue waves", *Nature*, vol. 450, pp. 1054–1057, 2007.

[60] J.M. Soto-Crespo, Ph. Grelu, and N. Akhmediev, "Dissipative rogue waves : Extreme pulses generated by passively mode-locked lasers", *Physical Review E*, vol. 84, pp. 016604, 2011.

[61] M.G. Kovalsky, A.A. Hnilo, and J.R. Tredicce, "Extreme events in the $\mathrm{T}i$:sapphire laser", *Optics Letters*, vol. 36, pp. 4449, 2011.

[62] C. Bonatto, M. Feyereisen, S. Barland, M. Giudici, C. Masoller, J.R. Rios Leite, and J.R. Tredicce, "Deterministic optical rogue waves", *Physical Review Letters*, vol. 107, pp. 053901, 2011.

[63] K. Schires, A. Hurtado, I.D. Henning, and M.J. Adams, "Rare disruptive events in polarisation-resolved dynamics of optically injected 1550 nm VCSELs", *Electronics Letters*, vol. 48, pp. 872, 2012.

[64] C. Kharif, E. Pelinovsky, and A. Slunyaev, *Rogue waves in the ocean*, Springer, 2013.

[65] S. Residori, U. Bortolozzo, A. Montina, F. Lenzini, and F.T. Arecchi, "Rogue waves in spatially extended optical systems", *Fluctuation and Noise Letters*, vol. 11, pp. 1240014, 2012.

[66] C. Risch and C. Voumard, "Self-pulsation in the output intensity and spectrum of $GaAs$-$AlGaAs$ cw diode lasers coupled to a frequency-selective external optical cavity", *Journal of Applied Physics*, vol. 48, pp. 2083–2085, 1977.

[67] A.S. Pikovsky and J. Kurths, "Coherence resonance in a noise-driven excitable system", *Physical Review Letters*, vol. 78, pp. 775–778, 1997.

[68] C. Masoller, "Noise-induced resonance in delayed feedback systems", *Physical Review Letters*, vol. 88, pp. 034102, 2002.

[69] M.A. Arteaga, M. Valencia, M. Sciamanna, H. Thienpont, M. Lo'pez-Amo, and K. Panajotov, "Experimental evidence of coherence resonance in a time-delayed bistable system", *Physical Review Letters*, vol. 99, pp. 023903, 2007.

[70] J.M. Buldú, J. García-Ojalvo, C.R. Mirasso, and M.C. Torrent, "Stochastic entrainment of optical power dropouts", *Physical Review E*, vol. 66, pp. 021106, 2002.

[71] J.F. Martinez Avila, H.L.D.de S. Cavalcante, and J.R. Rios Leite, "Experimental deterministic coherence resonance", *Physical Review Letters*, vol. 93, pp. 144101, 2004.

[72] J.M. Buldú, J. García-Ojalvo, and M.C. Torrent, "Delay-induced resonances in an optical system with feedback", *Physical Review Letters*, vol. 69, pp. 046207, 2004.

Publications

Chaos crisis and bistability of self-pulsing dynamics in a laser diode with phase-conjugate feedback

Martin Virte,* Andreas Karsaklian Dal Bosco, Delphine Wolfersberger, and Marc Sciamanna
Supélec, OPTEL Research Group, Laboratoire Matériaux Optiques, Photonique et Systèmes (LMOPS) EA-4423 , 2 Rue Edouard Belin, F-57070 Metz, France
(Dated: August 29, 2011)

A laser diode subject to a phase-conjugate optical feedback can exhibit rich nonlinear dynamics and chaos. We report here on two bifurcation mechanisms that appear when increasing the amount of light being fedback to the laser. First, we report on a full suppression of chaos from a crisis induced by a saddle-node bifurcation on self-pulsing, so-called external-cavity mode solutions (ECMs). Secondly, the feedback-dependent torus and saddle-node bifurcations on ECMs may be responsible for large regions of bistability between ECMs of different and high (beyond GHz) frequencies.

PACS numbers: 42.65.Sf, 05.45.-a, 42.55.Px, 42.60.Mi, 42.65.Hw

Phase-Conjugate optical Feedback (PCF) has been extensively used for applications where one needs to stabilize a laser diode output through phase or mode locking [1, 2] or to improve laser performances such as single-mode emission [3], spectral linewidth [4, 5] and intensity noise [6]. However experimental and theoretical works have shown that, depending on the feedback parameters, the laser diode also can exhibit complex nonlinear dynamics leading to chaos [7–17]. To summarize, when increasing the feedback strength, the laser diode is destabilized from its otherwise steady state dynamic and exhibits a sequence of bifurcations to chaos. Regions of chaos (also called 'bubbles') are interspersed by self-pulsing dynamics [12]. The oscillation frequency of these self-pulsations being close to a multiple of the external cavity frequency, these solutions have been called external cavity modes (ECM). An in-depth bifurcation analysis of these ECMs is however available only for weak optical feedback [15, 16], where one can also benefit from approximations of the ECM solutions [8, 11] and appropriate asymptotic methods [17]. Yet the experiments suggest that the laser spectral component at the external cavity frequency increases and broadens with the increase of feedback strength, hence indicating that restabilization of ECM and/or additional bifurcations on ECMs may be in order for larger feedback rates (see e.g. cases e to g of fig. 3 in Ref. [14]). This situation contrasts with the case of conventional optical feedback, where a continuous increase of feedback strength typically leads to an even more developed chaos such as coherence collapse [18].

In this paper, we extend the previously reported bifurcation analysis to larger values of the feedback strength. Using both direct numerical integration and continuation tools for delay-differential equations, we unveil two new bifurcation scenarios. First, when increasing the feedback strength, a full suppression of chaos may be observed because of a crisis from a saddle-node bifurcation on ECM. As a result, the laser diode is left in a purely regular self-pulsing dynamic with a frequency being a multiple of the external cavity frequency. Second, bistability between ECMs can appear when increasing the feedback strength, and leads to coexisting self-pulsing dynamics of very high frequencies (for our parameters, several tens of GHz). These results show a new configuration where a laser regular self-pulsing dynamic gets stabilized by the increase of feedback rate, other than the reported regular pulse package in conventional optical feedback [19, 20] or polarization self-modulation and square waveforms in polarization rotated feedback [21, 22].

We model the laser system using the so-called Lang-Kobayashi equations, i.e. time-delayed differential equations for the slowly varying optical field (Y) and the carrier inversion (Z). The field dynamics accounts for a delayed and phase-conjugated feedback field (Y^*). The model writes as follows, where the time-scale has been normalized by the photon lifetime (as done in Ref. [17]):

$$\frac{dY}{dt} = (1 + i\alpha)ZY + \gamma Y^*(t - \theta) \quad (1)$$

$$T\frac{dZ}{dt} = P - Z - (1 + 2Z)|Y|^2 \quad (2)$$

In these equations γ is the normalized feedback rate, θ is the normalized external delay, α stands for the linewidth enhancement factor, P for the pump parameter above threshold and T is defined as the ratio of carrier to photon lifetime. To simplify the comparison with previous works, we have taken the same values of the parameters as in Refs. [9, 12, 15–17]: $P = 0.0417$, $T = 1428$, $\alpha = 3$, $\theta = 476$. These are typical values of a diode laser working close to threshold and subject to feedback from a 10 cm distant mirror. The normalized feedback rate γ is our bifurcation parameter and will be varied between 0 and 0.07, which correspond to external mirror reflectivities from 0 to 3.35 %. The model is simple in that it does not account for the phase-conjugate mirror internal dynamic (typically on ns to s time-scale [23]) and the multiple delayed round-trips in the extended cavity (which may occur in

* martin.virte@supelec.fr

very strong feedback situations [24]). Still, it contains the main ingredients (ECMs and underlying bifurcations) to explain qualitatively the dynamics observed in experiments and it allows for a mathematical treatment using either numerical bifurcation tools or asymptotic mathematical analysis.

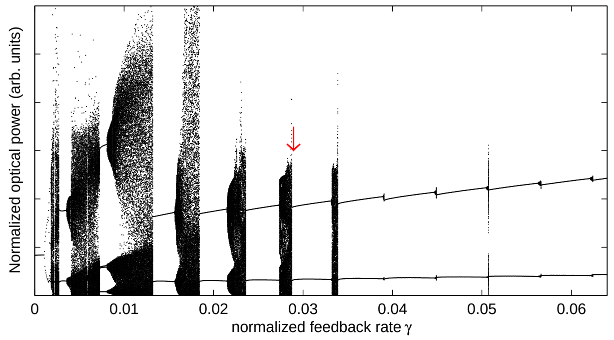

FIG. 1. Bifurcation Diagram for $\gamma \in [0, 0.07]$. It shows the extrema of the time series of the optical power versus the normalized feedback rate.

Figure 1 shows a bifurcation diagram of the extrema of laser output power ($|Y|^2$) versus the feedback rate γ. One recognizes the sequence of bifurcations at weak feedback rate ($\gamma < 0.015$) as reported in Ref. [12, 15, 16]: the laser steady-state destabilizes with a Hopf bifurcation to a ECM self-pulsing, which further undergoes a torus bifurcation to chaos. As the feedback rate increases the laser follows a sequence of three bubbles of chaos interspersed by ECM self-pulsing solutions. Interestingly when increasing the feedback rate further, the parameter range where chaos is seen (i.e. the size of the bubbles of chaos) shrinks progressively until chaos disappears for larger feedback rate values. For $\gamma > 0.035$ the laser diode is left in a purely regular self-pulsing dynamic corresponding to a ECM solution of the laser system. When increasing the feedback rate, bifurcations between ECMs lead to successive jumps between self-pulsing solutions of different frequencies, all being multiples of the external-cavity frequency (i.e. a property of ECM solution), but ECMs do not exhibit higher-order bifurcations to stable chaotic attractors.

To understand the mechanism leading to suppression of chaos, it is of interest to analyze in more detail the transition from chaos to ECM self-pulsing. The bifurcation diagram suggests an abrupt destabilization of chaos that is indicative of a crisis. This is confirmed in figure 2, where we plot time-traces of laser output power and projections of the trajectory in the reduced phase space (real vs. imaginary parts of the field), for $\gamma = 0.028795$ that is just before a transition from chaos to ECM self-pulsing indicated by the arrow in figure 1. In several time-intervals of the chaotic time-serie (1.a), the laser diode exhibits a self-pulsing dynamic that resembles very much the dynamic of the next appearing ECM (see e.g. a zoom in 2.a). This is also better seen in the phase space (1.b-2.b) where one recognizes the limit cycle dynamic of the ECM as contained in the larger chaotic attractor. When increasing the feedback rate, the chaotic attractor born on an ECM grows in size until it starts exhibiting large trajectories forming the ghost of the limit cycle trajectory of the next ECM, which is the signature of a so-called chaos crisis from a saddle-node bifurcation of a limit cycle (in our case an ECM solution). Such a crisis scenario, which happens for all bubbles of chaos starting from weak optical feedback, has been suggested also in Ref. [12], the originality being here to understand how the crisis combined with the saddle-node bifurcation on ECM may be responsible for a total disappearance of chaos for larger values of the feedback rate.

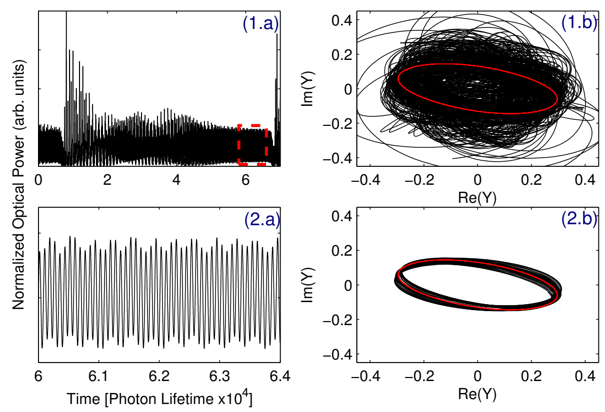

FIG. 2. Time-serie of output power (1.a) and phase-space trajectory (1.b) for $\gamma = 0.028795$. (2.a) is an enlargement of the boxed part with (2.b) its trajectory. In (1.b-2.b) the ellipse is the trajectory of the stable ECM about to appear.

To answer this question, one has to get a closer look into the saddle-node bifurcation of ECM and whether this bifurcation occurs for feedback rates smaller or larger than the torus bifurcation destabilizing ECM and leading to chaos. We have then complemented our numerical study by mathematical continuation techniques using the DDE-BIFTOOL package [25]. It allows us to follow stable or unstable branches of steady states or time-periodic solutions and to analyze their linear stability. Figure 3 complements the previous bifurcation diagram by showing the branches of ECMs (only the maximum of $|Y|^2$ is plotted) that successively appear when increasing the feedback rate. The stable (unstable) part of each branch is displayed in thick (thin) line. Each ECM is born from a saddle-node bifurcation (square) where the high-intensity solution only can be stable. Each ECM then destabilizes with a torus bifurcation (circle) when increasing the feedback rate. The interval of feedback rate values that separate the torus bifurcation of a previous ECM and the saddle-node bifurcation of the next ECM decreases as the feedback rate increases. Since the saddle-node bifurcation is responsible for the disappearance of chaos, this also explains that regions of chaos are observed for progressively smaller ranges of feedback rates as the feedback rate is increased. Furthermore, a sudden change of the bifurcation picture happens for $\gamma > 0.035$: the saddle-node bifurcation that creates the next stable ECM occurs for feedback rate smaller than the torus bifurcation that destabilizes the previous ECM. As a result the mechanism inducing the chaos crisis is present as soon as the ECM gets destabilized, and chaos is not observed anymore. This is a remarkable feature of the combination in our laser system of a chaos crisis mechanism and of a bifurcation mechanism that makes the position of torus and saddle-node bifurcation on limit cycles being dependent on the feedback rate. Control of chaos up to its full suppression is therefore rendered possible by varying the feedback strength.

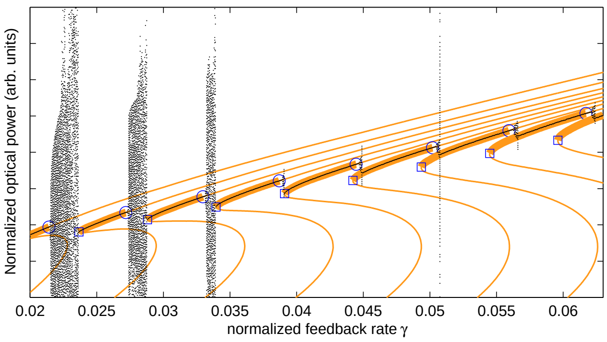

FIG. 3. Bifurcation diagram obtained by simulation and continuation method. In black is the simulation result and in orange is the continuation result. The stable part of the branch is in thick line while the unstable part is in thin line. Squares (resp. circles) are saddle-node (resp. torus) bifurcations.

The bifurcation mechanism explained in figure 3 has another consequence: bistability can be observed between ECM solutions when increasing the feedback rate. Another mechanism leading to bistability of locked solutions in a laser diode with phase-conjugate feedback has been reported in Ref. [15], but as also stated by the authors in a very small region of the parameters and with solutions having a small basin of attraction with respect to other stable attractors. As a result such a bistability was hardly observable in direct numerical integration only with the help of continuation methods where the system can be started with initial conditions in a close neighborhood of the coexisting solutions. In our case, not only the bifurcation leading to bistability is different but also bistability is seen in a large interval of feedback rate values, interval which moreover increases with the increase of feedback rate. Bistability between ECMs is clearly seen in figure 4 (a), where we plot the bifurcation diagrams of laser output power (only maximum of

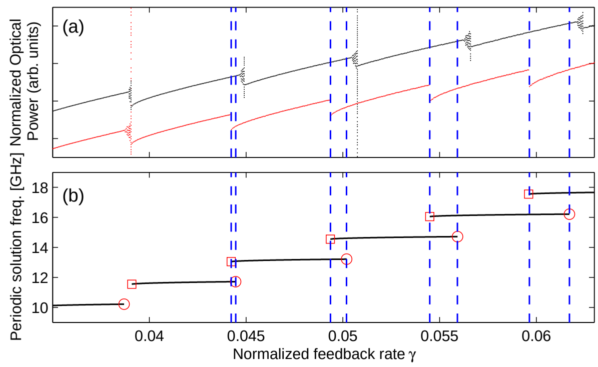

FIG. 4. Top: bifurcation diagram for increasing (top) and decreasing feedback (bottom) plotted on the same scale but shifted vertically for clarity. Bottom: the frequency of the periodic solutions (stable part only) obtained by continuation versus the normalized feedback rate. Dashed vertical lines bound the bistability regions.

$|Y|^2$ is plotted) for either increasing (top) or decreasing (bottom) feedback rate. We determine the boundaries of each region of bistability by looking to the feedback rate that corresponds to each saddle-node bifurcation (resp. torus bifurcation) creating (resp. destabilizing) an ECM. These boundaries are represented by pairs of vertical dashed lines. As we can see, all the states are easily accessible in simulation and the regions of bistability are quite large. In figure 4 (b) we show the frequencies of the ECM solutions as they bifurcate when increasing the feedback rate. The frequency separation between ECMs is close to the external cavity frequency. In our case the normalized external frequency is $f_{ext} = 1/\theta = 2.1.10^{-3}$, hence is about 1.5 GHz if one accounts for a photon lifetime of $\tau_p = 1.4$ *ps* as in Refs. [9, 12, 15, 16]. To illustrate the coexistence of two ECM solutions with different and possibly high frequencies, we show in figure 5 the time-series of the two regular self-pulsing dynamics observed for a normalized feedback rate of $\gamma = 0.0611$ (a-b), together with their corresponding **optical spectra (c,d). The zero frequency in figure 5 (c), (d) corresponds to the free laser frequency, which is the frequency reference frame of our equations** (1) **and** (2)**. The optical spectrum (c) [(d)] shows two peaks at about** 8 (8.75) **GHz and** -8 (-8.75) **GHz. Since the complex field trajectory is symmetric in the phase plane of the real vs imaginary parts and is centered on the** $(0, 0)$ **point, the optical spectrum shows no component at the zero frequency and symmetric peaks on negative and positive frequencies. One complete cycle for the complex field** Y **being equivalent to two cycles for** $|Y|^2$**, the time-series of the optical power in (a), (b) show modulations at about 16 GHz and 17.5 GHz, respectively.** The laser system will initially select one of the two coexisting self-pulsations at high frequencies. However a sustained perturbation or noise may induce random jumps between these two ECMs, with as a result a **time-averaged RF** spectral signature being made of two peaks, slightly shifted in frequency (shift being related to the external cavity frequency). The observation of such robust self-pulsations at controllable (with the feedback rate) and high frequencies, and moreover the possibility to observe bistability between these ECM solutions, is of interest for all-optical signal processing.

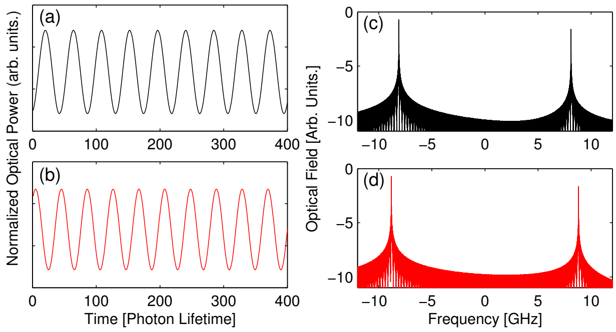

FIG. 5. Two time series of the light output power available for a normalized feedback rate of $\gamma = 0.0611$ (a) and (b) and the corresponding optical spectra in (c) and (d).

Finally, we have checked the robustness of the reported bifurcation mechanism when varying the laser and feedback parameters. First, the increase of the linewidth enhancement factor does not modify the reported bifurcation scenario, but increases the number and the size of the bubbles of chaos for weak optical feedback. Secondly, the reported findings are not specific to so-called short external cavity. We still observe the feedback induced suppression of chaos and ECM bistability, when increasing the delay or the pump parameter such that the delay becomes larger than the free-running laser relaxation-oscillation frequency. The increase of time-delay value however leads to additional bifurcations on ECMs which deserve further investigations. **This conclusion contrasts strongly with the COF case, where similar self-pulsing dynamics at the external cavity (EC) frequency is typically limited to so-called short external cavity [26]. This can be justified by the very different bifurcation mechanism leading to EC self-pulsing dynamics in both cases. In COF, the bifurcation mechanism is a Hopf bifurcation on a ECM, that is, a steady-state solution of the compound cavity system. The self-pulsing dynamics corresponds mathematically to a bridge of time-periodic solution connecting two Hopf bifurcations on two frequency detuned ECMs, or, equivalently to a ECM beating [27, 28]. Moreover, as one of the connecting ECMs is typically an unstable solution (called antimode), the self-pulsing dynamics gets easily destabilized to e.g. quasiperiodicity and chaos as one increases even slightly the feedback rate. This makes the observation of such ECM beating and Hopf bridge quite difficult. In the PCF case, the laser has only one stable steady state solution that gets destabilized through a Hopf bifurcation to a stable self-pulsing solution. As mentioned earlier, since the frequency of that solution is close to the external cavity frequency, that solution has been called ECM but by contrast to COF an ECM of the PCF system is a rotating solution with time-periodic intensity and not a time-constant intensity. The laser creates new such ECM solutions as the feedback increases, but all originates from the same and single steady state branch and not, as for the COF, from a possible beating or Hopf bridge on (ECM) steady state solutions. The stability of the EC self-pulsing dynamics in PCF (i.e. of ECM solution) is determined by the interplay between a saddle-node bifurcation and a torus bifurcation, hence makes it possible to observe a robust and fully stable self pulsing also when increasing the feedback rate or the external cavity length.**

In summary, we have reported on a new bifurcation scenario in a laser diode with phase-conjugate optical feedback. When increasing the feedback rate, the saddle-node bifurcation that creates a self-pulsating ECM solution (limit cycle) may occur for feedback rate value smaller than the one corresponding to the torus bifurcation of another ECM. This results first in a full suppression of chaos for larger values of the feedback rate, where the underlying bifurcation mechanism is a crisis from a saddle-node bifurcation on limit cycle. The laser then exhibits robust self-pulsating dynamics at frequencies being multiples of the external cavity frequency, hence adjustable. Secondly, this leads to bistability between self-pulsating ECM solutions of different and high frequencies. The reported bifurcation scenarios are observed in a large range of parameters. These conclusions have been obtained through direct numerical integration of an appropriate set of rate equations, but also from the use of advanced continuation tools for delay-differential equations. The reported dynamics are of interest for the all-optical generation of high frequency, microwave signals, and also the bistability is of interest for all-optical signal processing. Many of the reported bifurcation features, and in particular the existence of a robust self-pulsing dynamics at large feedback rates, contrasts with what is typically seen in conventional optical feedback. They motivate further investigations in experiments, where, although not detailed, reports show the existence of coexisting more regular attractors at large feedback rates.

The authors acknowledge the support of Conseil Regional de Lorraine, Fondation Supelec, Institut Carnot C3S, and COST European Action MP0702.

[1] L. Petersen, U. Gliese, and T. N. Nielsen, IEEE J. Quantum Electron. **30**, 2526 (1994).

[2] E. Miltenyi, M. O. Ziegler, M. Hofmann, J. Sacher, W. Elsaßer, E. O. Gobel, and D. L. MacFarlane, Opt. Lett. **20**, 734 (1995).

[3] M. LØbel, P. M. Petersen, and P. M. Johansen, Opt. Lett. **23**, 825 (1998).

[4] K. Vahala, K. Kyuma, A. Yariv, S.-K. Kwong, M. Cronin-Golomb, and K. Y. Lau, Appl. Phys. Lett. **49**, 1563 (1986).

[5] P. Kurz and T. Mukai, Opt. Lett. **21**, 1369 (1996).

[6] L. N. Langley and K. A. Shore, Opt. Lett. **18**, 1432 (1993).

[7] G. P. Agrawal and J. T. Klaus, Opt. Lett. **16**, 1325 (1991).

[8] G. H. M. van Tartwijk, H. J. C. van der Linden, and D. Lenstra, Opt. Lett. **17**, 1590 (1992).

[9] G. R. Gray, D. Huang, and G. P. Agrawal, Phys. Rev. A **49**, 2096 (1994).

[10] A. Murakami and J. Othsubo, IEEE J. Quantum Electron. **33**, 1825 (1997).

[11] W. A. van der Graaf, L. Pesquera, and D. Lenstra, Opt. Lett. **23**, 256 (1998).

[12] B. Krauskopf, G. R. Gray, and D. Lenstra, Phys. Rev. E **58**, 7190 (1998).

[13] O. Andersen, A. Fischer, I. Lane, E. Louvergneaux, S. Stolte, and D. Lenstra, IEEE J. Quantum Electron. **35**, 577 (1999).

[14] J. S. Lawrence and D. M. Kane, Phys. Rev. A **63**, 033805 (2001).

[15] K. Green, B. Krauskopf, and K. Engelborghs, Physica D: Nonlinear Phenomena **173**, 114 (2002).

[16] K. Green and B. Krauskopf, I. J. Bifurcation and Chaos **13**, 2589 (2003).

[17] T. Erneux, A. Gavrielides, K. Green, and B. Krauskopf, Phys. Rev. E **68**, 066205 (2003).

[18] D. Lenstra, B. Verbeek, and A. Den Boef, IEEE J. Quantum Electron. **21**, 674 (1985).

[19] T. Heil, I. Fischer, W. Elsaßer, and A. Gavrielides, Phys. Rev. Lett. **87**, 243901 (2001).

[20] A. Tabaka, K. Panajotov, I. Veretennicoff, and M. Sciamanna, Phys. Rev. E **70**, 036211 (2004).

[21] H. Li, A. Hohl, A. Gavrielides, H. Hou, and C. K.D., Appl. Phys. Lett. **72**, 2355 (1998).

[22] M. Sciamanna, F. Rogister, O. Deparis, P. Megret, M. Blondel, and T. Erneux, Opt. Lett. **27**, 261 (2002).

[23] D. H. DeTienne, G. R. Gray, G. P. Agrawal, and D. Lenstra, IEEE J. Quantum Electron. **33**, 838 (1997).

[24] L. N. Langley, K. A. Shore, and J. Mørk, Opt. Lett. **19**, 2137 (1994).

[25] K. Engelborghs, T. Luzyanina, and G. Samaey, *DDE-BIFTOOL v. 2.00*, Tech. Rep. (TW-330, Dept. of CS, K. U. Leuven, Belgium, 2002).

[26] A. Tager and K. Petermann, IEEE J. Quantum Electron. **30**, 1553 (1994).

[27] D. Pieroux, T. Erneux, B. Haegeman, K. Engelborghs, and D. Roose, Phys. Rev. Lett. **87**, 193901 (2001).

[28] M. Sciamanna, T. Erneux, F. Rogister, O. Deparis, P. Mégret, and M. Blondel, Phys. Rev. A **65**, 041801 (2002).

A Letters Journal Exploring the Frontiers of Physics

January 2013

EPL, **101** (2013) 24001 www.epljournal.org
doi: 10.1209/0295-5075/101/24001

Delay-induced deterministic resonance of chaotic dynamics

A. Karsaklian Dal Bosco, D. Wolfersberger and M. Sciamanna

Supélec, OPTEL Research Group and Laboratoire Matériaux Optiques, Photonique et Systèmes (LMOPS)
2 rue Edouard Belin, 57070 Metz, France, EU

received 22 November 2012; accepted 8 January 2013
published online 31 January 2013

PACS 42.65.Sf – Dynamics of nonlinear optical systems, optical instabilities, optical chaos and complexity and optical spatio-temporal dynamics
PACS 42.55.Px – Semiconductor lasers, laser diodes
PACS 42.60.Mi – Dynamical laser instabilities; noisy laser behavior

Abstract – We show that time-delayed feedback can induce an optimal regularity in the pulsating dynamics of a nonlinear system without the need for an additional noise source. This deterministic delay-induced coherence resonance is reported experimentally in the chaotic dynamics of a laser diode subject to a phase-conjugate optical feedback, when varying the amount of feedback light. Qualitatively similar resonance is found theoretically in the model of a time-delayed class-A laser. The resonance is therefore not related to an interplay between time-delayed dynamics and faster undamped relaxation oscillations and is thought to be generic for a large class of delayed nonlinear systems.

Introduction. – It is of common knowledge that the dynamics of a noise-driven nonlinear system can exhibit an optimal response to either an external modulation (stochastic resonance [1]) or to one of the system internal time scale (coherence resonance [2]). Stochastic resonance has been initially reported in bistable noise-driven systems, such as in neuronal systems and solid-state physics (for a review see, *e.g.*, [3]). A pioneering experiment was performed in optics using a bistable ring laser [4] and was later detailed using vertical-cavity surface-emitting lasers [5]. Stochastic resonance has also been reported in chaotic pulsating dynamics [6]. Coherence resonance was found initially in noise-driven excitable nonlinear systems. Excitable systems are systems that can fire a pulse when perturbed above a certain threshold and that cannot fire a second pulse before a given refractory time has passed. Examples are typically found in the generation of nerve pulses in biology [7]. The first experimental demonstrations of coherence resonance have been reported in electronic circuits [8] and in a laser diode with optical feedback [9]. As for stochastic resonance, coherence resonance has today been demonstrated for a large class of dynamical systems, including in the random-like motion between chaotic attractors [10] and in bistable systems with time delay [11].

Both coherence and stochastic resonance have recently been shown in deterministic chaotic systems, *i.e.*, without the addition of noise. In refs. [12,13] the increase of current leads to an optimal regularity of the time between chaotic laser diode power dropouts. In ref. [14] the chaotic fluctuations show an optimal entrainment to external modulation when the modulation time period is close to one of the multiples of the system time scale.

In this letter, we report on a significantly different case of deterministic coherence resonance (DCR) in the dynamics of a nonlinear system. The resonance occurs by simply increasing the amount of feedback signal in a time-delayed system. It is demonstrated experimentally in the chaotic dynamics of a laser diode with optical feedback: an optimal value of the feedback strength leads to an optimal regularity of the time between chaotic low-frequency fluctuations (LFF), all the other laser and feedback parameters remaining fixed. The previously reported case of DCR [12] originates from the complex interplay between the fast fluctuations at the system internal time scale (relaxation oscillations) —which play the role of driving noise-like forces— and the slower chaotic fluctuations at the time delay time scale. Hence it is typically observed close to the solitary laser threshold where the laser shows typically coexistence between stable steady state and excitable-like chaotic dynamics [13]. The purely delay-induced resonance shown here cannot be explained by these mechanisms. First, we find a qualitatively similar DCR in a model of a time-delayed class-A laser that shows chaotic dynamics resembling LFF but without the additional complexity of the laser diode

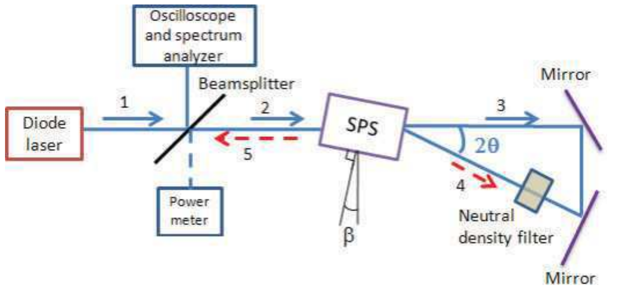

Fig. 1: (Colour on-line) Experimental setup. Beam 1 (5) is the emitted (PCF) beam. Beam 2 is the crystal incident beam. Counterpropagating beams 3 and 4 create the transmission grating in the crystal. The mirror reflectivity can be varied using a neutral density filter. The powermeter measures the PCF beam power.

relaxation oscillations [15]. Secondly, our experiment uses a phase-conjugate feedback (PCF) and the PCF laser system has no such steady-state but only pulsating solutions at multiples of the external cavity frequency [16,17].

Optical feedback experiment. – Our experimental setup is summarized in fig. 1. The laser is a 852 nm edge-emitting diode laser with threshold current of 18 mA. The phase-conjugate feedback is performed by nonlinear self-pumped four-wave mixing (FWM) in a $Sn_2P_2S_6 : Te$ crystal which dimensions are $6 \times 6 \times 11\,mm^3$. The orientation of the crystal has been set in order to minimize Fresnel losses from the crystal faces ($\beta = 26°$) and to optimize the wave mixing gain ($2\theta = 30°$). The beam undergoes phase conjugation and is then injected back into the laser cavity after a time delay of about 8.4 ns ($= L/c$ where L is the optical path of the pump beam, *i.e.* twice the distance laser-crystal plus the length of the FWM loop). PCF reflectivity is estimated from the ratio of the PCF power (component 5) with the crystal incident beam power (component 2). We achieve maximum PCF reflectivity of about 9% for an injection current of 60 mA. PCF is interesting in that it compensates for any phase shift and misalignment in the extended cavity, which are known to induce dynamical resonance of low-frequency chaotic dynamics [18].

Figure 2(a) shows a typical experimental time trace of LFF chaotic dynamics observed for a mirror reflectivity up to about 5%. As typical for LFF dynamics [19], and as predicted theoretically in a model of a laser with PCF [20], the dynamics is made of successive significant power dropouts, that occur randomly in time but with an average time between dropouts much slower than both the laser internal time scales and the external cavity time delay. In this case the times between dropouts range between 30 and 200 ns, while the relaxation oscillations period at this injection current is measured at about 0.125 ns and the time delay is of 8.4 ns. As shown in fig. 2(b), the corresponding power spectrum consists of low-frequency components at the LFF averaged frequency,

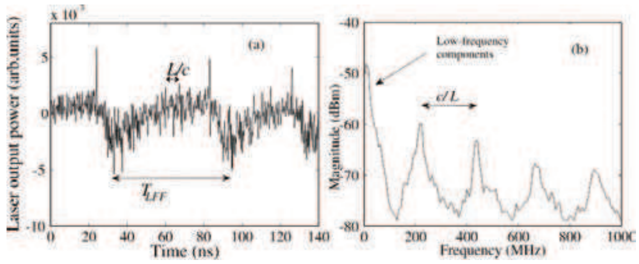

Fig. 2: (a): Experimental time trace showing typical chaotic LFF. (b): Corresponding power spectrum.

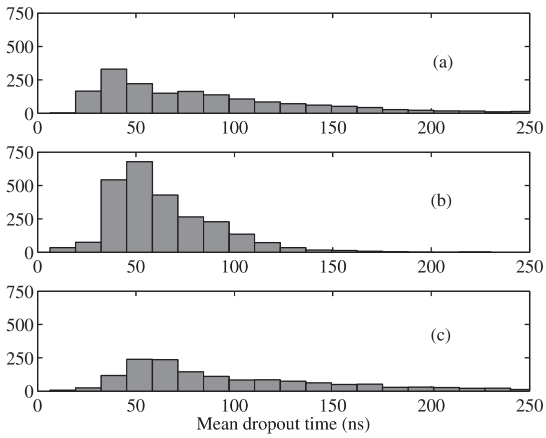

Fig. 3: Statistical distribution of the time between power dropouts T_{LFF}, for three increasing values of the mirror reflectivity: (a) 4.84%, (b) 6.14%, (c) 7.47%.

with additional peaks at multiples of c/L. Remnants of this self-pulsing dynamics at c/L frequency are seen in the LFF dynamics: the power recovers in a stepwise manner with damped relaxation oscillations that are reactivated at about every time delay as shown in fig. 2(a).

Time delay induces coherence resonance without external noise. – LFF dynamics have been seen [21] but never characterized in the PCF case. We first analyze the statistics of the time between power dropouts (T_{LFF}). For that purpose, we take advantage of the fact that T_{LFF} is much larger than any other laser or feedback time scales, and therefore we filter out the time traces (with a low-pass filter of 1 GHz bandwidth) so that we keep only the information on T_{LFF}. A typical statistical distribution of T_{LFF} is shown in fig. 3(a). Similarly to what has been reported for LFF dynamics in COF [22], the statistics shows no statistical event for times smaller than a given refractory time (here about 10 ns), and then a monotonously decreasing curve for larger times. Interestingly however, we find that an increase of the mirror reflectivity leads to a severe change of the statistical properties of T_{LFF}: the average T_{LFF} increases with the increase of the mirror reflectivity, but there is an optimal amount of this reflectivity for which the dropout time distribution is narrower around its averaged value

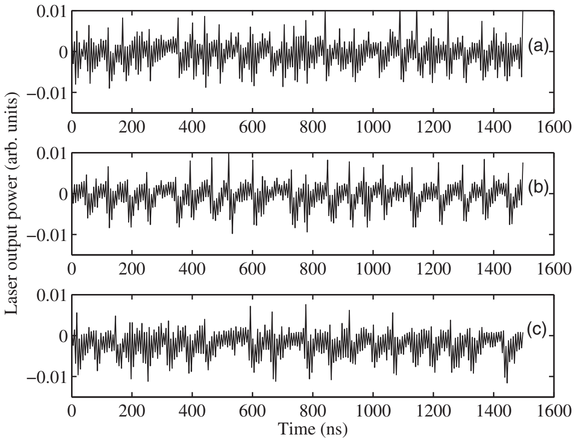

Fig. 4: LFF time series corresponding to the situation of fig. 3(a)–(c). Case (b) is the resonance case, with optimal regularity of the time between power dropouts.

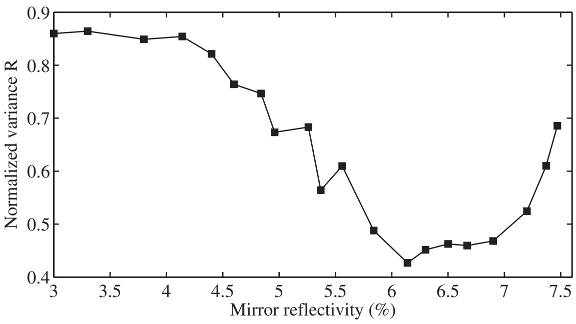

Fig. 5: Normalized variance $R = \frac{\sigma_{T_{LFF}}}{\langle T_{LFF} \rangle}$ as a function of the mirror reflectivity.

and therefore the standard deviation gets a minimum value (b). A further increase of the reflectivity leads to a statistical distribution similar to case (a) but with a larger averaged value of T_{LFF}. This feature is further confirmed when looking as the corresponding time traces in fig. 4. Case (b) shows more regular power dropouts than (a) or (c).

The LFF dynamics exhibits what we call a "delay-induced deterministic resonance", *i.e.*, varying the amount of feedback signal in the nonlinear system leads to an optimal response of the system to one of its dynamical time scales without the need for an external noise input. The coherence resonance-like phenomenon is evidenced in fig. 5, which plots the ratio of the dropout time standard deviation $\sigma_{T_{LFF}}$ with the averaged T_{LFF}, as a function of the mirror reflectivity. This normalized variance R exhibits a clearly distinguishable minimum at a particular value of the mirror reflectivity that corresponds to the resonance case (b) of fig. 4 and fig. 3 where the dropout time shows higher regularity. The curve shows three regions of qualitatively different features: 1) For small mirror reflectivity, the laser exhibits a route to chaos from undamped relaxation oscillations, which leads to a chaotic dynamics with dominating high-frequency components at either the relaxation oscillation frequency or the multiples of the external cavity frequency. There is no distinguishable power dropouts, and the dynamics shows a large dispersion of time between chaotic pulses together with a small averaged time between pulses. Therefore R is large. 2) For a larger PCF reflectivity, the low-frequency component ($f \leqslant 100$–$200\,\mathrm{MHz}$) of the power spectrum increases, which indicates the emergence of clearly distinguishable and slow power dropouts. The averaged time between dropouts increases with the increase of the mirror reflectivity, but more slowly than the decrease of the standard deviation of the time between dropouts. As a result R decreases when increasing the feedback strength up to a minimum value for a 6.14% mirror reflectivity. At that point the laser time series shows maximum regularity in the dropout times and coherence resonance is achieved. 3) Increasing the reflectivity leads to a more random sequence of power dropouts and $\sigma_{T_{LFF}}$ increases faster than $\langle T_{LFF} \rangle$ with the PCF reflectivity.

Delay-induced resonance in class-A chaotic power dropouts. – This purely delay-induced DCR (*i.e.* without noise and without modification of the internal system parameters) significantly differs from the current-induced DCR reported earlier [12]. The authors explain their current-induced DCR by the fast fluctuations at the relaxation oscillation time scale that are driving noise-like forces of a self-excitable deterministic system [23]. The competition between the dynamics at the relaxation oscillation frequency and the slow chaotic LFFs at the time scale related to time delay is known to be stronger when operating close to the laser threshold, where it also leads to locking of quasiperiodic dynamics known as synchronous LFFs [24]. The resonance is therefore observed when sweeping the current from below to above the solitary laser threshold. In our case the current is fixed at 60 mA (well above the threshold) and we claim that the resonance is purely delay-induced, *i.e.* that it does not link to or is not supported by current-dependent relaxation oscillation fluctuations. To demonstrate this, we deliberately simulate a model from a much simpler laser system than the one used in experiment: a class-A laser with feedback. By contrast to laser diodes or class-B lasers, class-A lasers like, *e.g.*, gas lasers do not exhibit relaxation oscillation-like dynamics because the carrier dynamics has been adiabatically removed and the dynamics is made of a single equation for the optical field [25]. With time delay the class-A laser model writes [26]

$$\frac{\mathrm{d}E}{\mathrm{d}t} = \mu(1+i\alpha)E - b(1+i\beta)|E|^2 E + a(1+i\epsilon)E(t-T_r), \tag{1}$$

where t is the time measured in units of $1/\gamma_\perp$ ($\gamma_\perp$ is the polarization decay rate), E is the complex electric field, μ (b) is a dimensionless gain (saturation) coefficient,

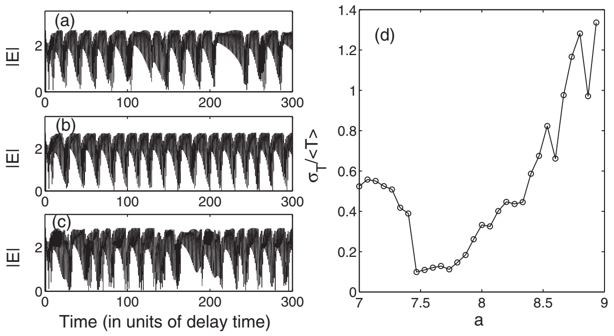

Fig. 6: Simulations of eq. (1). (a)–(c) Low-frequency power dropouts for $a = 7.2$, $a = 7.5$, $a = 8.3$, respectively. Panel (d) shows the ratio of standard deviation to mean value of the time between drops (T) as a function of a.

α is a detuning coefficient that is function of Δ and δ, where Δ (δ) is the detuning between the cavity frequency (atomic center frequency) and the laser frequency. β is a detuning coefficient that is function of δ. T_r is the normalized delay time. $a = (1 - R_2)\sqrt{R_2 R_3}/[R_2\sqrt{(}1 + \epsilon^2)\gamma_\perp \tau_{in}]$ is the normalized delayed feedback rate, where τ_{in} is the internal laser cavity round-trip time, R_2 (R_3) is the power reflectivity of the laser output mirror (external mirror). $(1 + i\epsilon)$ is the phase shift induced by optical feedback. We have simulated the dynamics of E for increasing values of a and the other parameters fixed as: $\mu = 0$ (laser pumped at threshold), $\alpha = 1.4$, $b = 1$, $\beta = 3$, $\epsilon = 0$ (the feedback phase is not taken into account), $T_r = 1$. Samples of chaotic time-series are shown in fig. 6 for increasing values of a, with the time scale being normalized by the time delay T_r. A close look shows fast pulsations of the laser output at a period close to T_r and dropouts that occur at random time intervals and on a much slower time scale, of the order of $20T_r$ or even more. As shown in fig. 6, the time interval between successive power dropouts gets an optimal regularity for an intermediate value of the feedback strength (b), if compared to the situation at smaller (a) or larger (c) feedback strength. This conclusion is confirmed by a plot of the ratio between standard deviation and mean value of the time between power dropouts $(\sigma_T/\langle T\rangle)$ as a function of the feedback rate a (d). This delay-induced resonance of chaotic dynamics is qualitatively similar to the one seen in our experiment, although the dynamical system exhibits no relaxation oscillation or internal dynamics faster than the delay time scale.

Discussion. – In summary, we have provided an experimental evidence for a new class of coherence resonance (CR) in a nonlinear system, which is observed without the need for an additional noise and for which the parameter inducing resonance is only the amount of feedback signal. This so-called deterministic delay-induced resonance is observed in the chaotic low-frequency fluctuations (LFF) of a laser diode with phase-conjugate feedback (PCF). For an optimal amount of feedback ratio, the laser diode exhibits an optimal regularity of the time between slow chaotic power dropouts. The mechanism inducing this deterministic CR is different from the current-induced CR shown in refs. [12,13] for at least two reasons: 1) we show theoretically that a qualitatively similar CR occurs in a simple model of a time-delayed class-A laser that shows no relaxation oscillations but only fundamental pulsations at the time delay, 2) the basic solutions of the PCF laser system are not steady states but self-pulsating solutions at the external cavity frequency, therefore the LFFs cannot be related to self-induced saddle-node type of excitability. Which are the bifurcations that lead to LFF in the PCF laser system is an interesting question, which is further stimulated here by the CR phenomenon. We anticipate the delay-induced CR to be generic to a large class of delayed nonlinear systems, as suggested by recent theoretical works in, *e.g.*, delayed logistic maps and diffusively coupled Rossler oscillators [27].

***

The authors thank A. A. Grabar for providing them with the SPS crystal. This work is supported by the the Conseil Régional de Lorraine, the Inter-University Attraction Pole Program IAP VII P7/35 "Photonics@be" and Agence Nationale de la Recherche (ANR) through the TINO project (ANR-12-JS03-005).

REFERENCES

[1] Benzi R., Sutera A. and Vulpiani A., *J. Phys. A*, **14** (1981) 453.
[2] Pikovski A. and Kurths J., *Phys. Rev. Lett.*, **78** (1997) 775.
[3] Gammaitoni L., Hänggi P., Jung P. and Marchesoni F., *Rev. Mod. Phys.*, **70** (1998) 223.
[4] McNamara B., Wiesenfeld K. and Roy R., *Phys. Rev. Lett.*, **60** (1988) 2626.
[5] Giacomelli G., Marin F. and Rabbiosi I., *Phys. Rev. Lett.*, **82** (1999) 675.
[6] Buldú J. M., Garcia-Ojalvo J., Mirasso C. R. and Torrent M. C., *Phys. Rev. E*, **66** (2002) 021106.
[7] Lindner B., Garcia-Ojalvo J., Neiman A. and Schimansky-Geier L., *Phys. Rep.*, **392** (2004) 321.
[8] Postnov D. E., Han S. K., Yim T. G. and Sosnovtseva O. V., *Phys. Rev. E*, **59** (1999) 3791(R).
[9] Giacomelli G., Giudici M., Balle S. and Tredicce J., *Phys. Rev. Lett.*, **84** (2000) 3298.
[10] Masoller C., *Phys. Rev. Lett.*, **88** (2002) 034102.
[11] Arizaleta Arteaga M., Valencia M., Sciamanna M., Thienpont H., López-Amo M. and Panajotov K., *Phys. Rev. Lett.*, **99** (2007) 023903.
[12] Martinez Avila J. F., de S. Cavalcante H. L. D. and Rios Leite J. R., *Phys. Rev. Lett.*, **93** (2004) 144101.
[13] Hong Y. and Shore K. A., *IEEE J. Quantum Electron.*, **41** (2005) 1054.
[14] Buldú J. M., Garcia-Ojalvo J. and Torrent M. C., *Phys. Rev. E*, **69** (2004) 046207.

[15] Pieroux D. and Mandel P., *Phys. Rev. E*, **67** (2003) 056213.

[16] Erneux T., Gavrielides A., Green K. and Krauskopf B., *Phys. Rev. E*, **68** (2003) 066205.

[17] Virte M., Karsaklian Dal Bosco A., Wolfersberger D. and Sciamanna M., *Phys. Rev. A*, **84** (2011) 043836.

[18] Meziane B., Besnard P. and Stephan G. M., *IEEE J. Quantum Electron.*, **31** (1995) 617.

[19] Hohl A. and Gavrielides A., *Phys. Rev. Lett.*, **82** (1999) 1148.

[20] O'Brien D., Huyet G. and McInerney J. G., *Phys. Rev. A*, **64** (2001) 025802.

[21] Lawrence J. S. and Kane D. M., *Phys. Rev. A*, **63** (2001) 033805.

[22] Yacomotti A. M., Eguia M. C., Aliaga J., Martinez O. E., Midlin G. B. and Lipsich A., *Phys. Rev. Lett.*, **83** (1999) 292.

[23] Martinez Avila J. F., de S. Cavalcante H. L. D and Rios Leite J. R., *Phys. Rev. Lett.*, **100** (2008) 044101.

[24] Gavrielides A., Newell T. C., Kovanis V., Harrison R. G., Swanston N., Yu D. and Lu W., *Phys. Rev. A*, **60** (1999) 1577.

[25] Tredicce J. R., Arecchi F. T., Lippi G. L. and Puccioni G. P., *J. Opt. Soc. Am. B*, **2** (1985) 173.

[26] Kuwashima F., Kitazima I. and Iwasawa H., *Jpn. J. Appl. Phys.*, **40** (2001) 601.

[27] Buryk J., Krawiecki A. and Buchner T., *Chaotic Model. Simul.*, **2** (2011) 363.

Extreme events in time-delayed nonlinear optics

Andreas Karsaklian Dal Bosco,* Delphine Wolfersberger, and Marc Sciamanna

Supélec, OPTEL Research Group and LMOPS Laboratory, 2 Rue Edouard Belin, Metz 57070, France

**Corresponding author: andreas.karsakliandalbosco@supelec.fr*

Received December 21, 2012; revised January 24, 2013; accepted January 27, 2013; posted January 29, 2013 (Doc. ID 182209); published February 25, 2013

We report experimentally on extreme events in the pulsating dynamics of an optical time-delayed system, i.e., a diode laser subject to a phase-conjugate feedback. We study the effect of the feedback strength on extreme events' properties. We show a transition to non-Gaussian statistics of the pulse intensity and an increased number of extreme events as the mirror reflectivity increases. The extreme event pulse is anticipated and followed by smaller pulses with time-delay periodicity. © 2013 Optical Society of America

OCIS codes: 190.3100, 250.5960, 190.5040.

Extreme events, rogue waves, and disruptive events are names often given to single events that may occur in many fields, such as hydrodynamics [1], plasma physics [2], and optics [3–5]. Those extreme events are waves of very high amplitude that can appear in a signal on a rare basis, thus breaking its otherwise smooth or regular evolution. Historically, the first extreme events were spotted in the ocean by sailors and were then described as huge lone waves arising very high above the calm average water level without warning. Many studies have been performed to account for their origin, their probability of occurrence, and the systems that could give birth to extreme events. Besides their first report in microstructured optical fibers showing supercontinuum emission [3], extreme events in optics have also been shown in mode-locked lasers [6,7] and laser diodes with optical injection [8,9].

We report here on extreme events in another well-known class of nonlinear optics, which is a system with time-delayed optical feedback. More specifically, our experiment uses a laser diode with phase-conjugate feedback (PCF). We show a transition to long-tailed non-Gaussian statistics of the pulse intensity and an increased number of extreme events as the mirror reflectivity increases. The single extreme event pulse is anticipated and is followed by pulses with time-delay periodicity. Upon increasing the feedback strength, a larger number of these time-delay-periodic pulses become extreme events and lead to a deviation from the log-Poisson statistics of the time between extreme events.

Our experimental setup is shown in Fig. 1(a). The laser is a 852 nm edge-emitting diode laser with 50 mW output power at a driving current of 60 mA. The PCF is performed by nonlinear self-pumped four-wave mixing in a $6\,\mathrm{mm} \times 6\,\mathrm{mm} \times 11\,\mathrm{mm}$ $Sn_2P_2S_6$:Te crystal. The whole ring cavity is the phase conjugation mirror (PCM) and the orientation of the crystal has been set in order to minimize Fresnel losses at the crystal faces ($\beta = 26°$) and to optimize the two-wave mixing gain ($2\theta = 30°$). The external cavity length $L = 54$ cm is the whole ring cavity length plus one roundtrip between the laser and the crystal. The related time delay is $\tau = 1.8$ ns. PCM reflectivity R is the ratio of the PCF power (component 5) with the crystal incident beam power (component 2). When the mirror reflectivity increases, the system undergoes a sequence of bifurcations to self-pulsing dynamics at frequencies close to the relaxation oscillation frequency or to the external cavity frequency and multiples, as predicted theoretically [10]. Additional secondary bifurcations lead to deterministic chaotic pulsing with a broadband RF spectrum showing enhanced frequency content at the multiples of the external cavity frequency. Chaos is observed already for $R = 1.3\%$; hence the parameter range where the dynamics is steady or time-periodic pulsing is very small. Figure 1(b) is a typical example of a chaotic time series—for $R = 4.4\%$—where we recognize an extreme event arising well above the signal average value. The red line labeled $\mathrm{AI} = 2$ is the threshold above which a pulse is considered as an extreme event, i.e., as defined in [1] twice the average peak height among one third of the highest peaks of the whole series (abnormality index $\mathrm{AI} = (H_f/H_s) > 2$).

Figure 2 shows the evolution of the laser output power versus time and the corresponding histograms when R increases. The red horizontal and vertical lines are the extreme events thresholds (different for each time series). Extreme events appear and their number increases when R increases. When $R = 1.8\%$ there is no pulse above the threshold; therefore the signal shows no extreme event. When R increases pulses appear that rise much higher than the signal's significant height. This

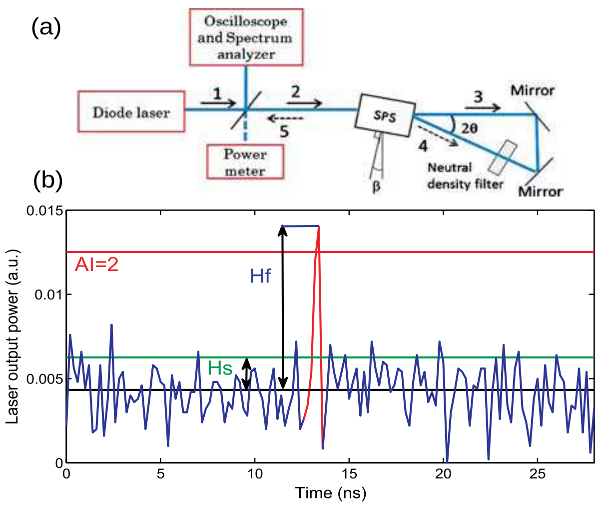

Fig. 1. (Color online) (a) Experimental setup. Beam 1 (5) is the emitted PCF beam. Beams 3 and 4 create the transmission grating. The mirror reflectivity is varied using a neutral density filter. (b) Extreme event pulse ($\mathrm{AI} = 2.23$).

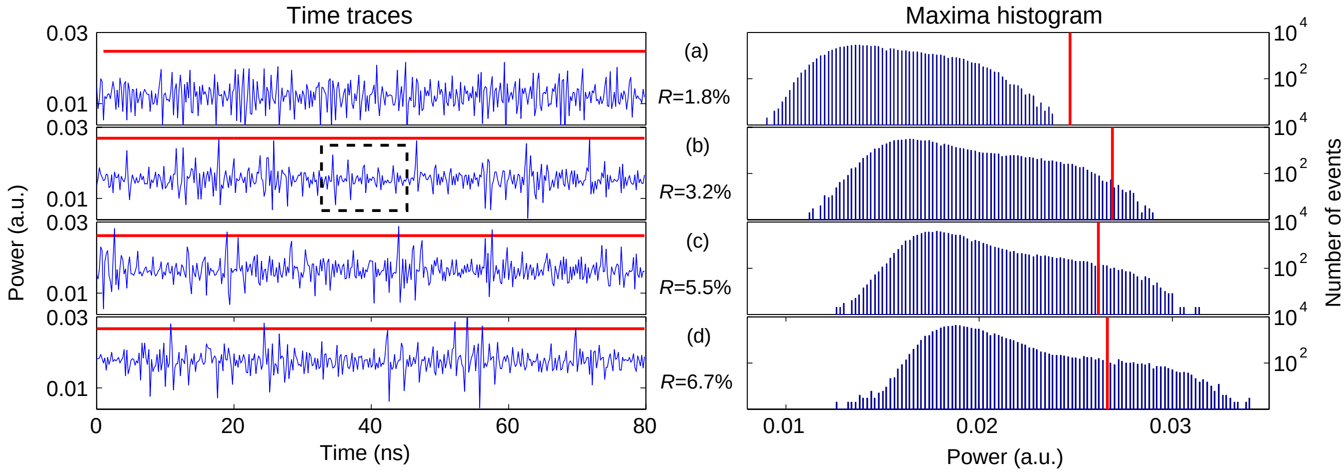

Fig. 2. (Color online) Time traces and histograms of the laser power for increasing R. Red horizontal and vertical lines are thresholds for extreme events.

induces a stretching of the statistics' shape, showing new concavity due to a higher number of events above the threshold in the statistics' tail. We achieve a maximum AI value (2.6) when $R = 7.7\%$. Figure 3 summarizes the increased number of extreme events as R increases (a) and the transition from Gaussian-shaped statistics of the pulses' power when R is small to long-tailed statistics with increasing probability for high-amplitude peaks when R is larger (b). Besides the AI criterion, the statistics' reshaping into a long-tailed shape is typically used to identify extreme events [11].

A careful analysis of Fig. 2 allows us, however, to distinguish between two kinds of extreme events. Indeed, although in chaotic dynamics most pulses are not regularly spaced in time, in our feedback laser system there are some that are clearly separated by the time-delay period, such as those shown in the dashed box of Fig. 2(b), and that are amplified when R increases. As in Figs. 2(b) and 2(c), extreme events appear as high lone peaks. Then, as shown in Fig. 2(d), bunches of small pulses that are separated by the time-delay period grow and end up by reaching the threshold as well; each pulse might thus count as an extreme event. These two situations of extreme events, either isolated pulses or bunches of pulses with time-delay periodicity, coexist in a single time series. The histograms of Fig. 2 consider both types of extreme events. To discriminate those two kinds of events, we considered that consecutive events separated by times below twice the delay (about 6 ns) belong to the same bunch. We find more extreme events of type I (isolated pulses) than of type II (bunches of pulses), although the ratio varies when increasing the mirror reflectivity. In a time series of 40 μs, we count 203 single events and 19 events in bunches (8%) when $R = 4.4\%$, while we have 959 single events and 272 events in bunches (22%) when $R = 7\%$. It is worth emphasizing that both types of extreme events are pulses (or pulse packages) that occur at randomly distributed time intervals much larger than the system time scale; hence they can be considered as rare events.

Even when extreme events appear as isolated pulses, they differ from what has been reported so far and keep the signature of the time-delayed feedback. This is better analyzed in Fig. 4. A single extreme event is basically made of a very short pulse surrounded by fast fluctuations. As shown in Fig. 4(a) and previously seen in Fig. 2, a single extreme event pulse is anticipated and followed by pulses that repeat periodically at the time-delay time scale. Figure 4(b) shows (in blue) 70 time series

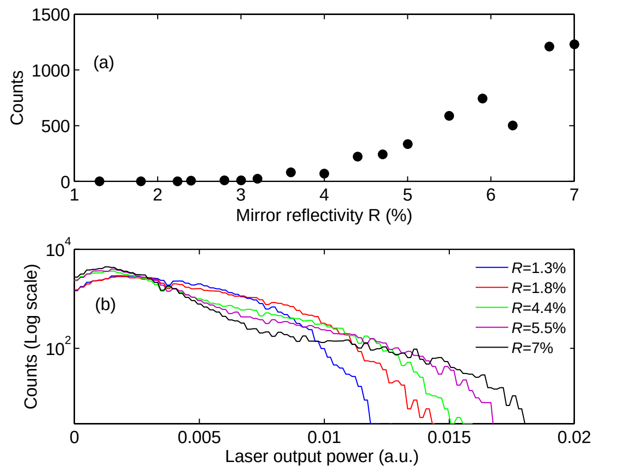

Fig. 3. (Color online) (a) Number of extreme events and (b) statistical distribution of the output power when increasing R.

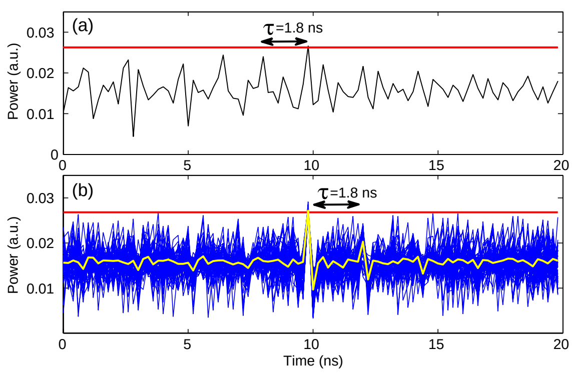

Fig. 4. (Color online) (a) Time series centered on one single extreme event and (b) superposition of 70 extreme events with corresponding averaged output power (yellow).

exhibiting single pulse extreme events when $R = 4.4\%$, each one being centered on the main pulse and plotted in a 20 ns time span. In all cases, the single extreme event has a well-defined pulse shape that is surrounded by pulses repeating at multiples of the time delay. From one time series to another, although the central peaks are superimposed, the smaller pulses at the time-delay periodicity remain uncorrelated. However, a general patterning is sketched when many traces are simultaneously plotted, showing power dropouts on each side of the extreme event, at multiples of the time delay and within a time interval of about 2–3 times the time-delay value. The same observation is made for other R values. We can conclude therefore that in our system extreme events are not merely single high-intensity pulses with immediate recovery to an average value as in [8] but rather high-intensity pulses coming along with very fast oscillations of smaller amplitude damped with the delay time scale.

Finally, we analyze in Fig. 5 the statistics of the time between extreme events. As has been recently measured in a spatially extended nonlinear optical system [11], the distribution of the waiting time between extreme events is thought to follow a Poissonian distribution when the time elapsed between extreme events numbered $k - 1$ and k is written in log scale: $w = \ln(t_k/t_{k-1})$. This is true also in our time-delayed system when R is small (dots) but increasing the feedback strength leads to a deviation from the log-Poissonian statistics (squares). The deviation occurs mostly for small values of w, where the events are distributed linearly in log scale but with a different slope. These small w values correspond to values of $t_k - t_{k-1}$ that are comparable to the time delay; hence the deviation originates from the delayed feedback. This is also expected from Fig. 4, where pulsating dynamics showing the periodicity of the time delay occur along with single extreme events. These pulses become extreme events when R increases, therefore adding new extreme events—of the type “bunch of pulses”—to the statistics. The time separation between these extreme events is still randomly distributed because the pulses at the time-delay periodicity remain uncorrelated from one bunch of pulses to another [Fig. 4(b)], but remains small in comparison to the time interval between single extreme events.

In conclusion, we reported experimentally on extreme events in an optical system with time-delay induced chaotic dynamics. The increased feedback strength yields an increased number of extreme events that fulfill the criterion relative to the AI, and exhibit statistics that show the typical long-tailed distribution. By contrast to other reported cases of extreme events, an extreme event pulse is anticipated and followed by pulses with delay periodicity that may exhibit extreme event properties when varying the feedback strength. The impact of noise on

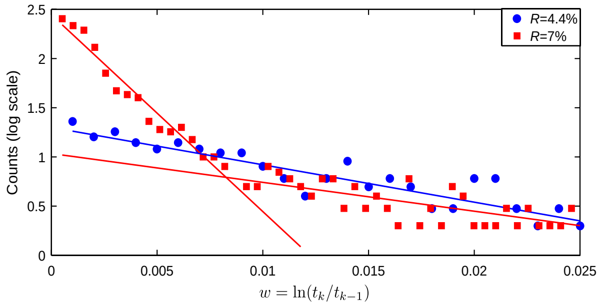

Fig. 5. (Color online) Statistical distribution of the time between extreme events for $R = 4.4\%$ (blue) and $R = 7\%$ (red).

the number of events and the statistics of the waiting times form an interesting question, which could be addressed by simulations of a rate equation model. Although the route to chaos is qualitatively well reproduced by a model with instantaneous phase conjugation [10], the analysis of extreme events might require one to account for the finite buildup time of the photorefractive grating [12].

The authors thank A. A. Grabar for the SPS crystal and M. Taki and E. Louvergneaux for their comments. This work is supported by the Conseil Régional de Lorraine, IAP P7/35 (BELSPO), and Agence Nationale de la Recherche (ANR) through the TINO project (ANR-12-JS03-005).

References

1. C. Kharif, E. Pelinovsky, and A. Slunyaev, *Rogue Waves in the Ocean* (Springer, 2009).
2. H. Bailung, S. K. Sharma, and Y. Nakamura, Phys. Rev. Lett. **107**, 255005 (2011).
3. D. R. Solli, C. Ropers, P. Koonath, and B. Jalali, Nature **450**, 1054 (2007).
4. J. M. Dudley, G. Genty, and B. J. Eggleton, Opt. Express **16**, 3644 (2008).
5. N. Akhmediev, A. Ankiewicz, and M. Taki, Phys. Lett. A **373**, 675 (2009).
6. J. M. Soto-Crespo, P. Grelu, and N. Akhmediev, Phys. Rev. E **84**, 016604 (2011).
7. M. G. Kovalsky, A. A. Hnilo, and J. R. Tredicce, Opt. Lett. **36**, 4449 (2011).
8. C. Bonatto, M. Feyereisen, S. Barland, M. Giudici, C. Masoller, J. R. Rios Leite, and J. R. Tredicce, Phys. Rev. Lett. **107**, 053901 (2011).
9. K. Schires, A. Hurtado, I. D. Henning, and M. J. Adams, Electron. Lett. **48**, 872 (2012).
10. M. Virte, A. Karsaklian Dal Bosco, D. Wolfersberger, and M. Sciamanna, Phys. Rev. A **84**, 043836 (2011).
11. S. Residori, U. Bortolozzo, A. Montina, F. Lenzini, and F. T. Arecchi, Fluct. Noise Lett. **11**, 1240014 (2012).
12. K. Green and B. Krauskopf, Opt. Commun. **231**, 383 (2004).